COMPUTATIONAL MODELLING STUDIES OF FeAl-X ALLOYS

(X: Pt, Ru, Pd and Ag)

By

CHRESTINAH SURRENDER MKHONTO

RESEARCH DISSERTATION

Submitted in fulfilment of the requirements for the degree of

MASTER OF SCIENCE

In

Physics

In the

FACULTY OF SCIENCES & AGRICULTURE

(School of Physical & Mineral Sciences)

At the

UNIVERSITY OF LIMPOPO (Turfloop Campus)

CO-SUPERVISOR: Prof H.R. Chauke

SUPERVISOR: Prof P.E. Ngoepe

2020

ABSTRACT

In this work, we present first-principles calculation on the structural, thermodynamic, mechanical and electronic stabilities of Fe-Al and FeAl-X (X: Pt, Pd, Ru and Ag) alloys at lower and high temperatures. These systems have recently attracted a lot of attention for both scientific and possible technological application in turbines, Steel-It coating, energy sector, boilers, pipes and automotive parts as a potential replacement of steel due to their excellent resistance to oxidation at high temperatures. However, they suffer limited room temperature ductility and a sharp drop in strength above 873 K.

We determined the lattice parameters, heats of formation, elastic constants, bulk to shear moduli, density of states, phonon dispersion curve and X-ray diffraction pattern for binary and ternary system at various concentrations between $0 \leq x \leq 10$. Furthermore, the lattice expansion, elastic constants, Gibbs free energy, X-ray diffraction pattern and radial distribution function were done on the most stable systems to determine the melting point of FeAl-X ternary systems.

A systematic investigation was performed on the stability of the Fe-Al alloys at zero K. We employed CASTEP code to evaluate the thermodynamic, elastic and electronic stability. Virtual crystal approximation was used to determine various atomic concentrations ($0 \leq x \leq 5$) of both Pt and Ru; this allowed more precise predictions on the materials' behaviour. Further analysis was done on the density of states to describe the behaviour of each phase near the Fermi level; these phases were observed at different percentage compositions. A supercell approach, DMol3 was also used to evaluate these systems at a larger scale ($0 \leq x \leq 50$). VASP and LAMMPS codes were used to determine the stability of these FeAl-X ternary systems at concentrations ($0 \leq x \leq 10$).

It was found that the equilibrium lattice parameters of the binary systems are in good agreement to within 2% with the available experimental data. The heats of formation showed that β2 FeAl phase was the most energetically stable system since it displayed the lowest value compared to all other binary systems. This observation accord well with the experimental phase diagram. It was also confirmed from the corresponding electronic DOS behaviour near the Fermi level.

Furthermore, the shear modulus (C') of these Fe-Al binary systems, i.e. FeAl, Fe_2Al_5, Fe_4Al_{13}, Fe_5Al_8, Fe_2Al and $FeAl_3$ were found to be positive fulfilling the condition of stability. The Fe_2Al_5 system was found to be the second most stable phase, followed by the monoclinic structure Fe_4Al_{13}. This observation was confirmed from the total DOS (where the Fermi level falls in the pseudogap, condition of stability).

We further employed virtual crystal approximation and supercell approaches to model various atomic compositions at $0 \leq x \leq 1$ and $0 \leq x \leq 50$ for Ag, Pt, Pd and Ru. The heats of formation, density of states and elastic constants were determined to describe the structural, thermodynamic and mechanical stability of these systems. It was found that the addition of Ag, Pt, Pd and Ru enhances the stability at lower atomic percentage composition below 0.5%. Interestingly, the addition of Pt and Ru was found to significantly improve the ductility of the ternary FeAl-X compound for 0.2 and 0.5 at. % compositions. These systems showed that the Fe-sublattice was the preferred doping site with promising improvement in strength on the properties. It was further deduced that Ag and Pd stabilize the FeAl-X system at atomic percentage compositions of 0.5 and 0.7 respectively.

Furthermore, a molecular dynamics-based LAMMPS-EAM was employed to model $Fe_{50-X}X_XAl$ doped systems with either Ag, Pt or Pd. The lattice site preferences of the dopant were deduced from their energy landscape. More importantly, Ag and Pd doped systems gave comparable transition temperatures to experimental findings of 1273 K and 1073 K, respectively. Their thermodynamic and mechanical stability trends showed promising properties for industrial applications, displaying stability at a high temperature below 1300 K. This was evident for Ag, Pt (0.5 at %) and Pd (0.7 at %) doping as was the most stable systems with respect to C_{ij}, ΔG, and RDF's which indicated to influence the elastic instability above 1200 K as well as the ductility of these systems. The XRD confirmed that the doped systems preserved the structural symmetry as expected.

DECLARATION

I declare that the dissertation hereby submitted to the University of Limpopo (Turfloop Campus) for the degree of Master of Science has not previously been submitted by me for a degree at this or any other university, that it is my own work both in design and execution, and that all material contained herein has been duly acknowledged.

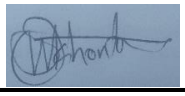

MS C.S. Mkhonto

[redacted] **Date: 02 March 2021**

ACKNOWLEDGEMENT

I would like to show gratitude towards:

- My Supervisor and advisor, Professor Hasani Richard Chauke and Co-supervisor Professor Phuti Ngoepe, who taught me never to go average but have the art of producing the best research and how to improvise.
- The Material Modelling Centre (MMC) members, who kept on encouraging and opening a door to assist, interesting sight of their view of life, academically and socially.
- My mom Elsie Malumane, Prof Chauke who have always encouraged me to pursue my studies through difficult times, encountering challenges.
- My spiritual Father Apostle J Daniels as well as Pastor Maiker, Pastor Jones we are spirit beings, at times one would feel hopeless, I felt I belong in a place of love, I am this far because I found God through Jesus to secure my life.
- Sponsors of this project: University of Limpopo (UL), Titanium Centre of Competence (TiCoC) and the National Research Foundation (NRF).

DEDICATIONS

This work is dedicated to:

My beautiful mother and sister

Elsie Malumane and Pretty Mkhonto

LIST OF TABLES

Chapter 1

In this chapter, we give a brief review of the theoretical and experimental studies of Iron-aluminides (Fe-Al) systems. Firstly, we give an overview and analysis on the binary systems, and elastic effect associated with ternary systems. Different types of binary systems will be presented followed by ternary FeAl-X as well as temperature dependence alloying with platinum (Pt), ruthenium (Ru), palladium (Pd) and silver (Ag). Platinum group metals will be briefly discussed and summarized along with the structural properties, intention of the study, aim and objectives and lastly, an outline of the dissertation.

1.1 Rationale

Iron-aluminides (Fe-Al) based alloys have attracted a lot of attention for their potential application in turbines, automotive parts, and steel-IT coating, due to their excellent resistance to oxidation at high temperatures, making them excellent candidates for high-temperature applications [1, 2]. These alloys are known to be cost-effective and their desirable strength is compatible with many ferritic and austenitic stainless steel [3].

However, these materials have been found to suffer from limited room temperature ductility and a sharp drop in strength above 873 K, making these alloys of less significance for use as structural materials [4]. Various attempts were made to improve the strength and ductility of the Fe-Al alloys, which include intercalation of third metal of Pt and Ru [5]. Previous studies have shown that ternary alloying can significantly enhance the structural, mechanical and thermodynamic properties in various alloys including Fe-Al binary systems [6]. Elements such as carbon, chromium and titanium have been investigated for ternary alloying in Fe-Al; however, were found to cause precipitation leading to decrease in strength [7].

Ternary addition of Pt, Pd, Ag, and Ru may significantly improve the ductility of the material through better control of composition and microstructures since Pt is a soft, ductile, resistant to oxidation, high-temperature corrosion and has

widespread catalytic use; whereas Ru is a hard, brittle but valuable as an addition to other metals and also as a catalyst. Pd and Ag, on the other hand, showed promising properties. These alloying elements have been reported to form steel components with increased strength, ductility, toughness; much resistance to environmental embrittlement and high-temperature gaseous conditions [6].

We employed CASTEP code as embedded in Materials Studio platform [8, 9] to investigate the elastic properties and density of states for the Fe-Al alloys. The PHONON code [10, 11] embedded in MedeA was used to determine the phonon dispersion curve and temperature dependence. This will allow more precise predictions than experiments can handle.

In this study, we perform first-principles calculations to investigate the structural, thermodynamic, electronic and mechanical properties of the binary Fe-Al alloys, with various Fe and Al concentrations. The effect of ternary alloying with Pt, Ru, Pd and Ag on the properties of FeAl system will be investigated. The composition of the alloying elements will be controlled using two approaches, that is the Virtual Crystal Approximation (VCA) which allow calculations on disordered systems to be carried out at the same cost as calculations for ordered structures [12]. The supercell approach, on the other hand, gives fewer compositions and the calculation becomes more experimental for small concentration (since the supercell has to be increased to achieve small concentration).

To allow more precise predictions and understanding of thermodynamic and mechanical properties, vibrational frequencies and configuration of systems for ternary FeAl-X doped systems, we determine the structural, electronic, elastic, phonons, RDF's, XRD's and temperature dependence from the binary FeAl alloy as the ground state to identify the stability condition of different systems.

1.2 Literature review

1.2.1 **Fe-Al**

Iron-aluminides (Fe-Al) based alloys are known to exhibit a combination of excellent oxidation and corrosion resistance after heat treating; making them

potential candidates for high-temperature applications such as in ferritic and austenitic stainless steel [13]. Moreover, these alloys are relatively cost-effective and display high ductility, strength, and low density. The oxidation resistance and low density of Fe-Al are believed to improve with Al content and are the main contributing factors for Fe-Al candidate role as a high-temperature material. However, Marker *et al*. found that Iron-aluminides based alloys may suffer from limited room temperature ductility and a sharp drop in strength above 873 K [14]. Various investigations were done on the Fe-Al systems to determine their competency in turbines, automotive parts and Industrial paint coatings engineered with stainless steel for superior protection [15]. These investigations were inspected by scanning electron microscopy (SEM), and chemical composition of the equilibrium phases, obtained by electron probe microanalysis (EPMA), crystal structures, the variation of the lattice parameters by X-ray diffraction (XRD) and differential thermal analysis (DTA) was applied to measure all types of transition temperatures. However, the Al-rich part of the Fe-Al phase diagram above 50 at. % Al has not yet been finally determined [15, 16]. Five different intermetallic phases (FeAl, $FeAl_2$, Fe_2Al_5, Fe_4Al_{13}, and Fe_5Al_8), were identified between 50 and 100 at. % composition range, and their crystal structures (see figure 1-1) [17]. The FeAl phase has a simple cubic (β2-type) crystal structure; whereas the Al-rich intermetallic phases, Fe_2Al_5 and Fe_4Al_{13} have complex structures of the orthorhombic and monoclinic type, respectively [18]. The high-temperature phase Fe_5Al_8, which was designated only as ***ε-phase*** in the literature due to its long time unknown structure, decomposed on cooling in a rapid eutectoid reaction and cannot be quenched at room temperature. This is due to its excellent oxidation and suffixation resistance [19, 20, 21].

Moreover, the binary phase diagram of the pure Fe-Al system is rather complex. In the Fe-rich side, there are two ordered phases β2 (FeAl) with a space group of Pm-3m and D03 (Fe_3Al) with a space group of Fm-3m and disordered body-centred α phase [22]. These phases are mutually separated by two-phase regions α + β2 and α + D03 [23]. At room temperature the Fe-Al alloy with 20 at. % Al belongs to the α + D03 region, around 23 at. % Al the structure becomes single-phase D03, at about 37 at. % Al a line of second-order transition separates

the D03 region and β2 region, persisting above 40 at. % Al. Intermetallic alloys with aluminium [24] content over 60 at. % is in the area of the phase equilibrium diagram that is considerably less investigated in comparison to the high-symmetry Fe_3Al and FeAl phases. The mixture of FeAl + $FeAl_2$ crystals results from the eutectoid reaction of the ε (Fe_5Al_8 and Fe_8Al_5) with a space group of I-43m with phase decomposition at 1365 K [25] . Thus, a single-phase homogeneous sinter which is composed of $FeAl_2$ with a space group of 14/mcm perytectoid grains was observed for the sample with aluminium content amounting to 68 at. % [26]. Recently, advances in the understanding of environmental embrittlement in intermetallic, including iron-aluminides, have resulted in a renewed interest in this system for structural applications [27].

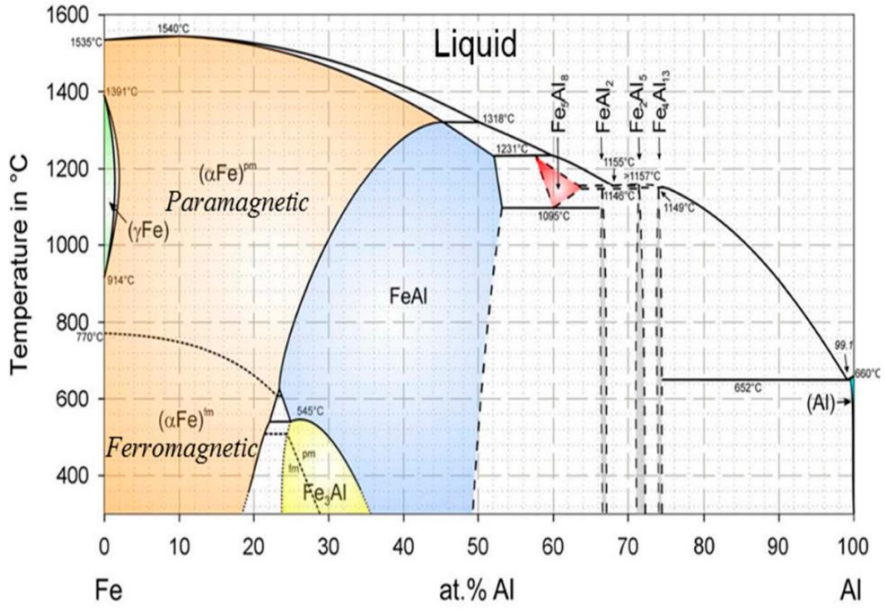

Figure 1-1**:** Binary phase diagram of Fe-Al alloys [17].

The β2 type intermetallic compounds that are composed of the iron group transition metal and aluminium, for example, NiAl, CoAl, and FeAl have been notable as high-temperature practical materials, and they have been investigated for mechanical, physical and structural properties [28]. Comparison of the diffusional behaviour among the NiAl, CoAl and FeAl phases is important to discuss the diffusion mechanisms because they have structural point defects in a different degree with each other. Hence, it is important to understand their

diffusional behaviour, which is closely related to the various physical properties such as phase transformation, deformation, and crystal growth [29]. Furthermore, the diffusion behaviour is expected to show complications in comparison with the pure metals, because of their peculiar point defects behaviour.

More work done previously illustrates the local density total energy and electronic structure calculations for NiAl, Ni_3Al, FeAl and Fe_3Al yielding lattice constants which agree well with the experiment. Cu_3Au and DO_3 structures were found as the ground states for Ni_3Al and Fe_3Al, respectively. Moreover, NiAl was found to be paramagnetic while Fe_3Al is ferromagnetic; and Ni_3Al and FeAl showed weak itinerant magnetic phases [30]. However, the addition of carbon to FeAl has not been successful as it leads to precipitation of graphite which causes a decrease in strength. In comparing with the previous measurements on ordered CoGa and FeAl, we find that structural vacancies are highly unlikely in these alloys and that thermal vacancies can satisfactorily account for the observed composition dependence as well as the temperature dependence of vacancy concentrations. A systematic DFT calculations was performed for the defect structure and concentration on β2 FeAl. Ab-initio was used for the binding energies calculations to make di-vacancy in stoichiometric for β2-FeAl. A multi-physics computational approach is utilized in order to analyse the dissimilar metal aluminium-to-steel friction stir welding (FSW) process and the formation of intermetallic compounds (IMCs) within the FSW joint. The thermodynamic stability of these compounds (Fe_3Al, FeAl, $FeAl_2$, Fe_2Al_5, $FeAl_3$ and Fe_4Al_{13}) is typically not described in thermodynamic databases. To overcome such limitation, a series of quantum-mechanical calculations are carried out. Using crystallographic data [31].

Computational analysis of the intermetallic formation during the dissimilar metal aluminum-to-steel friction stir welding process was done to address the problem of the effect of the friction stir welding process parameters on the extent of intermetallic compound formation. A multi-physics computational framework has been developed and applied to the case of dissimilar metal friction stir welding involving commercially pure (CP) aluminum and AISI 1005 low-carbon steel. To ensure computational accuracy and stability at a reasonable computational cost,

a mass-scaling algorithm is employed, which adaptively adjusts the material density in the finite elements controlling the stable time increment without significantly (< 1%) affecting the results [32].

1.2.2 **Ternary addition of FeAl-X**

The addition of Pt and Ru may significantly improve the ductility of the material through better control of composition and microstructures, especially improvements in tensile properties. Moreover, it has been reported to form steel components with improved strength, ductility, toughness and much resistance to environmental embrittlement and high-temperature gaseous conditions [33, 34].

Previous experimental studies have reported that a small amount of precious metals such as Pt, Ru, Pd, and Ag in FeAl improves the oxidation and corrosion resistance properties of FeAl alloy. An atomic concentration of 0.2 % Ru was found to significantly improve the corrosion and oxidation resistance of the Fe-Al alloys. Moreover, mechanical alloying produced four alloys i.e. FeAl-0.2 at. % Pd, FeAl-0.2 at. % Ru, FeAl-0.5 at. % Ag, FeAl-0.5 at. % Pt. on the other hand, concentrations above 0.5 at. % did not improve the oxidation and corrosion properties of the materials and in some cases even decreased the resistance to corrosion [25, 33].

This low-Al part of the phase diagram, the ternary system of Ru-Fe-Al at 1473 K was discovered (see figure 1-2) [27]. The β2-phase Ru-Al possesses an outstanding combination of properties, including ductility at room temperature, resistance to oxidation and corrosion, and phase stability up to its melting point which is above 2300 K [27].

Ru-steel Couplings type that is completely metallic, flexible though torsionally rigid, are available in various manufactures, plain or with two flexible elements, Sizeable length spacers and can also be manufactured upon a design which can be found to be of use in textile industries, chemical industries, petrochemical industries, and ventilation, etc.

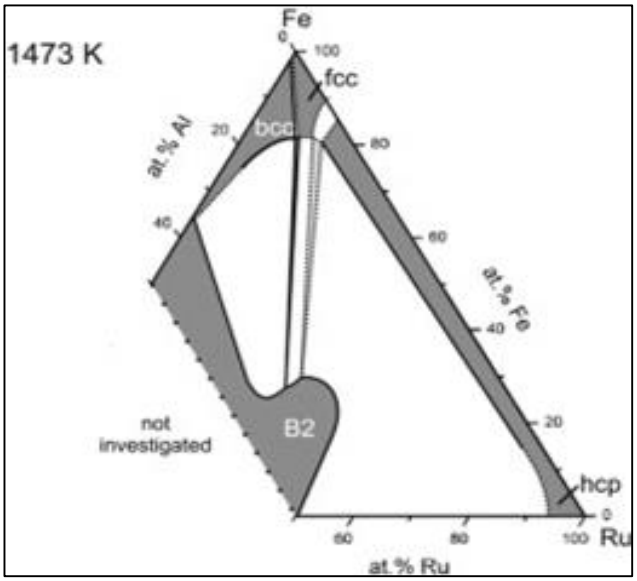

Figure 1-2: Ru-Fe-Al phase diagram at 1473 K for aluminium contents below 50 at. %; the dashed lines represent uncertain boundaries that still have to be experimentally confirmed [27].

DFT was used to investigate the structural, electronic and mechanical properties of Ru and Pt doped FeAl intermetallic. We employed the virtual crystal approximation (VCA) which allowed calculations on disordered systems to be carried out at the same cost as calculations for ordered structures. Small amounts of up to 0.5 at. % Pt and up to 0.2 at. % Ru were investigated to complement the previous experimental findings) [35].

It was established that additions of 0.2 at. % Ru to a Fe-40 at. % Al alloy improved the corrosion and oxidation resistance of the Fe-Al alloys. However, the findings revealed that the non-equilibrium processing significantly refined the grain size of the material. It was found that the coated materials effectively enhanced the oxidation and corrosion resistance of mild. Iron aluminides based on Fe_3Al and FeAl are highly oxidation and corrosion resistant and have potential for elevated temperature structural applications [36].

The Fe-Rich part of Fe-Al-Pt

Aluminium is one of the amphoteric elements incorporated into the Pt-Fe system to offer strong Pt-Al and Fe-Al covalent bonds, which not only weaken the

adsorption energy of the surface Pt atoms by giving rise to a compressive strain but also prevent the Fe atoms from further migrating and dissolving. With exception to a sample containing Pd, which shows sub-surface oxidation; Corrosion testing of the sintered compacts showed that the Ru and Pt containing alloys performed better than the as-cast alloys. Both the Pd and Ag containing samples suffered from pitting, and the Pd sample was corroded away completely during the test in a 3.8M H_2SO_4 solution [37]. It was concluded that there was a significant effect on the microstructure of the FeAl alloy due to the processing route used and that this also produced a significant effect on the hardness and corrosion resistance, with both improving when non-equilibrium processing was used [38].

Therefore, the corrosion behaviour of Fe_3Al intermetallic alloyed with 1 at. % Ag, Au, Pt, and Pd have been evaluated using polarisation curves, linear polarization resistance, and electrochemical impedance spectroscopy measurements compared with Ni-based alloy, namely Inconel 600 [39, 40].

Recent studies showed the effect of adding 1 at. % noble elements such as Pt, Pd, Ag, and Au on the oxidation resistance of Fe_3Al intermetallic alloy which has been carried out at the different mass range. Thus, the addition of Ag increased the mass gain, whereas Pd decreased it [39, 41]. In most of the cases, the scales were predominantly formed by Al_2O_3 with minor amounts of Fe_2O_3 and the scale spallation was found when the noble elements were randomly distributed on the surface [42], but when they were finely distributed, the scale did not spall. Thus, in all cases, the mass gain for Fe_3Al alloy was lower than Inconel 600 type alloy.

1.2.3 **Temperature dependence**

Previous studies stated that platinum group metal alloys (PGM) are of interest in industries as high-temperature materials. The PGMs offer the hope of developing exceptional alloys capable to withstand ultra-high temperature, at least 400 ^oC higher than the existing Ni-based alloys. These alloys have a unique combination of exceptional environmental resistance and high melting temperature. However, the PGM intermetallic alloys have very low ductility at room temperature [43].

PGM were found to be ductile and the third most abundant element found in the earth's crust. Platinum aluminium precipitates have the cubic $L1_2$ structure at high temperature and can be disfigured to a tetragonal. Chauke *et al.* have also made a study of the four different phases, their strength, weaknesses, and characteristics and how they react when affected by temperature [43]. The FeAl phase has a melting temperature of 1591 K and the application of thermodynamic calculations was used to mimic the change in Gibbs free energy for Fe_2Al_5 and $FeAl_3$ systems, showing the formation of Fe_2Al_5 first and followed by $FeAl_3$ compound during the welding process. It was reported that at 1273 K, 723 K and 293 K temperature of Fe_2Al_5 and $FeAl_3$ have ΔG of $\pm$165.828 $eV.K^{-1}$, $\pm$ 93.278 $eV.K^{-1}$ and $\pm$ 3.109 $eV.K^{-1}$ [44], respectively. Previous experimental findings indicated that CsCl carries the same symmetry of I-43m, similar to that of β2 FeAl system which also predicted to have ΔG_f^o energy of -4.294954 eV [45].

Mechanical properties

Intermetallic alloys based aluminides, especially FeAl (β2) and Fe_3Al (D03) phases, are known as materials with unique physical and mechanical properties [46]. Studies of FeAI alloys for high-temperature structural applications have been expanded to include improved weldability for crack-free joining. A base FeAI (β2-phase) binary alloy composition of Fe-36 at. % Al appears to offer a nearly optimum combination of oxidation/corrosion resistance and mechanical behaviour. Further studies of room-temperature brittleness of FeAI alloys have shown that hydrogen released at crack-tips from moisture in the air causes low ductility at room temperature, so that these alloys are not inherently brittle, but are sensitive to environmental effects. Thus, alloying effects that optimize mechanical behaviour must be balanced with those that produce acceptable weldability. Weldable FeAl alloys also have near-term potential as weld-overlay cladding upon conventional structural steels and other alloys to take advantage of their excellent oxidation/corrosion resistance [47].

However, the past four decades' research on intermetallic compounds has at least largely focussed upon mechanical properties, especially involving low-temperature ductility and high-temperature strength. Unfortunately, many intermetallics are brittle or semi-brittle at room temperature, rendering them

difficult to fabricate or utilize in structural applications. In recent years it has been found that brittleness in several aluminides and silicides arises from an extrinsic environmental effect that can be overcome by alloying, microstructural control or coating. Examples of such compounds that are adversely affected by moist environments are FeAl, Fe_3Al, Ni_3Al, and Ni_3Si. Now, intermetallic which is of interest for elevated temperature applications, such as the titanium aluminides, $MoSi_2$ and several Laves phases, often display inadequate creep resistance [48]. In some cases, such resistance has been improved by alloying or compositing. Other key issue for many intermetallics is the ability to process them cost-effectively. Finally, for most compounds, an insufficient database exists for designers to have confidence in replacing existing materials with intermetallic. These alloys are based on aluminides, especially FeAl (β2) and Fe_3Al (D03) phases, which are known as materials with unique physical and mechanical properties [46].

1.3 Structural properties

The Fe-Al alloys consist of eleven (11) types of structures with different compositions, as listed in table1-1. The atomic arrangements of the structures are shown in figure1-3. A series of Fe-Al binary alloys with nominal compositions between 57 and 67 at. % Al were produced from high purity Fe (99.98 wt. %) and Al (99.99 wt. %).

Table 1-1: components of the phase diagram

In all cases, the process of structural analysis was performed to determine the actual composition of alloys. The analyzed compositions, which are listed in table1-1, were found to agree with the nominal composition within 1.0 at. % Al. There is a general agreement in the literature that the high-temperature phase Fe_5Al_8 forms peritectically from the liquid and FeAl and decomposes by a eutectoid reaction into FeAl and $FeAl_2$. However, their reaction temperature varies strongly from 1480 K to 1505 K for the peritectic reaction and from 1353 K to 1376 K for the eutectoid reaction through thermal analysis. Fe_5Al_8 and Fe_2Al_5 form eutectic at 68-69 at. % Al and at a temperature in the range 1426 K to 1439

K. However, there is controversy about the reaction type in the formation of Fe_4Al_{13}. The question is whether the phase form peritectically or congruently from the melting point; most studied assessments tend to form peritectically. Moreover, it was reported that either eutectoid or perictectic, the composition is close to that of Fe_4Al_{13} [4, 49].

Structures	Space group	Prototype	Lattice Parameters (Å)	Volume ($Å^3$/atom)
Fe	Im-3m	-	a=2.862	10.367
Fe_2Al	14/mcm	Fe_2Al	a=b=4.052	67.777
			c=5.086	
Fe_2Al_5	P6_3/mmc	Fe_2Al_5	a=7.656	385.976
			b=6.415	
			c=4.218	
Fe_3Al	Fm-3m	$Fe_{2.8}Al$	a= 5.585	177.063
Fe_4Al_{13}	C2/m	Fe_4Al_{13}	a=15.492	726.527
			b=8.078	
			c=12.471	
Fe_5Al_8	I-43m	Cu_5Zn_8	a= 8.976	329.922
FeAl	Pm-3m	CsCl	a= 2.910	23.192
$FeAl_2$	I4/mcm	$FeAl_2$	a=4.8745	67.777
			b=6.4545	
			c=8.7361	
Fe_5Al_2	P6_3mmc	Fe_2Al_5	a=b=7.019	319.050
			c=7.472	
$FeAl_3$	Fm-3m	$FeAl_{2.8}$	a=6.654	235.650
			b=7.478	
			c= 4.633	
$Fe_{13}Al_4$	C2/m	$Fe_{13}Al_4$	a=15.489	
			b=8.036	584.347
			c=12.488	
Fe_8Al_5	I-43m	Cu_8Zn_5	a=8.973	302.085
Al	Fm-3m	-	a=4.041	16.583

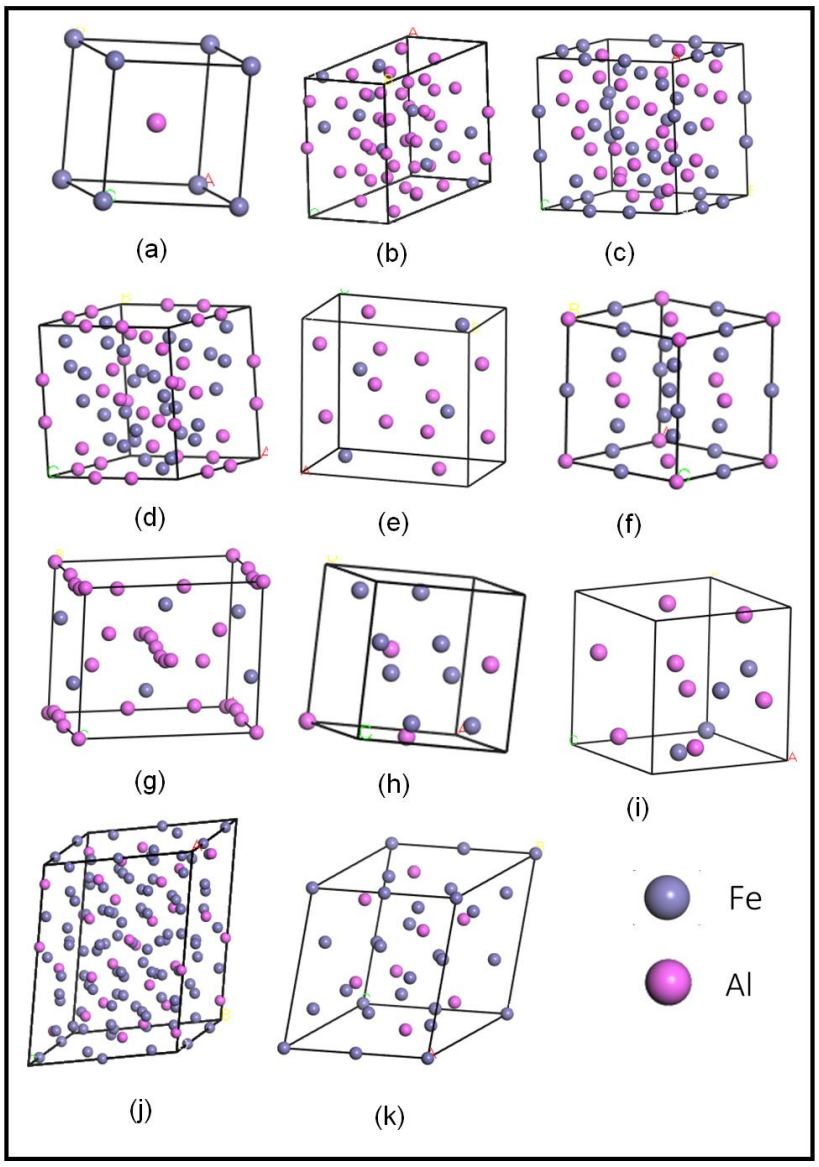

Figure 1-3: The atomic arrangement of different Fe-Al structures (a) FeAl (Pm-3m), (b) Fe_4Al_{13} (C2/m), (c) Fe_5Al_8 (I-43M), (d) Fe_8Al_5 (I-43m), (e) $FeAl_3$ (Fm-3m) (f) Fe_3Al (Fm-3m), (g) Fe_2Al_5 (P6_/mmc), (h) Fe_2Al (14/mcm), (i) $FeAl_2$ (I4/mcm) and (j) $Fe_{13}Al_4$ (C2/m) (k) Fe_5Al_2 (P6_3mc) [50].

The β2 FeAl structure has a cubic lattice parameter of a= 2.910 Å with a volume of 23.192 $Å^3$/atom. The $FeAl_2$ structure has triclinic lattice parameters of a=4.8745, b=6.4545, c=7.472 Å and volume of 23.192 $Å^3$/atom, the Fe_2Al_5 has an orthorhombic lattice parameter of a=7.656, b=6.415, c=4.218 Å and volume of 385.976 $Å^3$/atom where else Fe_4Al_{13} has lattice parameter of a=15.492,

b=8.078, c=12.471 Å and volume of 726.527 $Å^3$/atom as monoclinic structure. The remaining structures are inverse; hence they contain similar lattice systems.

1.4 Intentions of the study

The use of iron-aluminides in turbines, automotive parts and steel coating purposes in aggressive and corrosive environments has brought about great demand [33]. These developments have led to a demand for a continued search of more efficient precious metal alloys to enable and satisfy the requirements for enhancing stability and high-temperature properties. Their physical properties include low cost, low density, resistance to oxidation which improves strength and ductility for application [23]. Firstly, the convergence test calculation will be done in order to determine the appropriate k-points and cut-off energy. The equilibrium lattice constants will be deduced for geometry optimization calculation of binary and ternary structures. More importantly, the influence of ternary addition, FeAl-X (X= Pt, Pd, Ru, and Ag) will be evaluated by determining the lattice parameters, heats of formation, elastic properties, the density of states and X-ray diffraction pattern. Moreover, their phonon dispersion curves, radial distribution function, temperature dependence on the structural, electronic and mechanical properties will be performed. Lastly, the investigation of FeAl-X systems using both VCA and supercell approach will be done to establish their stability at 0 K. However, the temperature dependence on these systems will be performed using LAMMPS-EAM (large scale atomic molecular/massively parallel simulator-embedded atomic method) code [51].

Both applications of CASTEP and VASP will be employed within GGA-PBE. This functional is introduced to deal with correlated systems [55]. We employed planewave pseudopotential techniques as embodied in the Vienna Ab-initio simulation package (VASP) [52] code to describe the fundamental properties of the systems. The PHONON code [10] was used to determine their vibrational stability.

The main purpose of this work is to attain an elementary and fundamental understanding of the stabilities of transition metals of iron-aluminides, especially

the thermodynamic, mechanical, electronic and structural properties of these alloys. We investigated the ground state properties and stability of different structural phases; namely FeAl (Pm-3m), Fe_4Al_{13} (C2/m), Fe_5Al_8 (I-43M), Fe_8Al_5 (I-43m), $FeAl_3$ (Fm-3m), Fe_3Al (Fm-3m), Fe_2Al_5 (P6_/mmc), Fe_2Al (14/mcm), $FeAl_2$ (I4/mcm), $Fe_{13}Al_4$ (C2/m) and Fe_5Al_2 (P6_3mc). It was found that Fe_2Al is the least stable system and Fe_4Al_{13} as the third most stable, Fe_2Al_5 as the second most stable system and FeAl as the most stable binary phase.

The relative phase transition will also be determined with respect to temperature. Moreover, Pt, Pd, Ru, and Ag alloying will be performed on the FeAl for various concentrations. This will allow predictions on the effect of these precious metals.

Previous studies have shown that these transition metals have an outstanding effect on the structural, thermodynamic and electronic properties of FeAl. In the case of structural and thermodynamic properties, the equilibrium lattice parameters and heats of formation (ΔH_f) were calculated to indicate stable and meta-stable phases. It will be shown that the most stable and least stable phase yielded positive ΔH_f ($\Delta H_f > 0$) and negative ΔH_f ($\Delta H_f < 0$), respectively. It will be shown that the $Fe_{50}Al_{50}$ system is dormant, in agreement with the available phase diagram [17].

Further investigations on the stability will be performed by computing the electronic density of states (DOS), in particular observing electronic state's behaviour near the Fermi level ($E-E_f = 0$) for the possible pseudo gaps. To validate our work, we will also investigate mechanical properties; whereby we will perform first-principles phonon dispersion calculations, which play an important role in determining vibrational frequencies of materials. The elastic constants, bulk modulus, and shear modulus were used to evaluate the elasticity of Fe-Al and FeAl-X. The findings will be compared with available previous experimental findings.

1.5 Aim and objectives

The proposed research aims to investigate the structural, electronic, mechanical and thermodynamic stability of Fe-Al and FeAl-X intermetallic alloys at high temperatures.

The objectives of the studied systems are to:

I. Determine the k-points and cut-off energy convergence of Fe-Al alloys,
II. perform full geometry optimization of binary and ternary structures,
III. investigate the influence of ternary addition, FeAl-X (X= Pt, Ru, Pd and Ag for $0 \leq x \leq 10$),
IV. determine the lattice parameters, heats of formation, elastic properties, density of states and X-ray diffraction pattern of Fe-Al,
V. determine phonon dispersion curves,
VI. determine temperature effect on the structural, electronic and mechanical properties on FeAl-X,
VII. investigate FeAl-X ternary alloying using the supercell approach and LAMMPS code.
VIII. determine the lattice parameters, Gibbs free energy, elastic properties, radial distribution function and X-ray diffraction pattern of FeAl-X.

1.6 Outline of the dissertation

This dissertation is divided into seven chapters.

CHAPTER 1: Deals with the Rationale, literature review on Fe-Al alloys, Ternary additions, and temperature dependence; furthermore, it deals with structural properties, the intention of the study, aim and objectives and lastly, an outline of the dissertation.

CHAPTER 2: Provides an introduction to the method used and various software programs such as density functional theory, approximation methods i.e. local density approximation (LDA) and generalized gradient approximation (GGA), plane-wave pseudopotential method and simulation codes such as CASTEP, VASP, VCA, DMol3 and LAMMPS code (MD).

CHAPTER 3: Focuses on the cut-off energy, k-points, equilibrium lattice constants, mechanical stability, heats of formation, the density of states and phonon dispersion curves.

CHAPTER 4: Focuses on the heats of formation, elastic constants, density of states and X-ray diffraction pattern of $Fe_{50}Al_{50}$ and FeAl-X systems.

CHAPTER 5: Provides results on the temperature dependence of FeAl and FeAl-X by creating a supercell, considering properties such as the heats of formation, elastic constants and density of states.

CHAPTER 6: Focuses on temperature dependence using DMol3 technique and lattice expansion using LAMMPS code.

CHAPTER 7: Focuses on the summary and conclusion on the current work done to date as well as recommendations.

REFERENCES

Lastly provides references used to support the research work given.

Chapter 2

METHODOLOGY

In this chapter, we discuss the computational techniques used to investigate the properties of $Fe_{50-X}Al_{50}$-X systems. We have used the Ab-initio quantum mechanical methods based on density functional theory (DFT) [53], such as local density approximation (LDA), generalized gradient approximation (GGA), planewave pseudopotential methods implemented in the Cambridge sequential total energy package (CASTEP) [54], and the Vienna Ab-initio simulation package (VASP) [52, 55]. For Molecular dynamics (MD) calculations, we used Large-scale Atomic/Molecular Massively Parallel Simulator (LAMMPS) code [56] and DMol3 [57].

Introduction

In the current study, we employed density functional theory for predicting the ground-state energy of many-body systems. The DFT has made it feasible to calculate the ground state energy and charge density with remarkably accurate results for real solids [58]. Several factors have contributed to the present success of Ab-initio calculations for real material systems. The first is the availability of modern high-speed computers.

The DFT based planewave methods, CASTEP was to calculate convergence test, lattice parameters, heats of formation, density of states, elastic constants and XRD, whereas the VASP code was used to determine vibrational properties using phonon dispersion curves for binary Fe-Al and ternary FeAl-X phases. Furthermore, we employed the virtual crystal approximation (VCA) for the most preferred binary phase into a mixture/solution to determine suitable sub-lattice for alloying. This has made it possible to carry out calculations on real materials with sufficient accuracy which provided a meaningful detailed comparison with experimental measurements.

Now, the MD-based calculations were computed using $Dmol^3$ [57] and LAMMPS [51] codes. This is a computer simulation method for analysing the physical

movements of atoms and molecules. The LAMMPS code in particular embedded in MedeA [52] software package has been used. It is a method used to investigate the phase transformation of various system and in this case, various concentrations for FeAl-X alloys were investigated. MD is also designed to generate various compositions for different phases. This has served the purpose to be able to determine lattice expansion, temperature dependence, Radial distribution functions, X-ray diffraction pattern for ternary FeAl-X systems.

The DMol3 code has been used to calculate the temperature dependence of various composite for Fe-Al and Fe-Al-X systems. We firstly determined suitable time step that is, calculating the time interval for the system to function smoothly for it to be able to reach a steady-state. We also calculated the binding energy to determine at what temperature is the system able to withstand and maintain its symmetry (stability).

Furthermore, the advantage of using the DMol3 code is that it can model electronic structures and properties of organic and inorganic molecules, molecular crystals, covalent solids, metallic solids, as well as infinite surfaces.

The LAMMPS code has been used to calculate the effect of temperature on FeAl-X systems. It was employed to determine transition temperature, lattice expansion, heat capacity, entropy and enthalpy change, Gibbs free energy, elastic constants, RDF's as well as XRD at various concentrations. This code is highly robust and tries hard to flag many kinds of errors and warnings in the calculations run, as well as simulate designs to exploit large scale parallel computer architecture.

In the next section, we describe the DFT of many-body ground state energy of systems.

2.1 Density functional theory

Density functional theory (DFT) [53] is a quantum mechanical method used to investigate the ground state energies of many-body systems. Presently, it is the most successful approach to compute the electronic structure of materials.

Amongst many, it is the most popular and versatile methods available in condensed-matter physics, computational physics, and computational chemistry [8]. This method has made it feasible to calculate the charge density with remarkably accurate results for real solids. The first Hohenberg-Kohn (H-K) [59] theorem illustrates that the ground state properties of many-body systems can be uniquely determined by an electron density that depends on three spatial coordinates

$$E = E[\rho(r)], \tag{2-1}$$

where *E* is the total energy and ρ is the density. A guide to designing a meaningful DFT calculation has been described by Mattson *et al.* and Slater [53, 60].

The electron density and the total energy depend on the type and arrangements of the atomic nuclei. Therefore, one can write,

$$E = E[\rho(r), \{ R_{\propto} \}] \tag{2-2}$$

where the set $\{ R_{\propto} \}$ R_a denotes the positions of all atoms, α, in the system under consideration. Equation (2-2) is important for the understanding of electronic, structural and dynamic properties of matter at atomic-scale. It can also be used for, predicting the equilibrium structure of solids, the reconstruction of surfaces and equilibrium geometry of molecules adsorbed on the surfaces. The derivative of the total energy equation (2-2) with respect to the nuclear position of an atom gives the force acting on that atom. This enabled the efficient search for stable structures, the study of dynamical processes such as diffusion or the reaction of molecules on the surfaces. Most of the considerations in DFT here are based on the Born-Oppenheimer approximation which is assumed that the motions of the electrons are infinitely faster than those of the nuclei. This implies that the electronic structure is calculated for a fixed atomic arrangement and the atoms are then moved according to classical mechanics [61, 62].

In DFT, the total energy equation (2-1) is decomposed into three contributions, kinetic energy and coulomb energy due to classical electrostatic interactions among all charged particles in the system and a term called the exchange-correlation energy that captures all many-body interactions,

$$E = T_O + U + E_{xc} . \quad (2\text{-}3)$$

The most straightforward term is the Coulomb Energy U (the second term). It is purely classical and contains the electrostatic energy arising from the Coulomb attraction between electrons and nuclei, the repulsion between all electronic charges and the repulsion between nuclei,

$$\mathrm{U} = \mathrm{U_{en}} + \mathrm{U_{ee}} + \mathrm{U_{nn}}, \quad (2\text{-}4a)$$

with

$$\mathrm{U_{en}} = -\mathrm{e}^2 \sum_{\propto} \mathrm{Z}_{\propto} \int \frac{\rho(\mathrm{r})}{|\,\mathrm{r}-\mathrm{R}_{\propto}\,|}\,\mathrm{dr}, \quad (2\text{-}4b)$$

$$\mathrm{U_{ee}} = \mathrm{e}^2 \iint \frac{\rho(\mathrm{r})\rho(\mathrm{r}')}{|\,\mathrm{r}-\mathrm{r}'\,|}\,\mathrm{drdr}', \quad (2\text{-}4c)$$

$$\mathrm{U_{nn}} = \mathrm{e}^2 \sum_{\propto\propto'} \iint \frac{\mathrm{Z}_{\propto}\mathrm{Z}_{\propto'}}{|\,\mathrm{R}_{\propto}-\mathrm{R}_{\propto'}|}\ , \quad (2\text{-}4d)$$

where *e* is the elementary charge of a proton and *Z*α is the atomic number of atom a. The summations extend over all atoms and the integrations overall space. Once the electron density and the atomic numbers and positions of all atoms are known, expression (2-4b) to (2-4d) can be evaluated by using the techniques of classical electrostatics.

The kinetic energy term, T_0 (first term), is subtler. In DFT, the "real" electrons of a system are replaced by "effective" electrons with the same charge, mass, and density distribution. However, effective electrons move as independent particles in an effective potential, whereas the motion of a "real" electron is correlated with those of all other electrons. T_0 is the sum of the kinetic energies of all effective electrons moving as independent particles. Often, one does not explicitly make this distinction between real and effective electrons.

To account for the third term (E_{xc}). The set of waves that minimize the Kohn-Sham energy functional is given by the self-consistent solution of the equation,

$$\left[-\frac{\hbar^2}{2m}\nabla^2 V_{ion}(r) + V_H(r) + V_{XC}(r)\right]\psi_i(r) = \varepsilon_i \psi_i(r), \quad (2\text{-}5)$$

where ψ_i is the wave function of electronic state i, ε_i is the Kohn-Sham eigenvalue, E_{XC} is the exchange-correlation functional, which accounts for all

other complicated electronic contributions to the total energy. V_{ion} is the static total electron-ion potential and V_H is the Hartree potential of the electron given by,

$$V_H(r) = e^2 \int \frac{\rho\,(r')}{|r-r'|} d^3r'. \quad (2\text{-}6)$$

The exchange-correlation potential V_{XC} , is given formally by the functional derivative

$$V_{XC}(r) = \frac{\delta E_{XC}[\rho(r)]}{\delta\rho(r)} \quad (2\text{-}7)$$

$\rho(r)$, is the electron density given by,

$$\rho\,(r) = 2\sum_i |\psi_i(r)|^2. \quad (2\text{-}8)$$

Therefore, the Kohn-Sham total-energy functional is written as,

$$E = 2\sum_{occ} \varepsilon_i + \cup_{ion-ion} - \frac{e^2}{2}\iint \frac{\rho(r)\rho(r')}{r-r'} + E_{XC}[\rho(r]) - \int \rho(r)\, V_{XC} dr. \quad (2\text{-}9)$$

In order to evaluate the K-S explicitly, the E_{xc} needs to be determined and can be done through approximation method as described in the next section.

2.2 Approximation methods

2.2.1 **Local density approximation**

Local density approximation (LDA) is one of the simplest methods of describing the exchange-correlation energy of an electronic system; it is widely used in total-energy pseudopotential calculations [63]. The first approximation Kohn and Sham proposed was to consider the exchange-correlation energy which is locally the same as the one in the homogenous electron gas $\epsilon_{XC}(\rho(r))$ with the same density [64]. However, within the LDA, one assumes that the density functional of N particle system can be expressed in the following form,

$$E_{XC}^{LDA}[\rho] = \int d^3r \rho(r) \epsilon_{XC}(\,\rho(r)), \quad (2\text{-}10)$$

where $\epsilon_{XC}(\rho(r))$ is the exchange-correlation energy per particle of a uniform electron gas. The local density approximation, in principle, ignores correction to the exchange-correlation energy at a point *r* due to nearby homogeneities in the electron density.

Several different schemes have been developed for obtaining approximate forms for the functional; for the exchange-correlation energy. The simplest accurate approximation, for non-magnetic systems, is to assume that the exchange-correlation energy is dependent only on the local electron density d(r) around each volume element. Local density approximation (LDA) gives the correct sum rule for the exchange-correlation hole [65]

The exchange-correlation energy is taken from the known results of the many-electron interactions in an electron system of constant density (homogeneous electron gas). The LDA amounts to the following; at each point in a molecule or solid where there exists a well-defined electron density, it is assumed that an electron at such a point experiences the same many-body response by the surrounding electrons as if the density of these surrounding electrons had the same value throughout the entire space as at the point of the reference electron. The exchange-correlation energy of the total molecule or solid is then the integral over the contributions from each volume element. A large number of total energy calculations have shown that the LDA gives interatomic bond lengths within ±0.05 Å of experiment or better for a great variety of solids, surfaces, and molecules. However, the following systematic trends are found, i.e. most lattice parameters predicted with LDA are too short, weak bonds are noticeably too short, the bond between two magnesium atoms (which are closed-shell systems) and the length of hydrogen bonds such as that in the water dimmer; the binding energies calculated with the LDA are typically too large, sometimes by as much as 50 % in strongly bound systems and even more in weakly bound materials. Comparison with experimental results show that the LDA predicts densities, which are mostly too high (bond distances are too short).

2.2.2 **Generalized gradient approximation**

Generalized gradient approximation (GGA), adds the gradient of the density, |∇$\mathcal{n}$(r)|, as an independent variable. GGA functional has evolved in two main directions, which is 'parameter-free', where the new parameters are determined from known expansion coefficients and other exact theoretical conditions [66]. It includes only the density and its first derivative in the exchange-correlation potential. Furthermore, the exchange-correlation energy of GGA depends not only on the density of a particular coordinate r but also takes into account the gradient density at the same co-ordinate [67].

Although the derivation depends only on the most general features of the real-space construction behind PW91 [68], the resulting functional is close to numerical GGA; with the GGA correlation in the form,

$$E_C^{unif}[\rho_\uparrow, \rho_\downarrow] = \int d^3r\rho\,[\in_C^{unif}(r_s, \xi) + H(r_s, \xi, t)], \qquad (2\text{-}11)$$

where r_s is the local Seitz radius ($\rho = 3/4\pi r_s^3 = r_s^3 3\pi r^2$, $\xi = \rho_\uparrow - \rho_\downarrow/\rho$ is the relative spin polarization and t = | ∇_ρ|/2 $\Phi k_s\rho$ is a dimensionless density gradient.

The GGA for the exchange energy will be constructed from two conditions:
(a) Under the uniform density scaling described along with condition,
(b) E_X must scale like λ [30].
Thus, for ξ ≠ 0 everywhere, we must have,

$$E_X^{GGA} = \int d^3\,r\rho e_X^{unif} F_X(s), \qquad (2\text{-}12)$$

where $\epsilon_X^{unif} = \frac{-3e^2k_F}{4\pi}$, to recover the correct uniform gas limit, $F_x\,(0) = 1$.
As the LDA approximates the energy of the true density by the energy of a local constant density, it fails in situations where the density undergoes rapid changes such as in molecules. An improvement to this can be made by considering the gradient of the electron density, the so-called Generalized Gradient Approximation (GGA). Symbolically this can be written as,

$$E_{xc} = E_{xc}[\rho(r), \nabla\rho(r)]. \qquad (2\text{-}13)$$

Gradient-corrected density functionals suggested by Perdew, Becke, and Wang, Burke, and Ernzerhof [9] offer a remedy to the LDA as discussed in 2.2.1. The basic idea in these schemes is the inclusion of terms in the exchange-correlation expressions that depend on the gradient of the electron density and not only on its value at each point in space. Therefore, these corrections are also sometimes referred to as "non-local " potentials [9].

Most GGAs used in chemistry applications, e.g. Becke, Lee, Yang and Parr (BLYP) are empirical. The LYP correlation uses the Laplacian (second derivative) of the density and thus formally belongs to the third rung of Jacob's ladder [69] but is commonly classified as a GGA [53].

Meta-GGA functional from the third rung use Laplacians of the density and/or kinetic energy densities as additional degrees of freedom. Tao, Perdew, and co-workers recently constructed a parameter-free meta-GGA, TPSS [70]. There are also empirical meta-GGAs with parameters determined by fitting commonly called 'exact exchange', the general ized random phase approximation [71]. Therefore, the functional of the last rung will use E_{XX} and exact partial correlation.

2.3 Planewave pseudopotential method

2.3.1 **Planewaves and pseudopotentials**

Planewaves (PW) and pseudopotentials are the hallmark DFT of the method and they form a very natural alliance in describing the fundamental properties of systems. In PW pseudopotential method, the model system is constructed in 3D periodic supercell which allows Bloch's theorem to be applied to the electron wavefunctions,

$$\psi_{n,k}(r) = \cup_{nk}(r)\exp(ik.r), \qquad (2\text{-}14)$$

the function $U(r)$ has the periodicity of supercell. It can be of any suitable mathematical form and usually one chooses a series of expansion in terms of a set of basis functions. In PW pseudopotential, planewaves are used for this expansion, so that each single-electron wavefunctions $\psi_{n,k}$ is written as,

$$\psi_{n,k}(r) = \sum \mathrm{u}_{n,k}\,(G)\exp(i(k+G).r), \qquad (2\text{-}15)$$

the $U_{n,k}$ are the expansion coefficients. The wave vectors *G*' are such that the planewaves are commensurate with the supercell. Both the number of *G* -vectors in the sum and the number of *k's* considered should in principle be infinite. The exponential term is a planewave of wavevector *k* which must be commensurate with the entire system (i.e. not just the periodically-replicated cell). For an infinite system, there is an infinite number of *k* vectors, at each point of which solutions for $\psi_{n,k}$ exist. This simply reflects the fact that the number of electrons is infinite. However, a great simplification comes about when one realizes the change in $\psi_{n,k}$ where *k* becomes negligible for *k* -points that are close together. This means that one may calculate at a finite number of *k*-points; hence we refer to this idea as *k*-point sampling [72].

The set of vectors {*G*}, on the other hand, should in principle be infinite to obtain an exact representation of the wavefunction. This is never necessary because summing over a finite number of *G's* will yield sufficient accuracy. Planewaves basis set has many advantages, (i) it is unbiased, so all space is treated the same, (ii) it is complete, (iii) there is a single convergence criterion, (iv) planewaves are mathematically simple and their derivatives are products in k-space, (v) planewaves do not depend on atomic positions [68].

Its disadvantage is that (i) the number of planewaves needed is determined by the greatest curvature of the wavefunction and (ii) empty space has the same quality of representation and costs a region of interest [73].

The advantages i.e. the first three mean that one can always ensure that the basis set is adequate for a calculation by increasing the number of planewaves until the quantity of interest stops changing. In other words, the quality of the basis set depends on a single parameter, usually expressed as the energy of a free electron whose wavefunction has the same wavevector as the largest wavevector in the planewave basis,

$$E_c = \frac{\hbar^2(G+k)^2}{2m}, \qquad (2\text{-}16)$$

all planewaves of ‘energy’ less than the cut-off energy E_c are used in the expansion.

2.3.2 **Pseudopotential approximation**

The pseudopotential approximation allows the electronic wavefunctions to be expanded using a much smaller number of plane wave basis states. It is well known that most physical properties of solids are dependent on the valence electrons to a much greater extent than on the core electrons. The pseudopotential approximation exploits this by removing the core electrons and replacing the strong ionic potential by a weaker pseudopotential that acts on a set of pseudo wavefunctions rather than the true valence wavefunctions. An ionic potential, the valence wave function, corresponding pseudopotential, and pseudo wavefunction are illustrated in figure 2-1. The valence wavefunctions oscillate rapidly in the region occupied by the core electrons due to the strong ionic potential in this region. These regions maintain the orthogonality between the core wavefunctions and the valence wavefunctions, which is required in Pauli’s exclusion principle [74].

The pseudopotential is constructed in such a way that its scattering properties or phase shifts for the pseudo wavefunctions are identical to the scattering properties of the ion and the core electrons for the valence wavefunctions and are in such a way that the pseudo wavefunctions have no radial nodes in the core region. The phase shift produced by the ion core is different for each angular momentum component of the valence wave function and so the scattering from the pseudopotential must be angular momentum dependent.

The most general form for pseudopotential is:

$$V_{NL} = \sum_{lm} |\, lm\rangle V_l \rangle lm \,| \ , \qquad (2\text{-}17)$$

where $\langle lm$ are the spherical harmonics and V_l is the pseudopotential for angular momentum l. Acting on the electronic wave function, this operator decomposes the wave function into the spherical harmonics, each of which is multiplied by the relevant pseudopotential V_l.

A pseudopotential that uses the same potential for all the angular momentum components of the wave function is called a local pseudopotential. It is possible to produce arbitrary, predetermined phase shifts for each angular momentum state with a local potential, but there are limits to the amount that the phase shifts can be adjusted for the different angular momentum states [75], while maintaining the crucial smoothness and weakness of the pseudopotential. Without a smooth, weak pseudopotential it becomes difficult to expand the wavefunctions using a reasonable number of planewaves basis states.

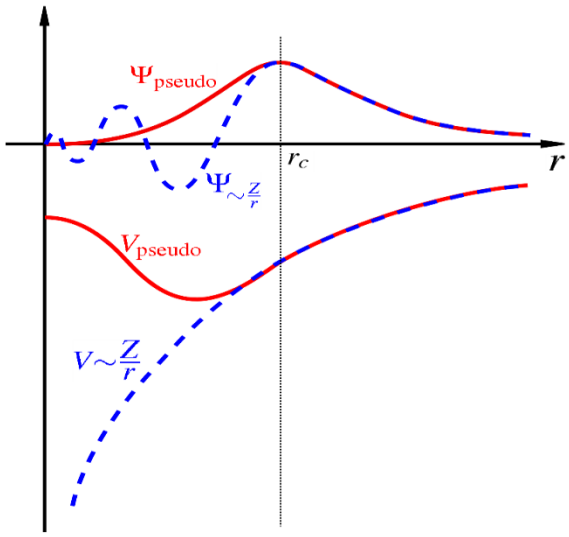

Figure 2-1: Comparison of a wavefunction in the Coulomb potential of the nucleus (blue) to the one in the pseudopotential [75].

2.3.3 **Projector augmented wave**

We can use the DFT to reduce many-body problems to solve a single-particle Schrödinger equation,

$$H\ |\psi_n\rangle = \epsilon_n\ |\psi_n\rangle \tag{2-18}$$

The wavefunctions contain cusps (and are oscillatory around each nucleus).
An approach for electronic structure calculations is described that generalizes both the pseudopotential method and the linear augmented-planewave (LAPW) [76] method in a natural way. The method allows high-quality first-principles molecular-dynamics calculations to be performed using the original fictitious

Lagrangian approach of Car and Parrinello. Like the LAPW method, it can be used to treat first-row and transition-metal elements with affordable effort and provides access to the full wave function. The augmentation procedure is generalized in that partial-wave expansions not determined by the value and the derivative of the envelope function at some muffin-tin radius, but rather by the overlap with localized projector functions. This approach is based on generalized separable pseudopotentials which can be regained by a simple approximation [77].

2.3.3.1 Projector Augmented-wave Functions

This method introduced smooth wavefunctions by a linear transformation operator T,

$$|\psi_n\rangle = T\ |\psi_n\rangle. \tag{2-19}$$

The linear methods can be subdivided into a variety of methods ranging from the most accurate linear augmented-plane-wave (LAPW) method to the linear muffin-tin orbital (LMTO) method. The linear methods deal with the full wave functions and treat all elements in the periodic table, i.e., *s*-, *p*-, *d*-, and *f*-electron systems, on the same footing. Constructed augmentation spheres $|\mathrm{r} - \mathrm{R}^{\mathrm{a}}| < \mathrm{r}_{\mathrm{c}}^{\mathrm{a}}$ around each atom a (one can imagine a muffin-tin), where $\mathrm{r}_{\mathrm{c}}^{\mathrm{a}}$ is a cut-off radius, a is the atom index, R^{a} is the atom position.

T is written *as,*

$$\mathrm{T} = 1 + \sum_{\mathrm{a}} \mathrm{T}^{\mathrm{a}}, \tag{2-20}$$

where T^a only acts in the augmentation sphere.

Chose a complete basis $|\phi_i^a\rangle$ *(*also called partial waves) inside the sphere. The smooth partial waves can be obtained using the T operator,

$$|\ \Phi_i^a\rangle = T\ |\ \Phi_i^a\rangle = \left(1 + \sum_{a'} T^{a'}\right) |\ \Phi_i^a\rangle$$

$$= (1 + T^a)\ |\ \Phi_i^a\rangle \tag{2-21}$$

because T^a only acts in the sphere, followings,

$$| \Phi_i^a\rangle = | \Phi_i^a\rangle \, for \, r > r_c^a \quad (2\text{-}22)$$

outside the sphere, i.e $\langle r| \Phi_i^a \rangle = \langle r| \Phi_i^a \rangle$ for $r > r_c^a$. We can now expand the smooth wavefunctions using the partial waves basis,

$$| \psi_n\rangle = \sum_i P_{ni}^a \, | \Phi_i^a\rangle, \quad (2\text{-}23)$$

inside the augmentation sphere.

The advantage of a planewave representation for the wavefunctions is its compactness. The memory footprint of a wave function is typically 10 times larger in a real-space grid representation compared to a planewave representation of similar accuracy. For this reason, it is important to use soft pseudo-wave functions that can be accurately represented on coarse grids. In previous work, until now, all applications of grid-based electronic structure calculations have used norm-conserving pseudopotentials [77].

One way to get smoother pseudo-wave functions is to relax the norm conservation of the wave functions and use ultrasoft pseudopotentials or the projector augmented wave PAW method. The PAW method works with soft-valence wave functions and similarly to the ultrasoft pseudopotential method [68], the wave functions need not be normalized. Contrary to the ultrasoft pseudopotential method, the PAW method is an all-electron method within the frozen core approximation, giving access to the true wave functions and the full electron density. The PAW method has been implemented for planewaves by several groups [78].

The combination of real-space grid-based methods and the PAW method is as an important step toward enabling larger calculations at a level of accuracy that is essentially all-electron in nature. There is a clear trend in electronic structure theory toward larger and more complex systems, for example, nanostructures, large bio-molecular complexes and extended defects in real materials systems that all quickly challenge present-day high-accuracy DFT codes, which are typically limited to, at most, a few hundred atoms. The great potential of the method presented here lies in the parallelization of the real-space algorithms. This makes it possible to make use of massively parallel computers [78].

2.4 Molecular dynamics

In this study, molecular dynamic [79] method was used to investigate the phase transformation of the Fe-Al-X ternary alloys by employing the LAMMPS-EAM [80] module in the MedeA environment [52].

MD simulations calculate the time-dependent behaviour of a molecule according to Newton's laws of motion [81]. However, it is commonly used computationally for simulation of solids, liquids and molecules respectively. It is the method that performs equilibrium statistical-mechanical calculations via simulation. However, it may be used to explore conformations, such as molecular adsorption sites on a surface. If frictional forces are added to the equations of motion, Langevin dynamics becomes possible, as does geometry optimisation via damped MD. Finally, extended Lagrangian methods allow thermostatic control of the temperature.

$$F_i = m_i a_i \tag{2-24}$$

where i=1,2,…,N in this equation, F_i denotes the force on the i^{th} particle, mi is the mass of the particle, and a_i is the acceleration [82].

Different ensembles in molecular dynamics

MD is the method of simulating kinetic and thermodynamic properties of molecular systems using Newton equations of motions. Usually, numerical integration of equation of motions in MD is accomplished using Verlet algorithm [83].

If all the forces which appear in the Newton equation of motions are related to the potential energy of the system, then the total energy of the system is conserved.

$$E = E_K + E_P \tag{2-25}$$

If the total number of atoms N and the volume V of the unit cell are also kept constant, then the MD simulations are said to be performed in the micro canonical (NVE) ensemble. Generally, if the simulation system is sufficiently large, the small part of it may be considered as a canonical system. For large NVE systems, the fluctuations in temperature are small, and it may be considered approximately

constant. However, there are situations in which temperature must be kept constant. For example, studying temperature induced unfolding of proteins requires precise temperature control. Therefore, for these classes of problems MD must reproduce an isothermal ensemble, such as canonical NVT ensemble, in which the number of particles, volume, and the temperature is fixed [84].

The constant-temperature, constant-pressure ensemble (NPT) allows control over both the temperature and pressure. The unit cell vectors are allowed to change and the pressure is adjusted by adjusting the volume. This is the ensemble of choice when the correct pressure, volume, and densities are important in the simulation. This ensemble can also be used during equilibration to achieve the desired temperature and pressure before changing to the constant-volume or constant-energy ensemble when data collection starts.

2.4.1 **Microcanonical ensemble**

In the microcanonical ensemble or NVE, the system is isolated from changes in moles (N), volume (V) and energy (E). It corresponds to an adiabatic process with no heat exchange. A microcanonical molecular dynamics trajectory may be seen as an exchange of potential and kinetic energy, with total energy being conserved. For a system of N particles with coordinates X and velocities V, the following pair of first-order differential equations may be written in Newton's notation as [85].

$$F(X) = -\nabla U(X) = M\dot{V}(\mathrm{t}), \tag{2-26}$$

$$V(t) = \dot{X}\,(t), \tag{2-27}$$

Where the potential energy function U(X) of the system is a function of the particle coordinates X.

2.4.2 **Canonical ensemble**

In statistical mechanics, a canonical ensemble or NVT, the system is isolated from changes in moles (N), volume (V) and temperature (T). It is a statistical ensemble that is used to represent the possible states of a mechanical system that is in thermal equilibrium with a heat bath. The system is said to be closed in

the sense that the system can exchange energy with a heat bath so that various possible states of the system can differ in total energy. The system's composition, volume, and shape are kept the same in all possible states of the system [85].
In simple terms, the canonical ensemble assigns a probability P to each distinct microstate given by the following exponential:

$$P = e^{\frac{A-E}{kT}} \quad \text{, where} \tag{2-28}$$

P= probability, A= free energy (Helmholtz free energy), E= total energy of the microstate, K= is Boltzmann's constant and T= temperature.

2.4.1 **Grand canonical ensemble**

The isothermal-isobaric ensemble a statistical mechanical ensemble that maintains constant temperature T and constant pressure P applied. It is also called the NPT-ensemble, where the number of particles is also kept as a constant. Notice that into the grand canonical (μVT) ensemble, the probability distribution function must also include N as its variable, because the number of particle can (in principle) be any non-negative integer at thermal equilibrium.
The NPT ensemble is also useful for measuring the equation of state of model systems whose virial expansion for pressure cannot be evaluated, or systems near first-order phase transitions.
Following the same approach as in the (NPT) ensemble, we obtain the equilibrium distribution of the grand canonical (μVT) ensemble as the following:

$$\rho(\{q_i\}\{q_{i,}\}N) = \frac{1}{Z} e^{-\beta(H(\{q_i\}\{q_i\}-\mu N)} \tag{2-29}$$

where

$$Z = \sum_{N=0}^{\infty} \int \prod_{i=1}^{3N} dq_i dp_i e^{-\beta(H(\{q_I\}\{P_I\})-\mu N)} \tag{2-30}$$

$$= \sum_{N=0}^{\infty} e^{\beta\mu N} Z(N,V,T) \tag{2-31}$$

ρ is grand canonical distribution and Z (N, V, T) is the normalization factor in the canonical ensemble for N particles.

2.4.2 **Embedded-atom method**

The Embedded-atom Method (EAM) [51] force field-based simulations provide a computational efficient description of structural, mechanical and thermal properties of metallic systems. These EAM calculations span length and time, this is inaccessible to first-principle methods. It captures a significant portion of the physical reality of metallic bonding developed by Daw and Baskes [86]. In this study, the Zhou interatomic force fields were applied. This approach represents the total energy of the system as two additive terms, a pairwise sum of interactions between atoms, and a term representing the electron density of each site as shown in the equation below,

$$U_{metallic} = \sum_{i=1}^{N-1} \sum_{j=i+1}^{N} \mathrm{V}(r_{ij}) + \sum_{i=1}^{N} \mathrm{F}\,(P_i) \qquad (2\text{-}32)$$

$$\rho_i = \sum_{j=1}^{N} \varphi_j\ (r_{ij}). \qquad (2\text{-}33)$$

2.5 Simulation Codes

2.5.1 **CASTEP**

CASTEP (Cambridge sequential total energy package) is a pseudo-potential total-energy code [87, 88] which employs special point integration over the Brillouin zone and a planewave basis for the expansion of the wavefunction. It is also referred to as a first principles code and consists of many capabilities to calculate any physical property of the system. In this code, the total energy of the system is used to derive many other quantities especially periodic systems. The periodic system is governed by periodic boundary conditions according to Bloch's theorem [89], states that in a periodic system each electronic wavefunction can be written as a product of a cell-periodic part and a wavelike part (equation 2-14). The cell periodic part, ψ, can then be expanded using a basis set consisting of a discrete set of plane waves whose wave vectors are reciprocal lattice vectors of the crystal. Therefore, each electronic function can be written as a sum of plane

waves $Exp^{[j(K+G).R]}$. This is applicable in the simplified form of the Kohn-Sham equations where the kinetic energy is diagonal, and the various potentials (electron-ion, Hartree, exchange-correlation) are described in terms of their Fourier transforms.

The CASTEP code was used to determine the appropriate k-point mesh and cut-off energy (refers to a convergence test). The ultra-soft pseudopotentials of Vanderbilt were employed so that cut-off energy is sufficient to converge the energy to within 1 meV/atom accuracy. The convergence of the total energies is determined with respect to the k-point sampling size. A force of 0.05 eV/Å was used with suitable stress of 0.5 GPa using Koelling-Harmon [88] for relativistic treatment. These are default set parameters. The CASTEP code has been used to calculate ground state properties such as equilibrium lattice parameters, electronic and elastic constant at 0 K. Furthermore, the code provide the VCA which is used to generate solid-state ternary or quaternary systems.

2.5.2 **Virtual crystal approximation**

The virtual crystal approximation (VCA) is an implementation for DFT methods and a pseudopotential based technique set out by Bellaiche and Vanderbilt [25]. VCA is a much simpler and computationally less expensive approach, to study a crystal with the primitive periodicity, but composed of fictitious ‘‘virtual’’ atoms that interpolate between the behaviour of the atoms in the parent compounds. The implementation of VCA with ultra-soft potentials can be expressed as,

$$V_{ext}(r,r') = \sum_I \sum_{\propto} w_{\propto}^I V_{PS}^{\propto}(r - R_{I\propto}, r' - R_{I\propto}), \qquad (2\text{-}34)$$

the expression is used for the generation of the total external potential as the sum of the nonlocal potentials of each atomic species, α, taken with the weights, w, of the component atoms in the mixture of Fe-Al-X ternary alloys. It offers the simplest approach to perform doping on a single unit cell, and neglects effects such as local distortions around atoms which cannot be expected to produce the finer details of the disordered structures accurately. In this study, ternary alloying (Fe-Al-X) were constructed to study the effect of the third element such as Pt, Pd, Ru and Ag on the electronic, elastic and high temperature systems.

2.5.3 **VASP**

The Vienna Ab-initio Simulation Package (VASP) is a first principle computational program for atomic scale materials modelling. It provides approximate solution to the many-body Schrödinger equation, either within density functional theory (DFT) [53], solving the Kohn-Sham equations [8], or within the Hartree-Fock (HF) [90] approximation, solving the Roothaan equations [91]. It is capable to simulate electronic structure calculations and quantum-mechanical molecular dynamics.
The interaction between ions and electrons is described using ultra-soft Vanderbilt pseudopotentials (US-PP) [77] or the projector augmented wave method (PAW) [78]. Both techniques allow a considerable reduction of the necessary number of planewaves per atom for transition metals and first row elements [52]. Forces and stresses can be easily calculated with VASP code and these are important to relax atoms into their instantaneous ground-state or minimum energy state. Similarly to CASTEP, the VASP code will be used to determine the equilibrium properties. More importantly it provides various platforms such as PHONON code [10] and LAMMPS code [82] in the materials design program. The PHONON code will be used to calculate the vibrational properties as well as LAMMPS code to determine temperature dependence.

2.5.4 **Molecular Dynamics**

Molecular dynamics (MD) simulation calculates the time dependent behaviour of a molecule according to Newton's law of motion [92]. However, it is commonly used computationally for simulation of solids, liquids and molecules respectively. This method is used to perform equilibrium statistical-mechanical calculations via simulation. For example the derivative of total energy with respect to atomic positions results in the forces and the derivative with respect to cell parameters gives stresses. These are then used to perform full geometry optimizations and possibly finite temperature molecular dynamics. Finally, extended Lagrangian methods allow thermostatic control of the temperature [93].

$$F_i = m_i \vec{a}_i, \quad \text{.....(2-35)}$$

where $i = 1,2, \ldots . N$ in this equation, F_i denotes the force on the i^{th} particle, m_i is the mass of the particle, and $\vec{a}_i$ is the acceleration. The MD calculations will be performed using DMol3 and LAMMPS code to evaluate the effect and strength of Fe-Al-X system at varied temperatures.

2.5.4.1 Dmol3

DMol3 [57, 94] is a technique which combines computational speed with the accuracy of quantum mechanical methods to predict materials properties reliably and quickly. It is used to model the electronic structure and properties of organic and inorganic molecules such as molecular crystals, covalent solids, metallic solids, and infinite surfaces using DFT [8, 53].

This mechanism is responsible for optimizing the unit cells of periodic systems and can also be used to calculate the mechanical properties (for example, the elastic constants) of various materials. The energy is minimized using a standard geometry optimization procedure. The elastic constant tensor is then calculated from the energies corresponding to each finite displacement.

DMol3 advanced

The DMol^3 advanced course offers a detailed introduction to accurate prediction of electronic properties, chemical reactions, IR and Raman spectra, optical properties, and electron transport properties such as band structure, density of states (DOS), electron densities, electrostatics, molecular orbitals, and atomic populations.

2.5.4.2 LAMMPS code

LAMMPS uses a powerful flowchart interface which enables the easy setting up of the complex calculations by connecting the stages. LAMMPS is one of the world's leading code today, which focuses on the high efficient execution of forcefield based simulations designed to exploit large scale parallel computer architecture [95].

LAMMPS has potentials for solid-state materials (metals, semiconductors) and soft matter (biomolecules, polymers) and coarse-grained or mesoscopic systems.

It can be used to model atoms or, more generically, as a parallel particle simulator at the atomic, meso, or continuum scale.

2.6 Theoretical background on calculated properties

2.6.1 **Heats of formation**

The heats of formation of compounds and associated entropies provide the basis for understanding and constructing phase diagrams. The Knowledge of these quantities offers the prospect of disentangling, which one of the observed phases might occur upon varying the means of fabrication. Such modelling of alloy phase behavior is of considerable technological relevance. The heat of formation can be estimated by:

$$\Delta H_f = E_c - \sum_i x_i E_i \qquad (2\text{-}36)$$

Where E_c is the calculated total energy of the compound, E_i is the calculated total energy of element i in the compound.

The heat evolved or absorbed during the formation of one mole of a substance from its component elements, a form of energy that is transferred by a difference in temperature. Hess's Law of Additive states that a series of equations can be added to obtain an overall reaction and if this is true, then the respective Heats of formation for the reactions can be algebraically added [96]. It has become quite common for electronic structure calculations of varying rigour to yield the total energy of a solid. This offers a prospect of estimating the stabilities of phases that are either unavailable or inaccessible experimentally and this, in turn, has implications for making phase diagram predictions.

Heats of formation from Ab-initio calculations have been successfully used to predict the stability of alloys and in the construction of their phase diagrams [97, 98].

2.6.2 **Density of states**

The density of states (DOS) of a system describes the number of states per interval of energy at each energy level that is available to be occupied. Unlike

isolated systems, like atoms or molecules in the gas phase, the density distributions are not discrete like a spectral density but continuous. A high DOS at a specific energy level means that there are many states available for occupation. A DOS of zero means that no states can be occupied at that energy level. In general, a DOS is an average over space and time domains occupied by the system. Local variations, most often due to distortions of the original system, are often called local density of states (LDOS). If the DOS of an undisturbed system is zero, the LDOS can locally be non-zero due to the presence of local potential.

The density of states plays an important role in the kinetic theory of solids. The product of the density of states and the probability distribution function is the number of occupied states per unit volume at given energy for a system in thermal equilibrium. Using two common distribution functions, assist on how to apply a distribution function to the density of states. This value is widely used to investigate various physical properties of matter [99, 100].

Calculating the density of states for small structures shows that the distribution of electrons changes as dimension is reduced; for quantum wires, the DOS for certain energies becomes higher than the DOS for bulk semiconductors, and for quantum dots, the electrons become quantized to certain energies [101].

2.6.3 **Elastic properties**

Elastic properties of a solid are important because they relate to various fundamental solid-state properties such as interatomic potentials, equation of state and phonon spectra. Elastic properties are also linked thermodynamically to the specific heat, thermal expansion, Debye temperature, melting point, and Gruneisen parameter. So, it is important to calculate the elastic constants of solids [102].

Accurate calculation of elasticity is essential for gaining an insight into the mechanical stability and elastic properties of solids. For cubic, tetragonal, orthorhombic and monoclinic crystals, there are three (C_{11}, C_{12}, C_{44}), six (C_{11}, C_{12}, C_{13}, C_{33}, C_{44}, C_{66}), nine (C_{11}, C_{22}, C_{33}, C_{12}, C_{13}, C_{23}, C_{44}, C_{55}, C_{66}) and thirteen

(C_{11}, C_{22}, C_{33}, C_{12}, C_{13}, C_{23}, C_{44}, C_{55}, C_{66}, C_{15}, C_{25}, C_{35}, C_{46}) independent elastic constants, respectively. Applying two kinds of strains on the cubic system give stresses relating to three elastic coefficients, producing an efficient method for obtaining elastic constants for the cubic systems. This method has been successfully used to study the elastic properties of a range of materials including metallic systems [103, 104] .

The current study focusses on the stability of β Fe-Al-X, and thus depends on the cubic lattice. The mechanical stability criteria for a cubic system is outlined [105] as follows:

$C_{44} > 0$; $C_{11} > |C_{12}|$ and $C_{11} + 2C_{12} > 0$;

Based on these three independent single crystal elastic constants of a cubic crystal, the elastic moduli are determined using the following expressions:

$$B = \frac{C_{11}-2C_{12}}{3},\ C' = \frac{C_{11}-C_{12}}{2},\ A = \frac{2C_{44}}{C_{44}-C_{12}}\ . \qquad (2\text{-}37)$$

2.6.3.1 Theory of elasticity

The perspective of materials physics includes the elastic constants (C_{ij}) which contain some of the most important information that can be obtained from ground-state total-energy calculations. A given crystal structure cannot exist in a stable or metastable phase unless its elastic constants obey certain relationships. The C_{ij} also determines the response of the crystal to external forces, as characterized by the bulk modulus, shear modulus, Young's modulus, and Poisson's ratio and so plays an important role in determining the strength of a material.

The calculated C_{ij} can then be used to check the experimental bulk and shear moduli, if available to calibrate model calculations. Also, the elastic constants are used to check the phase stability of proposed compounds. First-principles calculations can thus be used to predict the existence and properties of new materials and phases [102].

2.6.3.2 Definition of elastic constants

To determine the elastic constants of a crystal, a deformation of the unit cell is created by changing the Bravais lattice vectors R = (a, b, c) of the undisturbed unit cell to R′ = (a', b', c') using a strain matrix e:

$$\mathbf{R}' = R \begin{vmatrix} 1 + e_{xx} & \frac{1}{2}\, e_{xy} & \frac{1}{2} e_{xz} \\ \frac{1}{2} e_{yx} & 1 + e_{yy} & \frac{1}{2} e_{yz} \\ \frac{1}{2} e_{zx} & \frac{1}{2} e_{zy} & 1 + e_{zz} \end{vmatrix}$$

The deformation leads to a change of the total energy of the crystal,

$$U = \frac{E_{tot} - E_0}{V_0} = \frac{1}{2} \sum_{i=1}^{6} \sum_{j=1}^{6} C_I\, e_i e_j \qquad (2\text{-}38)$$

Where E_0 is the total energy of the unstrained lattice, V_0 is the volume of the undistorted cell and the C_{ij} are the elements of the elastic constant matrix with a notation that follows standard convention [106]. Both i and j run from 16 in the sequence {xx, yy, zz, yz, xz, xy}. The tensor of elasticity has 36 elements, the elastic constants, but maximally 21 of these are independent.

2.6.3.3 Calculation of elastic constants

The simplest case by far is the cubic system where there are only three independent Constants, C_{11}, C_{12}, and C_{44}. We use this case to illustrate how the stiffness matrix elements may be determined from strain fields. If the applied strain is $e_x = e$ with all other e_i equal to zero, the energy change is $U = \frac{C_{11}\, e^2}{2}$. This allows a unique determination of C_{11}, If $e_{yz} = e_{zy} = \frac{e}{2}$, other strain components are zero, then $U = \frac{C_{44}\, e^2}{2}$ and we have an independent determination of C_{44}. The bulk modulus B is the response to a uniform compression; so by applying the strain field $e_{xx} = e_{yy} = e_{zz} = e$ allows the computation of B via the relation $U = \frac{Be^2}{2}$. Similarly, the shear modulus can be calculated by using the strain field $e_{zz} = e; = e = e_{yy} = -\frac{e}{2}$, whereupon $U = \frac{3C\prime e^2}{2}$ [102, 106].

2.6.4 Phonon dispersion curves

Phonon is a collective excitation in a periodic, elastic arrangement of atoms or molecules in condensed matter, like solids and some liquids. Often designated a quasi-particle it represents an excited state in the quantum mechanical quantization of the modes of vibrations of elastic structures of interacting particles [107].

Phonons play a major role in many of the physical properties of condensed matter, like thermal conductivity and electrical conductivity [108].

The concept of phonons was introduced in 1932 by Soviet physicist Igor Tamm. The name phonon which translates to sound or voice because long-wavelength phonons give rise to sound. Shorter-wavelength higher-frequency phonons are responsible for the majority of the thermal capacity of solids. Because the atoms behave as if they are connected by tiny springs, their thermal energy or outside forces make the lattice vibrate. This generates mechanical waves that carry heat and sound through the material. A packet of these waves can travel throughout the crystal with definite energy and momentum.

Phonon density of states (or vibrational density of states) is defined in the same way as the electronic densities of states. The integral over the Brillouin zone goes over all 3N phonon bands, where N is the number of atoms in the cell. There are two popular conventions regarding the normalization of the phonon DOS. Either it can be normalized to unity or the total number of vibrational modes, 3N [74, 108].

The partial (or projected) phonon density of states is determined as a contribution from the given atom to the total phonon DOS. This is a useful concept that allows one to understand the nature of various branches in the phonon spectrum. The contribution to the partial density of states on atom i, from each phonon band, is evaluated using:

$$N_I(E) = \int \frac{dK}{4\pi^3} \; |e_j(i)\;|^2 \; \delta(E - E_n\,(K)) \qquad (2\text{-}39)$$

where e_j is the eigenvector (normalized to unit length) associated with the mode of energy E_j. The projected density of states is then obtained by summation of these contributions over all phonon bands. By constructing all the projected phonon DOS they sum up to the true phonon DOS. The phonon density of states (DOS) and phonon entropy of β2 FeAl were determined as functions of the Fe site vacancy concentration using several scattering techniques and were computed from first principles. Measurements at elevated temperature and pressure were performed to explore volume effects, to test the usefulness of the quasi-harmonic (QH) approximation, and to provide a comparison for the first-principles calculations. The brittleness of these alloys at ambient temperatures

hinders their use. An important characteristic of β2 FeAl is its propensity to develop an abnormally high equilibrium vacancy concentration at high temperature, particularly at off-stoichiometric Al-rich concentrations were the predominant defect in the vacancy on the Fe site of iron. These large vacancy concentrations xv can be retained at ambient temperature by quenching [109].

2.6.5 **Thermodynamic studies**

2.6.5.1 Gibbs free energy

In thermodynamics, the Gibbs free energy is a thermodynamic potential that measures the "useful" or process-initiating work obtainable from an isothermal, isobaric thermodynamic system. Gibbs energy is also the chemical potential that is minimized when a system reaches equilibrium at constant pressure and temperature. As such, it is a convenient criterion of spontaneity for processes with constant pressure and temperature. Every system seeks to achieve a minimum of free energy. Out of this general natural tendency, a quantitative measure as to how near or far a potential reaction is from this minimum is when the calculated energetics of the process indicates that the change in Gibbs free energy is negative [110].

In essence, this means that such a reaction will be favoured and will release energy. The energy released equals the maximum amount of work that can be performed as a result of the chemical reaction. In contrast, if conditions indicated a positive change in Gibbs free energy, then energy, in the form of work, would have to be added to the reacting system to make the reaction go [111]. Previous experimental findings show that CsCl which has the same symmetry (I-43m) to that of FeAl, states that ΔG_f^o has an energy of -4.294954 eV [45].

Gibbs free energy combines enthalpy and entropy into a single value. it is the energy associated with a chemical reaction that can do useful work. It equals the enthalpy minus the product of the temperature and entropy of the system.

$$G = H - TS. \quad (2\text{-}40)$$

At constant temperature

$$\Delta G = \Delta H - T\Delta S, \quad (2\text{-}41)$$

Δ*G* predicts the direction of a chemical reaction. If Δ*G* is negative, then the reaction is spontaneous. If Δ*G* is positive, then the reaction is non-spontaneous. where T is the absolute temperature in Kelvins. When ΔG is less than zero, there is a thermodynamic driving force for the reaction or process in the forward direction (as written). When ΔG is positive, then reactants are favoured instead. When ΔG=0 the system is at equilibrium (see figure 2-2) [110].

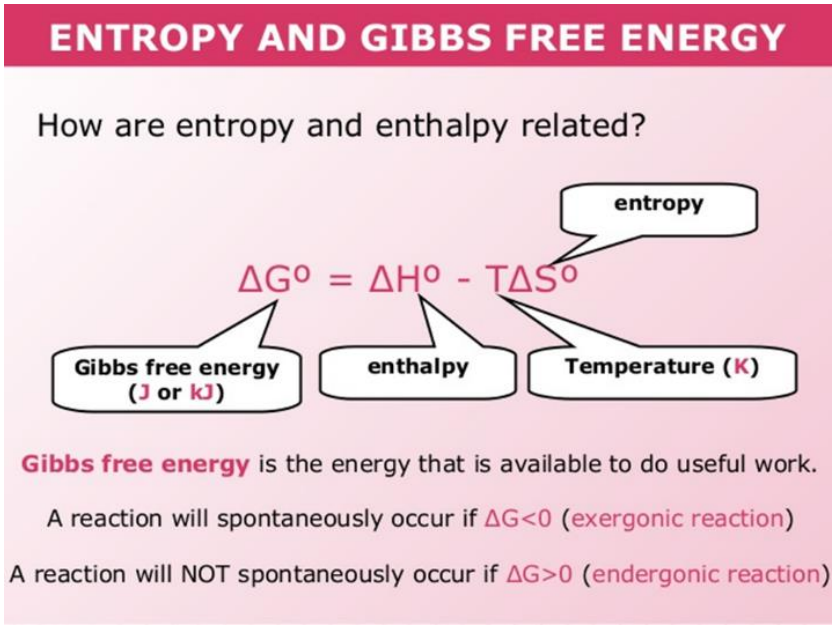

Figure 2-2: A description of Gibbs free energy equation and its representation [110].

Chapter 3

STABILITY OF BINARY Fe-Al SYSTEMS

In this chapter, we discuss the predicted DFT results on the structural, thermodynamic, electronic, mechanical and vibrational properties of Fe-Al alloys. In particular, we discuss the lattice constants, heats of formation, density of states (DOS), elastic constants and phonon dispersion curves. Our predicted results will be compared and contrasted with the available experimental and theoretical data. Two computational codes were used to perform calculations; namely CASTEP [9] and VASP [52].

3.1 Convergence test

The convergence test was performed successfully using DFT based calculations, this is about the plane wave cut-off energy and the number of k-points. In general, convergence tests are performed to achieve the accurate total energy and ground-state properties of a system. However, it is crucial to note that the number of k-points depends on the system of interest. In particular, metals require denser k-points than semiconductors.

In this study, the cut-off energy and k-point mesh parameters for Fe-Al systems were determined by performing single point calculation employing the plane wave CASTEP code using the ultra-soft pseudopotentials of Vanderbilt [73] within GGA-PBE. The appropriate cut-off and k-points will be used to accurately determine the ground state properties of Fe-Al systems.

Figure 3.1 shows the curves of total energy against the cut-off energy for Fe-Al alloys. The curves indicate that the total energy trend is similar across all the alloy systems, showing a constants slope from the cut-off energy of 300 up to 600 eV/atom. The energy cut-off of 500 eV was chosen for the Fe-Al structures since, at this point, the change in energy was negligible. The same calculations were done for all the other binary alloys.

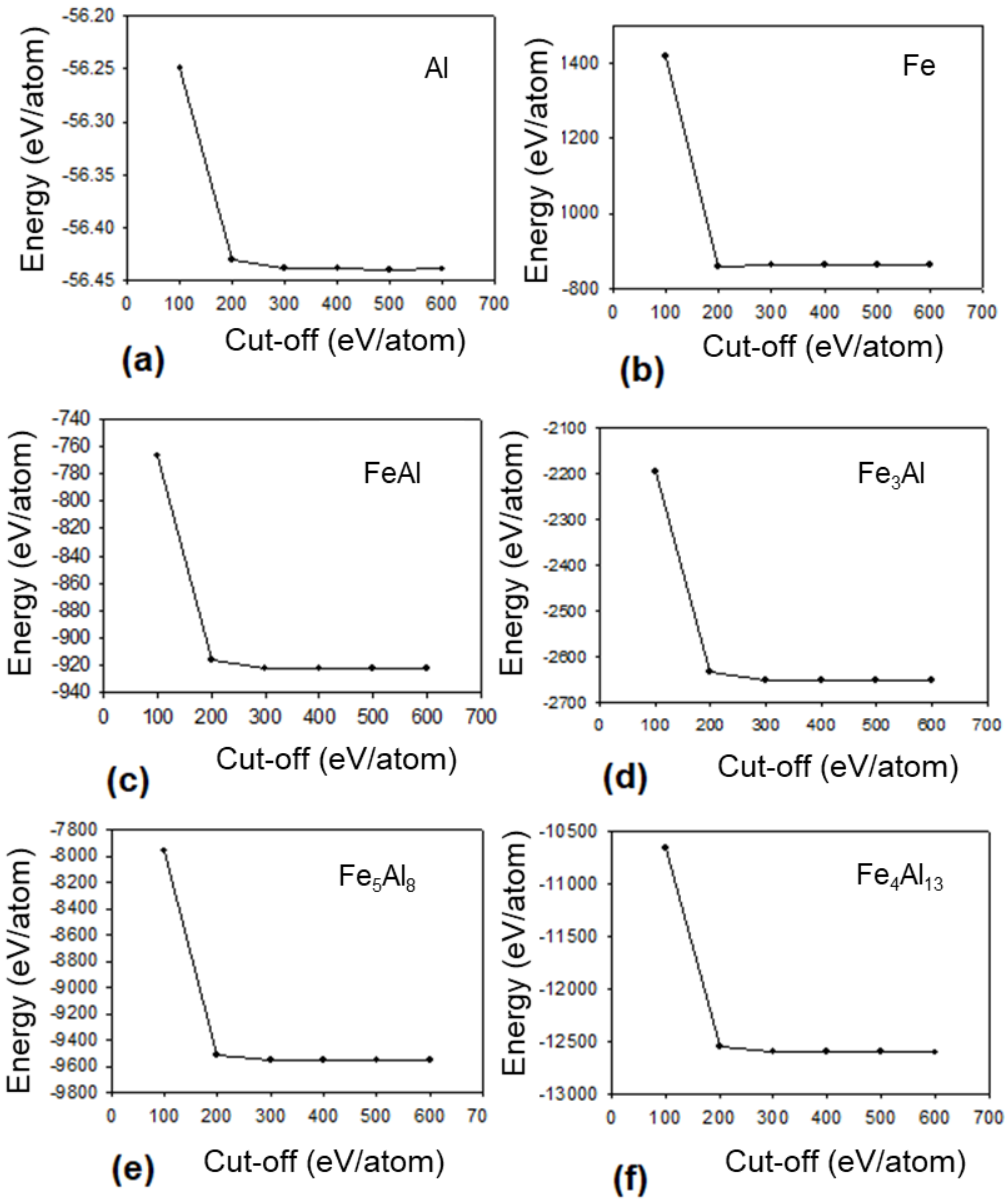

Figure 3-1: The graph of total energy (eV) versus cut-off energy for (a) Al, (b) Fe, (c) FeAl, (d) Fe_3Al, (e) Fe_5Al_8 and (f) Fe_4Al_{13}.

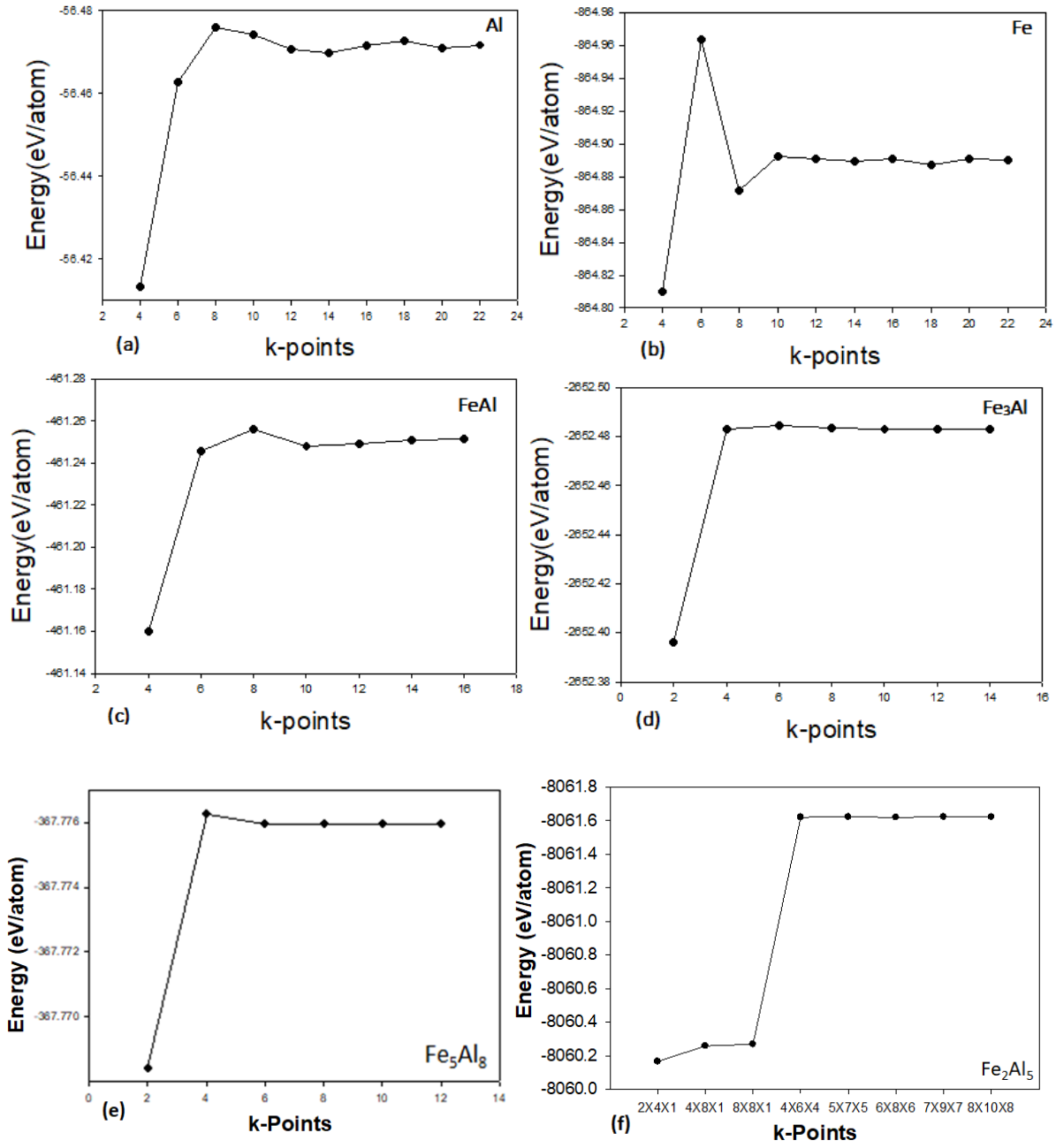

Figure 3-2: shows possible k-points for (a) Al, (b) Fe, (c) FeAl, (d) Fe_3Al, (e) Fe_5Al_8 and (f) Fe_2Al_5.

Secondly, we show the convergence test for the total energies for the k-point sampling size in the Brillouin zone integration using the Monkhorst-Pack scheme as shown in figure 3-2. We have carried out a total energy calculation at a fixed cut-off energy of 500 eV for each structure, while the number of *k*-points was varied. For example, in figure 3-2 (c), the cubic FeAl structure was calculated from 4X4X4 up to the largest number of 18X18X18 k-points mesh parameters. We note that the k-points mesh parameter of the cubic structure has already

converged to within 1meV energy difference at 10X10X10, satisfying the convergence criteria thereof. In considering the other systems, Fe, FeAl and Fe_3Al (in figure 3-2), a similar trend is observed. A k-point mesh parameter of 10X10X10 for cubic FeAl was chosen, while that of Fe_5Al_8 was 8X8X8. Lastly, Al and Fe_2Al_5 have a k-point mesh parameter of 12X12x12 and 5X7X5, respectively. Note that the equivalent number of k-points was used for the other binary and ternary systems in the study. These are determined by varying the k-spacing for each system.

3.2 Structural and thermodynamic properties of Fe-Al

Structural and thermodynamic properties of Fe-Al alloys were performed within the generalized gradient approximation using the energy cut-off of 500 eV. The volume and lattice parameters of the structures were allowed to vary. Calculations were carried out until a good convergence was obtained (the total energy of the system changed minimally). Optimization of the structural parameters (atomic positions and lattice parameters) was achieved by minimization of forces and stress tensors. The optimized structures (ground state structures) were used to calculate the heats of formation, DOS, elastic constants and Phonon dispersion curves which will be discussed in detail in the subsequent sections.

Table 3-1 shows the results of the equilibrium lattice constants and the heats of formation of Fe-Al alloys. The calculated lattice parameters are in good agreement with the available experimental findings. In general, we observed that the lattice parameter for the calculated systems agrees to within 3 % of the experimental values. For example, the calculated binary β2 FeAl structure gave an equilibrium lattice parameter of 2.852 Å which is in good agreement with the experimental value of 2.910 Å [98]. We also note that the Fe_4Al_{13} (C2/m) structure has an equilibrium lattice parameter of (a = 15.481, b = 8.665, c = 12.386) Å which is also in better agreement with the experimental findings of (a = 15.492, b = 8.078, c = 12.471) Å. The same comparison was done for all the other binary Fe-Al alloys between the calculated and experimental values (table 3-1).

The heats of formation (ΔH_f) of the Fe-Al systems is calculated as:

$$\Delta H_f = \frac{1}{N}[E^{FeAl} - [(1-x)E^{Fe} + xE^{Al}]],$$

where E^{FeAl} is the calculated total energy of the compound, E^{Fe} and E^{Al} is the calculated total energy of each element in the compound, N is the total number of atoms in the element and x and (1-x) is the fractional concentration of the constituent elements.

In Figure 3-3 we compared the heats of formation (ΔH_f) for Fe-Al alloys and their values are listed in Table 3-1. The solid common-tangent line was constructed to illustrate the ground-state structures of the different phases. Among the structures considered, the most favourable intermetallic phases on the Al-mesh side was found to be Fe_4Al_{13} 77 at. %, FeAl 50 at. % and Fe_2Al_5 72 at. %. On the Fe-mesh side, we found $FeAl_3$ 25 at. % to be more favourable. Note that, all the other phases not found on the solid common-tangent line are either meta-stable or unstable.

Now, comparing the calculated heats of formation with the experimental data available. We observed that the predicted heats of formation for the binary β2 FeAl system is in good agreement with the experimental findings to within 3 at. %. The most stable structure was found to be the FeAl with the heats of formation of -0.568 eV/atom compared to the experimental value of -0.520 eV/atom. The Fe_2Al_5 system was also found to be stable (second-lowest negative value) with the heat of formation of -0.468 eV/atom followed by Fe_4Al_{13} with the heats of formation of -0.458 eV/atom. More importantly, we observe a significant competition between Fe_2Al_5 and Fe_4Al_{13} with a small energy difference of 0.01 eV/atom. We also note that the β2 FeAl, $FeAl_3$, Fe_2Al_5, Fe_4Al_{13}, Fe_5Al_2, and $Fe_{13}Al_4$ phases agree well with the experimental lattice parameters. Furthermore, the $FeAl_2$, $FeAl_3$, Fe_2Al, Fe_3Al, Fe_5Al_2, Fe_5Al_8, Fe_8Al_5 and $Fe_{13}Al_4$ phases were found to be meta-stable since these systems displayed the highest heats of formation value with respect to FeAl.

Table 3-1: The equilibrium lattice parameters, volume, percentage concentrations, symmetry and heats of formation (ΔH_f) of Fe-Al alloys.

Structures	At %	Person symbol	Space group	Lattice Parameters (Å)		Volume (Å^3/atom)	ΔH_f (eV/atom)
				Cal	Exp/Theo		
Al	1	-	Im-3m	a=2.879	-	10.367	-
Fe_2Al	0.33	-	P1	a=3.986 b=6.924 c=8.788	-	22.592	-0.041
Fe_2Al_5	0.71	oC24	Cmcm	a=7.150 b=6.660 c=4.390	a=7.655 b=6.415 c=4.218 [4, 17]	55.139	-0.468
Fe_3Al	0.75	$D0_3$	Fm-3m	a=3.949	a=2.895 [105, 112]	44.266	-0.336
Fe_4Al_{13}	0.76	mC102	C2/m	a=15.481 b=8.665 c=12.386	a=15.492 b=8.078 c=12.471 [4]	42.737	-0.458
Fe_5Al_8	0.61	cI52	I-43m	a=7.539	a= 8.976 [4]	25.379	-0.376
FeAl	0.50	B2 (cP2)	Pm-3m	a=2.852	a= 2.908 [4, 105, 17]^{exp} a= 2.891, a=2.874 [32, 31]^{comp}	11.596	-0.568 (-0.520) [113]^{exp} (-0.331) [31]^{comp}
$FeAl_2$	0.67	aP19	P1	a=4.987 b=6.455 c=8.924	a=4.875 b=6.455 c=8.736 [4, 17]	22.592	-0.176
Fe_5Al_2	0.29	-	Cmcm	a=7.150 b=6.660 c=4.390	-	45.579	-0.141
$FeAl_3$	0.25	-	Fm-3m	a=6.634 b=7.368 c=4.821	-	58.913	-0.134
$Fe_{13}Al_4$	0.24	-	C2/m	a=15.489 b=8.036 c=12.488	-	34.373	-0.055
Fe_8Al_5	0.39	-	I-43m	a=7.321	-	23.237	-0.232
Fe	1	-	Fm-3m	a=4.862	-	16.583	-

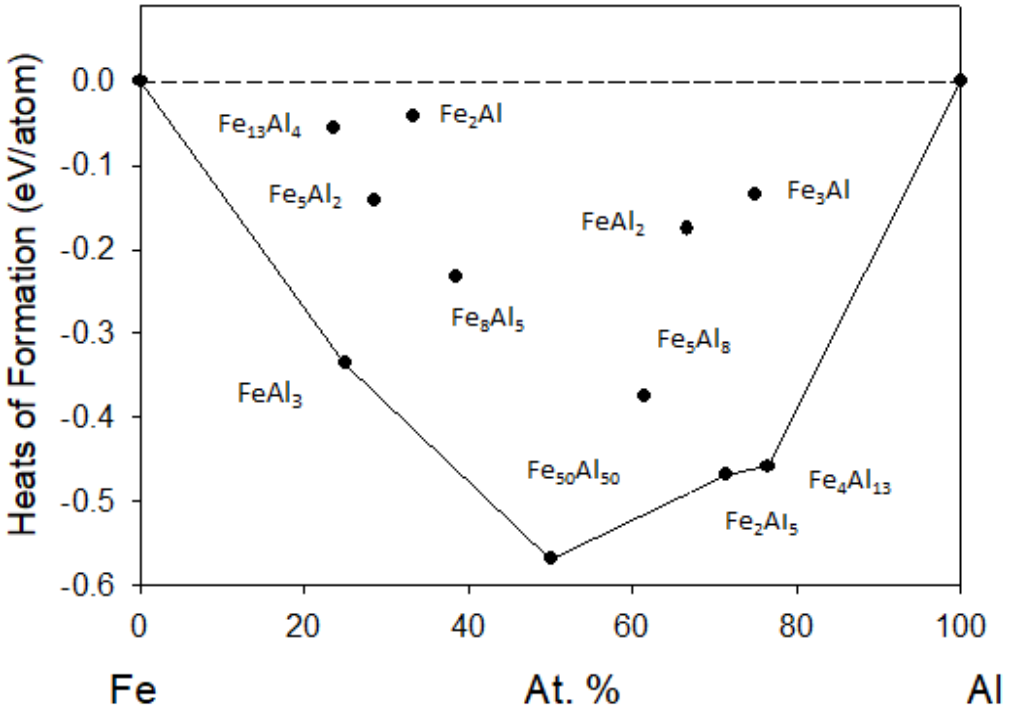

Figure 3-3: Heats of formation against atomic percentage for Fe-Al structures. The tangent line indicate the ground state structures.

3.3 Electronic properties of Fe-Al

The electronic density of states (DOS) was calculated to mimic the stabilities by observing the behaviour of electronic states near the Fermi level. This approach has been applied effectively in many studies and it is mainly to confirm or correlate the thermodynamic stability of intermetallic compounds [114, 115]. To better examine the difference in electronic structures of different crystal structures, we plot their density of states (DOS). The DOS is expressed in the number of states per atom per energy interval. We plot the DOS of Fe-Al systems at different compositions to compare their stabilities.

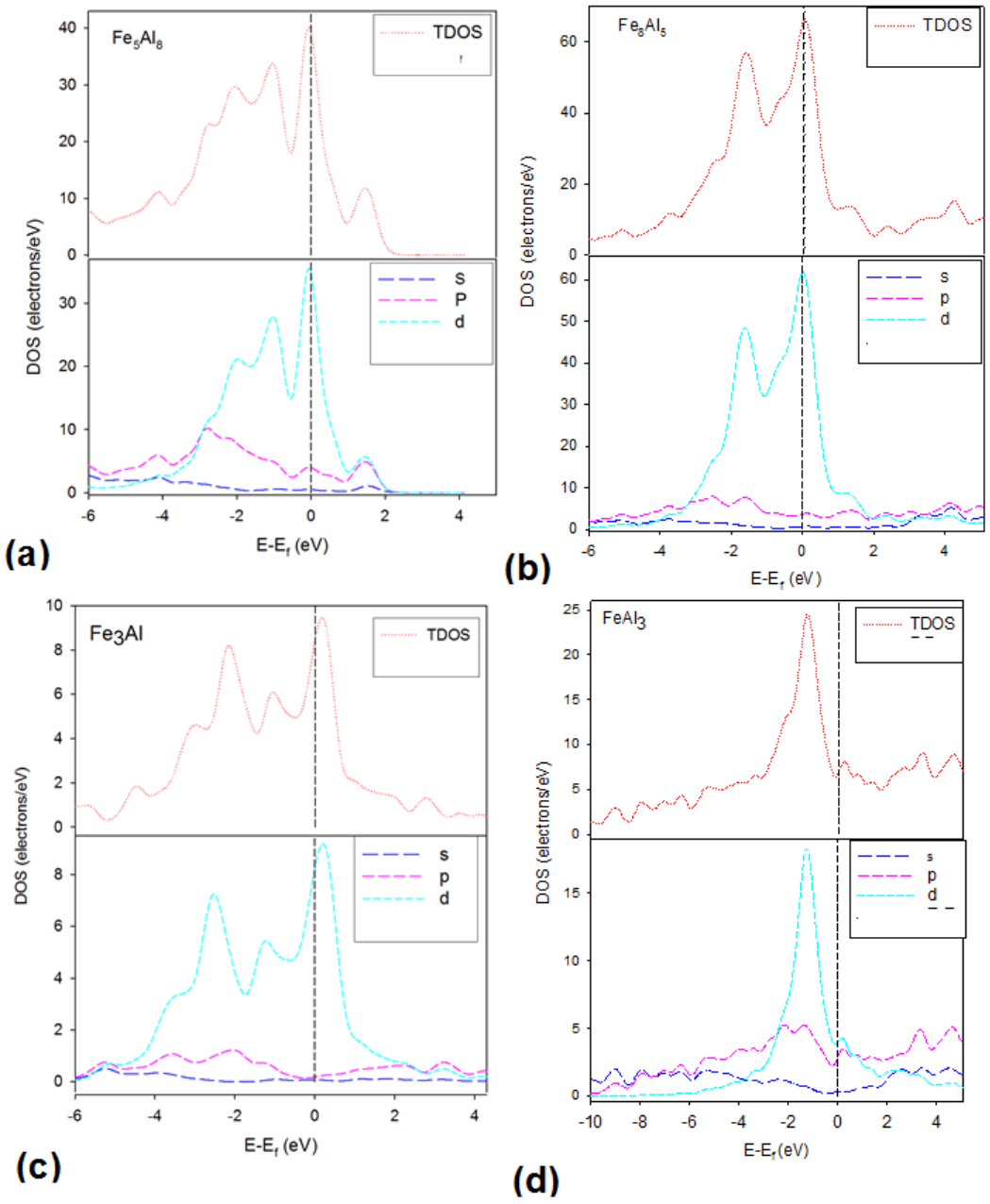

Figure 3-4: Total and partial density of states of (a) Fe_5Al_8, (b) Fe_8Al_5, (c) Fe_3Al and (d) $FeAl_3$ phases with Fermi level taken as energy zero ($E-E_f = 0$).

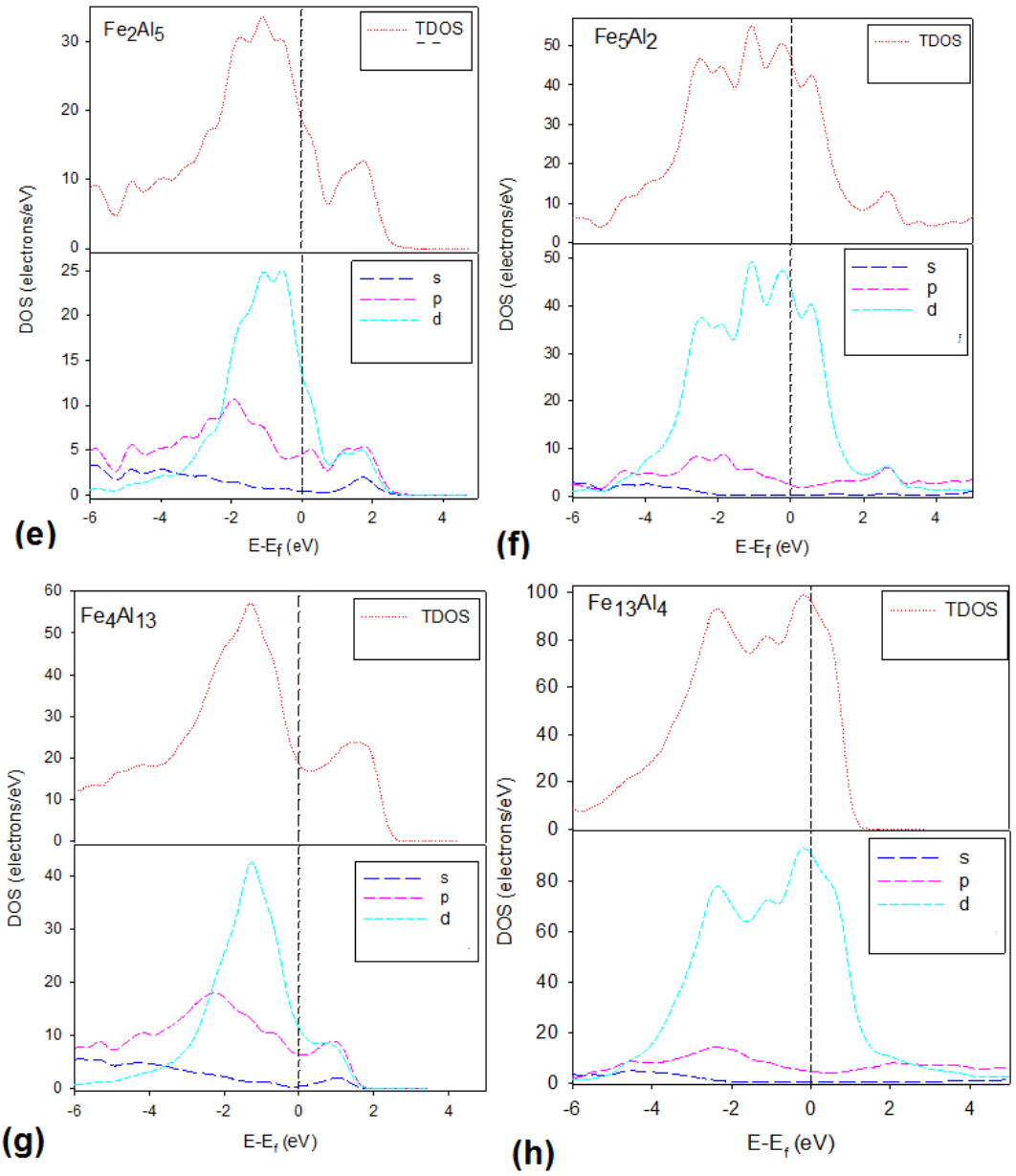

Figure 3-5: Total and partial density of states of (e) Fe_2Al_5, (f) Fe_5Al_2, (g) Fe_4Al_{13} and (h) $Fe_{13}Al_4$ phases with Fermi level taken as energy zero ($E-E_f = 0$).

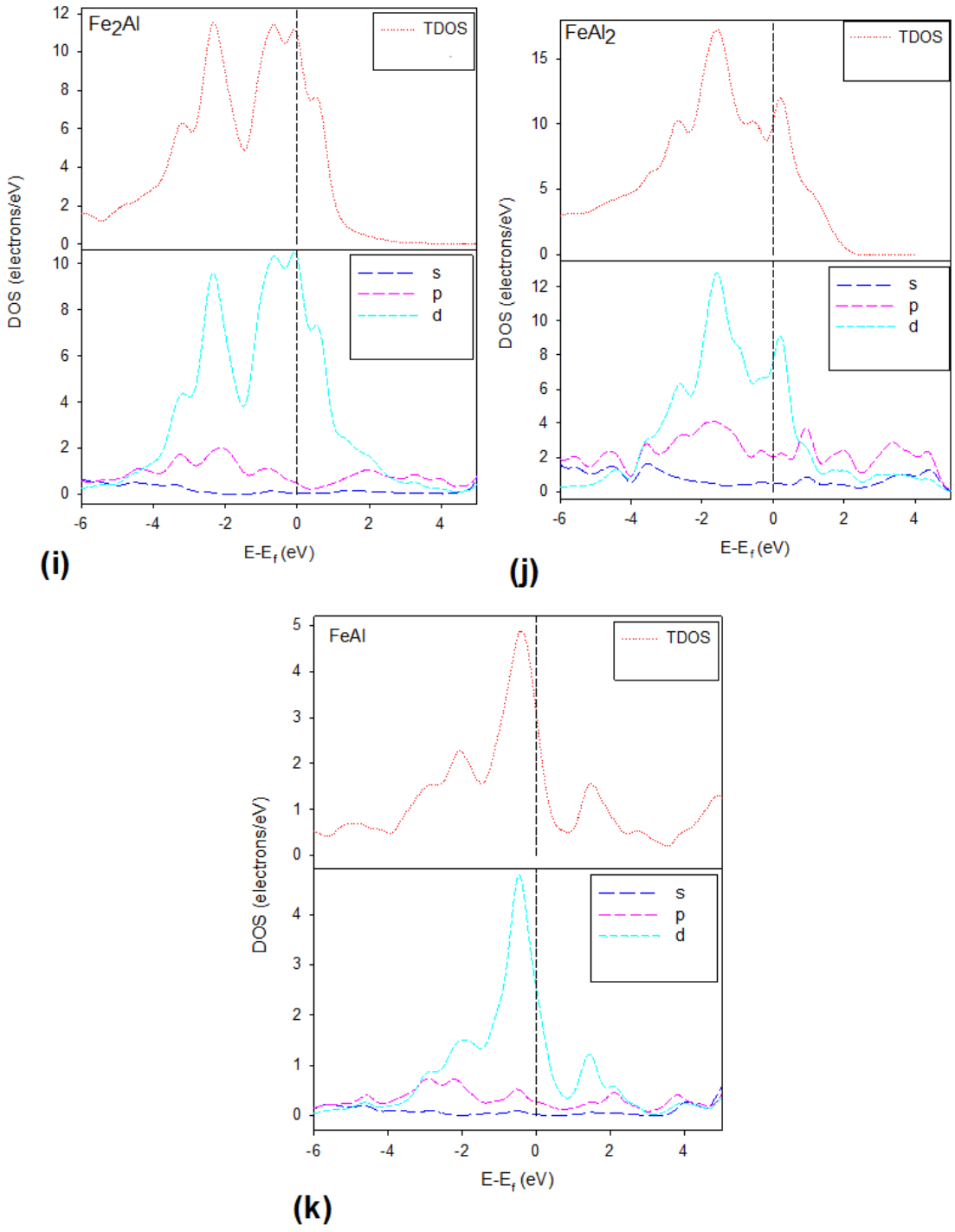

Figure 3-6: Total and partial density of states of (i) Fe_2Al, (j) $FeAl_2$ and (k) FeAl phases with Fermi level taken as energy zero ($E-E_f = 0$)

Firstly, we showed the total and partial density of states for binary Fe-Al systems in the 3:1 and 5:8 ratios (figure 3-4). We observe that the Fe_5Al_8 and Fe_8Al_5 systems show that the peaks lie at the top of the Fermi level which indicates the condition of instability and characterized by a strong *d*-orbital peak at E_f ($E-E_f = 0$). In figure 3-4, the $FeAl_3$ system was characterized by a pseudogap near the Fermi level confirming the condition of stability, while Fe_5Al_8, Fe_8Al_5, and Fe_3Al showed that the tDOS hit the top of the E_f indicating a condition of instability due to *d*-peak. In figure 3-5, the Fe_4Al_{13} system showed that the Fermi level fell within the pseudogap indicating the condition of stability and Fe_2Al_5 showed that the pseudogap fell to the right of the Fermi level, where else Fe_5Al_2 and $Fe_{13}Al_4$ showed that the tDOS and *d*-peak hit the top of the E_f stating the condition of instability.

In figure 3-6, Fe_2Al structures indicate that the tDOS and *d*-peaks lie at the top of the Fermi level which signifies the condition of electronic instability. The $FeAl_2$ system shows the condition of meta-stability as the Fermi level lies slightly to the left on the pseudogap. Moreover, the FeAl system shows that the pseudogap lies slightly to the right of the Fermi level which indicates a condition of electronic stability.

In conclusion, the systems displayed similar total DOS characterized by a strong *d*-orbital peak at E_f ($E-E_f = 0$). We observed that the partial DOS showed that the Fermi level hits the top of the *d*-peak which implies a condition of instability, this was so for Fe_2Al, Fe_5Al_8 Fe_5Al_2, and Fe_8Al_5 systems. However, for the most stable structure, the E_f fell deep in the pseudogap, indicating condition of stability, in particular Fe_4Al_{13} where else the FeAl structure showed the Fermi level to fall slightly to the right of the pseudogap. To compare the thermodynamic stability of Fe-Al systems, we plotted the total density of states (tDOS) shown in Figure 3-7. It is stated in literature that the DOS of structures with the same composition can be used to mimic the stability trend with respect to their behavior at the E_f (Fermi level), whereby the structure with the highest and lowest density of states at E_f considered the least and most stable, respectively [116, 117].

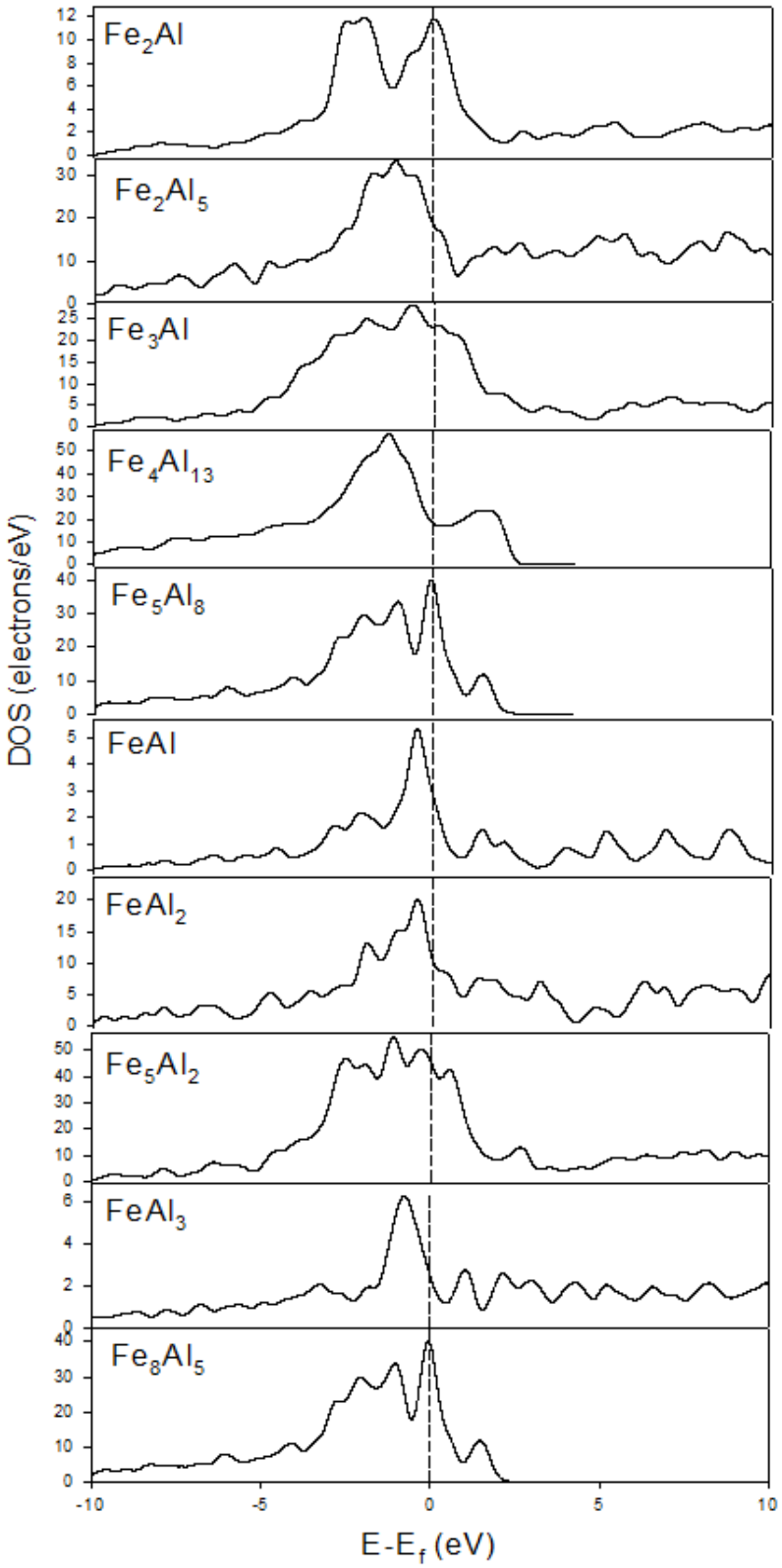

Figure 3-7: Total density of states graphs of the Fe-Al alloys. The Fermi level is taken as energy zero ($E-E_f = 0$).

In this study, we are also interested to establish an understanding of the stability trend by viewing the positioning of the E_f with respect to the pseudogap, which signifies the state of electrons of these systems. We note that the Fe_4Al_{13} peak near E_f was much broader with a pseudogap. It is clearly shown that FeAl, Fe_2Al_5 and Fe_4Al_{13} plots have a lower number of states near the E_f followed by $FeAl_3$. However, Fe_2Al, Fe_5Al_8, $FeAl_2$, Fe_5Al_2, Fe_3Al, and Fe_8Al_5 displayed the highest number of states at E_f which confirmed that these structures are the least stable. The DOS analyses were consistent with the stability trend as predicted by the heat of formation. This was also in agreement with the experimental observation of the β2 FeAl, Fe_2Al_5 and Fe_4Al_{13} structures as the most stable structures.

3.4 Elastic properties of Fe-Al

The calculated elastic constants for the binary Fe-Al alloys are listed in table 3-2. We performed full structural relaxation of the crystal systems to be able to predict the equilibrium elastic constants. Our predicted elastic constants were calculated at equilibrium and compared with experimental values. The elastic moduli such as bulk (B) and bulk to shear moduli (B/G) ratio of Fe-Al alloys are also listed in table 3-2. The mechanical stability criterion of different systems [105] is given as:

Stability criteria for cubic systems

$$C_{11} - C_{12} > 0,\ C_{11} + 2C_{12} > 0,\ C_{44} > 0$$

Orthorhombic systems

$$(C_{11} + C_{12} - 2C_{12}) > 0,\ (C_{11} + C_{33} - 2C_{13}) > 0,\ (C_{22} + C_{33} - 2C_{23}) > 0,\ C_{11} > 0,\ C_{22} > 0,\ C_{33} > 0,\ C_{44} > 0,\ C_{55} > 0,\ C_{66} > 0,\ (C_{11} + C_{22} + C_{33} + 2C_{12} + 2C_{13} + 2C_{23}) > 0.$$

For Hexagonal systems, the stability condition is:

$$C_{44} > 0,\ (C_{11}-C_{12}) > 0,\ C_{33}(C_{11} + C_{12}) > 2C_{13}^2$$

Monoclinic and triclinic systems

Monoclinic and triclinic crystal systems have 13 and 21 independent elastic constants, respectively.

The calculated shear moduli (C') is positive and indicates that all the structures under considerations are elastically stable except for the cubic Fe_3Al which showed a negative shear modulus (condition of instability). The elastic constants of FeAl and Fe_3Al were fitted to Ab-initio calculations in table 3-2 at zero temperature with suitable strain. All binary systems were found to be stable with respect to the elastic stability criterion properties except for Fe_3Al, where we observed that the system does not satisfy the stability criteria of $C_{11} > C_{12}$ which contributed to C' being negative.

The stability criteria also lead to a restriction on the magnitude of B which predicted high values of B for FeAl, $FeAl_2$, Fe_5Al_2 and $FeAl_3$ systems. Thus, from the predicted B values, we determined the ductility and brittleness using a method predicted by Pugh [118] which implied that: B/G predicts ductility if (B/G > 1.75) or brittleness if (B/G < 1.75). Note that the negative values of B/G also reflect the instability of the corresponding compounds. In this case, all values predict that the structures are brittle. The binary systems in figure 3-8 clearly show that all systems are stable satisfying stability criterion except for Fe_3Al at 25 at. %.

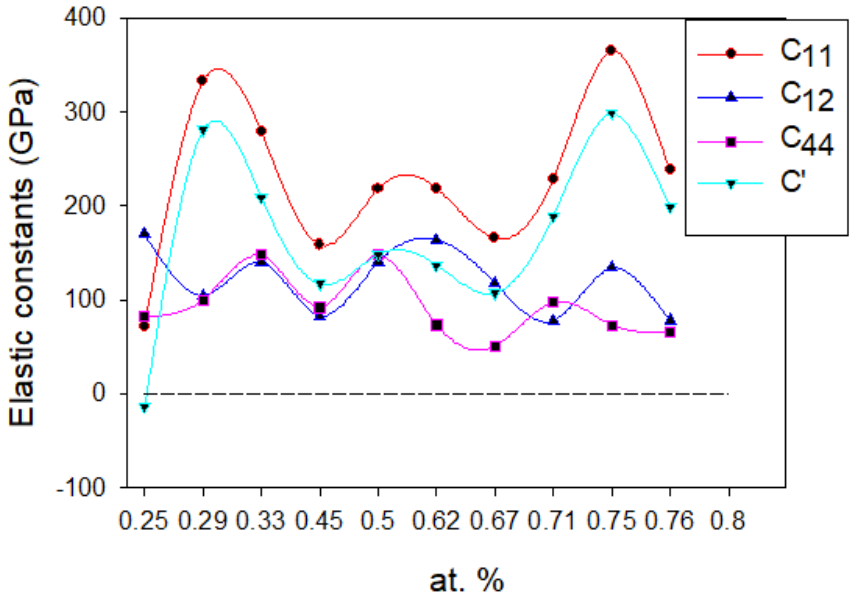

Figure 3-8: Graph of elastic constants of $Fe_{13}Al_4$, Fe_3Al, Fe_5Al_2, Fe_2Al, Fe_8Al_5, FeAl, Fe_5Al_8, $FeAl_2$, Fe_2Al_5, $FeAl_3$, Fe_4Al_{13} against at. %.

Table 3-2: Elastic moduli (GPa) for Fe-Al structures, bulk and shear moduli.

C_{ij}	Fe_2Al (P1)	Fe_2Al_5 (Cmcm)	Fe_3Al (Fm-3m)	Fe_4Al_{13} (C2/m)	Fe_5Al_8 (I-43m)	FeAl (Pm-3m) [17]	$FeAl_2$ (P1)	Fe_5Al_2 (Cmcm)	$FeAl_3$ (Fm-3m)	$Fe_{13}Al_4$ (C2/m)	Fe_8Al_5 (I-43m)
C_{11}	279.12	228.15	71.87	238.27	218.2	279.12 (192.26)	166.17	332.54	365.45	-	158.32
C_{12}	140.04	77.53	169.78	78.53	163.67	140.04 (116.96)	118.29	104.01	134.35	-	82.39
C_{22}	-	-	-	222.07	-	-	-	-	456.31	-	-
C_{33}	-	234.87	-	255.69	-	-	26.77	283.05	385.27	-	-
C_{44}	148.04	97.75	82.07	65.23	73.43	148.04 (120.16)	50.78	99.84	72.79	-	91.64
C_{55}	-	-	-	80.15	-	-	-	-	105.12	-	-
C_{66}	-	-	-	76.28	-	-	86.13	-	110.69	-	-
C_{13}	-	77.09	-	66.96	-	-	111.37	132.63	164.33	-	-
C_{15}	-	-	-	-0.22	-	-	-	-	-	-	-
C_{23}	-	-	-	38.11	-	-	-	-	-	-	-
C_{25}	-	-	-	0.65	-	-	-	-	-	-	-
C_{35}	-	-	-	8.14	-	-	-	-	-	-	-
C_{46}	-3.66		-	-	-	-	-	-	-	-	-
C'	69.54	75.31	-48.96	79.87	27.265	69.54	23.94	114.27	115.55	-	37.97
B	493.89	134.14	248.19	137.14	145.45	40090.89	95841.49	48790.71	14140.86	-	107.70
B/G	0.42	1.39	-0.05	1.45	0.94	0.01	0.00	0.01	0.02	-	0.35

3.5 Phonon dispersion curves of Fe-Al

The phonon dispersion curves of pure Iron-aluminides are calculated along the lines of the high symmetry in the Brillouin zone. The obtained phonon dispersion spectra are shown in figure 3-9, 3-10 and 3-11.

Figure 3-9 showed that FeAl, Fe_4Al_{13}, and Fe_2Al_5 are stable as there are no soft modes observed (below the zero-line) on the phonon dispersion curve, this is consistent with the C' and C_{44} which showed positive shear moduli in section 3.4. However, the Fe_3Al structure is said to be unstable since there are soft modes observed on the phonon curves (figure 3-9d), these soft modes are observed along Z and Γ high symmetry directions which are consistent with the calculated negative shear moduli (condition of instability).

Secondly, figure 3-10 shows that $FeAl_2$, Fe_5Al_8, Fe_8Al_5, and Fe_5Al_2 have imaginary soft modes below the zero-line of the phonon dispersion curves and are considered to be unstable; in particular, the FeAl system shows no soft modes. However; the Fe_5Al_2 (figure 3-10h) shows soft modes along A and Γ high symmetry direction, $FeAl_2$ also shows soft modes along the Γ and Γ direction. The Fe_5Al_8 is highly unstable at zero K, this could be that the structure exists at high temperature as shown in the phase diagram [17].

In figure 3-11, the imaginary soft modes are observed along the Z and Γ directions below the zero-line phonon curves, suggest that the $FeAl_3$ and Fe_2Al systems are unstable. These predictions suggest that the soft modes observed on the Fe-Al systems are well in accordance with the calculated shear moduli.

The stabilities of these systems listed are proven by the shown spectra which are in agreement with the experimental phase diagram [17]. The 2:1, 5:8, 1:2 and 8:5 ratio tends to be meta-stable from the predicted ΔH_f in agreement with the DOS. However, the C_{ij} are positive and inconsistent with the phonon curve showing instability, this is due to the elastic constant C_{44} being greater than C' ($(C_{11}-C_{12})/2$), which leads to the degeneracy of transverse [104] in the structure.

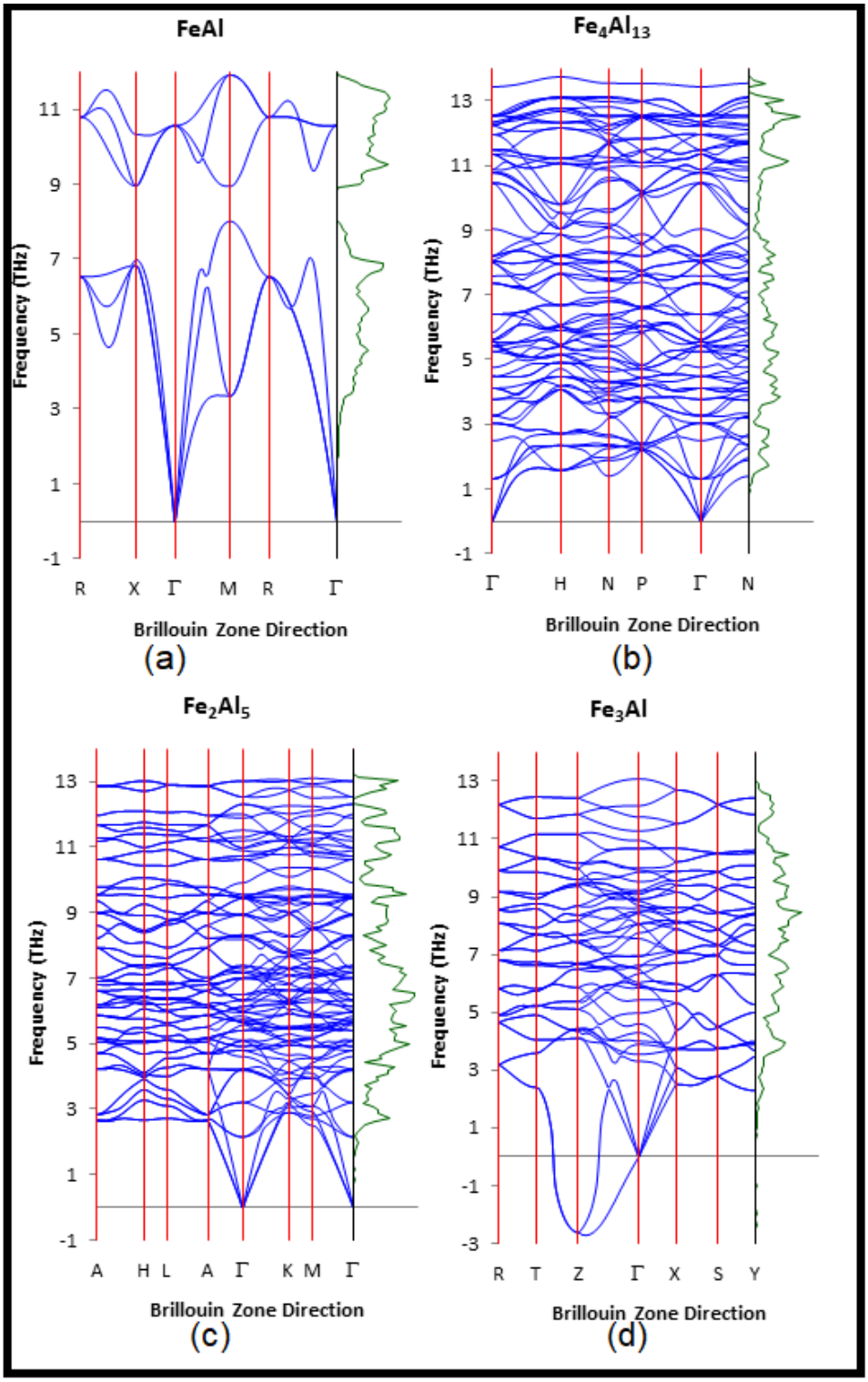

Figure 3-9: Phonon dispersion curves of FeAl, Fe_4Al_{13}, Fe_2Al_5 and Fe_3Al, structures.

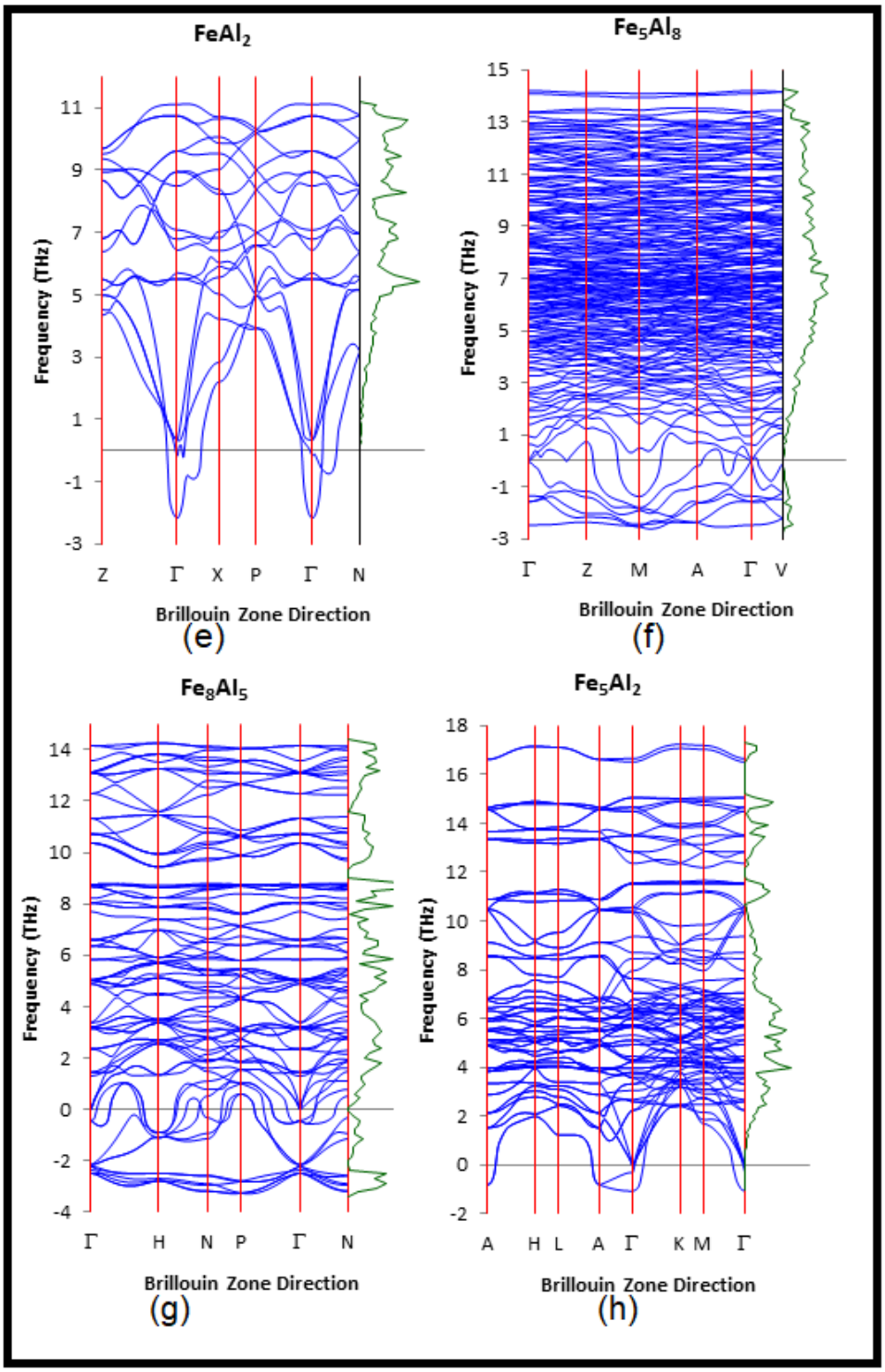

Figure 3-10: Phonon dispersion curves of $FeAl_2$, Fe_5Al_8, Fe_8Al_5 and Fe_5Al_2 structures.

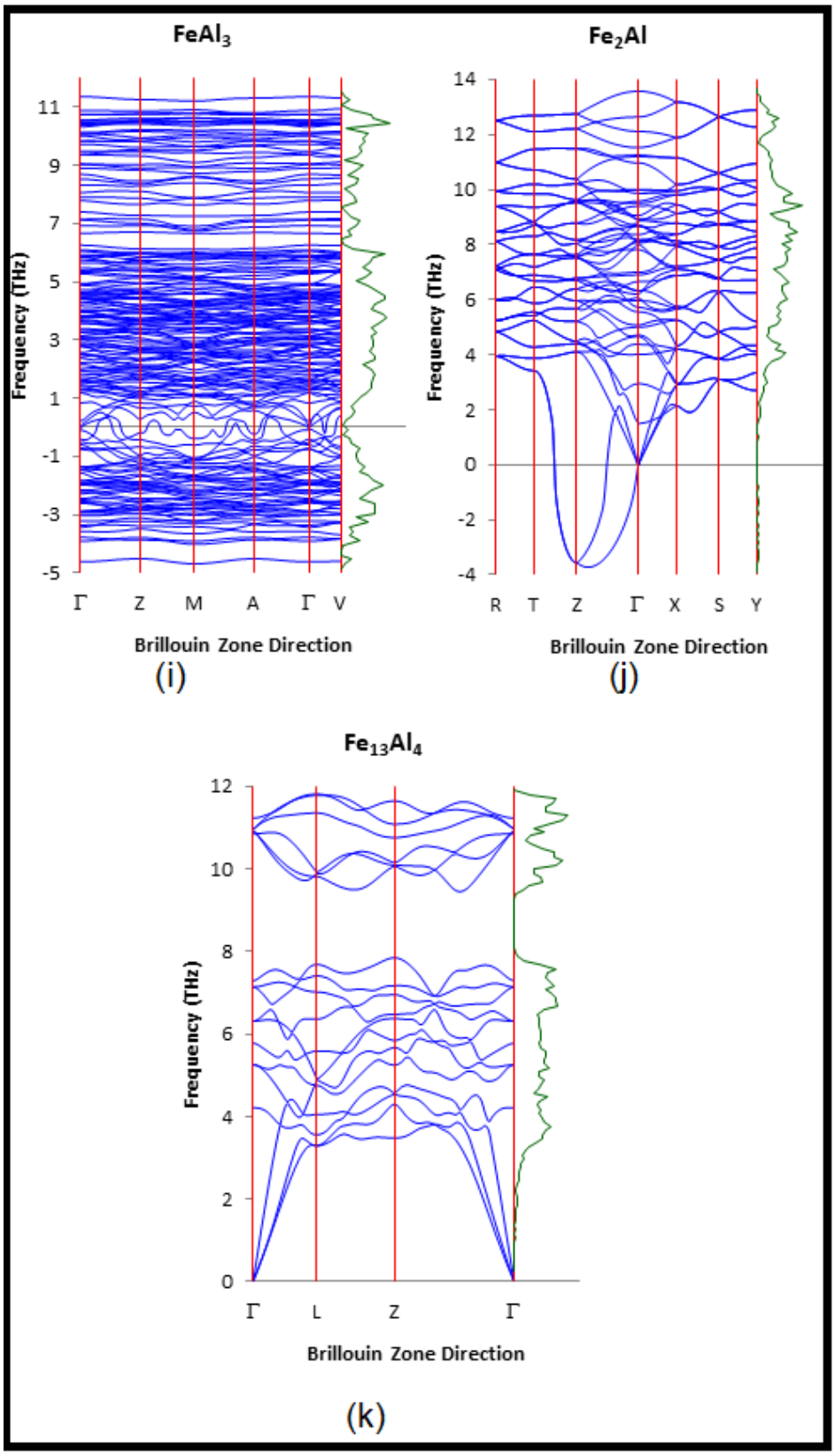

Figure 3-11: Phonon dispersion curves of $FeAl_3$, Fe_2Al and $Fe_{13}Al_4$ structures.

Chapter 4

TERNARY ALLOYING: FeAl-X

In this chapter, a detailed analysis of the Pt, Pd, Ru, Ag additions on the $Fe_{50}Al_{50}$ will be discussed. The structures were constructed using VCA which allows the formation of a mixture or a solution by addition of small concentrations in a system, as discussed in chapter 2 (see section 2.4 subsection 2.4.3). The thermodynamic, electronic and mechanical properties of $Fe_{50}Al_{50}$ doped systems will be discussed to mimic their stability.

4.1 The VCA model

We used the β2 FeAl structure to form different compositions of $Fe_{50-x}Al_{50}Xx$ and $Fe_{50}Al_{50-x}Xx$ with (X= Pt, Pd, Ru, Ag). Figure 4.1 shows the VCA representation, where the X elements are substitutional on either on the Fe or Al sub-lattice. Firstly, a concentration of 0.2 and 0.5 was chosen to validate the previous experimental findings [33]. A 0.2 at. % Ru/Pd and 0.5 at. % Pt/Ag have been constructed. Further calculations were performed for a different concentration between 0.1-0.9 at. % and 1-10 at. % to validate the suggested concentrations.

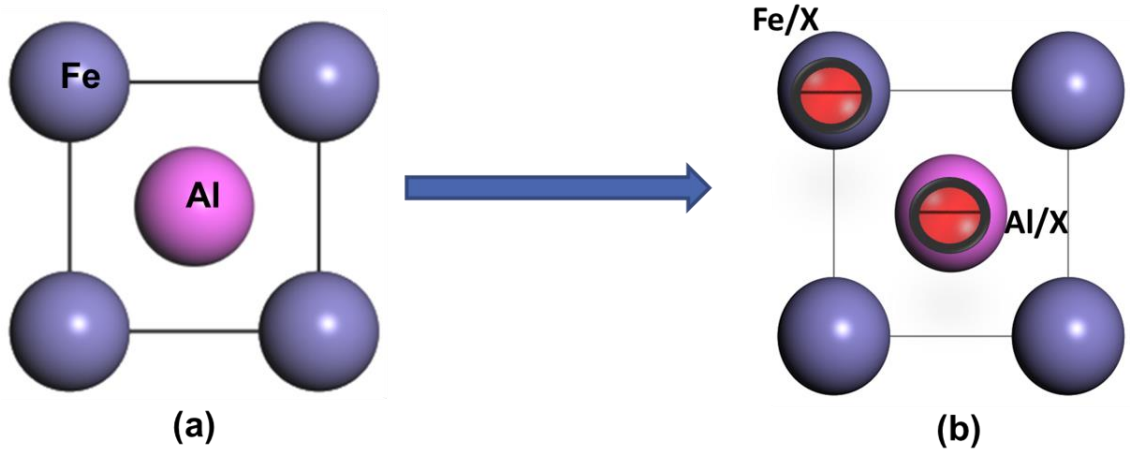

Figure 4-1: The VCA representation on (a) β FeAl (Pm-3m) structure, showing doping on either Fe or Al sub-lattice, (b) FeAl-X system, with X representing dopants (X= Pt, Ru, Pd and Ag).

4.2 Structural and thermodynamic properties of FeAl-X.

4.2.1 FeAl-X (X= Pt, Ru)

In this section, we focus on the Pt and Ru substitution on the $Fe_{50}Al_{50}$ to deduce the preferable sub-lattice. The recent experimental work indicated that 0.5 at. % Pt and 0.2 at. % Ru stabilizes the FeAl structure [33, 39]. This is used as a guideline and validation on the doping preferential and sub-lattice of the β-FeAl structure.

Firstly, the β2 FeAl structure was optimized before doping could take place. Secondly, the most energetically favourable structure was determined by checking Pt and Ru metal doping concentrations on either Fe or Al sub-lattice. Firstly, we calculated the equilibrium lattice parameters to deduce the ground state structure with respect to the total energy, and the heats of formation such that one with the lowest heats of formation value is regarded to be the most stable structure, (see the calculated data summarised in table 4-1).

The Al and Fe sub-lattice were investigated by the addition of 0.2 at. % Ru and 0.5 at. % Pt. Firstly, the addition of 0.2 at. % Ru addition on both sub-lattices showed a decrease in the lattice parameter of (2.848 Å) from $Fe_{50}Al_{50}$ (2.852 Å) and the volume (23.107 $Å^3$/atom) of the system. Now, doping on the Fe sub-lattice showed an increase in the lattice parameter (2.851 Å) and the volume (23.185 $Å^3$/atom) of the system. Lastly, when doping on the Al sub-lattice, we observed a slight decrease in the lattice parameter (2.848 Å) and a slight increase in the volume (23.108 $Å^3$/atom) of the system compared to doping on both sub-lattices. Secondly, considering the addition of the 0.5 at. %, when doping on both sub-lattices, we observed a constant value from the $Fe_{50}Al_{50}$ (2.852 Å) in the lattice parameter (2.852 Å) and a slightly higher value in the volume (23.220 $Å^3$/atom) of the system. Interestingly, when doping on the Fe sub-lattice we observed a similar value in the lattice parameter (2.852 Å) and a slight decrease in the volume (23.197 $Å^3$/atom) of the system. Lastly the Al sub-lattice showed an increase in the lattice parameter (2.853 Å) and similar volume (23.220 $Å^3$/atom) as compared to doping on both sub-lattices. We found that the lattice parameter with Ru addition at 0.2 % was found to be 2.851 Å with a volume of 23.185 $Å^3$/atom, while

for Pt addition at 0.5 % was found to be 2.852 Å with a volume of 23.197 $Å^3$/atom. The lattice parameter mismatches due to the volume for Ru and Pt was insignificant since all the composition gave lattice parameters between (2.80-2.90) Å.

The heats of formation per atom of FeAl-X is given by:

$$\Delta H_f = \frac{1}{N}[E_{total} - [(1-x)E_a + xE_b + \ldots\ldots]],$$

where E_a and E_b represents the total energy of the system a and b; N is the total number of atoms in the system, and x is the composition on each system. The heats of formation calculations, for the $Fe_{50}Al_{50}$ structure, reveal a significant competition between the cubic $Fe_{50-x}Al_{50}Pt_X$ and $Fe_{50-x}Al_{50}Ru_X$ structures as shown in table 4-1.

The β2 $Fe_{50}Al_{50}$ heats of formation value (-0.568 eV/atom) showed to be in good agreement with the experimental findings (-0.605 eV/atom) [98]. Furthermore, the Al and Fe sub-lattice were investigated by the addition of 0.2 at. % Ru and 0.5 at. % Pt. Firstly, the addition of 0.2 at. % Ru addition on both sub-lattices showed a decrease in the heats of formation (-0.453 eV/atom) from $Fe_{50}Al_{50}$ (-0.568 eV/atom) of the system. Now, doping on the Fe sub-lattice showed an increase in the heats of formation (-0.455 eV/atom) of the system. Lastly, when doping on the Al sub-lattice, we observed a decrease in the heats of formation (-0.452 eV/atom) of the system compared to doping on either both or the Al sub-lattices. Secondly, considering the addition of the 0.5 at. %, when doping on both sub-lattices, we observed a greater decrease in the heats of formation (-0.429 eV/atom) in comparison from the binary $Fe_{50}Al_{50}$ (-0.568 eV/atom) system. Interestingly, when doping on the Fe sub-lattice we observed a slight increase in the heats of formation (-0.431 eV/atom) of the system. Lastly, the Al sub-lattice showed a decrease in the heats of formation (-0.427 eV/atom)) as compared to doping on both sub-lattices. The predicted outcome illustrates that the Ru and Pt prefer the Fe sub-lattice with a composition of $Fe_{49.80}Al_{50.00}Ru_{0.2}$ and $Fe_{49.50}Al_{50.00}Pt_{0.5}$. We also note that $Fe_{50-x}Al_{50}Ru_X$ is more stable as compared to $Fe_{50-x}Al_{50}Pt_X$ phase. The predicted heat of formation was -0.333 eV/atom compared to the experimental value of -0.376 eV/atom (Breuer et al., 2001).

Table 4-1: Equilibrium lattice parameters, volume and heats of formation (ΔH_f) of the FeAl-Pt/Ru alloys.

Composition	Dopant (at. %)		Lattice parameter (Å)	Volume (Å^3/atom)	ΔH_f (eV/atom)
	Ru	Pt			
$Fe_{50}Al_{50}$	-	-	2.852	23.192	-0.568 (-0.605) [98]
$Fe_{49.90}Al_{49.90}Ru_{0.2}$	0.2	-	2.848	23.107	-0.453
$Fe_{49.80}Al_{50}Ru_{0.2}$	0.2	-	2.851	23.185	-0.455
$Fe_{50}Al_{49.80}Ru_{0.2}$	0.2	-	2.848	23.108	-0.452
$Fe_{49.75}Al_{49.75}Pt_{0.5}$	-	0.5	2.852	23.220	-0.429
$Fe_{49.50}Al_{50}Pt_{0.5}$	-	0.5	2.852	23.197	-0.431
$Fe_{50}Al_{49.50}Pt_{0.5}$	-	0.5	2.853	23.220	-0.427

4.2.2 **FeAl-X (X= Pt, Ru, Pd, Ag)**

In this section, we discuss the effect of doping with Pt, Ru, Pd, and Ag for the composition range of $1 \leq x \leq 10$ using VCA. The results are summarized in table 4-2 and 4-3. Doping with Pt between $1 \leq x \leq 10$ indicates an increase in the lattice parameter and volume up to 5 at. % and then begins to decrease up to 10 at. % Pt (table 4-2). However, at 8 at. % Pt there is a mishap in the volume of the system which may be due to structural failure. Now, doping with Ru, showed that the lattice parameter and volume decreases linearly as Ru concentration. Hence the inserted graphs assist in showing the behaviour of the Fe-Al-X systems at various compositions as guided by experimental preferential of 0.2 at. % Ru and 0.5 at. % Pt. The metal concentration of 0.2 at. % Ru/Pd and 0.5 at. % Pt/Ag was said to improve the corrosion resistance and oxidation properties of these alloys [6]. Thus, to improve the stability of our structures various properties and stability criteria were considered.

Table 4-2: Lattice parameter, Volume and Heats of formation (ΔH_f) of the $Fe_{50-x}Al_{50}Pt_x$ and $Fe_{50-x}Al_{50}Ru_x$ alloy

Composition	Dopant (At. %)	Lattice parameter (Å)	Volume (Å^3/atom)	ΔH_f (eV/atom)
	Pt			
$Fe_{49.00}Al_{50}Pt_1$	1	3.295	27.480	-0.0194
$Fe_{48.00}Al_{50}Pt_2$	2	3.375	29.600	-0.0823
$Fe_{47.00}Al_{50}Pt_3$	3	3.611	36.253	-0.1284
$Fe_{46.00}Al_{50}Pt_4$	4	3.623	36.610	-0.1706
$Fe_{45.00}Al_{50}Pt_5$	5	3.631	36.863	-0.2121
$Fe_{44.00}Al_{50}Pt_6$	6	3.585	35.484	-0.2540
$Fe_{43.00}Al_{50}Pt_7$	7	3.547	34.357	-0.2677
$Fe_{42.00}Al_{50}Pt_8$	8	3.512	33.358	-0.3391
$Fe_{41.00}Al_{50}Pt_9$	9	3.235	26.058	-0.3857
$Fe_{40.00}Al_{50}Pt_{10}$	10	3.396	30.142	-0.4320
	Ru			
$Fe_{49.00}Al_{50}Ru_1$	1	2.267	8.973	0.1334
$Fe_{48.00}Al_{50}Ru_2$	2	2.254	8.812	0.1709
$Fe_{47.00}Al_{50}Ru_3$	3	2.239	8.650	0.2082
$Fe_{46.00}Al_{50}Ru_4$	4	2.226	8.488	0.2454
$Fe_{45.00}Al_{50}Ru_5$	5	2.212	8.336	0.2824
$Fe_{44.00}Al_{50}Ru_6$	6	2.200	8.198	0.3192
$Fe_{43.00}Al_{50}Ru_7$	7	2.189	8.071	0.3559
$Fe_{42.00}Al_{50}Ru_8$	8	2.178	7.952	0.3925
$Fe_{41.00}Al_{50}Ru_9$	9	2.167	7.836	0.4289
$Fe_{40.00}Al_{50}Ru_{10}$	10	2.158	7.736	0.4652

We observe a linear decrease in the heats of formation as the at. % Pt is increased from 1 up to 10 at. %; however, a slightly greater decrease at 7 at. %, thus confirming the experimental suggestion of preference of a lower at. %, clearly the inserted graph in figure 4-2 depicts that indeed 0.5 at. % is a suitable concentration for the system. Secondly, at. % Ru showed a linear increase in the heats of formation as at. % is increased, indicating 0.2 at. % to be a suitable concentration for the system.

Doping Pd from 1 up to 10 at. % showed a fluctuation in the lattice parameter while we also observed a similar case of fluctuation in the volume of the system. Doping with Ag, showed fluctuation in the lattice parameter and volume of a system. Pd and Ag from 1 up to 10 at. % was plotted and incorporating 0.1 to 0.9 at. % as validation of the preferred concentration, See figure 4-3. A linear decrease in the heats of formation is observed as the at. % Pd is increased from 1 up to 10 at. %, thus confirming the experimental suggestion of preference of a lower at. %, hence the inserted graph depicts that indeed 0.5 at. % is a suitable concentration for the system. Secondly, at. % Ag showed a linear decrease in the heats of formation as at. % is increased, thus the smaller concentration of the inserted graph in figure 4-3 indicating 0.2 at. % to be a suitable concentration for the system.

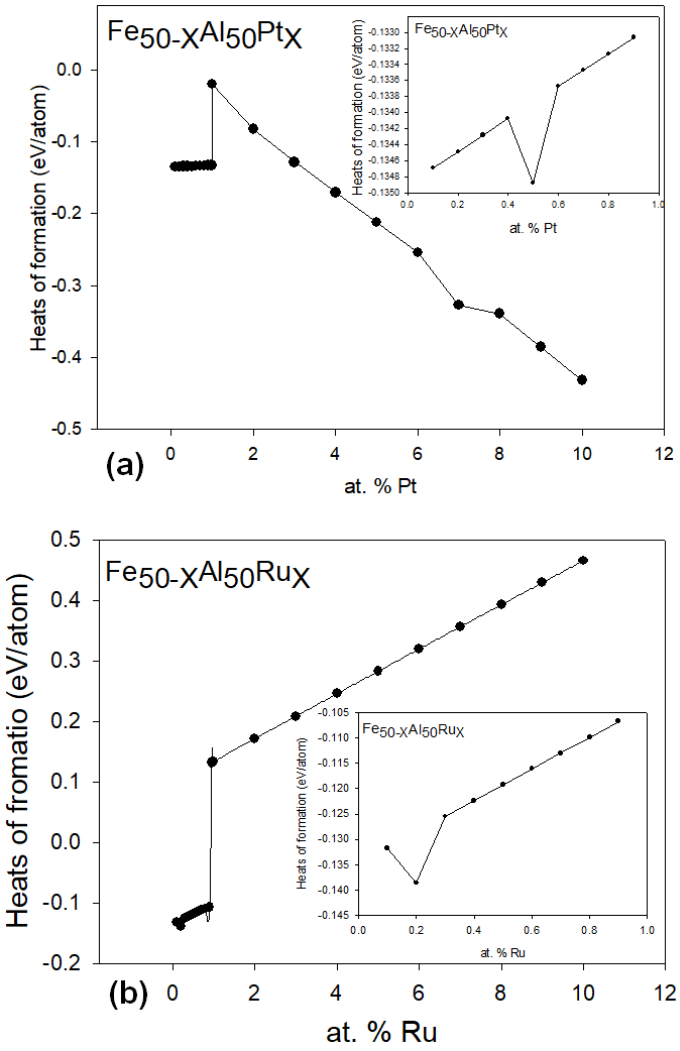

Figure 4-2: Heats of formation (ΔH_f) against the atomic percentage of (a) $Fe_{50-x}Al_{50}Pt_x$ and (b) $Fe_{50-x}Al_{50}Ru_x$ alloys. The insert in (a) and (b) shows the trend between 0.1 to 0.9 at. %.

Further substitutions were done at smaller concentrations for Pt, Pd, Ag and Ru ($0.1 \leq x \leq 0.9$) of $Fe_{50}Al_{50}$ as validation for the preferred concentration according to experimental findings. We calculated the equilibrium lattice parameters and the heats of formation, the lattice parameter of Pd was found to be 6.943 Å with a volume of 334.727 $Å^3$/atom and 5.757 Å with a volume of 190.760 $Å^3$/atom for Ag.

Table 4-3: Lattice parameter, Volume, and Heats of formation (ΔH_f) of the $Fe_{50-x}Al_{50}X_x$ doped with Pd and Ag ($1 \leq x \leq 10$) alloy

Composition	Dopant (at. %)	Lattice parameter (Å)	Volume (Å^3/atom)	ΔH_f (eV/atom)
	Pd			
$Fe_{49.00}Al_{50}Pd_1$	1	6.844	320.627	-0.2379
$Fe_{48.00}Al_{50}Pd_2$	2	5.706	185.743	-0.2291
$Fe_{47.00}Al_{50}Pd_3$	3	5.998	215.757	-0.2184
$Fe_{46.00}Al_{50}Pd_4$	4	6.372	258.748	-0.2027
$Fe_{45.00}Al_{50}Pd_5$	5	6.306	250.768	-0.1935
$Fe_{44.00}Al_{50}Pd_6$	6	6.275	247.030	-0.1848
$Fe_{43.00}Al_{50}Pd_7$	7	6.198	238.086	-0.1766
$Fe_{42.00}Al_{50}Pd_8$	8	5.765	191.600	-0.1698
$Fe_{41.00}Al_{50}Pd_9$	9	6.222	240.893	-0.1633
$Fe_{40.00}Al_{50}Pd_{10}$	10	6.083	225.126	-0.1554
	Ag			
$Fe_{49.00}Al_{50}Ag_1$	1		187.845	-0.2367
$Fe_{48.00}Al_{50}Ag_2$	2	6.513	276.280	-0.2169
$Fe_{47.00}Al_{50}Ag_3$	3	5.173	138.458	-0.2088
$Fe_{46.00}Al_{50}Ag_4$	4	5.943	209.909	-0.1911
$Fe_{45.00}Al_{50}Ag_5$	5	6.249	244.032	-0.1797
$Fe_{44.00}Al_{50}Ag_6$	6	5.769	192.051	-0.1694
$Fe_{43.00}Al_{50}Ag_7$	7	5.828	197.929	-0.1584
$Fe_{42.00}Al_{50}Ag_8$	8	5.419	159.169	-0.1500
$Fe_{41.00}Al_{50}Ag_9$	9	5.745	189.583	-0.1403
$Fe_{41.00}Al_{50}Ag_{10}$	10	5.738	188.955	-0.1319

Clearly, the preferred doped composition gave the lowest heats of formation at. 0.5 % as shown in table 4-4 for $Fe_{50-x}Al_{50}Pt_x$ and $Fe_{50-x}Al_{50}Ag_x$. Moreover, $Fe_{50-x}Al_{50}Ru_x$ and $Fe_{50-x}Al_{50}Pd_x$ doping in table 4-4 denotes that 0.2 at. % is the preferred concentration in terms of stability of the structure which is in agreement with the experimental findings. Among the structures considered, the most favourable intermetallic phases were found to be $Fe_{49.80}Al_{50}Ru_{0.2}$, $Fe_{49.50}Al_{50}Pt_{0.5}$,

$Fe_{49.50}Al_{50}Ag_{0.5}$ and $Fe_{49.80}Al_{50}Pd_{0.2}$ with the lowest heats of formation. Pd addition showed that at 0.2 at. % is the most stable composition in agreement with experimental findings [33] .

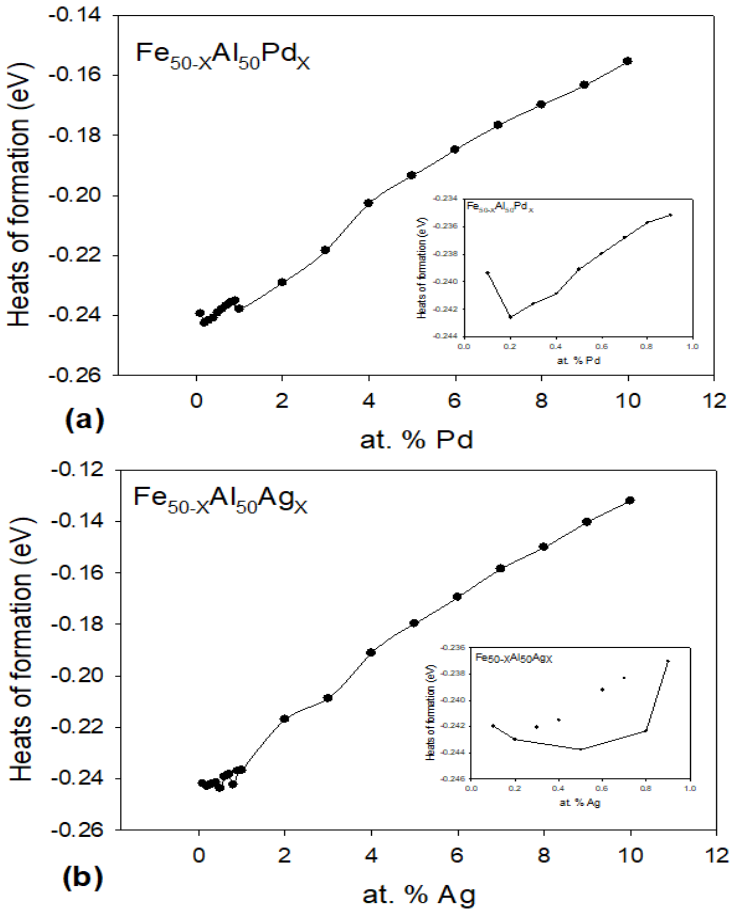

Figure 4-3: Heats of formation (ΔH_f) against an atomic percentage of (a) $Fe_{50-x}Al_{50}Pt_X$ and (b) $Fe_{50-x}Al_{50}Ru_X$ alloys. The insert in (a) and (b) shows the trend between 0.1 to 0.9 at. %.

Table 4-4 shows that at 0.35, 0.38, 0.45 and 0.48 at. % Pt may be considered meta-stable. Table 4-3 denotes that from 0.4 at. % Ru the system becomes less stable (decrease in heats of formation), thus 0.2 at. % of Ru is regarded as the most stable (lowest heats of formation). However, these phases have not been reported in the literature. At (0.3, 0.4, 0.6 and 0.7) at. % implied that the stability decreases as the concentrations for Ag increased. However, it is clear that at 0.5 at. % Ag, the structure becomes the most stable which is in agreement with experimental findings.

Table 4-4: **Heats of formation (ΔH_f) of the $Fe_{50-x}Al_{50}Pt_x$ alloy.**

Composition	Dopant (at. %)	Lattice parameter (Å)	Volume (Å^3/atom)	ΔH_f (eV/atom)
	Pt			
$Fe_{49.90}Al_{50}Pt_{0.1}$	0.1	2.2761	9.077	-0.4367
$Fe_{49.80}Al_{50}Pt_{0.2}$	0.2	2.264	8.931	-0.4321
$Fe_{49.70}Al_{50}Pt_{0.3}$	0.3	2.354	10.042	-0.4449
$Fe_{49.60}Al_{50}Pt_{0.4}$	0.4	2.777	16.495	-0.4480
$Fe_{49.50}Al_{50}Pt_{0.5}$	0.5	2.852	23.191	-0.4605
	Ru			
$Fe_{49.90}Al_{50}Ru_{0.1}$	0.1	2.809	23.135	-0.4513
$Fe_{49.80}Al_{50}Ru_{0.2}$	0.2	2.851	23.185	-0.4520
$Fe_{49.70}Al_{50}Ru_{0.3}$	0.3	2.279	23.099	-0.4517
$Fe_{49.60}Al_{50}Ru_{0.4}$	0.4	2.279	23.079	-0.4504
$Fe_{49.50}Al_{50}Ru_{0.5}$	0.5	2.275	23.063	-0.4501
$Fe_{49.40}Al_{50}Ru_{0.6}$	0.6	2.273	23.045	-0.4498
$Fe_{49.30}Al_{50}Ru_{0.7}$	0.7	2.272	23.028	-0.4495
$Fe_{49.20}Al_{50}Ru_{0.8}$	0.8	2.271	23.011	-0.4492

Table 4-5: **Heats of formation (ΔH_f) of the $Fe_{50-x}Al_{50}Pd/Ag$ alloys**

Composition	Dopant (at. %)	Lattice parameter (Å)	Volume (Å^3/atom)	ΔH_f (eV/atom)
	Pd			
$Fe_{49.00}Al_{50}Pd_{0.1}$	0.1	6.853	321.914	-0.2394
$Fe_{48.00}Al_{50}Pd_{0.2}$	0.2	6.943	334.727	-0.2425
$Fe_{47.00}Al_{50}Pd_{0.3}$	0.3	6.290	248.866	-0.2416
$Fe_{46.00}Al_{50}Pd_{0.4}$	0.4	6.503	274.990	-0.2409
$Fe_{45.00}Al_{50}Pd_{0.5}$	0.5	6.893	327.444	-0.2391
$Fe_{44.00}Al_{50}Pd_{0.6}$	0.6	6.887	326.652	-0.2379
$Fe_{43.00}Al_{50}Pd_{0.7}$	0.7	6.875	324.944	-0.2368
$Fe_{42.00}Al_{50}Pd_{0.8}$	0.8	6.560	282.326	-0.2357
$Fe_{41.00}Al_{50}Pd_{0.9}$	0.9	6.526	277.958	-0.2352
	Ag			
$Fe_{49.00}Al_{50}Ag_{0.1}$	0.1	6.936	333.628	-0.2419
$Fe_{48.00}Al_{50}Ag_{0.2}$	0.2	5.327	151.149	-0.2429
$Fe_{47.00}Al_{50}Ag_{0.3}$	0.3	6.545	280.386	-0.2421
$Fe_{46.00}Al_{50}Ag_{0.4}$	0.4	6.688	299.168	-0.2415
$Fe_{45.00}Al_{50}Ag_{0.5}$	0.5	5.757	190.760	-0.2434
$Fe_{44.00}Al_{50}Ag_{0.6}$	0.6	6.856	322.308	-0.2392
$Fe_{43.00}Al_{50}Ag_{0.7}$	0.7	6.498	274.392	-0.2383
$Fe_{42.00}Al_{50}Ag_{0.8}$	0.8	6.102	227.192	-0.2423
$Fe_{41.00}Al_{50}Ag_{0.9}$	0.9	6.145	264.046	-0.2370

4.3 Effect of Ru/Pt on the electronic properties of β2 FeAl

The electronic density of states was determined in order to mimic the stability of systems at the Fermi level. The lower the electronic states at the Fermi level, the stable is the systems. Various concentrations were doped on different sub-lattices in order to observe the most stable system; this was done to validate the preferred atomic site (0.2 at. % Ru and 0.5 at. % Pt on Fe-lattice) on the binary phase $Fe_{50}Al_{50}$.

Figure 4-4 shows the DOS of $Fe_{50}Al_{49.50}Ru_{0.2}$, $Fe_{49.50}Al_{50}Ru_{0.2}$, $Fe_{49.90}Al_{49.90}Ru_{0.2}$, $Fe_{49.75}Al_{49.75}Pt_{0.5}$, $Fe_{50}Al_{49.50}Pt_{0.5}$ and $Fe_{49.50}Al_{50}Pt_{0.5}$ structures. The *s* and *p*-orbital contributions are negligible since they play little role in the bonding except to donate some electrons to vacant states. The DOS peaks of the high-temperature phases tend to behave similarly due to the little concentration addition of Pt and Ru. The structure with the highest and lowest density of states at E_f was considered the least and most stable, respectively.

Figure 4-4 illustrates the total and partial density of states for each system on different sub-lattices for Platinum and Ruthenium doping. Figures 4-4 (a), (b), (c), (d), (e) and (f) show that their pseudogap lies slightly to the right of the fermi level which all show the condition of electronic stability. However, the heats of formation calculated in table 4-1 assisted in identifying the most preferable sub-lattice substitution, in this case, the Fe sub-lattice ($Fe_{49.50}Al_{50}Pt_{0.5}$ and $Fe_{49.80}Al_{50}Ru_{0.2}$) was the most preferable for both Pt and Ru doping since they showed to have the lowest heats of formation.

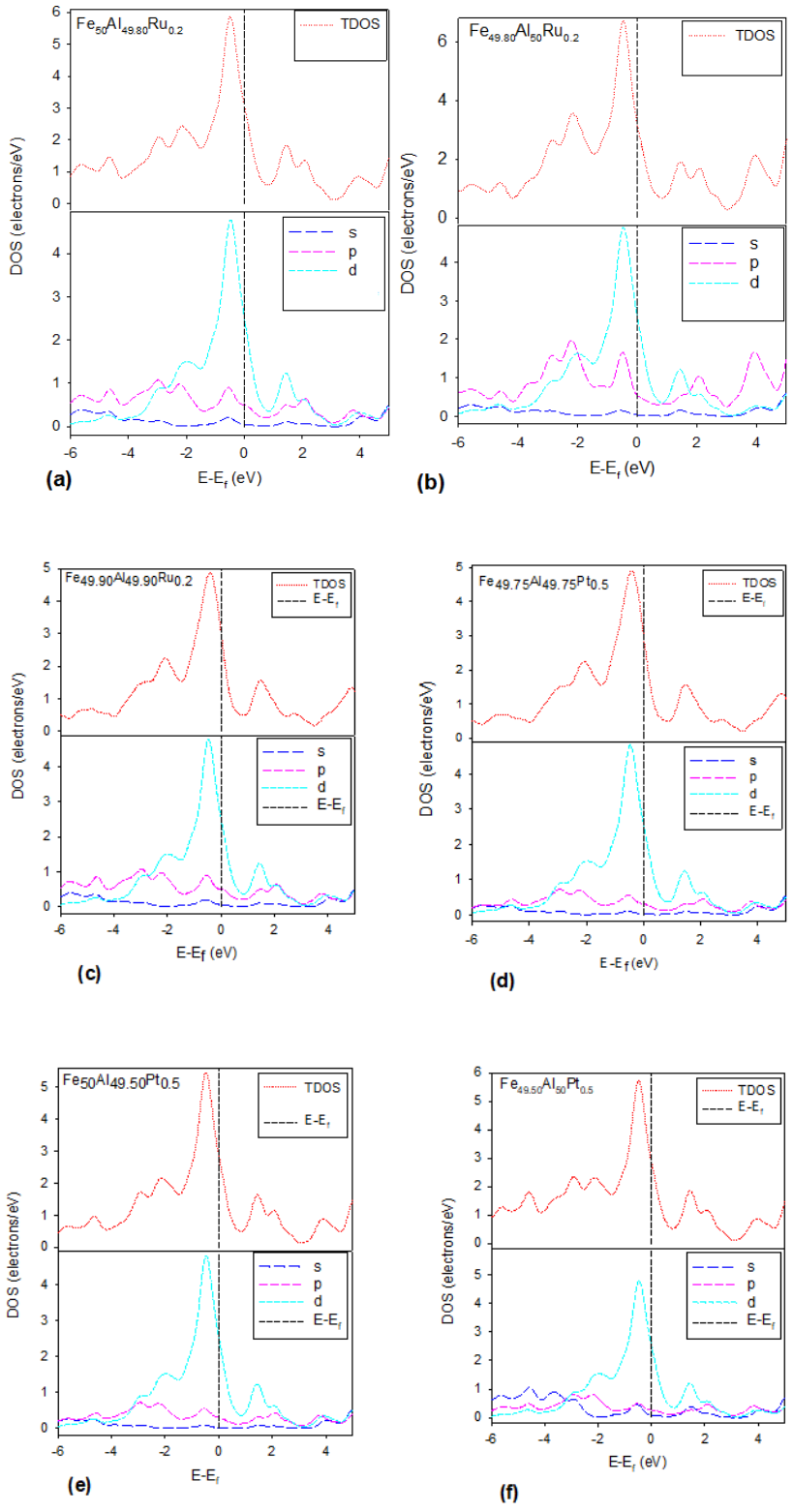

Figure 4-4: Total and partial density of States after doping of (a) $Fe_{50}Al_{49.80}Ru_{0.2}$, (b) $Fe_{49.80}Al_{50}Ru_{0.2}$, (c) $Fe_{49.90}Al_{49.90}Ru_{0.2}$, (d) $Fe_{49.75}Al_{49.75}Pt_{0.5}$, (e) $Fe_{50}Al_{49.50}Pt_{0.5}$ and (f) $Fe_{49.50}Al_{50}Pt_{0.5}$ structures with Fermi level is taken as energy zero ($E\text{-}E_f = 0$)

4.4 Electronic density of states $Fe_{50-X}Al_{50}X$

4.4.1 DOs for $Fe_{50-X}Al_{50}Pt/Ru$

The electronic density of states (DOS) was calculated to mimic the stabilities by observing the behaviour of electronic states near the Fermi level. This approach has been used effectively in many studies and is mainly used to confirm or correlate the thermodynamic stability of intermetallic compounds [114, 115]. Firstly, we showed the total and partial density of states for binary FeAl system in Figure 4-5 (a). We observe that the structure was characterized by a pseudogap near the Fermi level (confirming a metallic behaviour character). A more noticeable Fe *d*-peak was observed, which forms a strong hybridization with the Al *p*-orbital. More importantly, we saw that the Fermi level fell slightly on the left of the pseudogap, which signifies electronic stability in agreement with the predicted heats of formation (i.e. a good correlation).

Figures 4-5 (b) and 4-5 (c) show the total and partial density of states for $Fe_{49.5}Al_{50}Pt_{0.5}$ and $Fe_{49.8}Al_{50}Ru_{0.2}$, respectively. It is clear from the plot that doping with Pt and Ru slightly changed the behaviour of the electronic structure, in particular, shifting of the Fermi level with respect to the pseudogap. Note that the two plots show 0.5 at. % Pt and 0.2 at. % Ru doped on the Fe sub-lattice, the partial DOS for Al are similar, while those for Fe/Pt (in Figure 4-5 (b)) and Fe/Ru (in Figure 4-5 (c)) were different. A small peak at about -0.5 eV was sharper for Ru doped system. More importantly, we noticed that the pseudogap lies slightly to the right of the Fermi level for 0.2 at. % Ru, while 0.5 at. % Pt lies at the right of the Fermi level indicating condition of electronic stability. Similar behaviour is observed for the binary phase (Figure 4-5 (a)) were the pseudogap lies slightly to the right of the Fermi level.

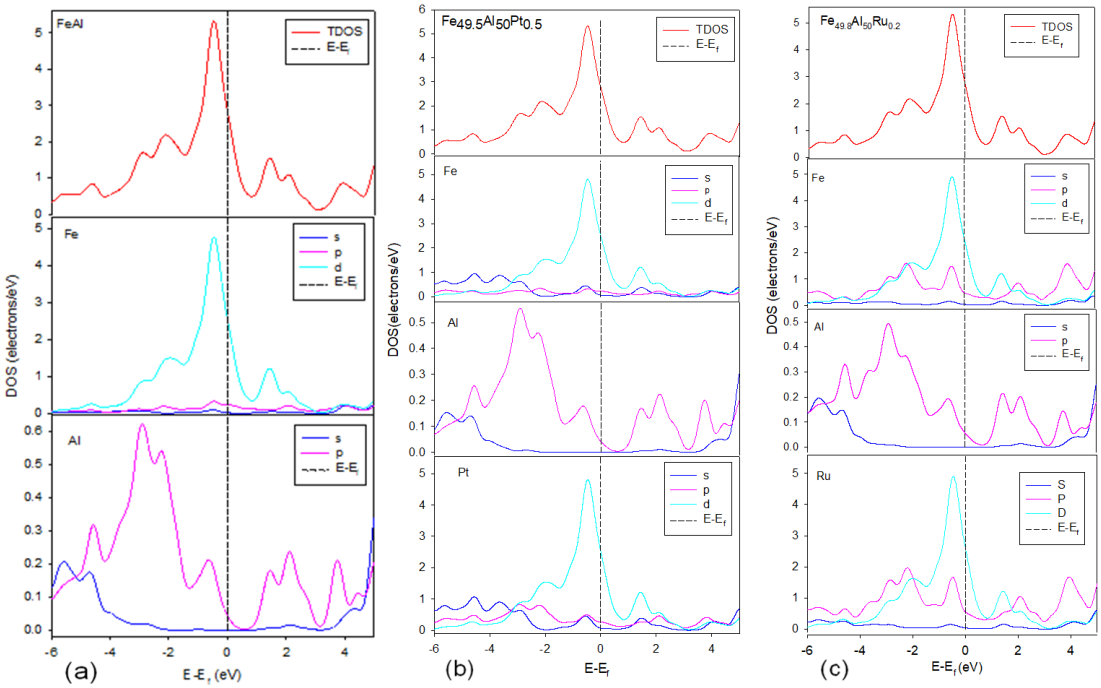

Figure 4-5: Total and partial density of states of (a) binary FeAl and ternary (b) $Fe_{49.50}Al_{50}Pt_{0.5}$ and (c) $Fe_{49.80}Al_{50}Ru_{0.2}$ systems, with the Fermi energy taken as energy zero ($E\text{-}E_f = 0$).

4.4.2 DOs for $Fe_{50\text{-}x}Al_{50}$Pd/Ag

Figure 4-6 shows the partial and total density of states of Pd and Ag doped on FeAl system. These systems display similar total DOS characterized by a strong *d*-orbital peak at E_f ($E\text{-}E_f = 0$). We see that the Fermi level hits the top of the *d*-peak in both cases, while for Pd doped the DOS is broader (figure 4-6 (a)). The peak is due to the strong contribution of the 4*d*-orbital and less contribution of the *s*- and *p*-orbital. This signifies electronic stability which is in good agreement with the predicted heats of formation. The small sharp peak at about ~0.5 eV (figure 4-7 (b)) emanates from hybridization of the 4*d*-orbitals (Fe, Ag) and 2*p*-orbital. Now, we conclude the electronic DOs for 0.2 and 0.5 at. %, for they confirm to be the most stable dopants according to experimental findings for the Ru, Pd, Pt, Ag systems.

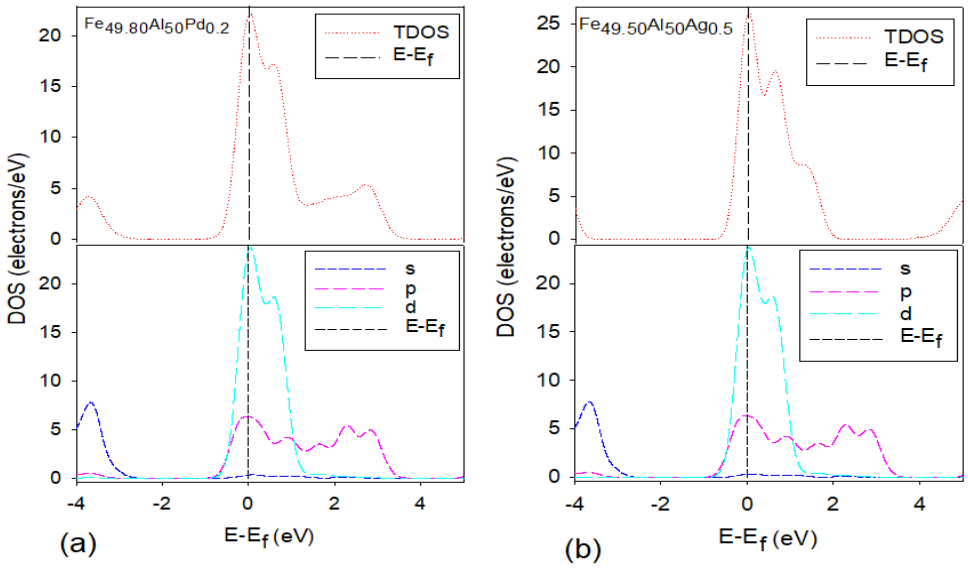

Figure 4-6. Total and partial density of states of FeAl after doping: (a) $Fe_{49.80}Al_{50}Pd_{0.2}$, (b) $Fe_{49.50}Al_{50}Ag_{0}$. The Fermi energy is taken as the energy zero (E- E_f = 0).

4.4.3 **TDOs for $Fe_{50-X}Al_{50}Pt/Ru$ for 0.1 ≤ X ≤ 0.9 at. %**

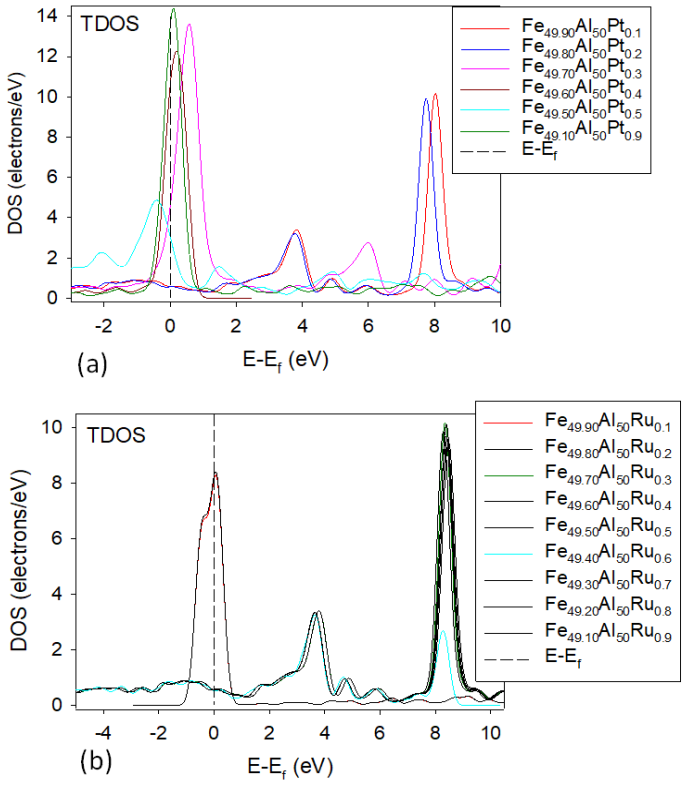

Figure 4-7: Total density of states of (a) $Fe_{50-X}Al_{50}Pt_X$ and (b) $Fe_{50-X}Al_{50}Ru_X$ systems, with the Fermi energy taken as energy zero (E-E_f = 0).

The total density of states for $Fe_{50-X}Al_{50}Pt_X$ and $Fe_{50-X}Al_{50}Ru_X$ are shown in figure 4-8 (a) and (b). In figure 4-8 (a) we observed that the plots $Fe_{49.90}Al_{50}Pt_{0.1}$ and $Fe_{49.80}Al_{50}Pt_{0.2}$ show similar trends; their energies are almost similar. These two ternaries have the lowest density of states at the Fermi level followed by $Fe_{40.50}Al_{50}Pt_{0.5}$. However, the $Fe_{47.30}Al_{50}Pt_{0.3}$, $Fe_{49.60}Al_{50}Pt_{0.4}$, and $Fe_{49.10}Al_{50}Pt_{0.9}$ have the highest number of states at E_f which means they are least stable as compared to the other two ternaries.

In figure 4-8 (b) we observed that the plots $Fe_{49.80}Al_{50}Ru_{0.2}$, $Fe_{49.80}Al_{50}Ru_{0.2}$, $Fe_{49.70}Al_{50}Ru_{0.3}$, $Fe_{49.60}Al_{50}Ru_{0.4}$, $Fe_{49.50}Al_{50}Ru_{0.5}$, $Fe_{49.40}Al_{50}Ru_{0.6}$, $Fe_{49.30}Al_{50}Ru_{0.7}$, $Fe_{49.20}Al_{50}Ru_{0.8}$ $Fe_{49.10}Al_{50}Ru_{0.9}$ and $Fe_{49.80}Al_{50}Ru_{0.2}$ show similar trends; their energies are almost similar. These ternaries have the lowest density of states at the Fermi level. However, $Fe_{47.90}Al_{50}Ru_{0.1}$ has the highest number of states at E_f which means it is least stable than the other ternaries.

4.5 Effect of Pt/Ru/Ag on the elastic properties of β2 FeAl

To evaluate the elastic stability of the ternary systems, we calculated the elastic constants (C_{ij}) for $Fe_{50}Al_{49.80}Ru_{0.2}$, $Fe_{49.80}Al_{50}Ru_{0.2}$, $Fe_{50}Al_{49.50}Pt_{0.5}$, $Fe_{49.50}Al_{50}Pt_{0.5}$, $Fe_{49.90}Al_{49.90}Ru_{0.2}$ (50:50) and $Fe_{49.75}Al_{49.75}Pt_{0.5}$ (50:50) dopant at different concentrations as shown in Table 5-8 Note that the symmetry was unchanged, and only three independent elastic constants (C_{11}, C_{12} and C_{44}) have been found for the cubic lattice. The mechanical stability criteria of a cubic system [105] are given as:

$$C_{44} > 0,\ C_{11} > |C|_{12},\ C_{11} + 2C_{12} > 0,$$

and shear is

$$G = \frac{1}{2}\left[\frac{C_{11} - C_{12} + 3C_{44}}{5} + \frac{5C_{44}(C_{11} - C_{12})}{4C_{44} + 3(C_{11} - C_{12})}\right].$$

Furthermore, the calculated shear moduli (C') was positive, indicating the all compounds under considerations were elastically stable (Mouhat *et al.*, 2014). The elastic stability criteria also led to a restriction on the magnitude of *B*. Since

B is a weighed average of C_{11} and C_{12} and stability requires that C_{12} be smaller than C_{11}, we were then left with the result that *B* was required to be intermediate in value between C_{11} and C_{12}: $C_{12} < B < C_{11}$. We predicted high values of B for all systems with the lowest values corresponding to stable compounds. Thus, from the predicted B values, we determined the ductility and brittleness of these compounds from the ratio of bulk to shear moduli. Pugh proposed the *B/G* ratio predicted ductility if > 1.75 or brittle if < 1.75 for the cubic Fe-Al alloys in Table 5-5 [118]. Note also that the negative values of *B/G* also reflected the instability of the corresponding compounds, which was not the case for the Fe-Al-X alloys.

Table 4-6: Elastic constants (C_{ij}) of the FeAl-Pt, Ru alloys.

Structures	C_{11} (GPa)	C_{12} (GPa)	C_{44} (GPa)	C′ (GPa) $[1/2\,(C_{11} - C_{12})]$	G (GPa)	B (GPa)	B/G (GPa)
$Fe_{50}Al_{50}$	279.1	140.0	148.0	209.09	109.31	186.401	1.705
$Fe_{49.90}Al_{49.90}Ru_{0.2}$	283.0	141.4	148.3	212.3	110.219	187.892	1.705
$Fe_{49.80}Al_{50}Ru_{0.2}$	279.4	140.6	147.4	209.1	108.942	186.885	1.715
$Fe_{50}Al_{49.80}Ru_{0.2}$	282.2	140.7	148.2	211.8	110.144	188.590	1.712
$Fe_{49.75}Al_{49.75}Pt_{0.5}$	282.5	147.9	147.9	208.5	107.828	187.304	1.737
$Fe_{49.50}Al_{50}\,Pt_{0.5}$	278.9	139.9	147.5	208.9	101.799	186.243	1.707
$Fe_{50}Al_{49.50}\,Pt_{0.5}$	282.0	139.3	147.9	212.4	103.487	186.917	1.693

Table 4-7: Elastic constants (C_{ij}) of the $Fe_{50-X}Al_{50}Pt_X$ alloys

Structures	C_{11} (GPa)	C_{12} (GPa)	C_{44} (GPa)	C′ (GPa) $[1/2(C_{11}-C_{12})]$	G (GPa)	B (GPa)	B/G (GPa)
$Fe_{49.90}Al_{50}Pt_{0.1}$	616.257	312.718	330.507	459.898	241.841	413.898	1.711
$Fe_{49.80}Al_{50}Pt_{0.2}$	579.682	349.566	357.209	404.899	227.145	426.272	1.877
$Fe_{49.70}Al_{50}Pt_{0.3}$	-94.474	389.611	400.517	-289.279	-316.7	228.249	-0.721
$Fe_{49.50}Al_{50}Pt_{0.5}$	278.900	139.900	147.5	208.900	101.799	186.243	1.707

Table 4-8: Elastic constants (C_{ij}) of $Fe_{50-X}Al_{50}Ru_X$ alloys

Structures	C_{11} (GPa)	C_{12} (GPa)	C_{44} (GPa)	C' (GPa) [1/2(C_{11}-C_{12})]	G (GPa)	B (GPa)	B/G (GPa)
$Fe_{49.90}Al_{50}Ru_{0.1}$	584.111	311.366	306.286	136.373	221.366	402.281	1.817
$Fe_{49.80}Al_{50}Ru_{0.2}$	279.400	140.600	147.400	69.400	108.942	186.885	1.716
$Fe_{49.70}Al_{50}Ru_{0.3}$	604.198	311.376	328.129	146.411	237.356	408.983	1.723
$Fe_{49.60}Al_{50}Ru_{0.4}$	604.806	320.229	335.024	142.289	237.611	415.088	1.747
$Fe_{49.50}Al_{50}Ru_{0.5}$	587.679	330.379	337.991	128.65	229.493	416.146	1.813
$Fe_{49.40}Al_{50}Ru_{0.6}$	124.404	110.867	111.697	6.7685	42.6185	115.379	2.707
$Fe_{49.30}Al_{50}Ru_{0.7}$	562.339	353.454	347.863	104.443	215.262	423.082	1.965
$Fe_{49.20}Al_{50}Ru_{0.8}$	565.167	360.736	352.378	102.216	215.187	428.879	1.993
$Fe_{49.10}Al_{50}Ru_{0.9}$	558.484	365.732	353.959	96.376	210.998	429.982	2.038

To understand the phase transition and the variation of elastic properties, the Fe-Al metallic bond and electronic structure of these alloys are studied.

Figure 4-9 (a) and (b) Showed the elastic constants of the doped $Fe_{50-X}Al_{50}$-Pt/Ru structures were determined to establish the mechanical stability trend with respect to the atomic percentage respectively. Plot (a) indicates that C_{11} and C' lies below zero at which indicates condition of instability. However, in figure (b) they are positive which satisfies the stability conditions of the cubic lattice. The calculated shear moduli (C') was also positive, indicating elastic stability. However, the C' for Pd shows the condition of instability since it lies below zero at 0.6 at. % this is due to C_{11} and C_{12} being negative.

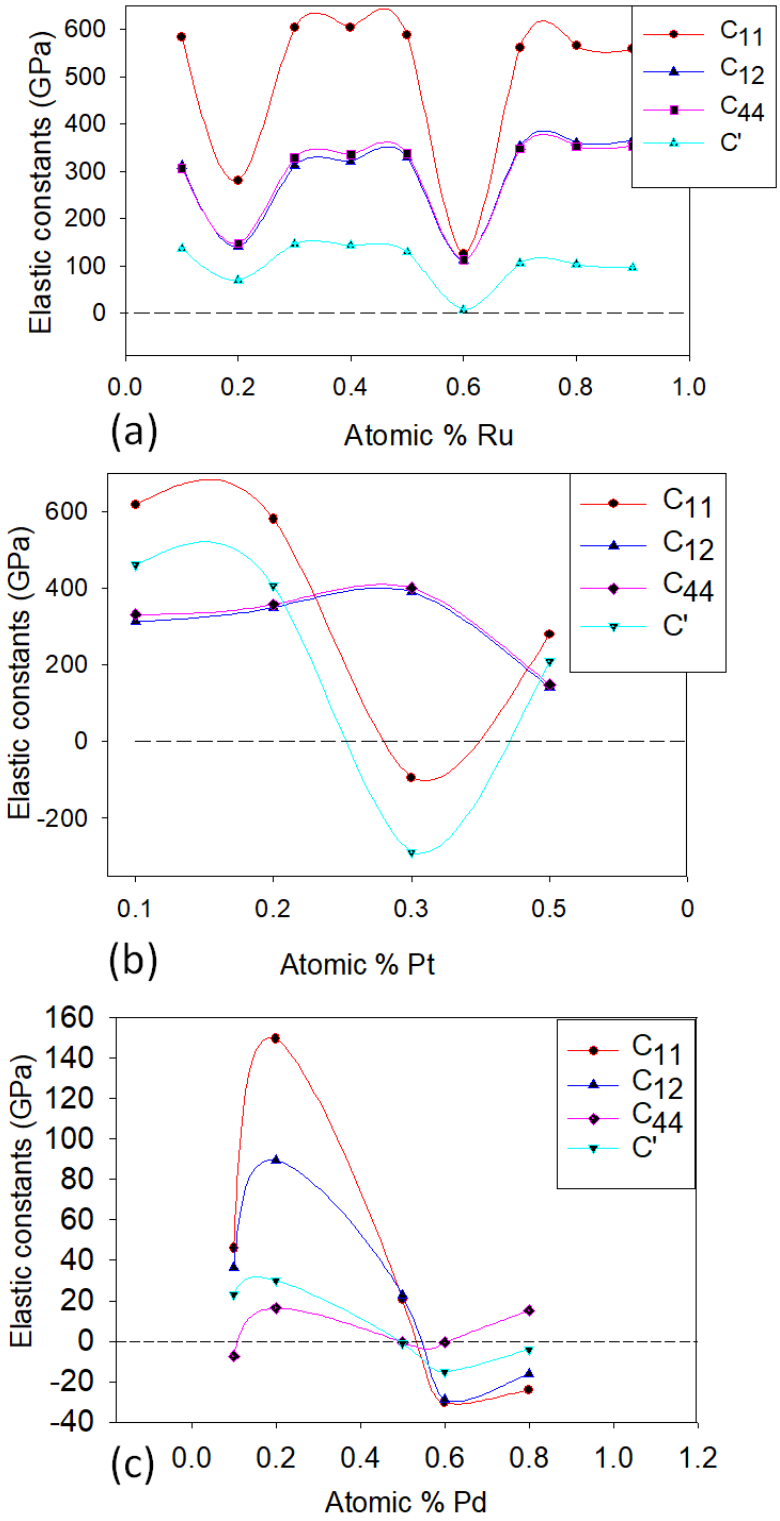

Figure 4-8: The graph of the elastic constants and C' against atomic percentage for the (a) $Fe_{50-x}Al_{50}Pt_x$ and (b) $Fe_{50-x}Al_{50}Ru_x$ and (c) $Fe_{50-x}Al_{50}Pd_x$.

In order to investigate the elastic stability of the ternary systems, we calculated the elastic constants (C_{ij}) for $Fe_{49.80}Al_{50}Pd_{0.2}$, $Fe_{49.50}Al_{50}Ag_{0.5}$, $Fe_{49.50}Al_{50}Pt_{0.5}$ and $Fe_{49.80}Al_{50}Ru_{0.2}$ systems at different concentrations. Note that the symmetry was unchanged during doping, and thus three independent elastic constants (C_{11}, C_{12}, and C_{44}) have been found for the cubic lattice.

We observed that all independent elastic constants are positive and satisfy the stability conditions for Ru doped. Furthermore, the calculated shear moduli is positive ($C' > 0$) indicating that the structure is elastically stable (see figure 2 (b)). The elastic constants in figure 2(a) confirmed instability at 0.3 at. % Pt, while Figure 2 (c) shows that C' is positive below 0.5 at. % Pd (condition of stability). However, the structure shows negative behaviour (instability) above 0.5 at. % Pd. The elastic stability criteria for ductility and brittleness as proposed by Pugh was used [118]. In this case, the predicted B/G ratio for Pd and Ag is greater than 1.75 (indicating ductility), while those for Ru and Pt are less than 1.75 (brittleness).

4.6 XRD-analysis on the $Fe_{50-X}Al_{50}$Ru/Pt doped structures

The XRD pattern for β2 FeAl was calculated using density functional theory. The XRD pattern for doped $Fe_{50}Al_{50}$-X with Pt and Ru are shown in figure 4-11. Thus the XRD peaks shown for the different systems are used to identify and distinguish different phases and intensities between 20-80 a.u.

In figure 4-10 (a) Ru addition from 0.1 to 0.9 at. % showed that the structure remains unchanged (similar XRD pattern). However, figure 4-10 (b) Pt addition displays different patterns. We observe a similar pattern from 0.1 to 0.3 at. % Pt. interestingly for 0.4 and 0.5 patterns are unique with the emergence of smaller peaks. Their energy difference is very small showing more preference on the 0.5 at. % (stable). Above 0.5 at. % Pt, the patterns are similar but less in energy (less stable). In figure 4-11 (a) Pd addition from 0.1 to 0.9 at. % showed that the structure remains unchanged (similar XRD pattern). However, figure 4-11 (b) Ag addition displays different patterns. We observed similar pattern from 0.1, 0.3 to 0.4 and 0.6 to 0.9 at. % Ag. Interestingly for 0.2 and 0.5 patterns are unique with a shift in the large peak at 20 2theta (º). Their energy difference is very small

showing more preference on the 0.2 at. % (stable). Above 0.5 at. % Ag, the patterns are similar but less in energy (least stable).

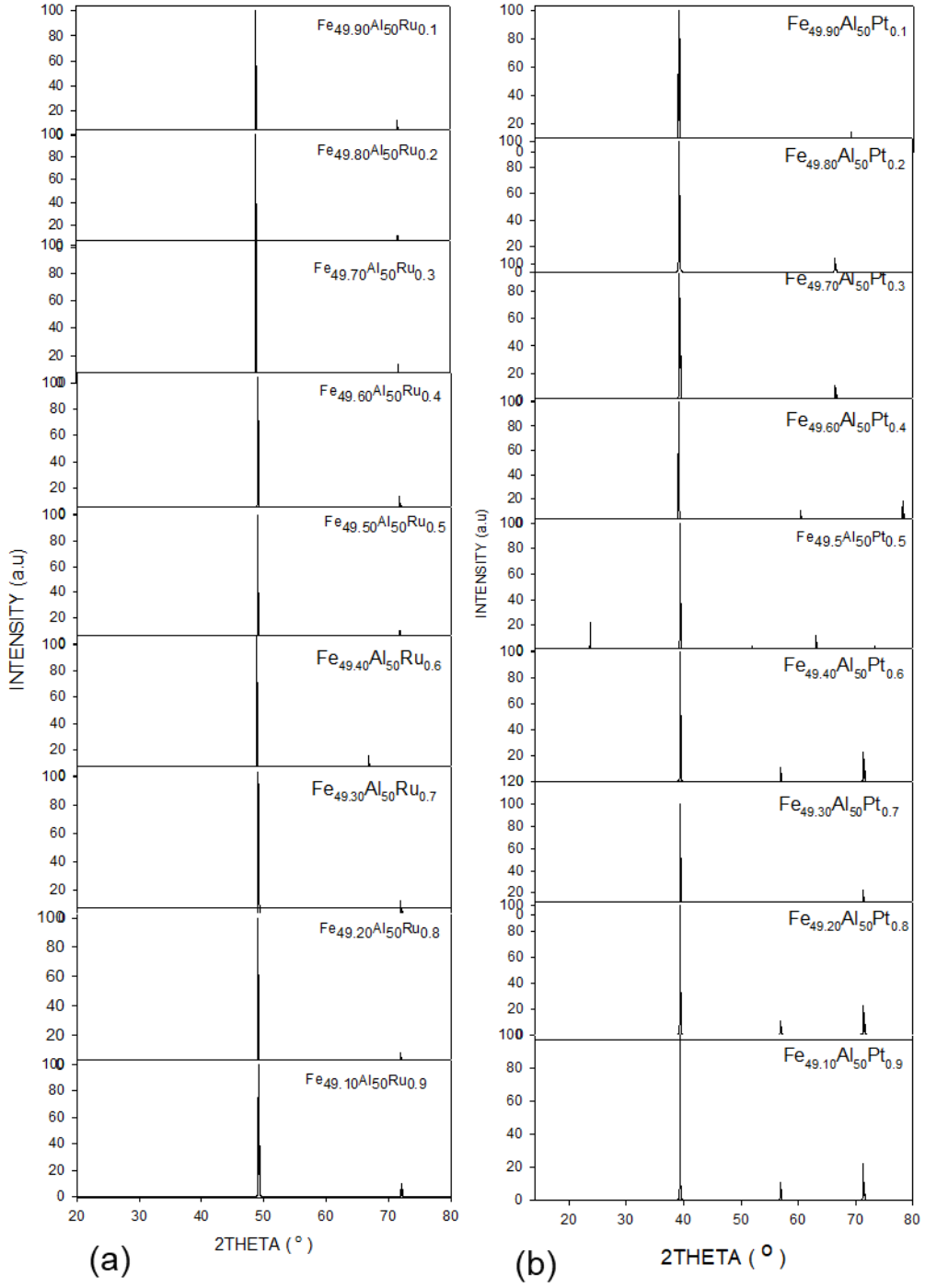

Figure 4-9: XRD patterns of doped (a) $Fe_{50-x}Al_{50}Ru_X$ and (b) $Fe_{50-x}Al_{50}Pt_X$.

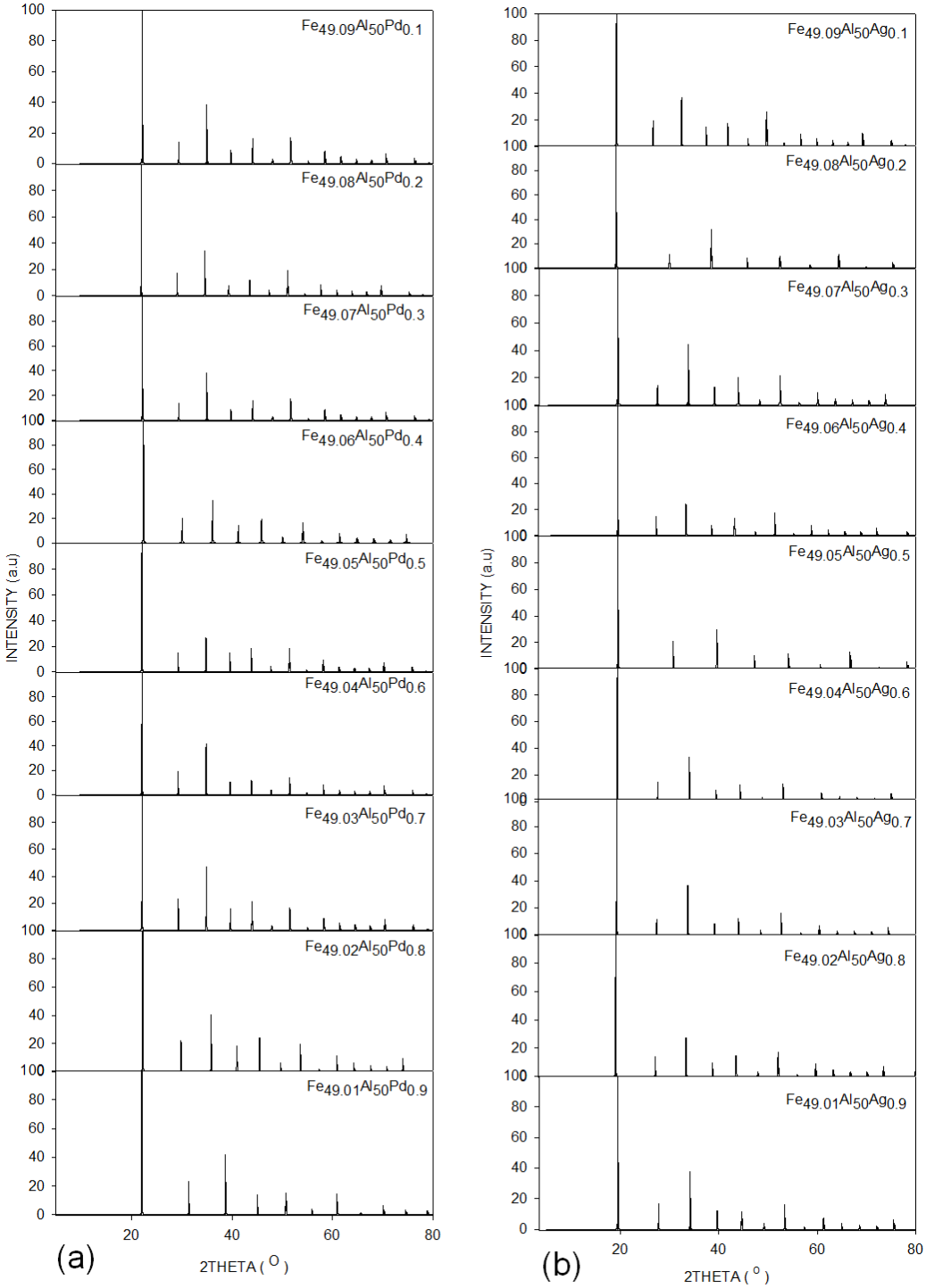

Figure 4-10: XRD patterns of doped (a) $Fe_{50-x}Al_{50}Pd_x$ and (b) $Fe_{50-x}Al_{50}Ag_x$.

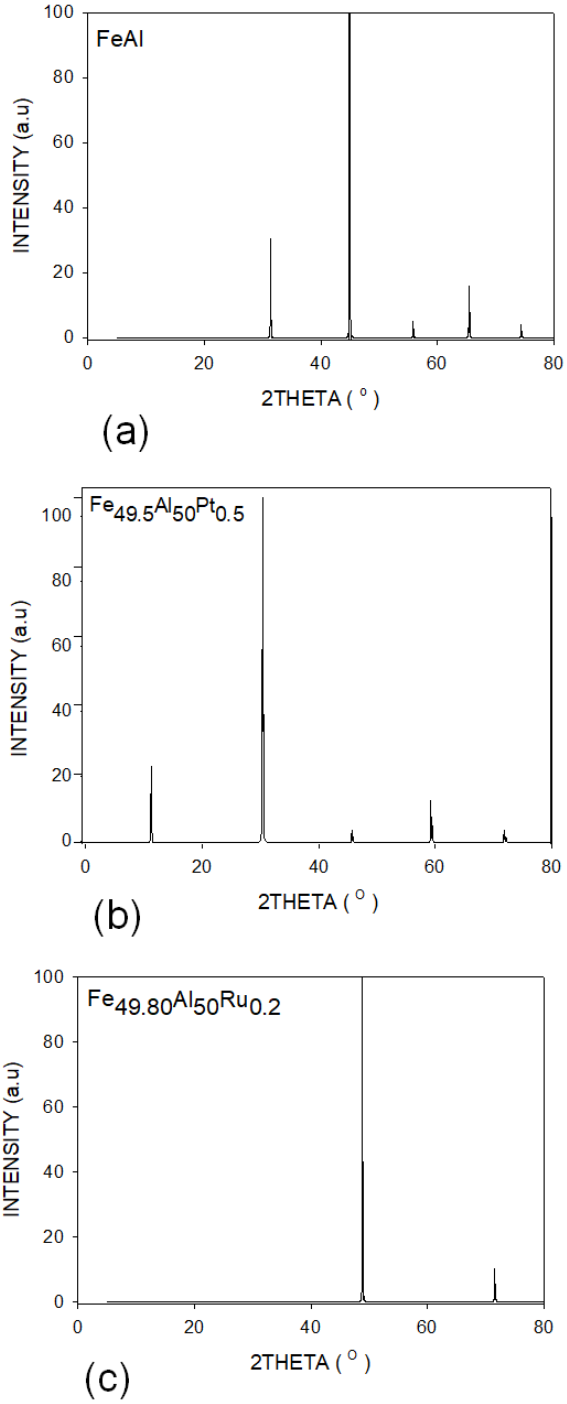

Figure 4-11: XRD patterns of (a) binary FeAl and doped (b) $Fe_{49.50}Al_{50}Pt_{0.5}$ and (c) $Fe_{49.80}Al_{50}Ru_{0.2}$.

Now, we compare the most stable phases for (a) binary FeAl and the stable compounds (b) $Fe_{49.5}Pt_{0.5}$ and (c) $Fe_{49.8}Al_{50}Ru_{0.2}$, observing the X-ray diffraction patterns as shown in Figure 4-12. These plots displayed similar peaks before and

after doping. However, the doping intensity of Pt was much similar to the binary FeAl phase where else for Ru was completely different from the FeAl phase. Most notable was the high-intensity peak at about (32-80) a.u. This XRD pattern confirmed the structure and their similarity may be attributed to the type of lattice used.

Chapter 5

TERNARY ALLOYING: SUPERCELL APPROACH

In this chapter, we investigate the Pt, Ru, Pd and Ag substitution on the β2-$Fe_{50}Al_{50}$ to deduce the preferable doping site on either Fe or Al sub-lattice. The supercell approach was used to determine the effect of FeAl-X systems with respect to heats of formation, elastic constants and density of states. Recent experimental work indicated that concentrations between $0 \leq x \leq 50$ stabilizes the FeAl structure [23]. Thus the validation of compositions will be discussed.

5.1 The supercell approach

To carry out the supercell approach on these ternary systems a suitable number of bands (nextra bands) in the system were used to balance the number of electrons in the system. This was achieved by determining the reasonable number of bands by varying the percentage corresponding to a certain number of bands, that is 7n (30 %), 8n (10 %), 9n (40 %), 10n (45 %), 11n (48 %), 12n (50 %). In this work, we focus on the thermodynamic, electronic and mechanical properties of $Fe_{50}Al_{50}$-X doped intermetallic.

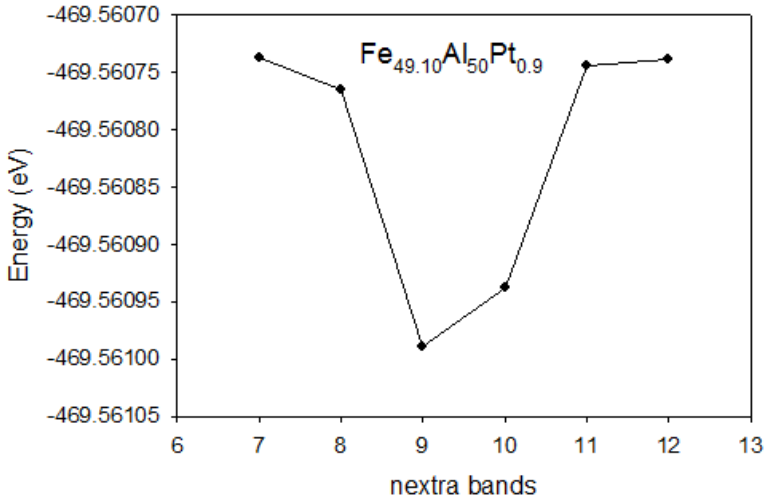

Figure 5-1: Graph of total energy against number of bands for $Fe_{49.10}Al_{50}Pt_{0.9}$.

Figure 5-1 is a graph of energy against nextra bands for $Fe_{49.10}Al_{50}Pt_{0.9}$ system. This plot was used to determine the most preferred nextra band with the lowest energy using the supercell approach. In particular, 9n (40 %) was found to be the most suitable nextra band for the calculation, sufficing for all the other systems.

5.2 The Fe sub-lattice

Table 5-1 illustrates the lattice parameter, volume and heats of formation for Pt and Ru at. % doping on the Fe-mesh side. We observed that on the Fe-mesh side there is an increase in the lattice parameters as the at. % is increased. Pd and Ag doping in table 5-2 showed a similar increasing pattern in the lattice parameter as we increased the at. % of the systems. We determined the effect of doping with Pt, Ru, Pd, and Ag between $1 \leq x \leq 50$ composition range and the volume and heats of formation are tabulated as mentioned above.

The heats of formation per atom of Fe-Al-X is given by:

$$\Delta H_f = \frac{1}{N}[E_{total} - [(1-x)E_a + xE_b + \ldots\ldots]],$$

where E_a and E_b represents the total energy of the system *a* and *b*; N is the total number of atoms in the system, x and (1-x) is the fractional concentration of the constituent elements. We observed that as the at. % for Pt is increased on the Fe-sub-lattice the ΔH_f also increases. However, a sudden drop is observed at 37.5 at. % with the energy of -0.403 eV/atom. Secondly, Ru doping showed that the at. % is increased as the ΔH_f is increased until 37.5 at. % then depreciates. However, at 31.25 at. % showed to be the most stable and energy difference of -0.165 eV/atom.

The heats of formation calculations showed that $Fe_{18.75}Al_{50}Pd_{31.25}$ at. % Pd has an energy of -0.208 eV/atom (lowest instability). However, Ag doping showed that $Fe_{18.75}Al_{50}Ag_{31.25}$ and $Fe_{6.25}Al_{50}Ag_{43.75}$ are the most stable with the most negative energy of -0.233 eV/atom and -0.296 eV/atom, respectively. These systems showed an energy difference of 0.063 eV/atom. Figure 5-2 was used to quantify table 5-1 and 5-2 that as the atomic concentration is increased, the heats of formation also decreases to the lowest energy and most stable system. We

observed that Pt doping is the most stable followed by Ru doping, then Ag doping and lastly Pd doping as the least stable for the system with the lowest energy.

Table 5-1: Lattice parameter, Volume, and Heats of formation (ΔH_f) for doped FeAl-X (X= Pt/Ru) structures.

Structure	Lattice parameter (Å)	Volume (Å^3/atom)	ΔH_f (eV/atom)
Platinum (Pt)			
$Fe_{43.75}Al_{50}Pt_{6.25}$	2.921	12.46	-0.199
$Fe_{37.5}Al_{50}Pt_{12.5}$	2.958	6.466	-0.16
	1.479		
$Fe_{31.25}Al_{50}Pt_{18.75}$	2.979	13.417	-0.442
	3.024		
$Fe_{25}Al_{50}Pt_{25}$	3.033	13.948	-0.564
$Fe_{18.75}Al_{50}Pt_{31.25}$	3.045	14.557	-0.685
$Fe_{12.5}Al_{50}Pt_{37.5}$	3.136	7.576	-0.403
	1.541		
$Fe_{6.25}Al_{50}Pt_{43.75}$	3.158	15.747	-0.928
$FeAl_{50}Pt_{50}$	1.597	2.036	-0.131
Ruthenium (Ru)			
$Fe_{43.75}Al_{50}Ru_{6.25}$	2.901	12.209	-0.095
$Fe_{37.5}Al_{50}Ru_{12.5}$	2.917	6.226	-0.056
	1.464		
$Fe_{31.25}Al_{50}Ru_{18.75}$	2.939	12.670	-0.13
$Fe_{25}Al_{50}Ru_{25}$	2.955	12.909	-0.148
$Fe_{18.75}Al_{50}Ru_{31.25}$	2.975	13.143	-0.165
$Fe_{12.5}Al_{50}Ru_{37.5}$	2.986	6.687	-0.091
	1.499		
$Fe_{6.25}Al_{50}Ru_{43.75}$	3.007	13.591	-0.026
$FeAl_{50}Ru_{50}$	1.511	1.725	-0.027

Table 5-2: Lattice parameter, Volume, and Heats of formation (ΔH_f) of doped FeAl-X (X= Pd/Ag) structures.

Structures	Lattice parameter (Å)	Volume (Å^3/atom)	ΔH_f (eV/atom)
Palladium (Pd)			
$Fe_{43.75}Al_{50}Pd_{6.25}$	2.926	12.324	-0.104
$Fe_{37.5}Al_{50}Pd_{12.5}$	2.984 1.477	6.337	-0.065
$Fe_{31.25}Al_{50}Pd_{18.75}$	2.970 3.143	13.046	-0.156
$Fe_{25}Al_{50}Pd_{25}$	3.489	13.453	-0.182
$Fe_{18.75}Al_{50}Pd_{31.25}$	2.988 3.489	13.899	-0.208
$Fe_{12.5}Al_{50}Pd_{37.5}$	3.324 1.491	7.1767	-0.117
$Fe_{6.25}Al_{50}Pd_{43.75}$	3.266	14.809	-0.127
$FeAl_{50}Pd_{50}$	1.665	1.904	-0.032
Silver (Ag)			
$Fe_{43.75}Al_{50}Ag_{6.25}$	2.926	12.51	-0.109
$Fe_{37.5}Al_{50}Ag_{12.5}$	2.984 1.477	6.575	-0.07
$Fe_{31.25}Al_{50}Ag_{18.75}$	2.97 3.143	13.86	-0.171
$Fe_{25}Al_{50}Ag_{25}$	3.489	14.586	-0.202
$Fe_{18.75}Al_{50}Ag_{31.25}$	2.988 3.489	15.579	-0.233
$Fe_{12.5}Al_{50}Ag_{37.5}$	3.324 1.491	8.2342	-0.132
$Fe_{6.25}Al_{50}Ag_{43.75}$	3.266	17.408	-0.296
$FeAl_{50}Ag_{50}$	1.665	2.3108	-0.231

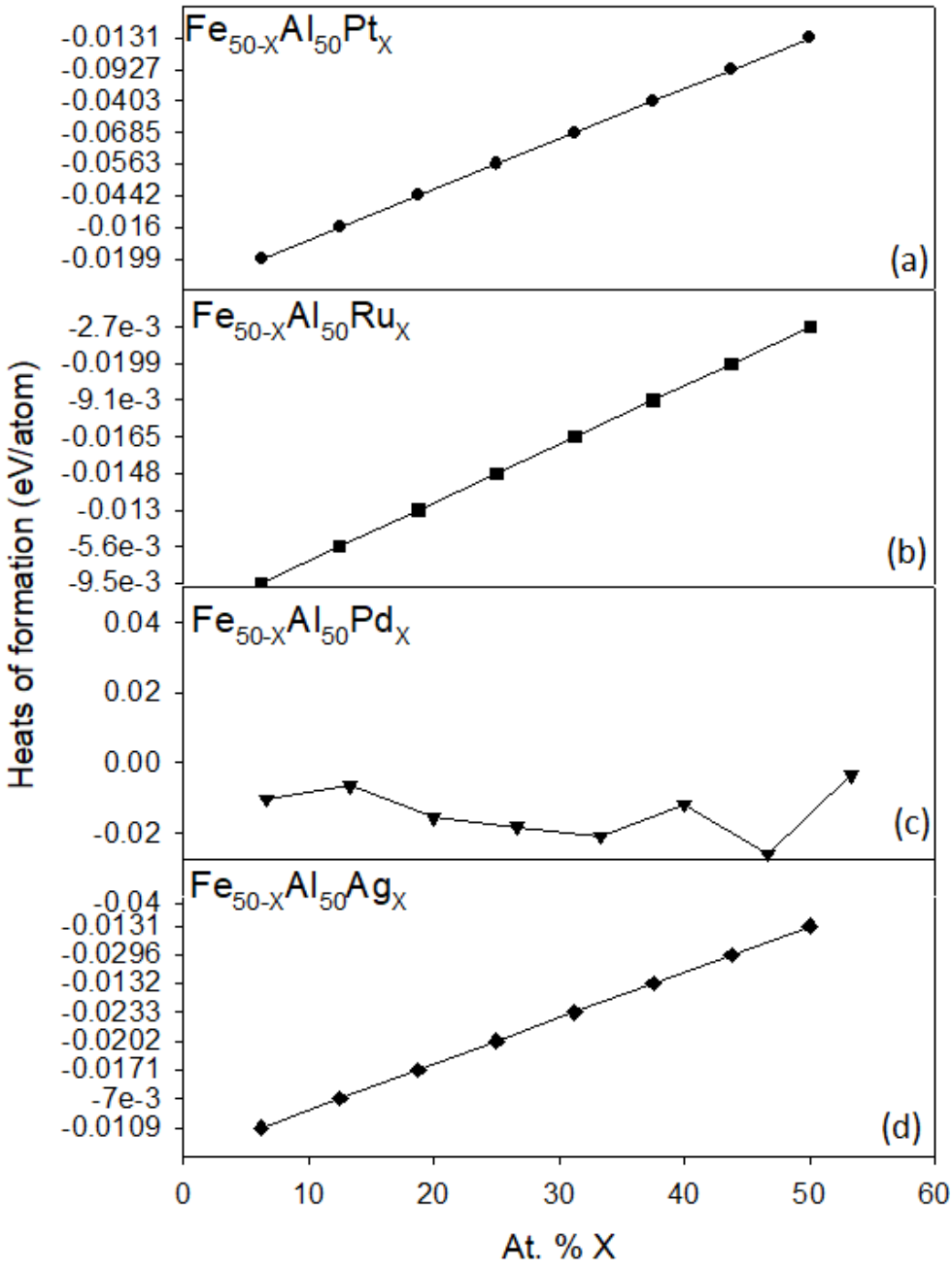

Figure 5-2: The graphs of heats of formation for the (a) $Fe_{50-x}Al_{50}Pt_x$, (b) $Fe_{50-x}Al_{50}Ru_x$, (c) $Fe_{50-x}Al_{50}Pd_x$, and (d) $Fe_{50-x}Al_{50}Ag_x$.

Table 5-3 and 5-4 shows the elastic constants, shear moduli, and ratio of bulk to shear modulus (GPa) of doped $Fe_{50-x}Al_{50}$-Pt/Ru/Pd/Ag systems. The shear moduli (C') in table 5-3 shows that all the systems are positive for Pt doping,

sufficing the stability criteria where else $Fe_1Al_{50}Pt_{50}$ does not satisfy stability which is not the main focus of the present study. Pt doping showed that as the atomic concentration is increased the ratio of bulk to shear modulus (B/G) becomes more ductile >1.75 with $Fe_{6.25}Al_{50}Pt_{43.75}$ as the most ductile system with a value of 3.504 GPa. The C' factor shows that most systems are positive for Ru doping which is a condition of stability. Ru doping showed that as the atomic concentration is increased the ratio of bulk to shear modulus (B/G) showed ductility >1.75 and $Fe_{25}Al_{50}Pt_{25}$ was found to be the most ductile system with a value of 3.504 GPa.

The elastic shear moduli for Pd shows the condition of stability at various concentrations in table 5-4. Seemingly, for Ag doping, the shear moduli also show the condition of stability. The B/G ratio for Ag concentration is regarded as promising material as their values are closer to the ductility value (B/G >1.75), however, $Fe_{6.25}Al_{50}Ag_{43.75}$ showed to be the most ductile system with a value of 3.111 GPa. We also observed that the ratio of bulk to shear moduli for Pd increases in ductility as the at. % was increased, specifically for $Fe_{6.25}Al_{50}Pd_{43.75}$ as the most stable system with a value of 2.284 GPa.

Figure (5-3 a) showed that the independent elastic constants for Pt doping for all concentrations considered are positive satisfying the cubic stability criterion. The shear moduli are positive indicating that the structures are elastically stable. Similarly, in figure (5-3 b) the C' is positive for Ru addition (condition of stability). However, figure (5-3d) for Pd structure showed positive behaviour (condition of stability) for all atomic concentrations.

Thus, the elastic stability criteria for ductility and brittleness in table 5-3 and 5-4 was observed by B/G ratio for all systems and the stability was validated in figure 5-3 by C_{11}, C_{12}, C_{44} and C' since they all lie above the zero lines.

Table 5-3: Elastic constants, bulk modulus and B/G ratio (GPa) of doped $Fe_{50-x}Al_{50}$-Pt/Ru systems.

Structures	C' (GPa) $[\frac{1}{2}(C_{11}-C_{12})]$	G (GPa)	B (GPa)	B/G (GPa)
Pt				
$Fe_{43.75}Al_{50}Pt_{6.25}$	94.571	112.682	175.754	1.559
$Fe_{37.5}Al_{50}Pt_{12.5}$	74.209	90.339	162.304	1.797
$Fe_{31.25}Al_{50}Pt_{18.75}$	86.231	96.379	159.909	1.659
$Fe_{25}Al_{50}Pt_{25}$	58.320	77.003	147.949	1.921
$Fe_{18.75}Al_{50}Pt_{31.25}$	55.458	52.371	150.447	2.873
$Fe_{12.5}Al_{50}Pt_{37.5}$	8.108	42.013	147.232	3.504
$Fe_{6.25}Al_{50}Pt_{43.75}$	17.577	40.330	141.308	3.504
$FeAl_{50}Pt_{50}$	-0.358	15.625	138.341	8.854
Ru				
$Fe_{43.75}Al_{50}Ru_{6.25}$	63.241	100.92	210.787	2.088
$Fe_{37.5}Al_{50}Ru_{12.5}$	95.492	114.75	188.419	1.642
$Fe_{31.25}Al_{50}Ru_{18.75}$	74.165	102.052	180.857	1.772
$Fe_{25}Al_{50}Ru_{25}$	74.577	42.013	147.232	3.504
$Fe_{18.75}Al_{50}Ru_{31.25}$	78.748	100.129	166.441	1.662
$Fe_{12.5}Al_{50}Ru_{37.5}$	78.082	97.330	184.644	1.898
$Fe_{6.25}Al_{50}Ru_{43.75}$	80.729	100.000	186.633	1.866
$FeAl_{50}Ru_{50}$	80.555	98.795	190.419	1.927

In all cases, these processes were performed to determine the actual composition of alloys. The analyzed compositions, which are listed in table1-1, were found to agree with the nominal composition within 1.0 at. % Al. There is a general agreement in the literature that the high-temperature phase Fe_5Al_8 forms peritectically from the liquid and FeAl and decomposes by a eutectoid reaction into FeAl and $FeAl_2$. However, their reaction temperature varies strongly from 1480 K to 1505 K for the peritectic reaction and from 1353 K to 1376 K for the eutectoid reaction through thermal analysis. Fe_5Al_8 and Fe_2Al_5 form eutectic at 68-69 at. % Al and at a temperature in the range 1426 K to 1439 K. However, there is controversy about the reaction type in the formation of Fe_4Al_{13}. The question is whether the phase form peritectically or congruently from the melting point; most studied assessments tend to form peritectically. Moreover, it was reported that either eutectoid or perictectic, the composition is close to that of Fe_4Al_{13} [4, 49]

Figure (5-5 a, b, c, g, and h) for Pd showed that they are unstable due to the sharp peak observed at the top of the Fermi level, characterized by a strong *d*-orbital. However, figure (5-5 d, e, and f) shows that they are considered to be stable due to the pseudogap that lies within the Fermi level for each system.

Figure (5-6 a and b) for Pt are considered unstable due to the sharp peak that lies at the Fermi level. However, figure (5-6 c and d) shows that they are electronically stable for the pseudogap lies slightly to the right and to the left of the Fermi level, respectively. Moreover, figure (5-6 e and f) are regarded as stable since the pseudogap lies slightly to the left of the fermi level, where else figure (5-6 g and h) are unstable due to the sharp peak at the Fermi level dominating in the tDOS.

Table 5-4: Elastic constants, bulk modulus and B/G ratio (GPa) of doped $Fe_{50-x}Al_{50}$-Pd/Ag systems.

Structures	C' (GPa) $[\frac{1}{2}(C_{11}-C_{12})]$	G (GPa)	B (Gpa)	B/G (GPa)
Pd				
$Fe_{43.75}Al_{50}Pd_{6.25}$	62.646	96.276	175.479	1.823
$Fe_{37.5}Al_{50}Pd_{12.5}$	78.172	97.497	160.392	1.645
$Fe_{31.25}Al_{50}Pd_{18.75}$	82.045	96.513	148.663	1.540
$Fe_{25}Al_{50}Pd_{25}$	60.559	82.08	143.277	1.746
$Fe_{18.75}Al_{50}Pd_{31.25}$	52.265	64.641	134.476	2.080
$Fe_{12.5}Al_{50}Pd_{37.5}$	18.276	56.404	128.817	2.284
$Fe_{6.25}Al_{50}Pd_{43.75}$	23.248	48.944	123.24	2.517
Ag				
$Fe_{43.75}Al_{50}Ag_{6.25}$	56.782	92.526	168.688	1.823
$Fe_{37.5}Al_{50}Ag_{12.5}$	61.728	89.089	139.03	1.561
$Fe_{31.25}Al_{50}Ag_{18.75}$	77.175	78.365	116.87	1.491
$Fe_{25}Al_{50}Ag_{25}$	33.195	56.535	99.954	1.768
$Fe_{18.75}Al_{50}Ag_{31.25}$	52.789	48.340	80.285	1.661
$Fe_{12.5}Al_{50}Ag_{37.5}$	11.319	61.461	64.306	1.046
$Fe_{6.25}Al_{50}Ag_{43.75}$	3.456	16.532	51.430	3.111
$FeAl_{50}Ag_{50}$	-3.416	-9.352	39.984	-4.275

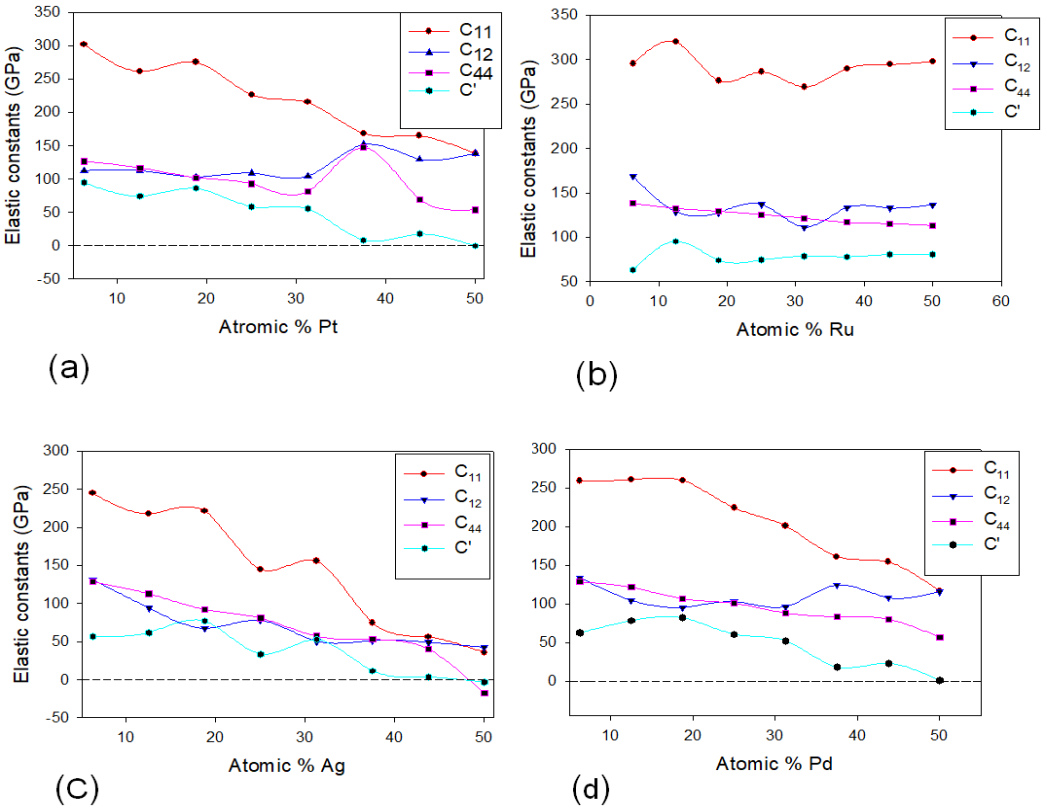

Figure 5-3: the graph of the elastic constants and c' against atomic percentage for the (a) $Fe_{50-x}Al_{50}Pt_x$, (b) $Fe_{50-x}Al_{50}Ru_x$, (c) $Fe_{50-x}Al_{50}Ag_x$, (d) $Fe_{50-x}Al_{50}Pd_x$.

Figure (5-7 a, b, c and d) for Ru doping showed electronic stability due to pseudogap that lies slightly to the right of the E_f. However, figures (5-7 e, f, and g) are considered unstable due to the peak that lies at the top of the Fermi level.

Lastly, we observed that Pt at. % is the most stable and in good agreement with the DOS and mechanical stabilities. The Ru concentration also correlates well with the DOS and noted similar observation for Pd at. %. The most stable concentration for Ag is $Fe_{43.75}Al_{50}Ag_{6.25}$, $Fe_{37.5}Al_{50}Ag_{12.5}$, $Fe_{31.25}Al_{50}Ag_{18.75}$, $Fe_{25}Al_{50}Ag_{25}$, and $Fe_{18.75}Al_{50}Ag_{31.25}$ and correlates very well with the mechanical properties and density of states therein.

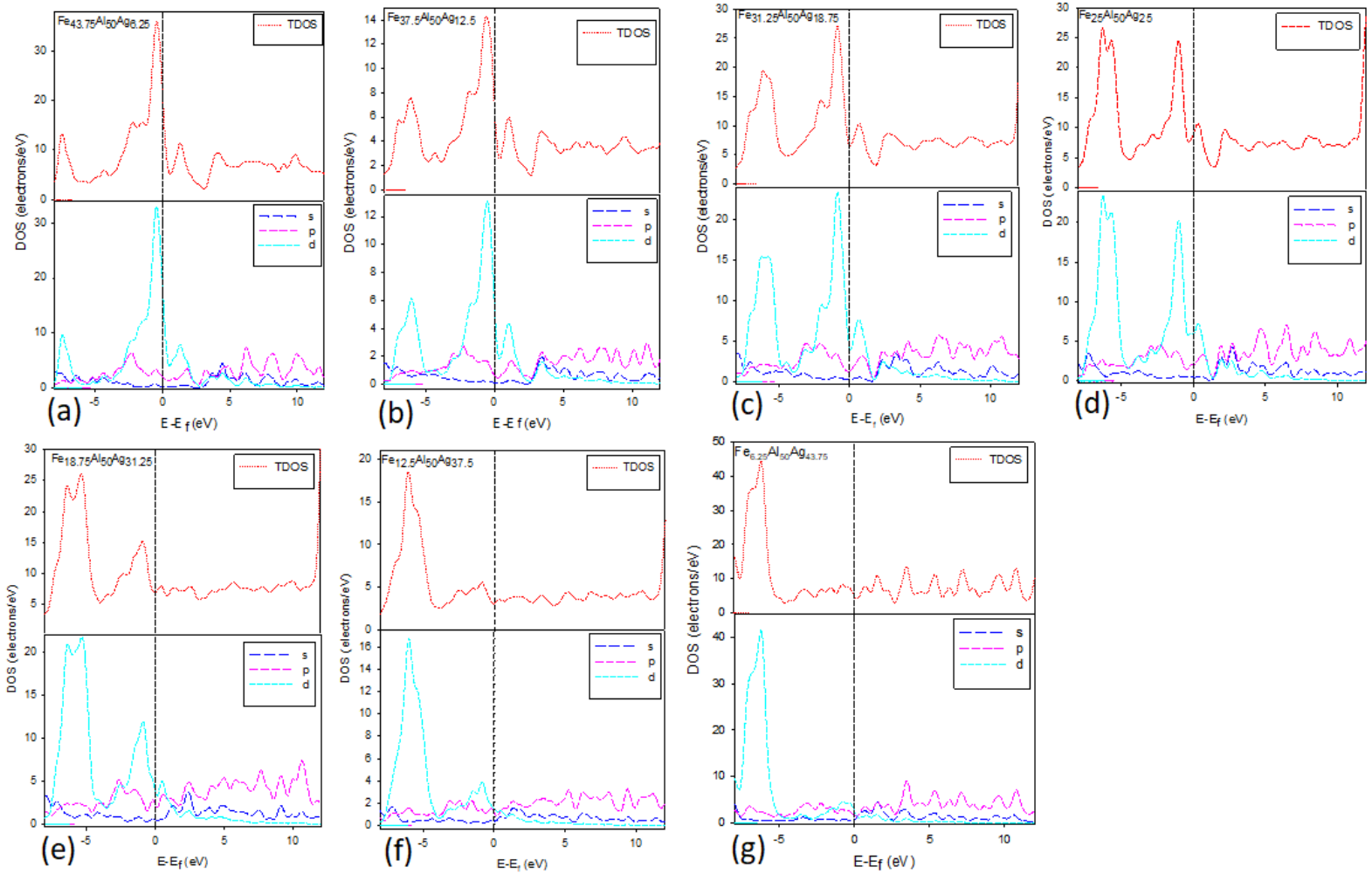

Figure 5-4: The graphs of total and partial density of states for (a) $Fe_{43.75}Al_{50}Ag_{6.25}$, (b) $Fe_{37.5}Al_{50}Ag_{12.5}$, (c) $Fe_{31.25}Al_{50}Ag_{18.75}$, (d) $Fe_{25}Al_{50}Ag_{25}$ (e) $Fe_{18.75}Al_{50}Ag_{31.25}$, (f) $Fe_{12.5}Al_{50}Ag_{37.5}$, (g) $Fe_{6.25}Al_{50}Ag_{43.75}$, (h) $FeAl_{50}Ag_{50}$, with Fermi level taken as energy zero ($E-E_f = 0$).

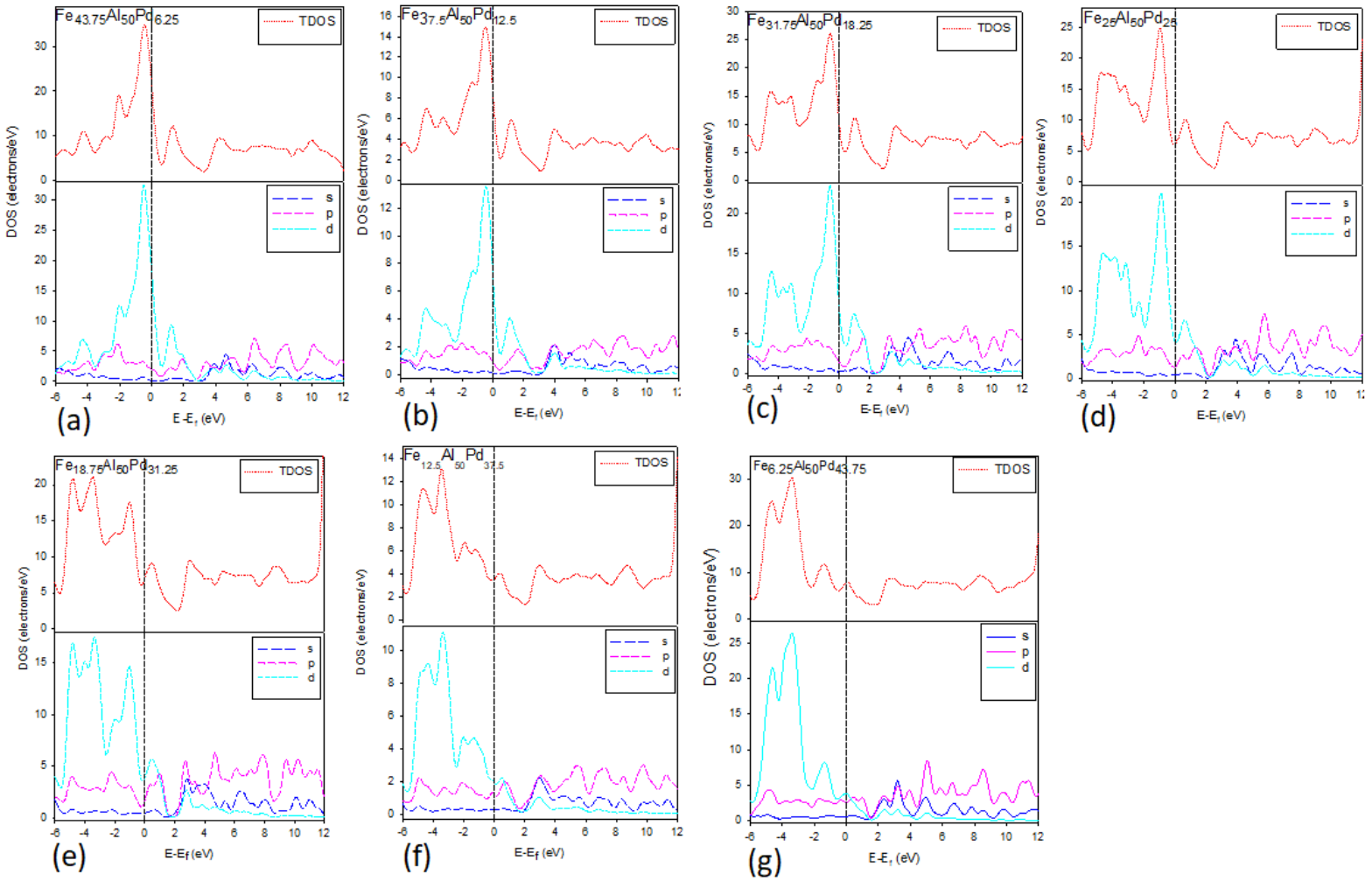

Figure 5-5: The graphs of total and partial density of states for (a) $Fe_{43.75}Al_{50}Pd_{6.25}$, (b) $Fe_{37.5}Al_{50}Pd_{12.5}$, (c) $Fe_{31.25}Al_{50}Pd_{18.75}$, (d) $Fe_{25}Al_{50}Pd_{25}$ (e) $Fe_{18.75}Al_{50}Pd_{31.25}$, (f) $Fe_{12.5}Al_{50}Pd_{37.5}$, (g) $Fe_{6.25}Al_{50}Pd_{43.75}$, (h) $FeAl_{50}Pd_{50}$ with Fermi level taken as energy zero ($E-E_f = 0$)

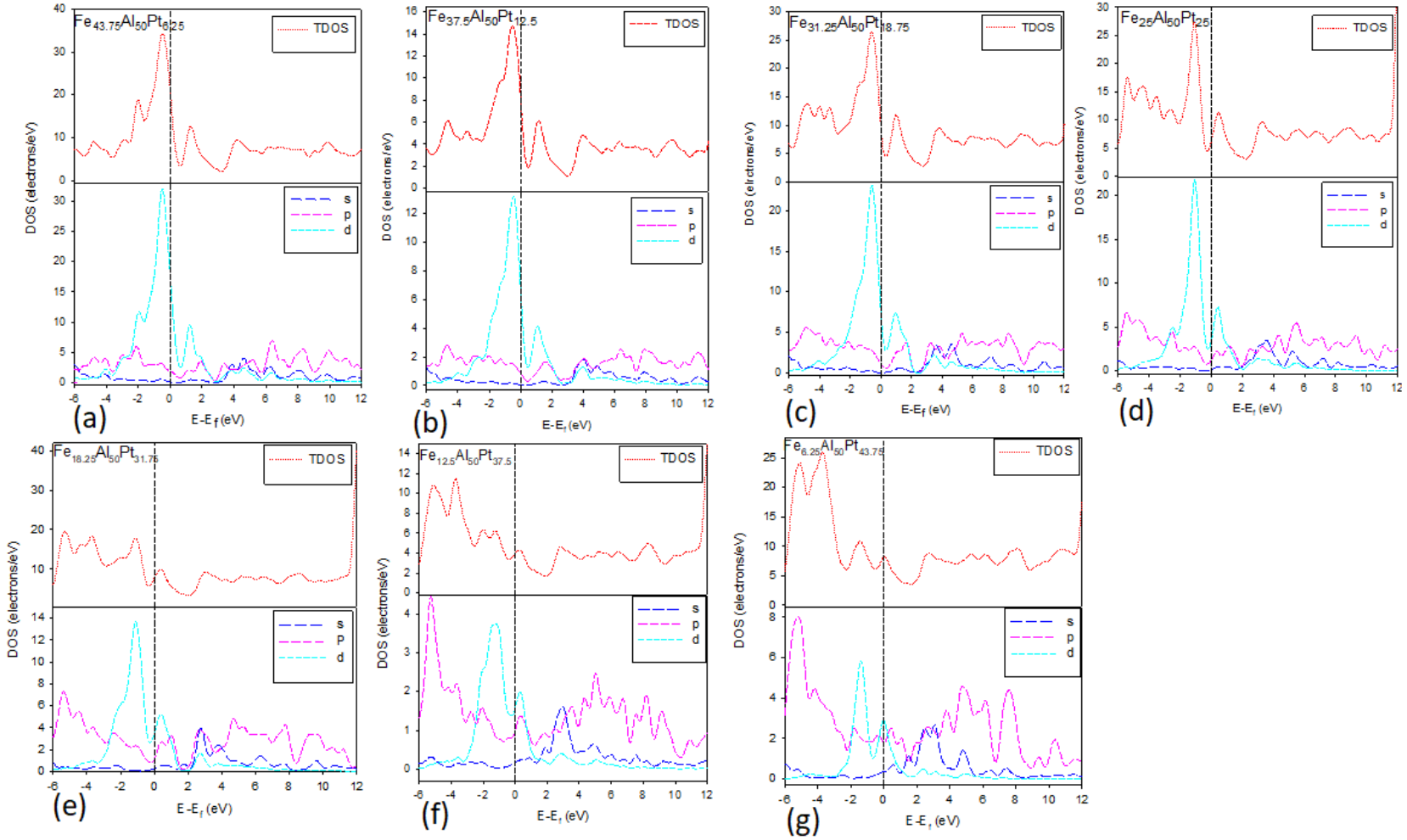

Figure 5-6: The graphs of total and partial density of states for (a) $Fe_{43.75}Al_{50}Pt_{6.25}$, (b) $Fe_{37.5}Al_{50}Pt_{12.5}$, (c) $Fe_{31.25}Al_{50}Pt_{18.75}$, (d) $Fe_{25}Al_{50}Pt_{25}$, (e) $Fe_{18.75}Al_{50}Pt_{31.25}$, (f) $Fe_{12.5}Al_{50}Pt_{37.5}$, (g) $Fe_{6.25}Al_{50}Pt_{43.75}$, (h) $FeAl_{50}Pt_{50}$,with fermi level taken as energy zero ($E\text{-}E_f = 0$).

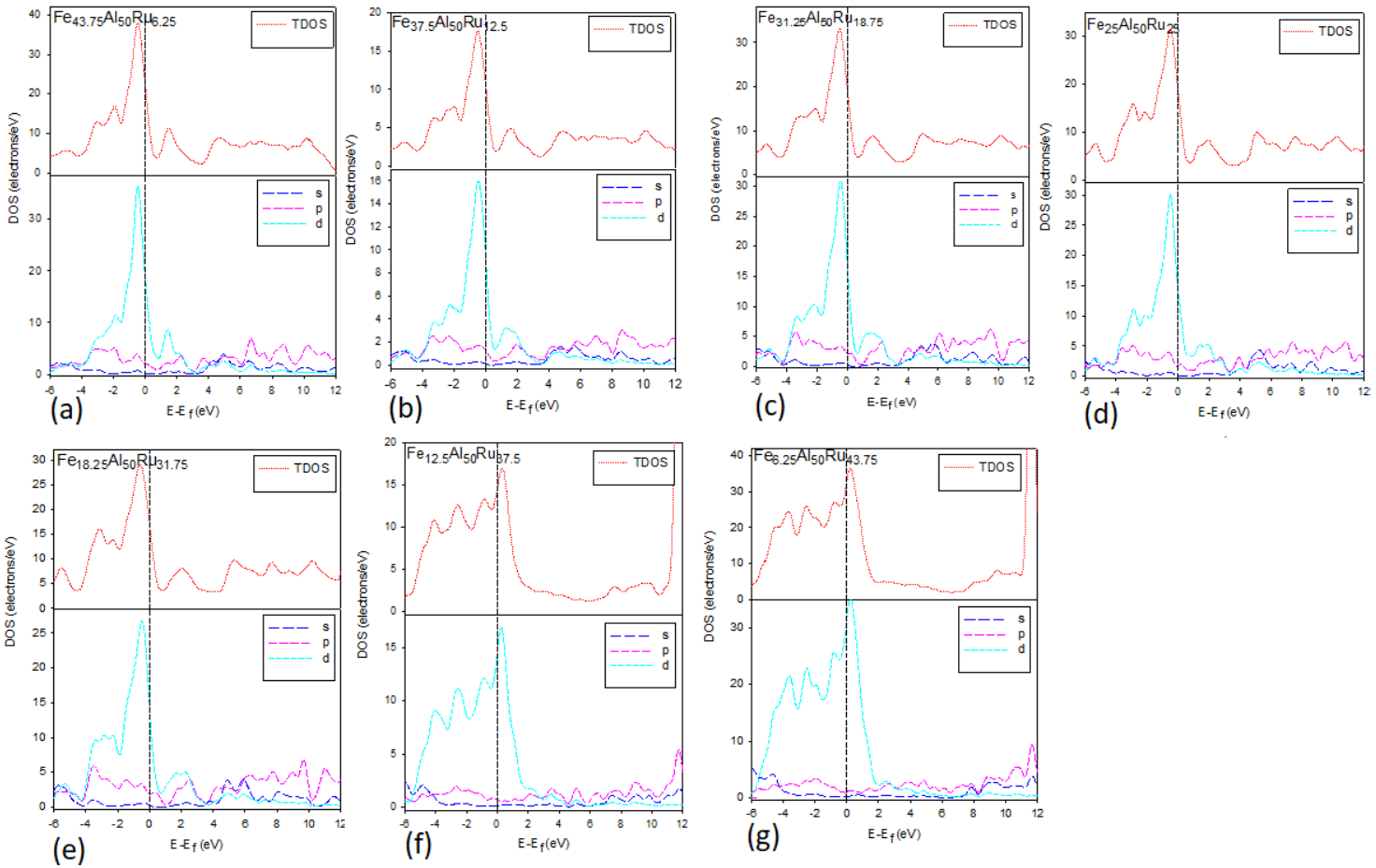

Figure 5-7: The graphs of total and partial density of states for (a) $Fe_{43.75}Al_{50}Ru_{6.25}$, (b) $Fe_{37.5}Al_{50}Ru_{12.5}$, (c) $Fe_{31.25}Al_{50}Ru_{18.75}$, (d) $Fe_{25}Al_{50}Ru_{25}$, (e) $Fe_{18.75}Al_{50}Ru_{31.25}$, (f) $Fe_{12.5}Al_{50}Ru_{37.5}$, (g) $Fe_{6.25}Al_{50}Ru_{43.75,}$ with Fermi level taken as energy zero ($E-E_f = 0$).

5.3 The Al sub-lattice

Table 5-5 illustrates the lattice parameter, volume and heats of formation for Pt and Ru at. % doping on the Al-mesh side. We observed an increase in the lattice parameters as the at. % was increased. In table 5-6 Pd and Ag doping showed a similar increasing pattern in the lattice parameter as we increased the at. % of the systems. We further investigated the effect of doping with Pt, Ru, Pd, and Ag between $1 \leq x \leq 50$ composition range; the volume and heats of formation are tabulated below.

We observed that as the at. % Pt is increased the stability of the ΔH_f also increased. However, at 31.25 and 43.75 at. % the system showed the lowest ΔH_f with energy of -0.722 eV/atom and -0.979 eV/atom, respectively. Secondly, Ru doping shows that as the at. % is increased the ΔH_f is increased. Moreover, 31.25 and 43.75 at. % showed to be the most stable with energy of -0.201 eV/atom and -0.251 eV/atom, respectively. Thirdly, table 5-6 illustrates that for Pd doping, as the at. % is increased the ΔH_f becomes more stable (lowest energy with energy of -0.245 eV/atom and -0.311 eV/atom, respectively. Lastly, Ag doping showed that as the at. % has increased the stability with regard to the ΔH_f also increased. However, 31.25 and 43.75 at. % showed to be the most stable with energy of -0.269 eV/atom and -0.347 eV/atom, respectively.

Figure 5-8 was used to validate table 5-5 and 5-6 that as the atomic concentration is increased, the heats of formation also increases to the most negative and stable system. It is observed that Pt doping is the most negative (most stable) followed by Ru doping, then Ag doping and lastly Pd doping as the least stable with respect to the ΔH_f.

Table 5-5: Heats of formation (ΔH_f) of doped FeAl-Pt/Ru structures.

Structure	Lattice parameter (Å)	Volume (Å^3/atom)	ΔH_f (eV/atom)
	Pt		
$Fe_{50}Al_{43.75}Pt_{6.25}$	5.819	12.317	-0.207
$Fe_{50}Al_{37.5}Pt_{12.5}$	4.102	6.337	-0.168
	6.025		
$Fe_{50}Al_{31.25}Pt_{18.75}$	5.85	13.101	-0.464
	6.125		
$Fe_{50}Al_{25}Pt_{25}$	3.647	3.354	-0.148
	4.033		
$Fe_{50}Al_{18.75}Pt_{31.25}$	5.303	13.882	-0.722
	7.897		
$Fe_{50}Al_{12.5}Pt_{37.5}$	6.049	7.0336	-0.425
	3.075		
$Fe_{50}Al_{6.25}Pt_{43.75}$	6.14	14.469	-0.979
$Fe_5Al_0Pt_{50}$	3.085	1.835	-0.134
	Ru		
$Fe_{50}Al_{43.75}Ru_{6.25}$	5.769	12.000	-0.102
$Fe_{50}Al_{37.5}Ru_{12.5}$	4.065	6.039	-0.063
	5.849		
$Fe_{50}Al_{31.25}Ru_{18.75}$	5.833	12.221	-0.152
$Fe_{50}Al_{25}Ru_{25}$	4.181	3.088	-0.043
	2.826		
$Fe_{50}Al_{18.75}Ru_{31.25}$	5.975	12.395	-0.201
$Fe_{50}Al_{12.5}Ru_{37.5}$	5.979	6.190	-0.112
	2.771		
$Fe_{50}Al_{6.25}Ru_{43.75}$	5.857	12.558	-0.251
$Fe_{50}AlRu_{50}$	2.935	1.581	-0.034

Table 5-6: Heats of formation (ΔH_f) of doped FeAl-Pd/Ag structures.

Structures	Lattice parameter (Å)	(Volume (Å^3/atom)	ΔH_f (eV/atom)
	Pd		
$Fe_{50}Al_{43.75}Pd_{6.25}$	2.898	12.175	-0.111
$Fe_{50}Al_{37.5}Pd_{12.5}$	2.047	6.197	-0.072
	2.959		
$Fe_{50}Al_{31.25}Pd_{18.75}$	2.911	12.67	-0.178
$Fe_{50}Al_{25}Pd_{25}$	2.043	3.229	-0.052
	1.548		
$Fe_{50}Al_{18.75}Pd_{31.25}$	2.578	13.039	-0.245
	3.925		
$Fe_{50}Al_{12.5}Pd_{37.5}$	3.046	6.669	-0.139
	1.438		
$Fe_{50}Al_{6.25}Pd_{43.75}$	3.009	13.617	-0.311
$Fe_{50}AlPd_{50}$	1.509	1.718	-0.042
	Ag		
$Fe_{50}Al_{43.75}Ag_{6.25}$	2.952	12.33	-0.116
$Fe_{50}Al_{37.5}Ag_{12.5}$	2.925	6.369	-0.077
$Fe_{50}Al_{31.25}Ag_{18.75}$	1.463	13.181	-0.193
	2.942		
$Fe_{50}Al_{25}Ag_{25}$	3.047	13.602	-0.232
$Fe_{50}Al_{18.75}Ag_{31.25}$	2.976	14.061	-0.269
	3.072		
$Fe_{50}Al_{12.5}Ag_{37.5}$	3.031	7.745	-0.154
	2.766		
$Fe_{50}Al_{6.25}Ag_{43.75}$	2.026	15.276	-0.347
	3.126		
$Fe_{50}AlAg_{50}$	1.557	1.888	-0.047

Table 5-7 and 5-8 show the elastic constants, shear moduli, and bulk to shear modulus ratio (GPa) of doped $Fe_{50-X}Al_{50}$-Pt/Ru/Pd/Ag systems. The shear moduli (C') in table 5-7 showed that most systems are positive for Pt doping, satisfying the stability criteria except for $Fe_{50}Al_{6.25}Pt_{43.75}$ which showed instability due to the negative value. The C' factor showed that most systems are positive for Ru doping, satisfying the stability criteria.

However, $Fe_{50}Al_{18.75}Pt_{31.25}$ and $Fe_{50}Al_{6.25}Pt_{43.75}$ failed to satisfy the stability criteria; hence are regarded to be unstable. Pt doping showed that as the concentration

is increased the B/G ratio became increased (increase ductility) >1.75. We see that $Fe_{50}Al_{12.5}Pt_{37.5}$ is the most ductile system with a value of 3.092 GPa. Ru doping showed that as the atomic percentage is increased the ratio of bulk to shear modulus (B/G) gave values above >1.75. It was observed that $Fe_{25}Al_{50}Pt_{25}$ is the most ductile system with a value of 3.399 GPa.

The elastic shear moduli (C') and the ratio of bulk to shear moduli for Pd doping are shown in table 5-7 and 5-8 to determine the elastic stability and brittleness to ductility at various concentrations. We observed that $Fe_{50}Al_{18.75}Pt_{31.25}$ and $Fe_{50}Al_{6.25}Pt_{43.75}$ do not satisfy the stability criteria since the shear moduli show negative values of -14.891 GPa and -18.208 GPa, respectively. For Ag doping, the shear moduli also showed condition of stability from 6.25 to 37.5 concentrations. $Fe_{50}Al_{6.25}Ag_{43.75}$ is considered unstable with a value of -18.208 GPa. We also observed that as the at. % Pd has increased the ratio of bulk to shear moduli increases (increase in ductility). Particularly, $Fe_{50}Al_{25}Pd_{25}$ is the most ductile system with 2.595 GPa. Furthermore, the B/G ratio for Ag at. % showed that $Fe_{50}Al_{12.5}Pd_{37.5}$ is the most ductile system with a value of 3.373 GPa.

Figure (5-9a) shows that all the independent elastic constants for Pt addition satisfy the stability criteria for cubic systems. We observed that the shear moduli are positive for Pt addition indicating that the structures are elastically stable. Figure (5-9b) shows that C'>0 below 30 at. % is positive (condition of stability) where else above this concentration C'<0 the system becomes unstable for Ru (condition of instability). The Ag addition (figure 5-9c) shows a positive C' behaviour (condition of stability) for all atomic concentrations. Lastly, in figure (5-9d), we see that Pd addition gave positive values (C'>0) for all atomic concentrations (condition of stability).

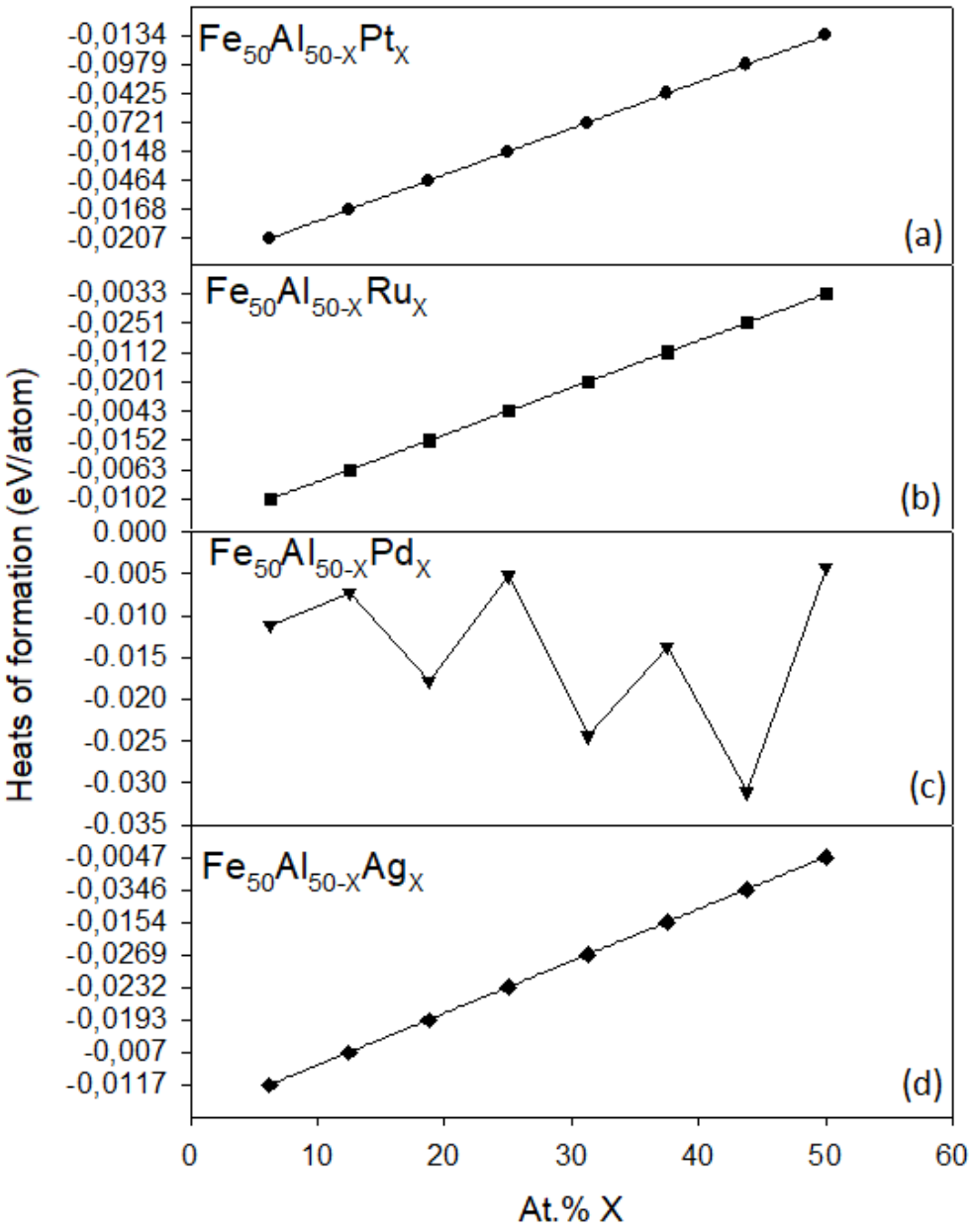

Figure 5-8: The graphs of heats of formation for the (a) $Fe_{50}Al_{50-x}Pt_x$, (b) $Fe_{50}Al_{50-x}Ru_x$, (c) $Fe_{50}Al_{50-x}Pd_x$, and (d) $Fe_{50}Al_{50-x}Ag_x$.

Table 5-7: Shear moduli, bulk modulus and B/G ratio (GPa) of doped $Fe_{50}Al_{50-x}Pt/Ru$ systems

.

Structures	C' (GPa) $\frac{1}{2}(C_{11}-C_{12})]$	G (GPa)	B (GPa)	B/G (Gpa)
	Pt			
$Fe_{50}Al_{43.75}Pt_{6.25}$	50.054	93.039	174.445	1.875
$Fe_{50}Al_{37.5}Pt_{12.5}$	132.741	84.683	179.499	2.119
$Fe_{50}Al_{31.25}Pt_{18.75}$	53.839	82.238	190.768	2.319
$Fe_{50}Al_{25}Pt_{25}$	32.247	69.285	183.847	2.654
$Fe_{50}Al_{18.75}Pt_{31.25}$	103.96	70.364	146.749	2.086
$Fe_{50}Al_{12.5}Pt_{37.5}$	9.275	59.739	184.702	3.092
$Fe_{50}Al_{6.25}Pt_{43.75}$	-10.934	8.713	159.459	18.3
$Fe_{50}AlPt_{50}$	-22.848	-8.104	175.066	-21.602
	Ru			
$Fe_{50}Al_{43.75}Ru_{6.25}$	83.387	61.539	126.081	2.049
$Fe_{50}Al_{37.5}6Ru_{12.5}$	111.869	108.285	199.714	1.844
$Fe_{50}Al_{31.25}Ru_{18.75}$	53.796	89.801	195.295	2.174
$Fe_{50}Al_{25}Ru_{25}$	128.067	67.509	229.504	3.399
$Fe_{50}Al_{18.75}Ru_{31.25}$	-15.727	-46.519	218.184	-4.69
$Fe_{50}Al_{6.25}Ru_{43.75}$	-15.309	-21.964	232.801	-10.599
$Fe_{50}AlRu_{50}$	15.895	66.355	251.42	3.789

Table 5-8: Shear moduli, bulk modulus and B/G ratio (GPa) of doped $Fe_{50}Al_{50-x}$Pd/Ag systems.

Structures	C' (GPa) $\frac{1}{2}(C_{11}-C_{12})]$	G (GPa)	B (GPa)	B/G (GPa)
	Pd			
$Fe_{50}Al_{43.75}Pd_{6.25}$	50.884	94.537	188.107	1.989
$Fe_{50}Al_{37.5}Pd_{12.5}$	141.403	93.307	170.768	1.83
$Fe_{50}Al_{31.25}Pd_{18.75}$	35.45	79.559	169.529	2.131
$Fe_{50}Al_{25}Pd_{25}$	134.081	64.135	166.437	2.595
$Fe_{50}Al_{18.75}Pd_{31.25}$	101.364	73.381	147.639	2.011
$Fe_{50}Al_{12.5}Pd_{37.5}$	-14.891	244.6	131.86	0.539
$Fe_{50}Al_{6.25}Pd_{43.75}$	-18.208	-30.089	54.636	-1.816
$Fe_{50}AlPd_{50}$	-17.054	0.6405	143.04	223.308
	Ag			
$Fe_{50}Al_{43.75}Ag_{6.25}$	50.517	93.483	159.17	1.703
$Fe_{50}Al_{37.5}Ag_{12.5}$	36.24	85.289	156.339	1.833
$Fe_{50}Al_{31.25}Ag_{18.75}$	36.019	67.771	125.817	1.856
$Fe_{50}Al_{25}Ag_{25}$	28.259	58.743	125.284	2.133
$Fe_{50}Al_{18.75}Ag_{31.25}$	10.848	41.482	107.679	2.596
$Fe_{50}Al_{12.5}Ag_{37.5}$	64.929	17.512	59.069	3.373
$Fe_{50}Al_{6.25}Ag_{43.75}$	-18.208	-30.089	54.636	-1.816
$Fe_{50}AlAg_{50}$	-10.059	13.823	93.658	6.775

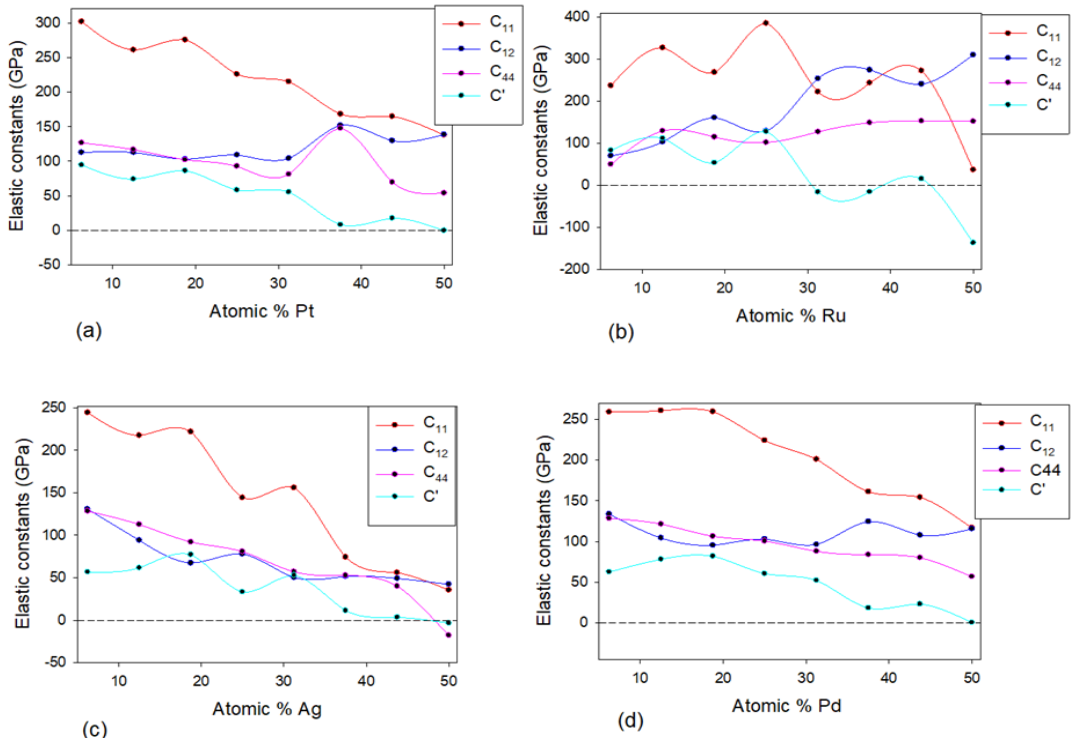

Figure 5-9: The graph of the elastic constants and C' against atomic percentage for the (a) $Fe_{50-x}Al_{50}Pt_x$, (b) $Fe_{50-x}Al_{50}Ru_x$, (c) $Fe_{50-x}Al_{50}Ag_x$, (d) $Fe_{50-x}Al_{50}Pd_x$.

The electronic density of states (DOS) were determined to mimic the stabilities by observing the behaviour of electronic states near the Fermi level. We showed the total and partial density of states for ternary FeAl-X systems in Figure 5-10, 5-11, 5-12 and 5-13

Figure (5-10 a, b, c and d) for Ag system show that they are electronically unstable for the peak lies at the top of the Fermi level, this is contributed by the strong *d*-orbital in the partial DOS observed in the tDOS of the system. Figure (5-10e and f) show that they are electronically unstable, where else figure (5-10g) clearly shows that the pseudogap lies slightly to the right of the Fermi level of the system which implies that it is electronically stable.

Figure (5-11 a, b, c, and d) for the Pd system shows that they are unstable by the sharp peak observed at the top of the Fermi level. Seemingly, figures (5-11 d, e, and f) are considered unstable due to the sharp peaks at the fermi level on each system.

Figure (5-12a) Pt system is electronically stable although the pseudogap lies slightly to the right, while figure (5-12 b, c, d, and 5-12 e, f, g) are considered unstable due to the sharp peak that lies at the Fermi level. Moreover, figures (5-13 a and b) are regarded as stable since the pseudogap lies slightly to the right of the fermi level and also within the Fermi level, respectively. While figure (5-13 c, d, and 5-13 e, f, g) are electronically unstable due to the *d*-orbital at the fermi level dominating in the tDOS.

In conclusion, comparing the Fe sub-lattice and the Al sub-lattice with respect to the thermodynamic properties (heats of formation) and mechanical properties (elastic constants), the supercell approach clearly indicates a preference of doping on the Al sub-lattice since the heats of formation are more negative (most stable) and the brittleness-to-ductility ratio also shows the preference of the Al sub-lattice for the values are much greater than 1.75. The electronic properties (DOS) predictions also show more stability on the Al sub-lattice.

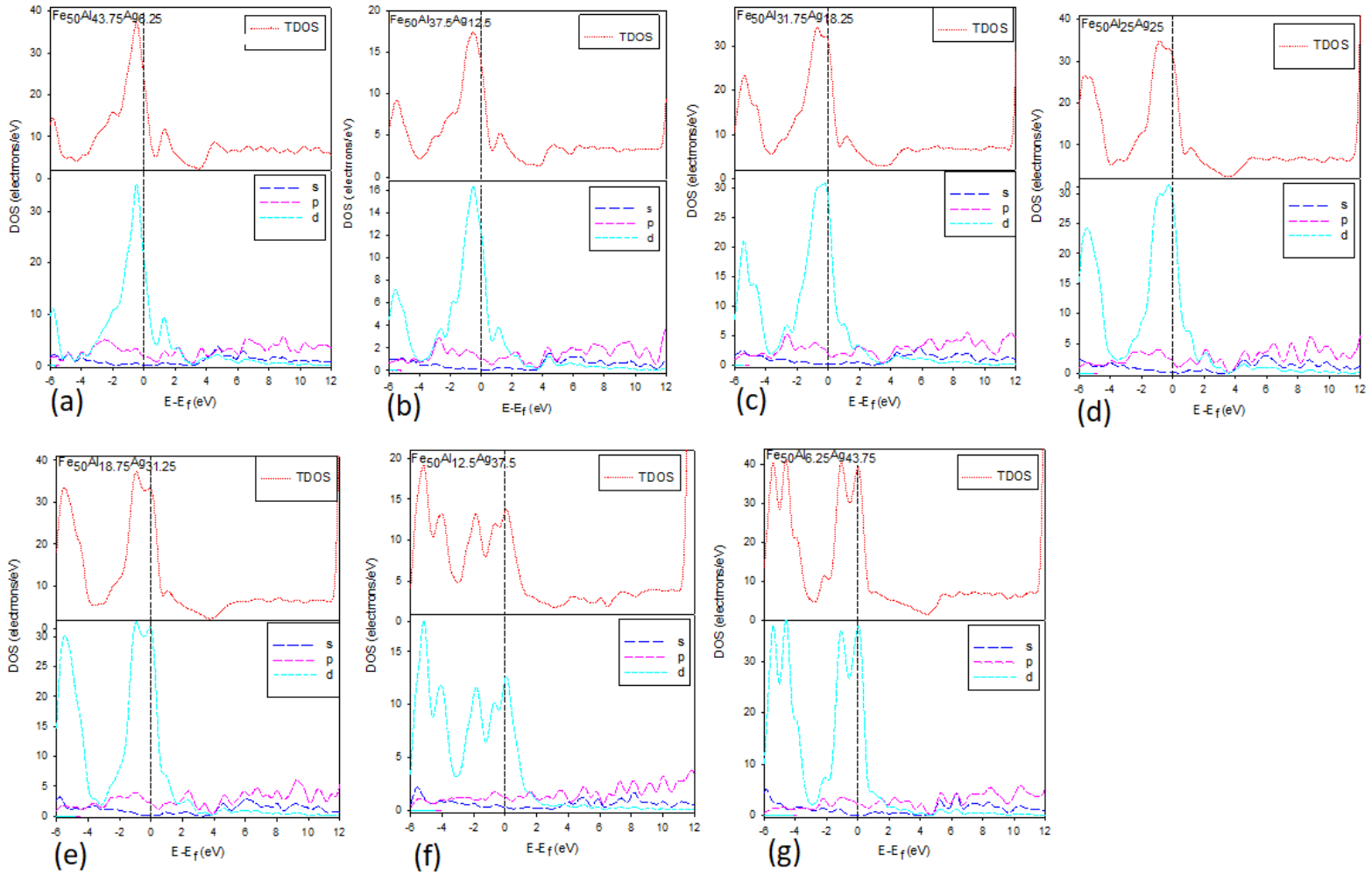

Figure 5-10: The graphs of total and partial density of states for (a) $Fe_{50}Al_{43.75}Ag_{6.25}$, (b) $Fe_{50}Al_{37.50}Ag_{12.5}$, (c) $Fe_{50}Al_{31.25}Ag_{18.75}$, (d) $Fe_{50}Al_{25}Ag_{25}$, (e) $Fe_{50}Al_{18.75}Ag_{31.25}$, (f) $Fe_{50}Al_{12.50}Ag_{37.5}$, (g) $Fe_{50}Al_{6.25}Ag_{43.75}$ with Fermi level taken as energy zero ($E\text{-}E_f = 0$).

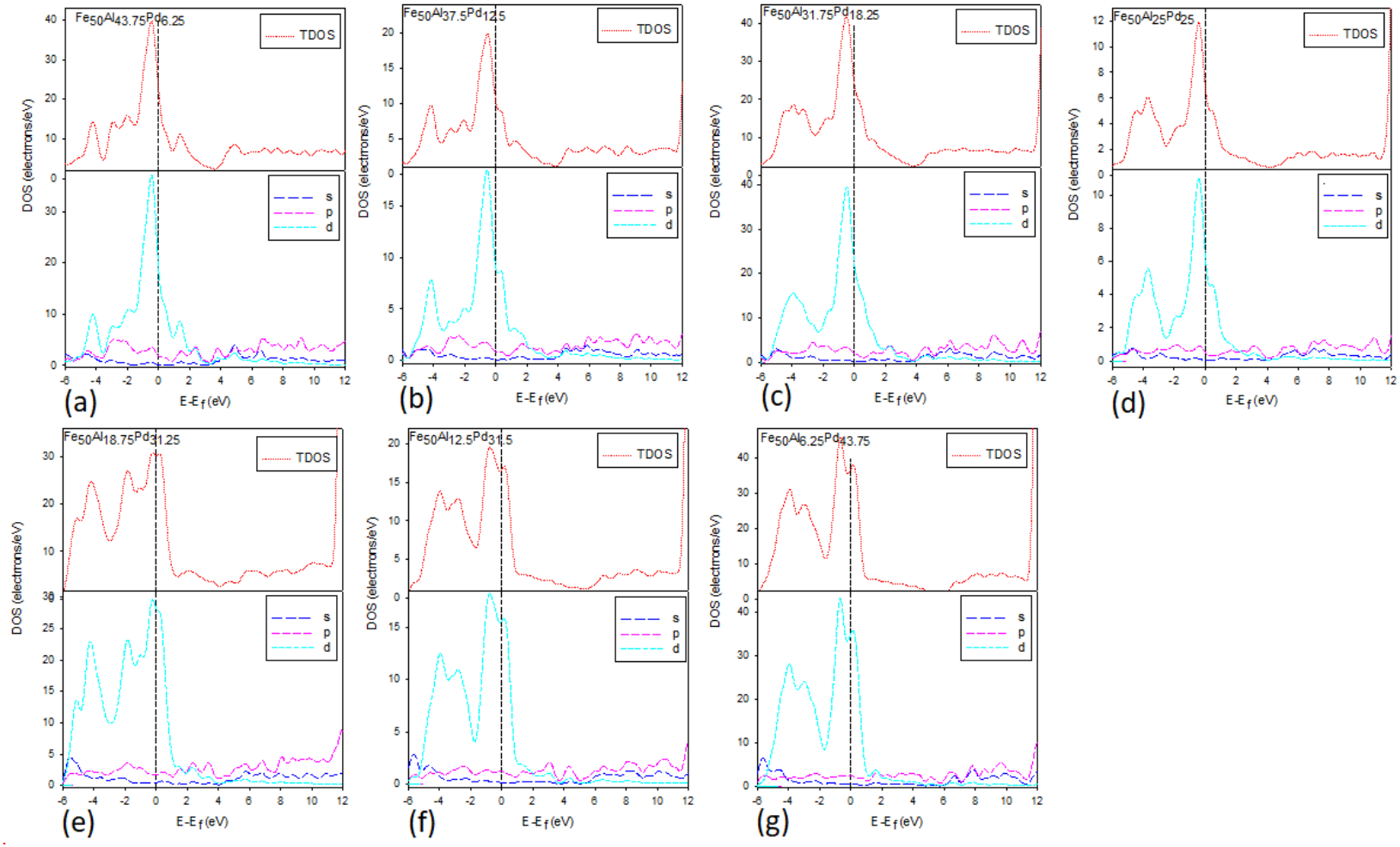

Figure 5-11: The graphs of total and partial density of states for (a) $Fe_{50}Al_{43.75}Pd_{6.25}$, (b) $Fe_{50}Al_{37.50}Pd_{12.5}$, (c) $Fe_{50}Al_{31.25}Pd_{18.75}$, (d) $Fe_{50}Al_{25}Pd_{25}$, (e) $Fe_{50}Al_{18.75}Pd_{31.25}$, (f) $Fe_{50}Al_{12.50}Pd_{37.5}$, (g) $Fe_{50}Al_{6.25}Pd_{43.75}$, (h) $Fe_{50}AlPd_{50}$ with Fermi level taken as energy zero ($E-E_f = 0$).

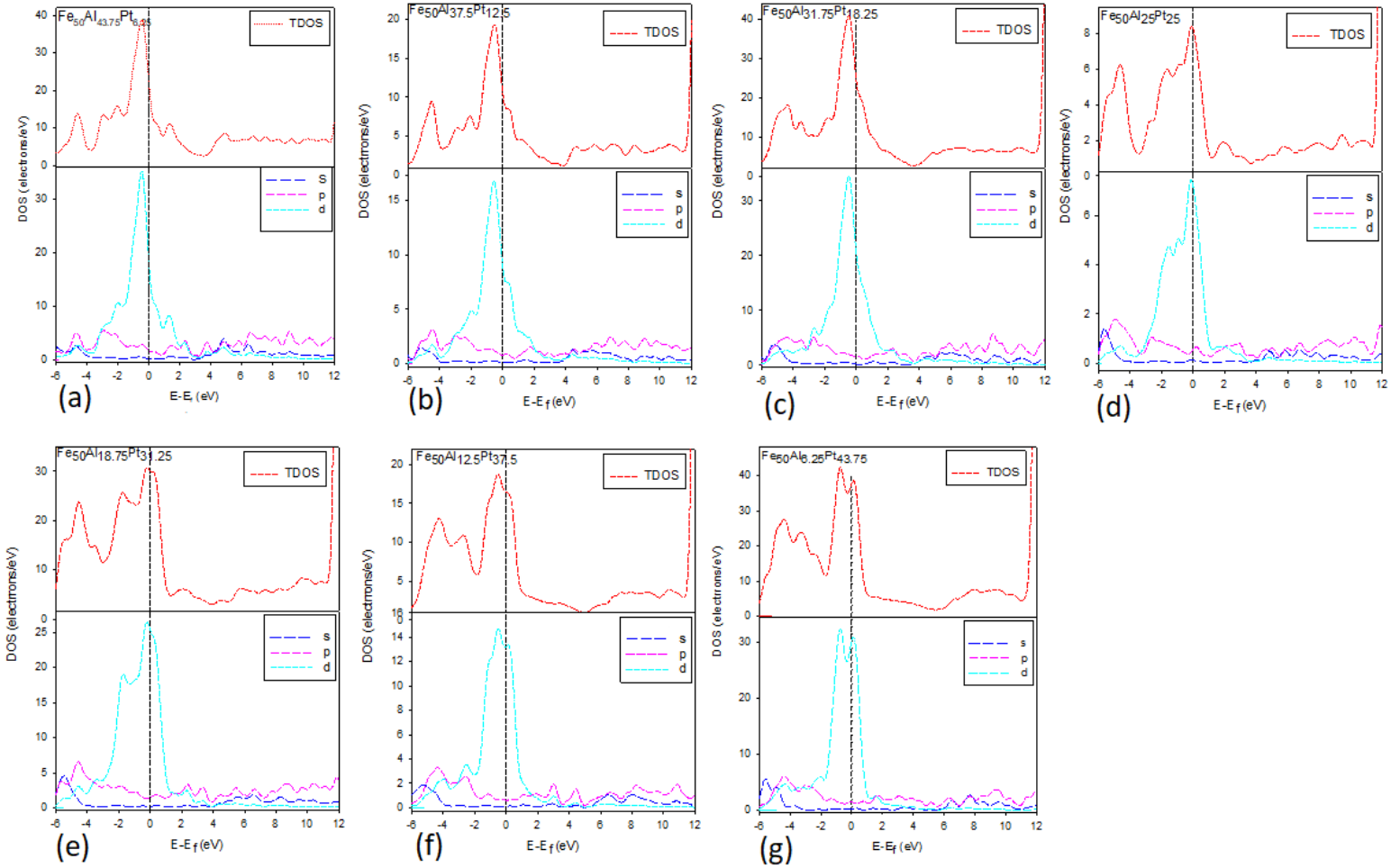

Figure 5-12: The graphs of total and partial density of states for (a) $Fe_{50}Al_{43.75}Pt_{6.25}$, (b) $Fe_{50}Al_{37.50}Pt_{12.5}$, (c) $Fe_{50}Al_{31.25}Pt_{18.75}$, (d) $Fe_{50}Al_{25}Pt_{25}$, (e) $Fe_{50}Al_{18.75}Pt_{31.25}$, (f) $Fe_{50}Al_{12.50}Ag_{37.5}$, (g) $Fe_{50}Al_{6.25}Pt_{43.75}$ with Fermi level taken as energy zero ($E-E_f = 0$).

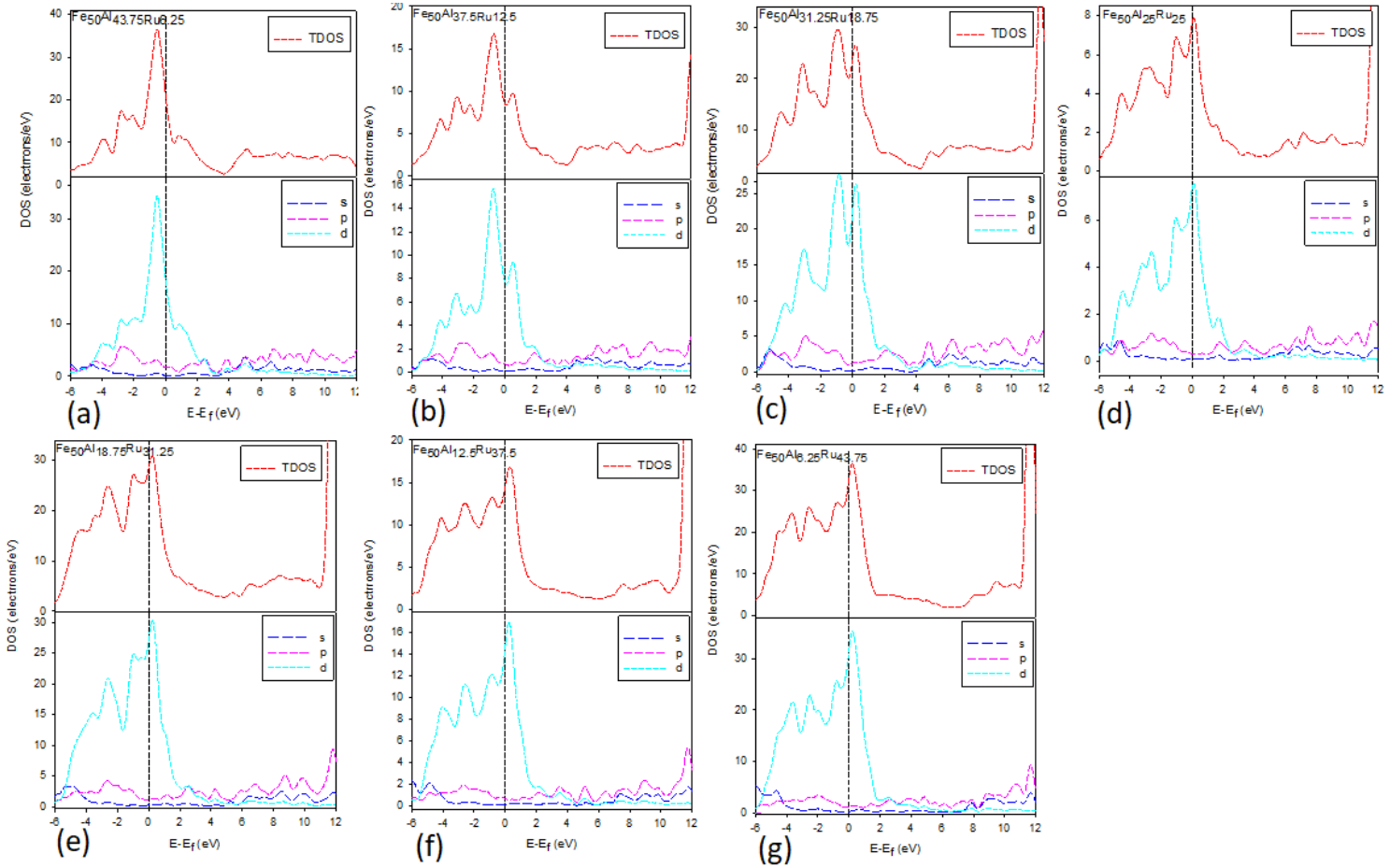

Figure 5-13: The graphs of total and partial density of states for (a) $Fe_{50}Al_{43.75}Ru_{6.25}$, (b) $Fe_{50}Al_{37.50}Ru_{12.5}$, (c) $Fe_{50}Al_{31.25}Ru_{18.75}$, (d) $Fe_{50}Al_{25}Ru_{25}$, (e) $Fe_{50}Al_{18.75}Ru_{31.25}$, (f) $Fe_{50}Al_{12.50}Ru_{37.5}$, (g) $Fe_{50}Al_{6.25}Ru_{43.75}$ with Fermi level taken as energy zero ($E-E_f = 0$).

Chapter 6

TEMPERATURE DEPENDENCE

In this chapter, an analysis of how Pt, Ru, Pd and Ag dopants influence the properties of $Fe_{50}Al_{50}$ structure will be discussed. DMol3 technique [57] and LAMMPS-EAM code [51] were employed to investigate the ternary $Fe_{50-x}Al_{50}X$ alloys at different temperatures using the NVT ensemble. The binding energy (E_b) and elastic constants (C_{ij}) were evaluated to predict stability. The Gibbs free energy (ΔG) [111] and X-ray diffraction pattern (XRD) are also discussed. Various compositions of 0.2 and 0.5 at. % X (X= Pt, Pd, Ru, Ag) were considered to determine the stability and transition temperature. These compositions were chosen based on the previous literature. An additional composition of 0.7 at. % X has also been considered as one possible concentration with promising properties.

6.1 Time step for $Fe_{50}Al_{50}$ and $Fe_{49.80}Al_{50}Ru_{0.2}$

In this section, the focus is mainly on the validation of 0.2 and 0.5 at. % X from previous experimental findings [33]. Firstly, we have ascertained that the sufficient number of time-step is used, this is done by performing total energy calculations as a function of time-step using Dmol3. The number of time-step is important for the process of calculating the time interval for which simulation will progress smoothly to deduce desirable results. For this purpose, we used the $Fe_{50}Al_{50}$ and $Fe_{49.80}Al_{50}Ru_{0.2}$ systems to determine the suitable number of time-step. Figure 6-1 (a) and (b) shows the graph of energy against time-step for binary $Fe_{50}Al_{50}$ and doped $Fe_{49.80}Al_{50}Ru_{0.2}$ systems. We observed that from 1 to 16 ps the system is at equilibrium; whereby at 16 ps a transient value is observed indicating that the system reached a steady state. In figure 6-1 (b) we observed similar transient value where the system reached a steady state at 16 ps. Thus,

a time step of 16 ps has been chosen and will be used throughout the MD calculation for all the Fe-Al-X systems.

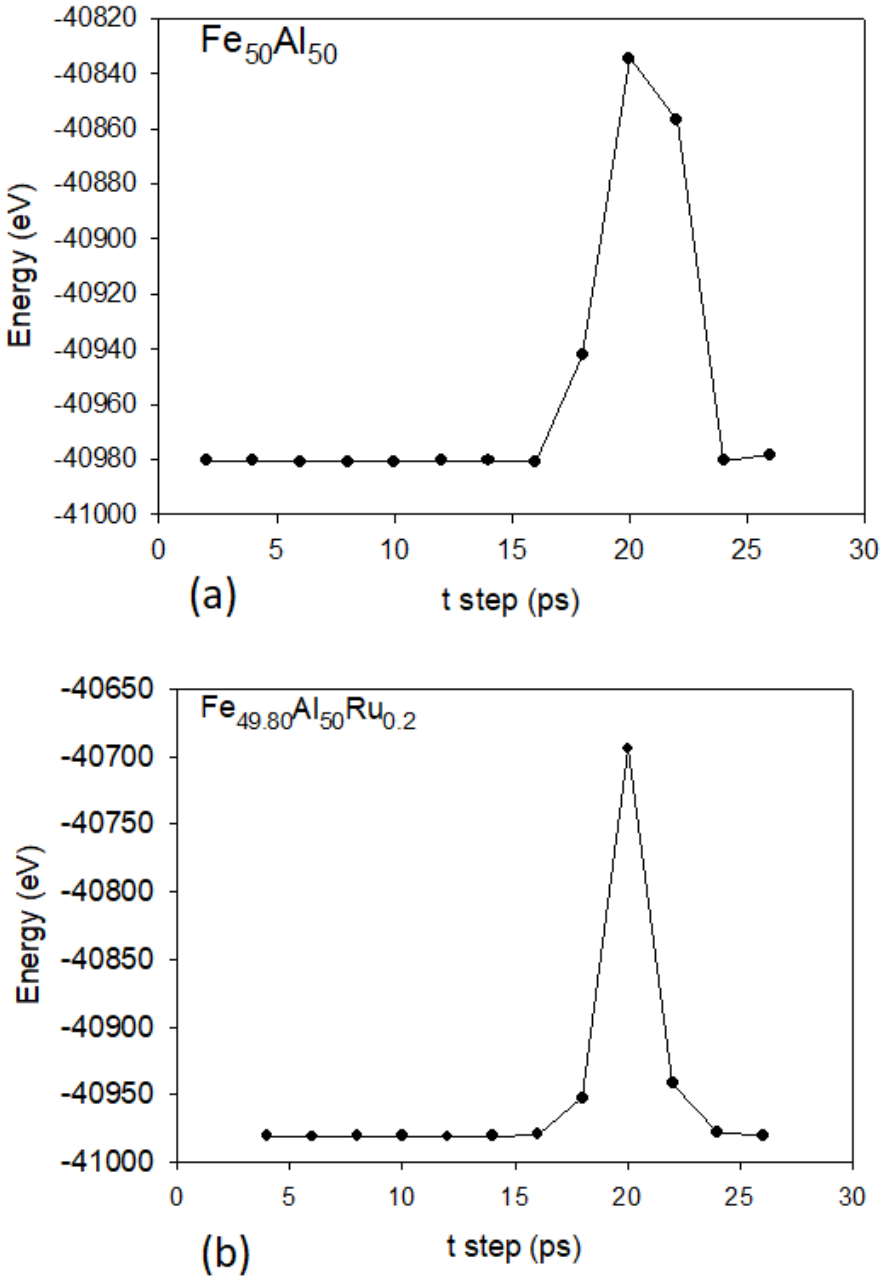

Figure 6-1: Graph of energy against time-step for (a) β2 $Fe_{50}Al_{50}$ and doped (b) $Fe_{49.80}Al_{50}Ru_{0.2}$.

6.2 Effect of temperature on FeAl-X (X= Pt/Pd/Ru/Ag)

To determine the effect of temperature on the structural and thermodynamic properties of binary $Fe_{50}Al_{50}$ and ternary $Fe_{50-x}Al_{50}X$ alloys, we performed the MD

calculations using DMol3 technique, NVT ensemble with a time step of 16 ps. In this case, the binding energy is considered to establish at what temperature is the system able to withstand and maintain its symmetry or configuration, i.e. deduce the stability at a certain temperature range.

Figure 6-2 (a), (b), (c) and (d) show the graph of binding energy against the temperature of $Fe_{50}Al_{50}$ doped with 0.2 at. % Ru or Pd and 0.5 at. % Ag. These concentrations were adopted from the literature [33]. It was reported that Ru and Pd addition are potential candidates for stabilizing the binary $Fe_{50}Al_{50}$ at 0.2 at. %, while Pt and Ag at 0.5 at. % compositions.

Recall that according to literature, the binary FeAl system has limited room temperature ductility above 873 K [119]. In figure 6-2 (a), we note that the binding energy curves for the binary $Fe_{50}Al_{50}$ phase is stable up to 900 K and becomes less stable above this temperature (displaying high values of E_b). This observation is in good agreement with the experimental findings [4]. Figure 6-2 (b) and (d) show similar trend compared to the $Fe_{50}Al_{50}$ (figure 6-2 a).

The binding energy of each system varies according to the effect of alloying elements Pd, Ru, and Ag. Clearly, the addition of 0.2 at. % Ru showed a higher transition temperature of 1000 K, slightly lower for Ag (900 K), as compared to the experimental value of 1273 K and 1073 K [120, 121]. The Pd doped on $Fe_{50}Al_{50}$ showed that the lowest transition temperature is at 400 K (figure 6-2 c). The Ag and Ru doped systems showed a sudden jump at 900 K and 1000 K, respectively, which implies that the systems are unstable above this temperature range.

To investigate the elastic stability of $Fe_{49.80}Al_{50}Pd_{0.2}$, $Fe_{49.50}Al_{50}Ag_{0.5}$, $Fe_{49.50}Al_{50}Pt_{0.5,}$ and $Fe_{49.80}Al_{50}Ru_{0.2}$ ternary systems, we calculated the elastic constants (C_{ij}) and the ratio of bulk to shear moduli (B/G) for these systems as shown in table 6-1. Note that the symmetry of the systems was unchanged, and only three independent elastic constants (C_{11}, C_{12}, and C_{44}) have been found for the cubic lattice. We found that the $Fe_{49.50}Al_{50}Ag_{0.5}$ and $Fe_{49.80}Al_{50}Pd_{0.2}$ alloy systems are ductile since the ratio of bulk to shear modulus value is greater than

1.75 (B/G >1.75) which is a criterion proposed by Pugh [118] to determine the ductility and brittleness of a material (as discussed in chapter 4 section 4-4). In contrast, the $Fe_{49.80}Al_{50}Ru_{0.2}$ and $Fe_{49.50}Al_{50}Pt_{0.5}$ showed brittleness characteristic behaviour since the B/G ratio is less than 1.75 (B/G< 1.75) and gave 1.72 and 1.707 GPa, respectively. Previous computational data reported a significantly high binding energy with a value of 0.57 eV, which indicated a strong tendency for vacancy clustering and vacancies annealed out to be open structures such as dislocations, voids or grain boundaries. However, the current study on the $Fe_{50}Al_{50}$ showed to be stable up to 900 K at 9.9 eV.

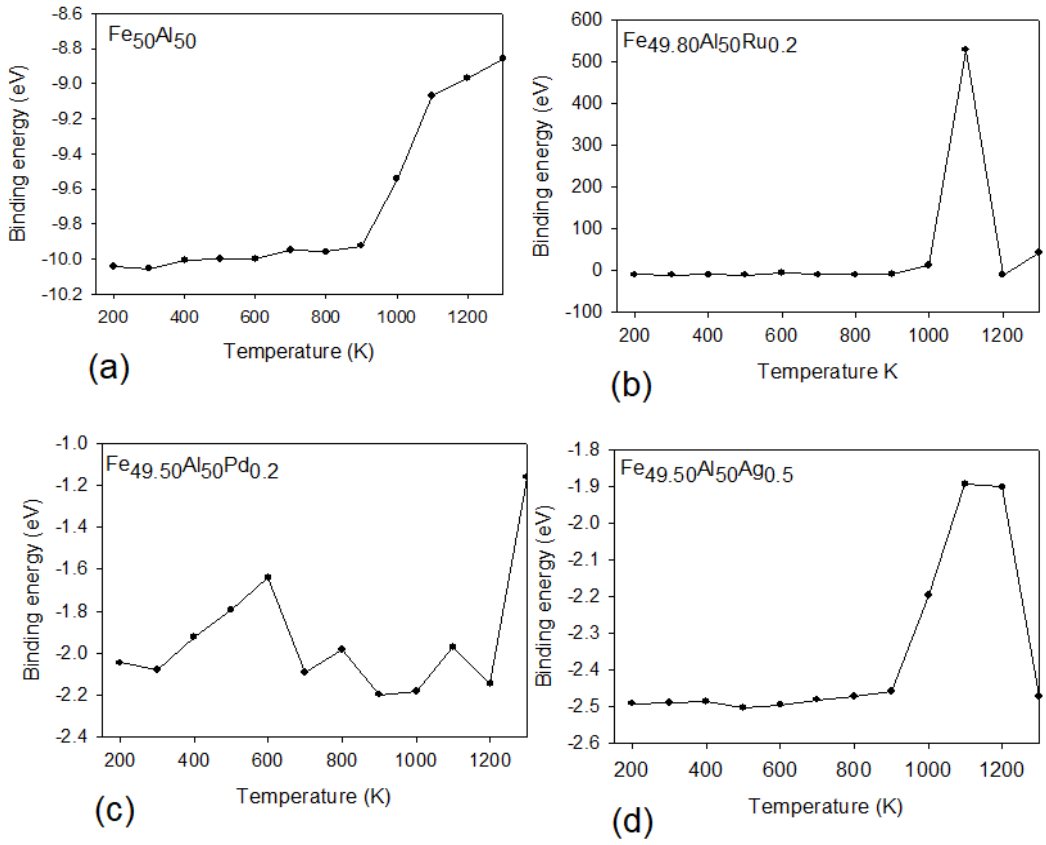

Figure 6-2: Time step against energy for (a) β2 $Fe_{50}Al_{50}$, doped (b) $Fe_{49.80}Al_{50}Ru_{0.2}$ (c) $Fe_{49.80}Al_{50}Pd_{0.2}$ and (d) $Fe_{49.50}Al_{50}Ag_{0.5}$.

Table 6-1 lists the elastic moduli's for Pt, Pd, Ag and Ru at. % ternary systems. The elastic stability criteria were used to determine the ductility and brittleness of a system using a method implemented by Pugh [118]. The calculated shear moduli (C') show a positive behaviour indicating that all concentrations under

considerations are elastically stable. We observed that the independent elastic constants for all doped systems are positive and satisfy the stability conditions for a cubic system. The elastic constants confirmed instability at 0.3 at. % Pt, while Ru addition was more favourable. $Fe_{49.50}Al_{50}Ag_{0.5}$ system shows instability for C_{11}, C_{12} and C_{44} this is due to C_{44}> C' leading to the degeneracy of transverse in the system.

Table 6-1: Elastic constants, bulk modulus and B/G ratio of doped $Fe_{50}Al_{50}$ systems

Structures	C_{11} (GPa)	C_{12} (GPa)	C_{44} (GPa)	C' (GPa)	B (GPa)	G (GPa)	B/G (GPa)
$Fe_{49.80}Al_{50}Pd_{0.2}$	149.6	89.5	16.4	30.1	18.5	7.1	2.57
$Fe_{49.80}Al_{50}Ru_{0.2}$	279.4	140.6	147.4	69.4	186.9	108.9	1.72
$Fe_{49.50}Al_{50}Pt_{0.5}$	278.9	139.9	147.5	208.9	186.2	101.8	1.71
$Fe_{49.50}Al_{50}Ag_{0.5}$	-1.3	-15.4	-16.6	7.1	48.6	10.7	4.50

6.3 LAMMPS code calculations

In this section, we employed the molecular dynamics (MD) method to investigate the effect of temperature on FeAl-X ternary alloys using LAMMPS-EAM module. The Zhou interatomic potentials [80] are invoked within the MedeA environment [52]. A supercell approach was used to generate various compositions of FeAl-X, this was achieved by lowering the symmetry to P1. This code employs specific forcefield preferences such as forcefield atom types and forcefield charges. Each FeAl-X ($0 \leq x \leq 1$) system was subjected to high temperatures between 200 K and 3000 K using a flow chart with various stages running consecutively (see figure 6-3).

The flow chart specifies up to 7 various stages, for example:

Stage 1: Description of the flow chart,

Stage 2: The variables (temperature range) of a system,

Stage 3: Table for the variables to be used,

Stage 4: Supercell of the chosen system to be investigated,

Stage 5: LAMMPS (initialize the cut-off, velocity and the type of ensemble to be used),

Stage 6: The sequential for loop in order to run the set cell for the density and rho (ρ) calculations,

Stage 7: The table for printing of results for analysis.

The above stages can lead to determining different properties including the melting temperature of the systems at particular temperatures. An NVT ensemble was employed in order to observe the phase transition as the temperature is increased for each system. The number of atoms and volume was kept constant as the temperature is varied from 200 K – 3000 K.

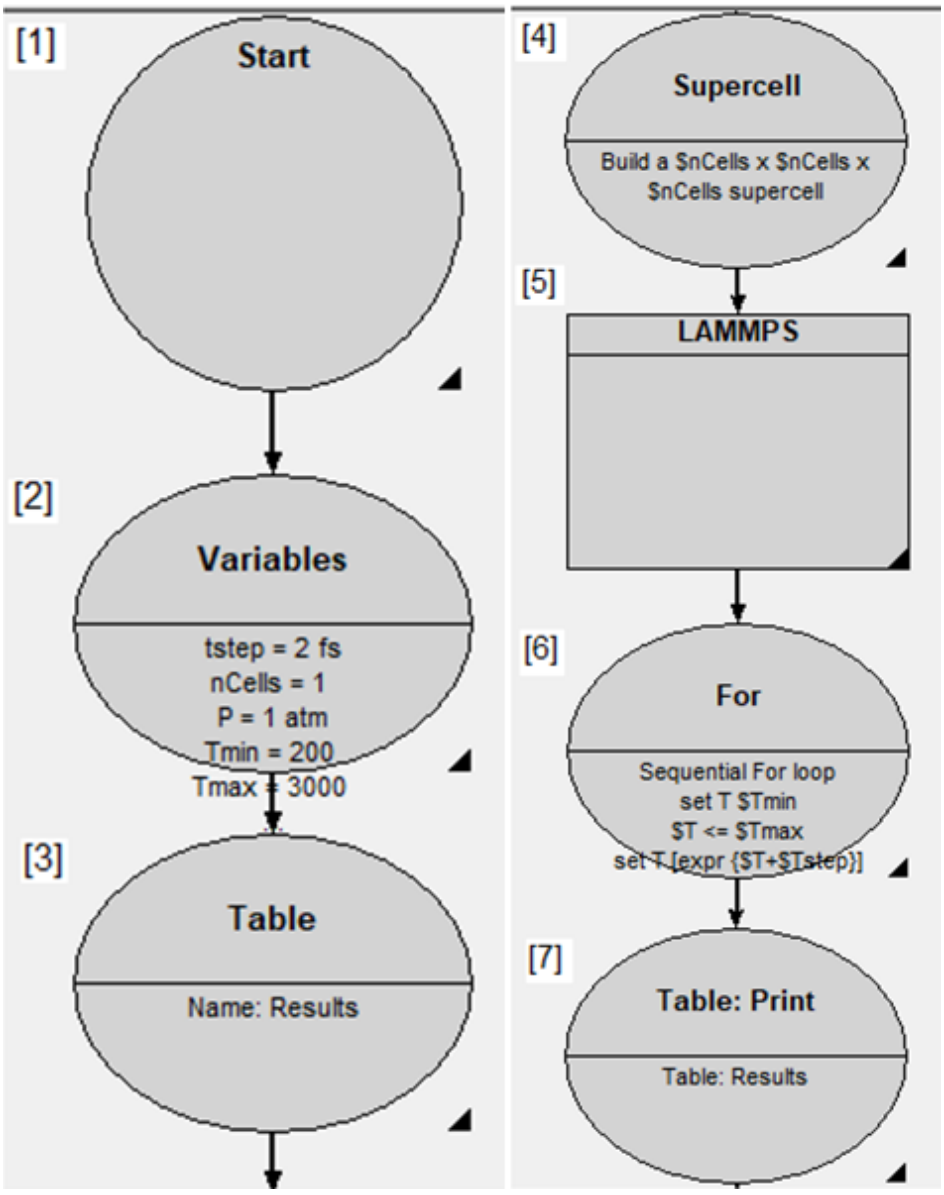

Figure 6-3: An example of a flow chart: LAMMPS code showing the 7 stages.

6.3.1 **Lattice expansion**

In order to determine the lattice expansion of β2 FeAl and ternary FeAl-X systems the MD calculations were carried out up to 3000 K. Firstly, the binary FeAl has been calculated to determine possible transition temperature. Secondly, the effect of temperature on binary β2 FeAl and ternary FeAl-X systems were also calculated (for 0.5 and 0.7 at. % Ag, Pd and Pt) to establish the extent of how the lattice expands at various concentrations and temperatures. Note that Ru addition was not considered in the MD calculations using LAMMPS code due to the unavailability of potentials in the database.

Table 6-2: Lattice parameters, transition temperatures and c/a ratio of binary $Fe_{50}Al_{50}$ and doped $Fe_{50}Al_{50}X$ systems.

Structures	At. %	Lattice parameters (Å)	Transition temperature	Lattice parameters (Å)	Space group	New phase (Symmetry)	ratio c/a
$Fe_{50}Al_{50}$	-	a=b=c=5.820	2493.9 K	a=10.316 b=62.205 c=13.247	P1	Orthorhombic	0.779
$Fe_{49.50}Al_{50}Ag_{0.5}$	0.5		2601.5 K	a=12.680 b=56.508 c=12.189		tetragonal	1.141
$Fe_{49.30}Al_{50}Ag_{0.7}$	0.7		2500.2 K	a=54.964 b=17.708 c=8.726		Orthorhombic	0.159
$Fe_{49.50}Al_{50}Pd_{0.5}$	0.5		2597.9 K	a=15.714 b=10.692 c=51.645		Orthorhombic	0.304
$Fe_{49.30}Al_{50}Pd_{0.7}$	0.7		2595.3 K	a=11.101 b=57.435 c=13.211		Orthorhombic	0.84
$Fe_{49.50}Al_{50}Pt_{0.5}$	0.5		2598.6 K	a=15.996 b=12.994 c=41.484		Orthorhombic	2.594
$Fe_{49.30}Al_{50}Pt_{0.7}$	0.7		2601.2 K	a=11.734 b=53.572 c=13.390		Orthorhombic	0.961

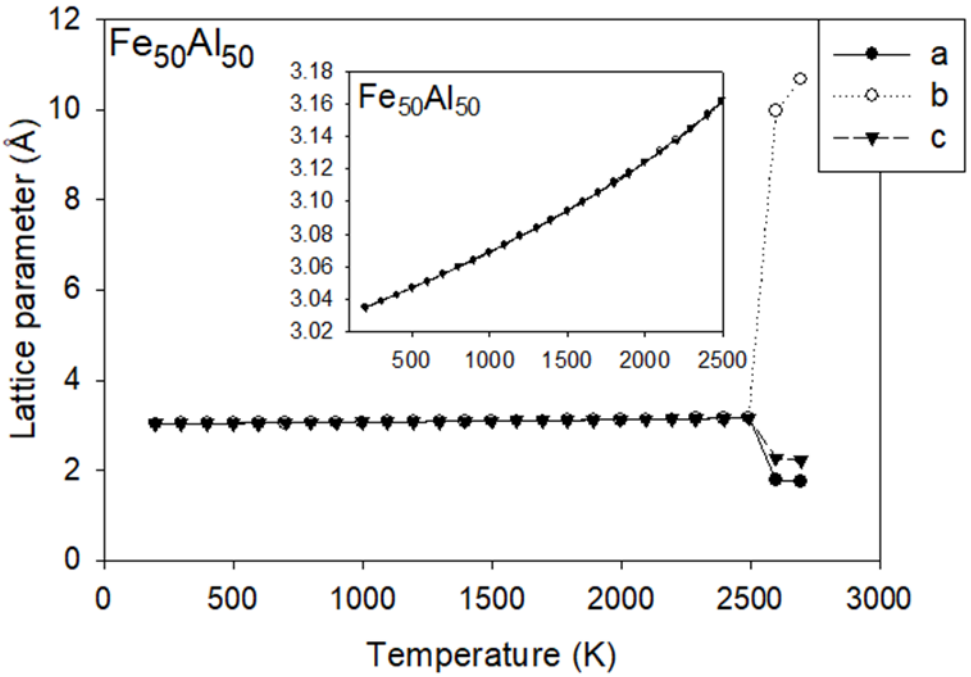

Figure 6-4: Lattice parameters *a, b, c* of FeAl at a temperature range of 200 K to 3000 K.

Figure 6-4 shows the graph of the lattice parameter against temperature for $Fe_{50}Al_{50}$ system, the insert is set as a guideline to show precisely the trend in temperature. Now, as the temperature is increased there is an exponential increase in the lattice parameter from 200-2500 K. The lattice parameters *(a*, *b*, *c)* are similar in value as the temperature is increased and maintains a cubic system up to 2400 K. Beyond this temperature, we observe a new phase transition to an orthorhombic phase with lattice constants of a= 10.316, b=62.205 and c=13.247 Å and $\alpha=\beta=\Upsilon=90.0^{o}$.

Figure 6-4, 6-5, 6-6 and 6-7 shows the graphs of lattice parameter against temperature for $Fe_{49.5}Ag_{0.5}Al_{50}$ and $Fe_{49.3}Ag_{0.7}Al_{50}$; $Fe_{49.5}Pd_{0.5}Al_{50}$ and $Fe_{49.3}Pd_{0.7}Al_{50}$; $Fe_{49.5}Pt_{0.5}Al_{50}$ and $Fe_{49.3}Pt_{0.7}Al_{50}$ systems, respectively. According to previous studies, it was stated that binary FeAl has a melting temperature of 1255 K [120] and the ternary alloys $Fe_{50-X}Pd_XAl_{50}$ and $Fe_{50-X}Ag_XAl_{50}$ are said to have a melting temperature of 1273 K and 1073 K [121].

We observed structural phase changes at various temperatures. For example, in figure 6-5a, the Ag doped system (at 0.5 and 0.7 at. % Ag) preserves the cubic phase up to 2500 K, however, beyond this temperature the structure transforms from cubic to tetragonal phase with lattice parameters a= 11.734, b=53.572 and

c=13.39 Å. Similar behaviour is observed for Pd and Pt doped systems in Figures 6-6 and 6-7, respectively. However, this transition temperature and phases are slightly different. The summary of temperature and new structures are given in table 6-1.

We see in figure 6-5, the phase transition for 0.5 and 0.7 at. % Pd is observed at lattice parameter of a=15.715, b=10.687 and c=51.475 Å and a=18.994, b=19.009 and c=18.975 Å, respectively. Furthermore, figure 6-6, the phase transition for 0.5 and 0.7 at. % Pt is observed at lattice parameter of a=15.996, b=12.994 and c=41.484 Å and a=12.68, b=56.508 and c=12.189 Å, respectively.

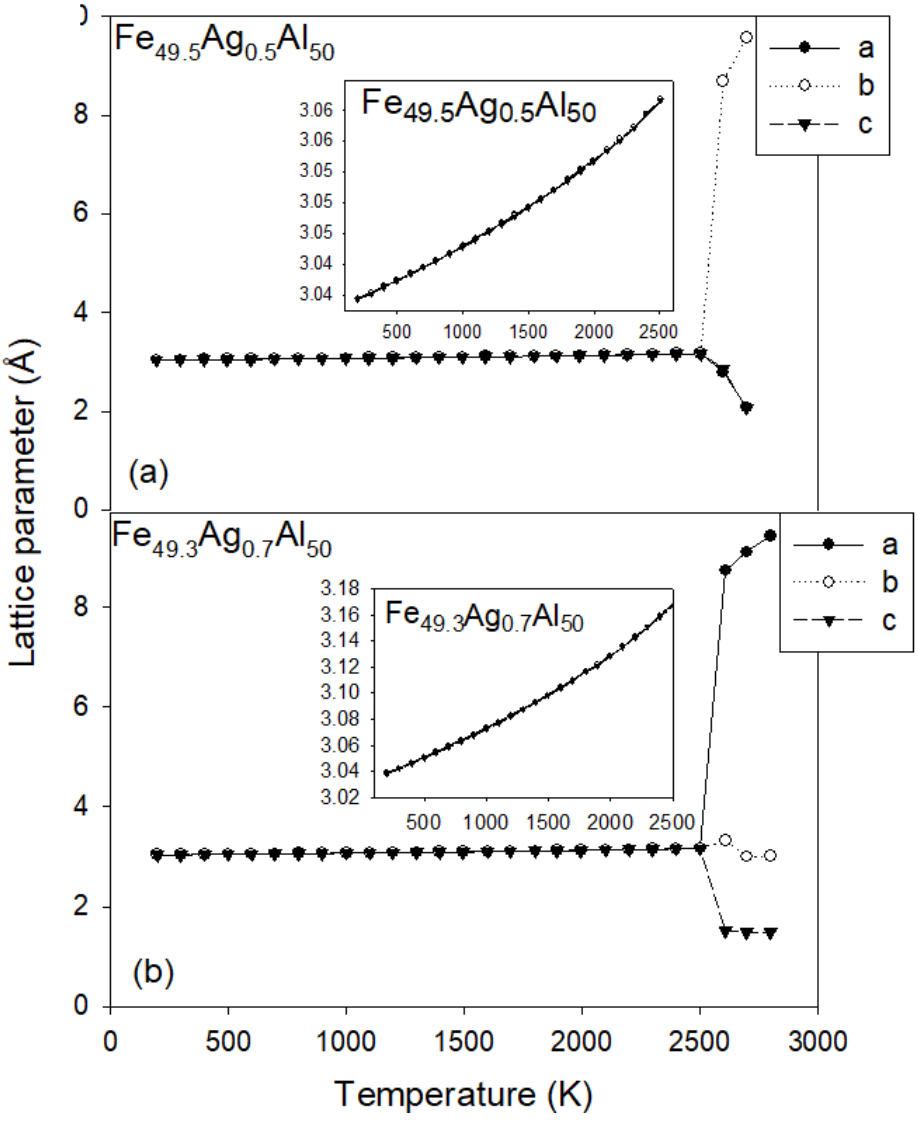

Figure 6-5: Lattice parameters a, b, c of (a) $Fe_{49.5}Ag_{0.5}Al_{50}$, (b) $Fe_{49.3}Ag_{0.7}Al_{50}$, structures. The insert shows the trend between 200 K and 2500 K.

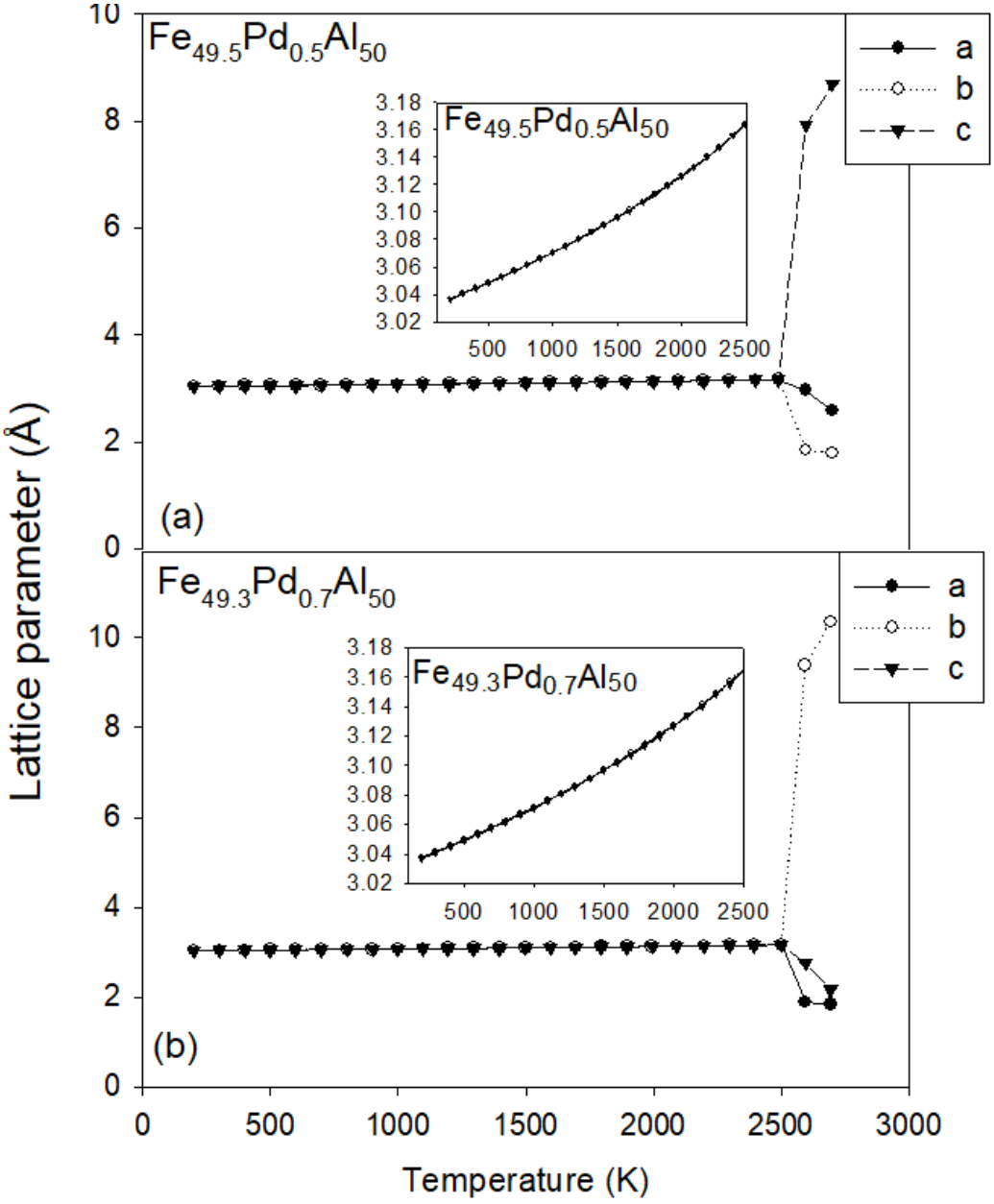

Figure 6-6: Lattice parameters a, b, c of (a) $Fe_{49.5}Pd_{0.5}Al_{50}$ (b) $Fe_{49.3}Pd_{0.7}Al_{50}$, structures. The insert shows the trend between 200 K and 2500 K.

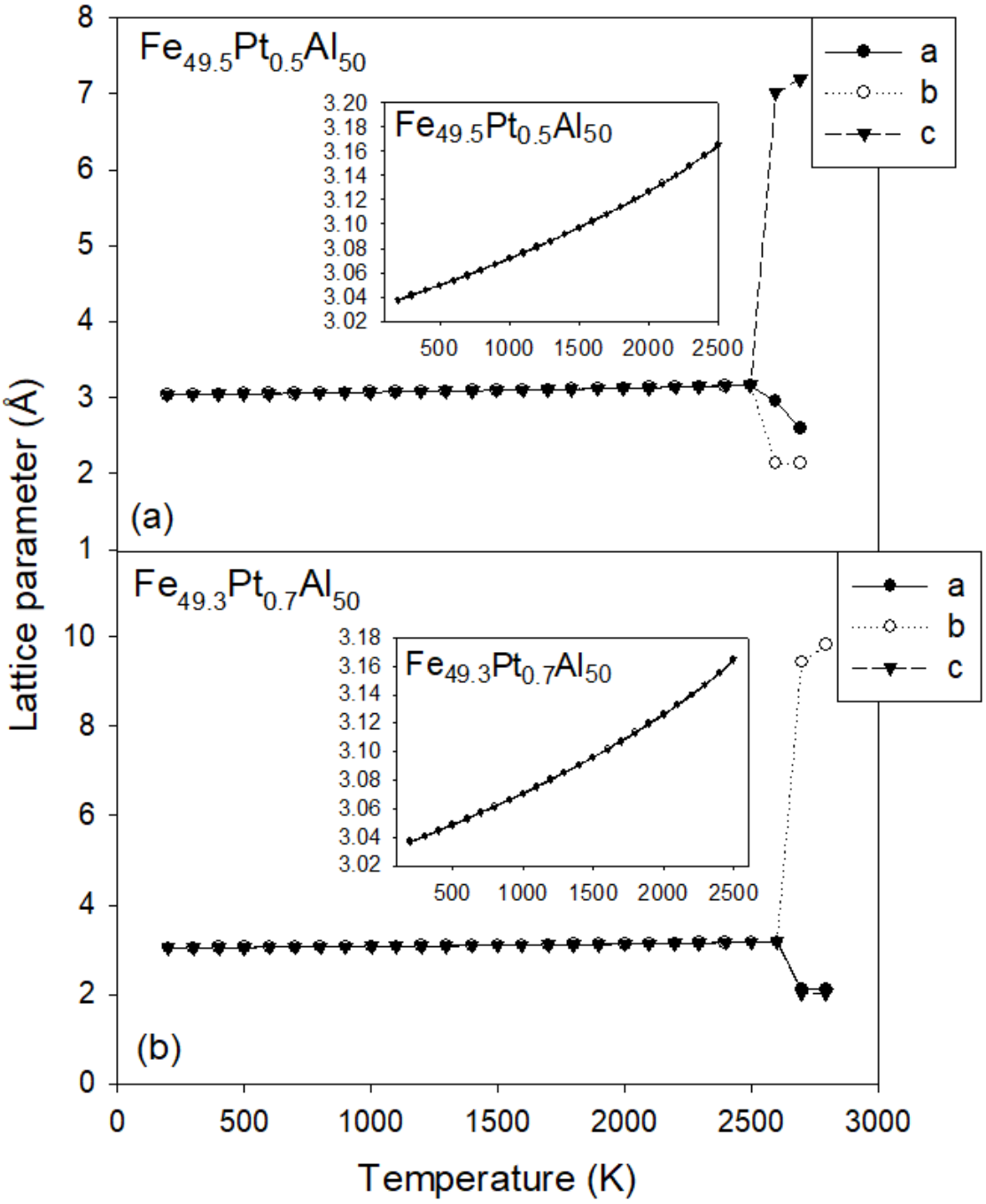

Figure 6-7: Lattice parameters a, b, c of (a) $Fe_{49.5}Pt_{0.5}Al_{50}$ and (b) $Fe_{49.3}Pt_{0.7}Al_{50}$ structures. The insert shows the trend between 200 K and 2500 K.

6.3.2 **Thermodynamic properties**

Thermodynamic properties such as constant-volume heat capacity (C_v), change in enthalpy (ΔH), change in temperature (ΔT), change in vibrational entropy (ΔS_{vib}) and change in Gibbs free energy (ΔG) have been calculated in order to

understand temperature dependence or thermodynamic behaviour of ternary FeAl-X system at different temperature range.

The constant-volume heat capacity is important for predicting the amount of heat required in order to raise the system's temperature by one degree. This is essential for minimizing the measure of molecular disorder within the systems and can be obtained from the plot of the total energy and temperature relationship. The C_v is extracted with respect to the tangent trendline such that the change in vibrational entropy can be calculated as:

$$\Delta s_{vib} = \int_{T_1}^{T_2} \frac{C_v}{T} dt, \quad \text{.....(6-1)}$$

where T_2 and T_1 are the maximum and minimum temperatures, C_v is the constant-volume heat capacity and T is temperature integrated with respect to T_2 and T_1. The vibrational entropy change assists to determine whether the reaction becomes more or less spontaneous as well as in the predictions of the change in Gibbs free energy [44].

The change in enthalpy for each system is given as:

$$\Delta H = U + PV, \text{.....(6-2)}$$

where U is the internal energy, P is the pressure and V is the volume for each system. Thus, the enthalpy change can be calculated as:

$$\Delta \mathrm{H} = H_2 - H_1$$

$$= (U + PV)_{T_2} - (U + PV)_{T_1} \text{..... (6-3)}$$

The change in enthalpy contributes to the behaviour of the system when exposed to temperature.

Thus, the change in Gibbs free energy is given by,

$$\Delta G = \Delta H - \Delta(TS) \quad \text{.....(6-4)}$$

where ΔH is enthalpy change, ΔT is the temperature change and ΔS is the change in vibrational entropy [110]. From the above illustrations, the C_v, ΔH and Δs_{vib} was

used to make predictions for the ΔG for binary $Fe_{50}Al_{50}$ and ternary $Fe_{50-X}Al_{50}X$ systems, (in the following subsection).

Constant-volume heat capacity

The constant volume heat capacity measures the amount of heat necessary to raise the temperature of a system by one degree Celsius. To determine C_v, a tangent line was constructed on the graph to firstly determine the accuracy of the points plotted of the system. The accuracy is observed when the tangent line is equal to unity (R^2=1). This also assists to obtain the total energy equation for calculating C_v.

Table 6-3: Presents the measure of the tangent line (R^2) and the equation used to obtain C_v of binary FeAl and ternary FeAl-X alloys.

Systems	**R^2**	**Total energy equation**
$Fe_{50}Al_{50}$	1	9e-06T^2+0.1055T-1264.8
$Fe_{49.5}Ag_{0.5}Al_{50}$	1	9E-06T^2+0.1051T-1257.1
$Fe_{49.3}Ag_{0.7}Al_{50}$	0.999	9E-06T^2+0.1058T-1254.0
$Fe_{49.5}Pd_{0.5}Al_{50}$	1	9E-06T^2+0.1064T-1259.9
$Fe_{49.3}Pd_{0.7}Al_{50}$	1	9E-06T^2+0.1055T-1257.0
$Fe_{49.5}Pt_{0.5}Al_{50}$	1	9E-06T^2+0.1054T-1262.0
$Fe_{49.3}Pt_{0.7}Al_{50}$	0.999	1E-05T^2+0.1034T-1259.8

Now, we calculated the C_v for the ternary systems, to observe the effect of alloying with Pt, Pd, and Ag for 0.5 at. % and 0.7 at. %. Similarly, the R^2 was used to calculate the accuracy of the trendline with respect to the points within the system at each temperature. The total energy equation (table 6-3) was obtained for binary $Fe_{50}Al_{50}$ and each ternary $Fe_{50-X}X_XAl_{50}$ system within the stable temperature range curve, i.e. 200 K – 2600 K against the total energy of each system of every temperature point. We observed that $Fe_{49.5}Ag_{0.5}Al_{50}$, $Fe_{49.5}Pt_{0.5}Al_{50}$, $Fe_{49.5}Pd_{0.5}Al_{50}$ $Fe_{49.3}Pd_{0.7}Al_{50}$ have an accuracy of 1; however, $Fe_{49.3}Ag_{0.7}Al_{50}$ and $Fe_{49.3}Pd_{0.7}Al_{50}$ have an accuracy of 0.999 implying that the energy values are accurate to the tangent line (less scattered).

Figure 6-8 shows the total energy against temperature for binary $Fe_{50}Al_{50}$ from 200 K to 2500 K. The plot shows an increasing pattern with an increase in temperature (figure 6-8 (a)). We deduced the equation for determining the C_v for the whole system as well as for each point in the system as shown in figure 6-8 (b). The C_v was calculated by differentiating the equation from figure 6-8 (a) with respect to temperature in eV/K. The C_v value was calculated to be 0.106 eV/K for the whole system and the tangent line (R^2) accuracy is 1. However, the C_v curve in figure 6-8 (b) for each point within the system showed to increase as the temperature is increased.

Figure 6-9, 6-10, 6-11 shows the graph of total energy against temperature for ternary $Fe_{50}Al_{50}X$ systems from 200 K to 2600 K. These plots show a linear increase as the temperature is raised. From these figures, we deduced the equation for determining the C_v (in table 6-3) for the whole system as well as for each point in the system.

The C_v values were calculated to be 0.105 eV/K for $Fe_{49.5}Ag_{0.5}Al_{50}$ and $Fe_{49.3}Ag_{0.7}Al_{50}$, 0.106 eV/K for $Fe_{49.5}Pd_{0.5}Al_{50}$ and $Fe_{49.3}Pd_{0.7}Al_{50}$, 0.265 eV/K for $Fe_{49.5}Pt_{0.5}Al_{50}$ and 0.266 eV/K for $Fe_{49.3}Pt_{0.7}Al_{50}$. However, the C_v curve in figure 6-9 (b) shows a fluctuation between 200 K and 1000 K, where else figure 6-9 (a), 6-10 and 6-11 for each point within the system showed an increase as the temperature is increased.

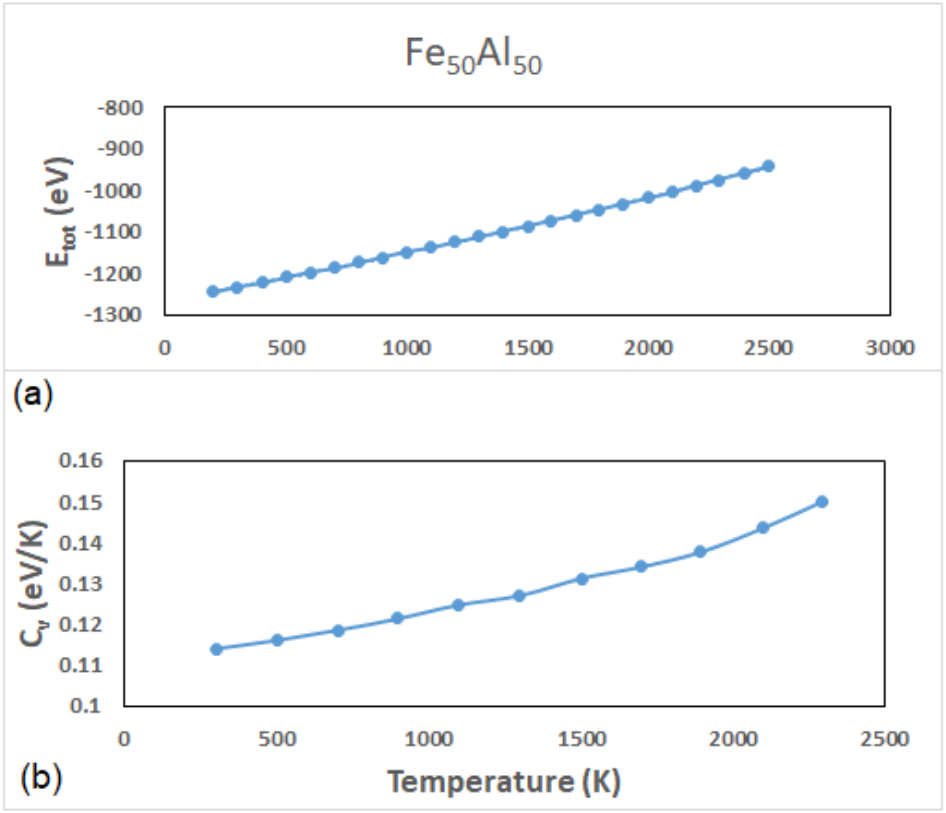

Figure 6-8: Graph of binary $Fe_{50}Al_{50}$ (a) total energy against and (b) constant-volume heat capacity against temperature.

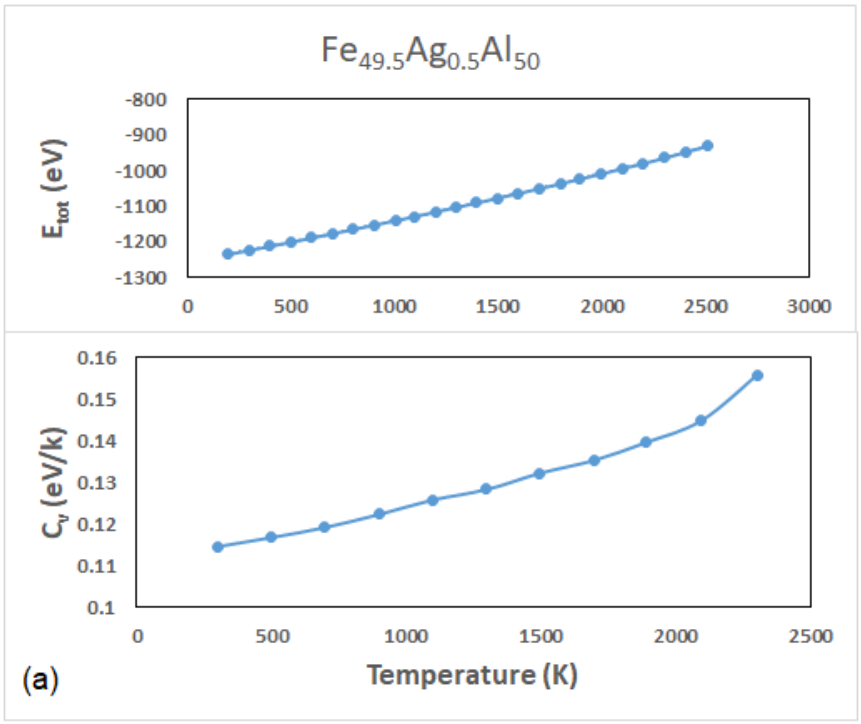

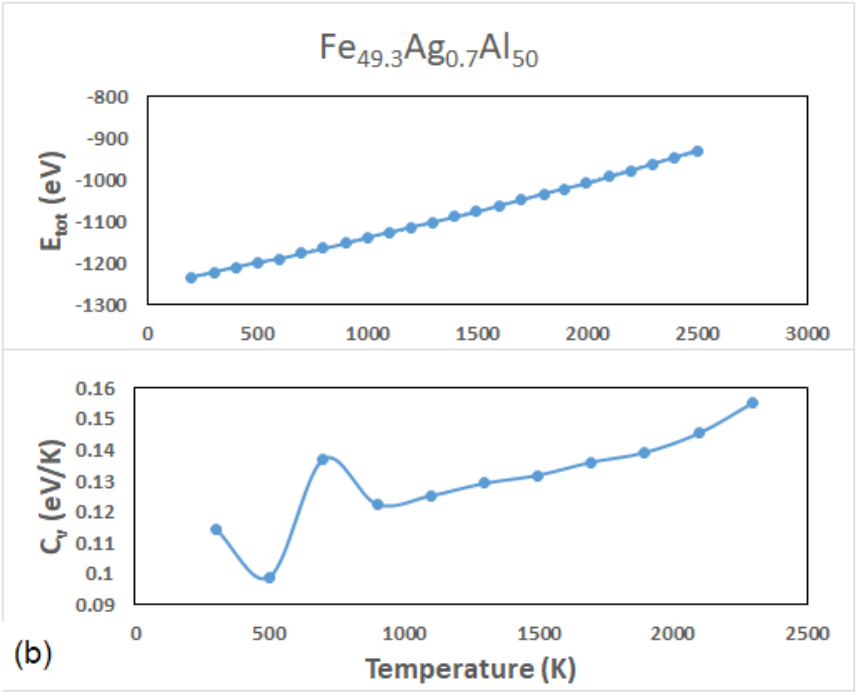

Figure 6-9: Graph of (a) $Fe_{49.5}Ag_{0.5}Al_{50}$ total energy and constant-volume heat capacity against temperature and (b) $Fe_{49.3}Ag_{0.7}Al_{50}$ total energy and constant-volume heat capacity against temperature.

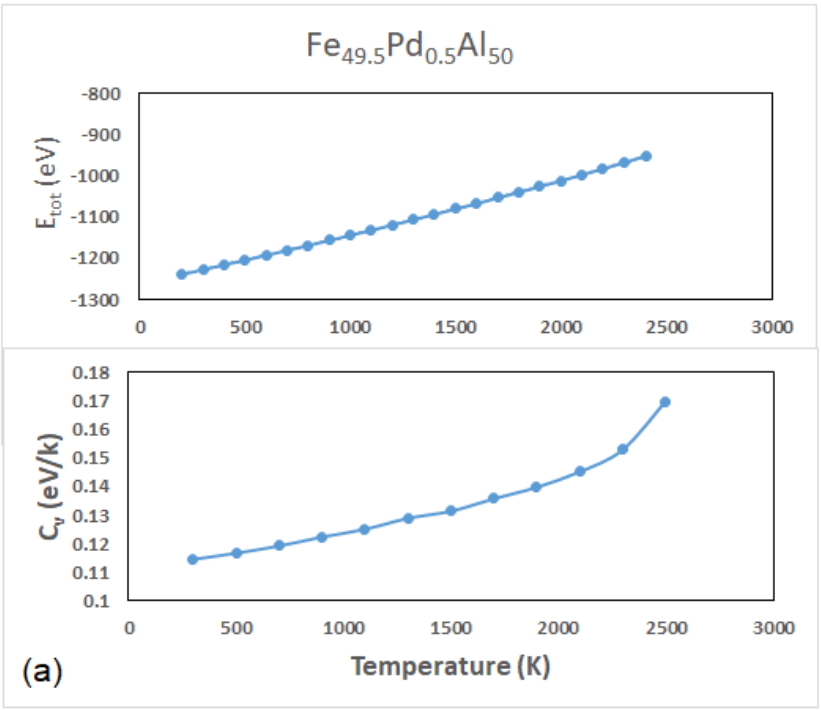

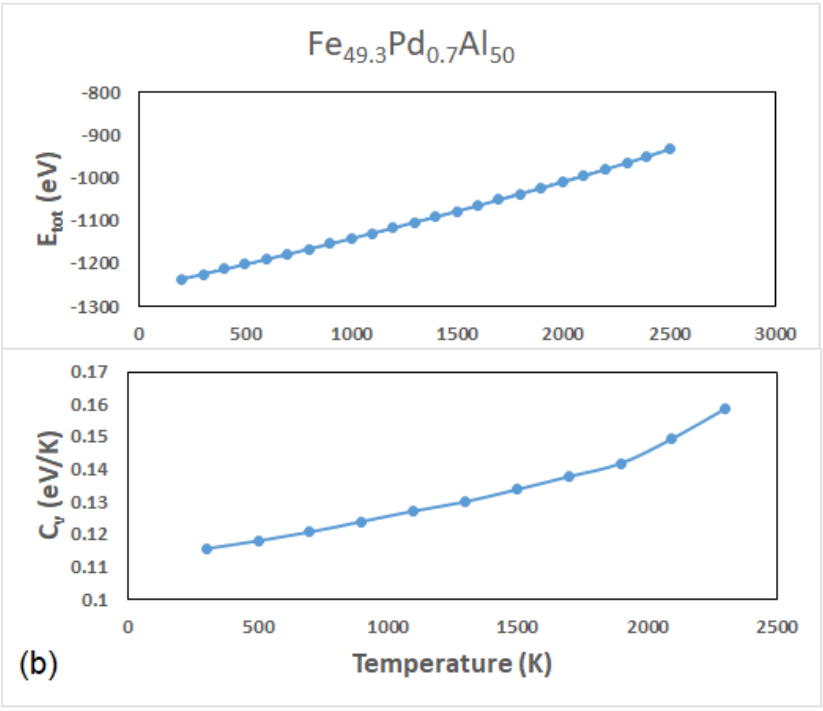

Figure 6-10: Graph of (a) $Fe_{49.5}Pd_{0.5}Al_{50}$ total energy and constant-volume heat capacity against temperature and (b) $Fe_{49.3}Pd_{0.7}Al_{50}$ total energy and constant-volume heat capacity against temperature.

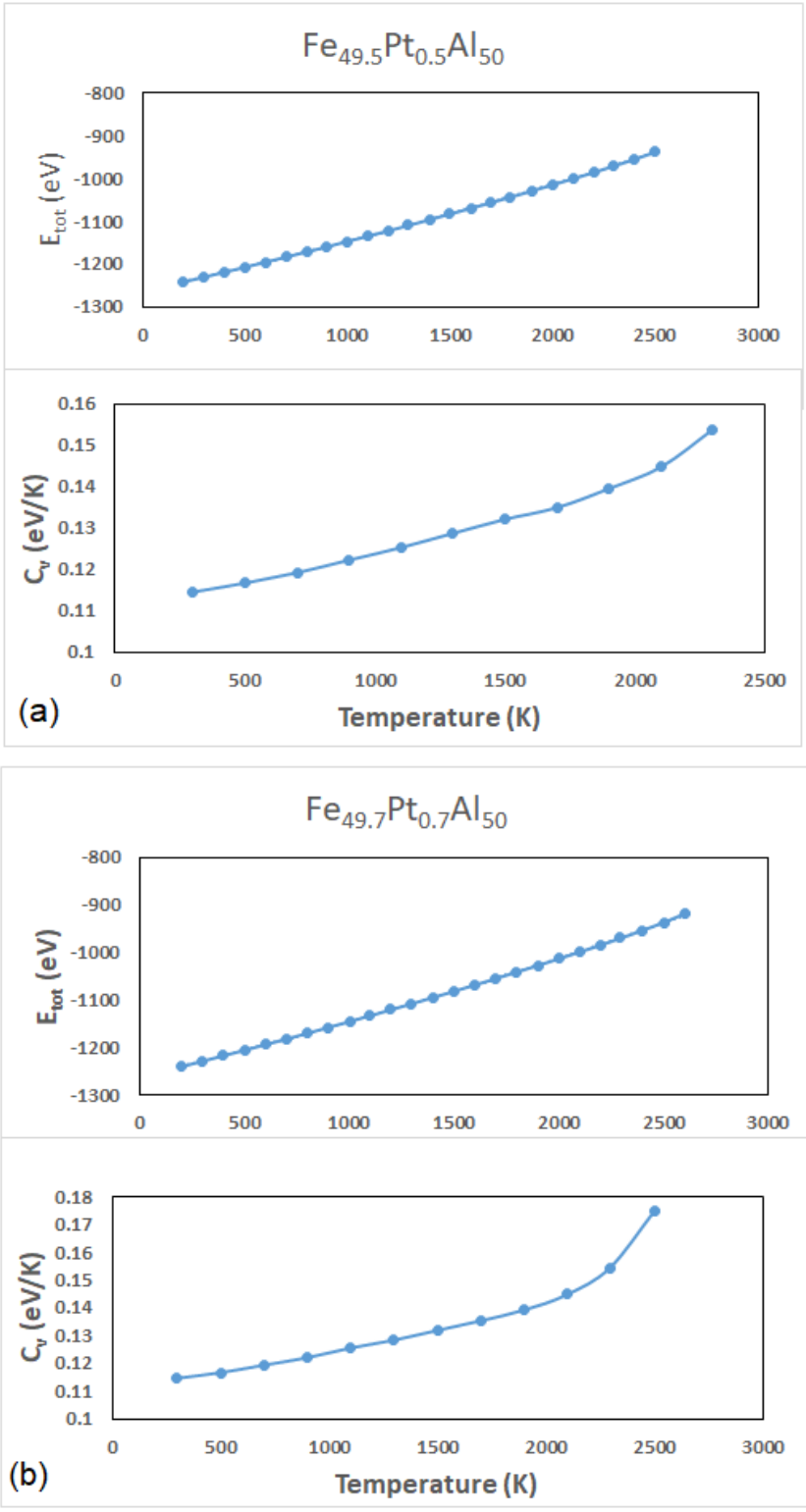

Figure 6-11: Graph of (a) $Fe_{49.5}Pt_{0.5}Al_{50}$ total energy and constant-volume heat capacity against temperature and (b) $Fe_{49.3}Pt_{0.7}Al_{50}$ total energy and constant-volume heat capacity against temperature.

Gibbs free energy

Gibbs free energy assists to mimic phase equilibrium composition at various temperatures and pressures. This is possible through determining the entropy change as well as enthalpy change for each system. It also determines the direction and extent of chemical change, i.e energy is released (exergonic) or energy is absorbed (endergonic) reaction which contributes to deducing whether the reaction is spontaneous or non-spontaneous. Figure 6-12 illustrates the plot of change in Gibbs free energy against temperature from 200 K to 2600 K. The graph is used to determine the phase equilibrium for all the various systems. It can be clearly seen that ΔG for binary $Fe_{50}Al_{50}$ and ternary systems $Fe_{49.5}Ag_{0.5}Al_{50}$, $Fe_{49.3}Ag_{0.7}Al_{50}$, $Fe_{49.5}Pd_{0.5}Al_{50}$, $Fe_{49.3}Pd_{0.7}Al_{50}$, $Fe_{49.5}Pt_{0.5}Al_{50}$, $Fe_{49.3}Pt_{0.7}Al_{50}$ that they all display an endergonic spontaneous reaction since they display negative value [110].

Table 6-4: Presents the constant-volume heat capacity (C_v), change in enthalpy (ΔH), change in temperature (ΔT), change in vibrational entropy (ΔS_{vib}) and change in Gibbs free energy (ΔG) of FeAl-X alloys.

Structures	**C_v (eV/K)**	**ΔH (eV)**	**ΔT (K)**	**ΔS_{vib} (eV/K)**	**ΔG (eV)**
$Fe_{50}Al_{50}$	0.106	301.552	2293.8	0.266	-309.058 (-207.285) [44]
$Fe_{49.5}Ag_{0.5}Al_{50}$	0.105	304.423	2305.9	0.266	-308.947
$Fe_{49.3}Ag_{0.7}Al_{50}$	0.105	303.177	2300.5	0.265	-307.376
$Fe_{49.5}Pd_{0.5}Al_{50}$	0.106	303.166	2202.5	0.267	-296.078
$Fe_{49.3}Pd_{0.7}Al_{50}$	0.106	286.814	2302.0	0.265	-310.777
$Fe_{49.5}Pt_{0.5}Al_{50}$	0.265	321.710	2299.1	0.265	-315.206
$Fe_{49.3}Pt_{0.7}Al_{50}$	0.266	302.809	2401.1	0.266	-309.717

It is also noted from table 6-4 that the ΔH predicted values indicate an endothermic reaction for all systems. This endothermic reaction is contributed by $\Delta H>0$ and $\Delta S_{vib}>0$ producing $\Delta G<0$ (negative) which is regarded to be a spontaneous reaction. The predicted values for the change in vibrational entropy

show a favourable condition for an endothermic reaction of the FeAl-X systems. We found that $Fe_{49.5}Ag_{0.5}Al_{50}$, $Fe_{49.3}Pd_{0.7}Al_{50}$ and $Fe_{49.5}Pt_{0.5}Al_{50}$ gave the phase equilibrium values of -308.947 eV/K, -310.777 eV/K and -315.206 eV/K, respectively. However, the $Fe_{49.3}Pd_{0.7}Al_{50}$ system indicates to be the most spontaneous reaction with the lowest negative change in Gibbs free energy which implies that it is easier to form at 0.7 at. % Pd at about 2398 K.

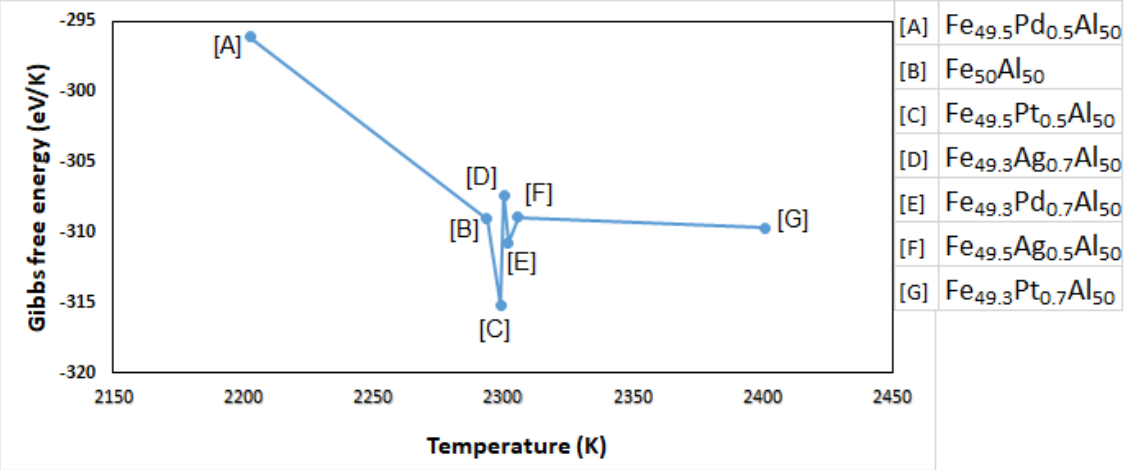

Figure 6-12: Gibbs free energy of (A) $Fe_{49.5}Pd_{0.5}Al_{50}$, (B) $Fe_{50}Al_{50}$, (C) $Fe_{49.5}Pt_{0.5}Al_{50}$ (D) $Fe_{49.3}Ag_{0.7}Al_{50}$ (E) $Fe_{49.3}Pd_{0.7}Al_{50}$ and (F) $Fe_{49.5}Ag_{0.5}Al_{50}$ and (G) $Fe_{49.3}Pt_{0.7}Al_{50}$ intermetallic at different temperatures.

6.3.3 **Analysis of elastic moduli and bulk to shear moduli**

The calculated elastic constants for the binary FeAl and ternary FeAl-X alloys are shown in figure 6-13 to 6-16. The elastic constants of FeAl-X alloys were calculated at various temperature ranges of 200 K - 2500 K. Note that the predictions of the elastic constants were calculated at equilibrium. Their elastic moduli and bulk to shear moduli (B/G) ratio of FeAl-X alloys were plotted to observe the strength of these alloys at different temperatures. More importantly to validate the stability of $Fe_{50}Al_{50}$, $Fe_{49.5}Ag_{0.5}Al_{50}$, $Fe_{49.3}Ag_{0.7}Al_{50}$, $Fe_{49.5}Pd_{0.5}Al_{50}$, $Fe_{49.3}Pd_{0.7}Al_{50}$, $Fe_{49.5}Pt_{0.5}Al_{50}$, $Fe_{49.3}Pt_{0.7}Al_{50}$ systems. The stability criteria as discussed in chapter 1 are adopted in determining the ductility and brittleness following a method proposed by Pugh [118].

C_{ij}: The β2 structure (figure 6-13a) shows that the elastic constants are stable up to 1200 K since C_{11} is greater than zero below this temperature showing a sudden

increase in C', and above 1300 K we observed instability up until 2400 K (since C_{11} is decreased). C_{11}~C_{12} suggesting a coupling of elastic moduli.

B/G: Furthermore, (figure 6-13b) indicates the precise brittleness/ductility behaviour below 1200 K. The system is ductile (B/G> 1.75) below 900K, and brittleness is observed for 900K (B/G~19). However, above this value, the system shows low values of B/G ratio. The system showed poor ductility above 1300 K.

***C_{ij}*:** In figure 6-14, it is clear that the elastic constants decrease as the temperature is increased up to 2500 K. The C_{ij} curve satisfies the stability condition for a cubic system in both 0.5 and 0.7 at. % Ag for the entire temperature range. Thus, both systems are mechanically stable. The trend for the two compositions are similar.

***B/G*:** Now in figure 6-14a, the B/G ratio increases gradually and reaches maximum ductility (B/G~9 at about 1300 K) and beyond this point we observe a decrease in ductility resulting in a parabolic behaviour. Above 1400 K we observed a reduction in ductility until it reaches brittleness at 2500 K. In figure 6-14b, the B/G increases gradually up to a maximum point (B/G~9, Temp~ 1400 K). The 0.5 and 0.7 at. % Ag showed similar trends.

***C_{ij}*:** Figure 6-15 satisfy the stability condition for a cubic system for 0.5 at. % Pd and indicating instability above 1300 K with C' of -0.42 GPa, where else at 0.7 at. % Pd showed stability for the entire temperature range. Interestingly, the trend for 0.5 and 0.7 at. % Pd are different.

***B/G*:** Now in figure 6-15a, the B/G increases and shows ductility up to (B/G~ 5, Temp~ 1200 K) and beyond this point we observe a fluctuation which may be attributed to poor ductility. In figure 6-15b, the trend is different and display maximum ductility (B/G~9, Temp~1500 K). Above 1500 K we observed a reduction showing ductility, however, the system remains ductile throughout the entire temperature range.

***C_{ij}*:** Figure 6-16 shows the addition of Pt in the system. Interestingly, the trend is the opposite of that of the Pd curve for 0.5 and 0.7 at. % addition. The curve satisfies the stability condition for a cubic system for 0.5 at. % Pt showed stability

for the entire temperature range, where else at 0.7 at. % showed instability above 1300 K with C' of -1.045 (C'<0). The elastic constants decrease as the temperature is increased leading to a coupling of C_{11} and C_{12} at about 1200 K. Thus resulting in elastic instability of C'~C_{44}~0.

***B/G*:** Now in figure 6-16a, the B/G increases reaching maximum ductility (B/G~9, Temp~1300 K) and beyond this point we observe a decrease in ductility. The structure remains ductile for the entire concentration up to 2500 K. In figure 6-16b, the B/G increases gradually up to (B/G~27, Temp~1200 K). Above 1300 K we observed a reduction in ductility until it reached brittleness at 2500 K. A possible poor ductility is observed above 1300 K due to fluctuation of B/G ratio.

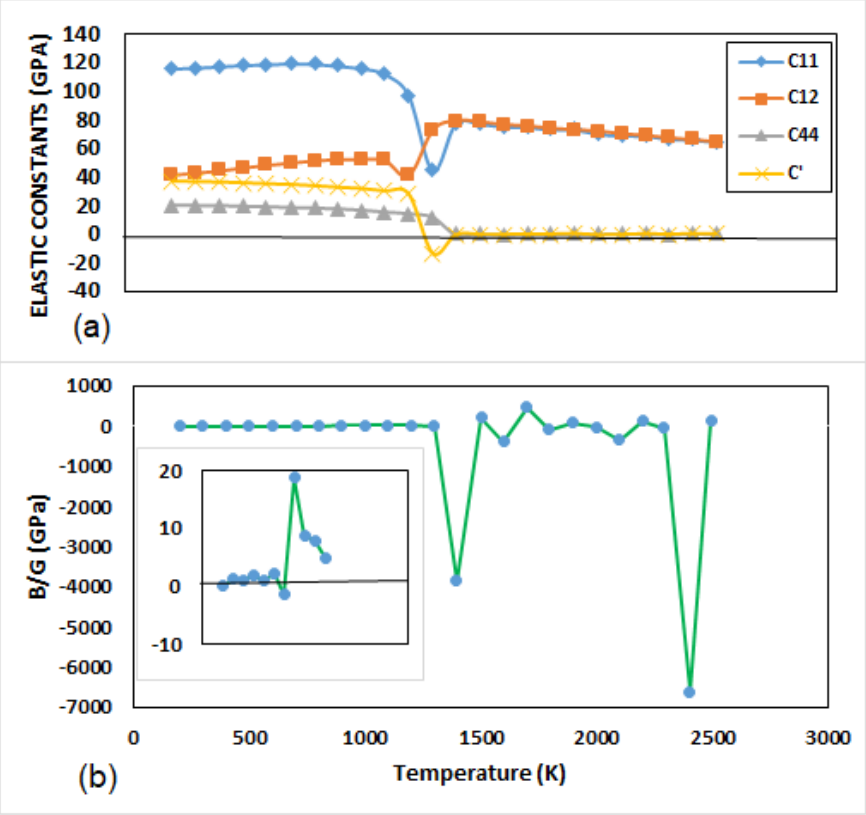

Figure 6-13: The elastic constants (GPa) of $Fe_{50}Al_{50}$ structure. The insert shows the trend between 200 K and 1200 K, the horizontal line indicates the limit of ductility/brittleness (B/G=1.75).

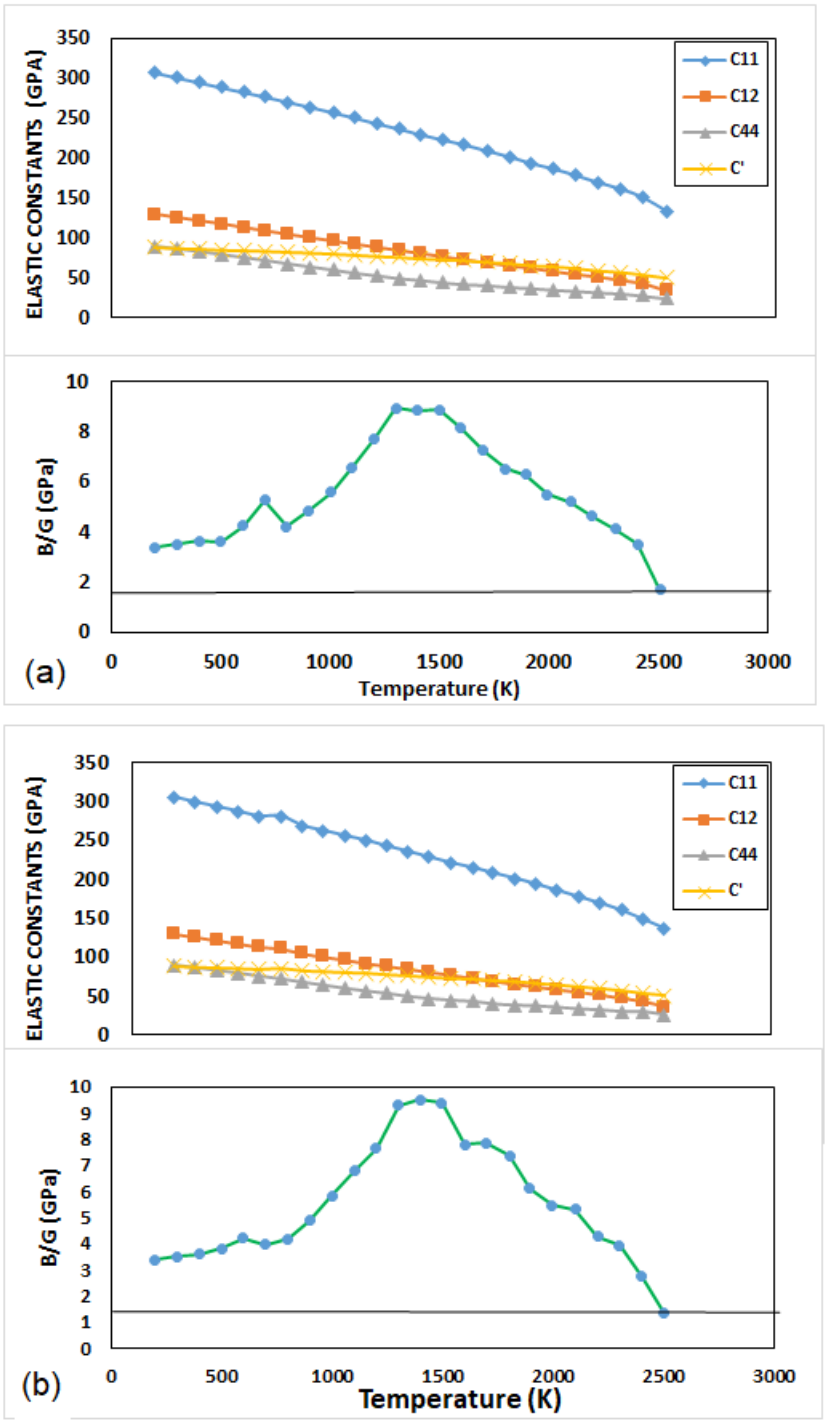

Figure 6-14: The elastic constants (GPa) for (a) $Fe_{49.5}Ag_{0.5}Al_{50}$ and (b) $Fe_{49.3}Ag_{0.7}Al_{50}$ structures, the horizontal line indicates the limit of ductility/brittleness (B/G=1.75).

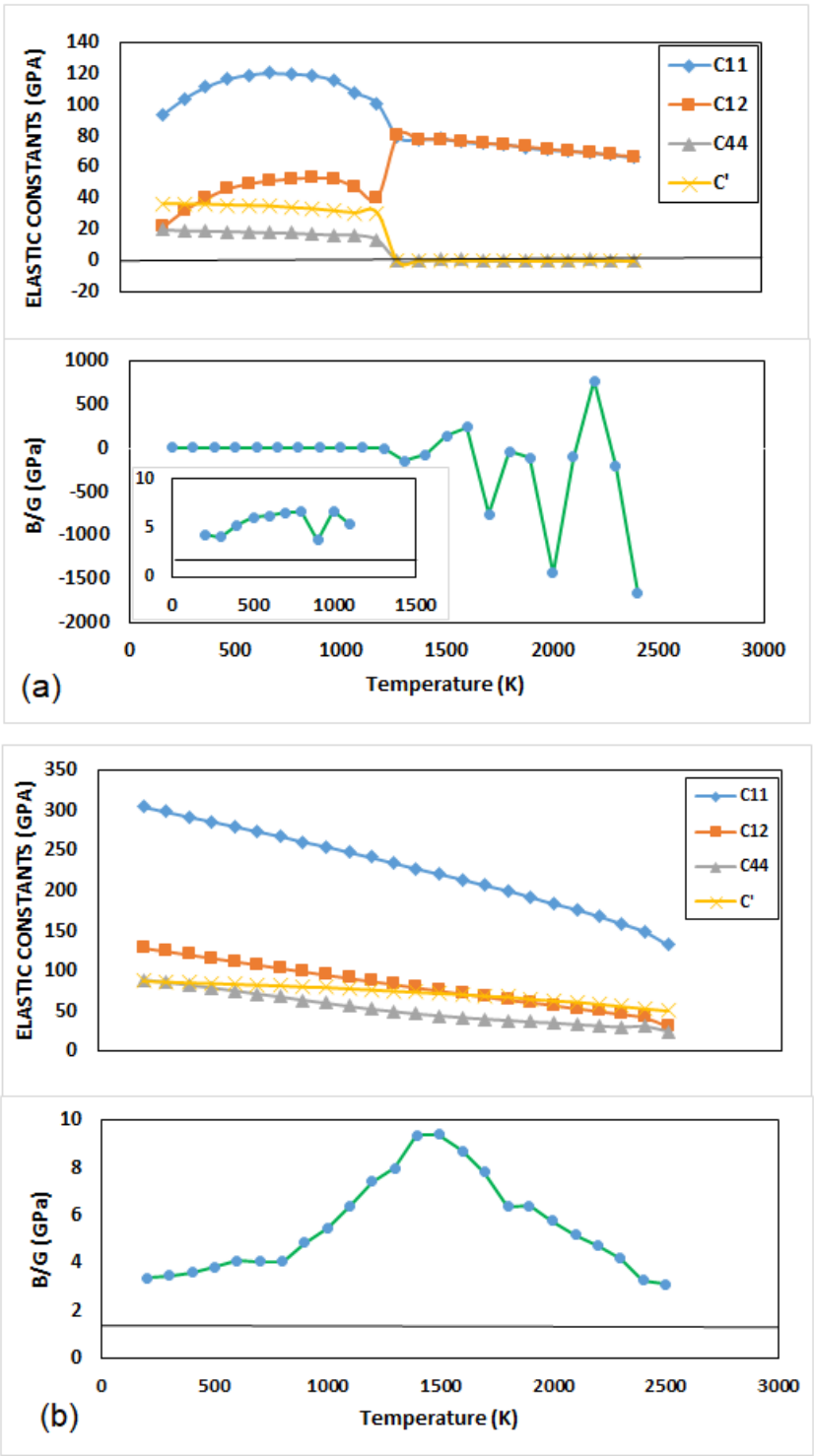

Figure 6-15: The elastic constants (GPa) for (a) $Fe_{49.5}Pd_{0.5}Al_{50}$ and (b) $Fe_{49.3}Pd_{0.7}Al_{50}$ structures. The insert in figure 6-17a shows the trend between 200 K and 1200 K, the horizontal line indicates the limit of ductility/brittleness (B/G=1.75).

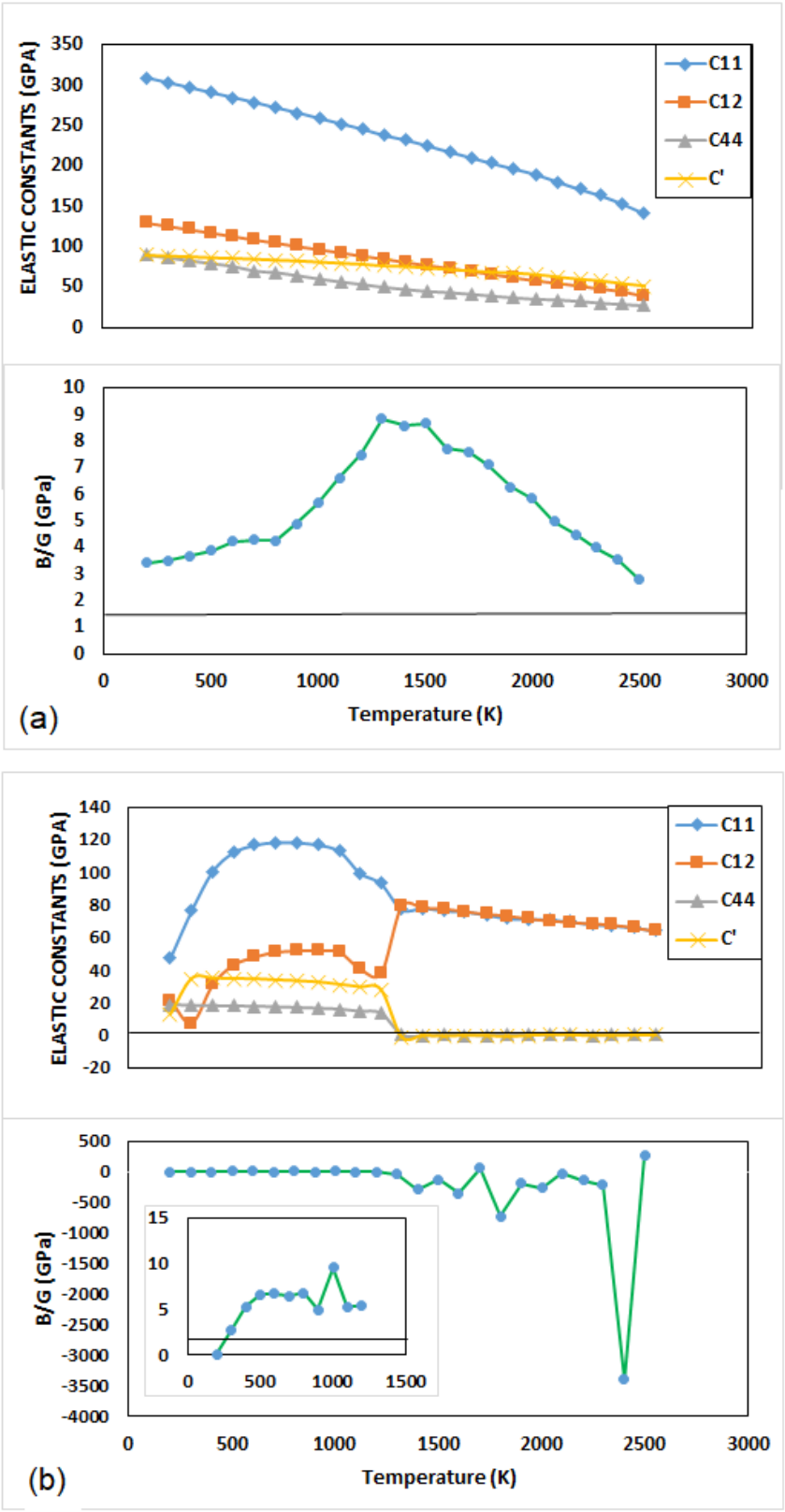

Figure 6-16: The elastic constants (GPa) for (a) $Fe_{49.5}Pt_{0.5}Al_{50}$ and (b) $Fe_{49.3}Pt_{0.7}Al_{50}$ structures. The insert in figure 6-18b shows the trend between 200 K and 1296 K, the horizontal line indicates the limit of ductility/brittleness (B/G=1.75).

6.3.4 **Radial distribution function**

An MD simulation was performed to identify melting points for binary $Fe_{50}Al_{50}$ and ternary FeAl-X systems from 100K to 2400K temperature range. The total RDF's of these systems are shown at different temperatures in figure 6-17. Lowering of temperatures on the systems increases peak sharpness implying the systems are highly structured; however, as the temperature is increased we observed broadening of peaks which implies a weakening of the systems.

The RDF pair distribution plots (a) $Fe_{50}Al_{50}$ and (b) $Fe_{49.5}Ag_{0.5}Al_{50}$ indicates that the systems are well ordered, however, at 1500K we observe a decrease in sharpness showing broadening of peaks at 1000 K and fading of peaks at 2400K decreasing the radius of the system and Weakening/melting of structures around 13 Å. We also observed that figure (c) $Fe_{49.3}Pd_{0.7}Al_{50}$ and (d) $Fe_{49.5}Pt_{0.5}Al_{50}$ shows that from 100K the systems are highly structured due to the sharp peaks and broadening of peaks at 1000 K and fading of peaks at 2400K showing a decrease in radius of the system and distribution of atoms around 10 Å.

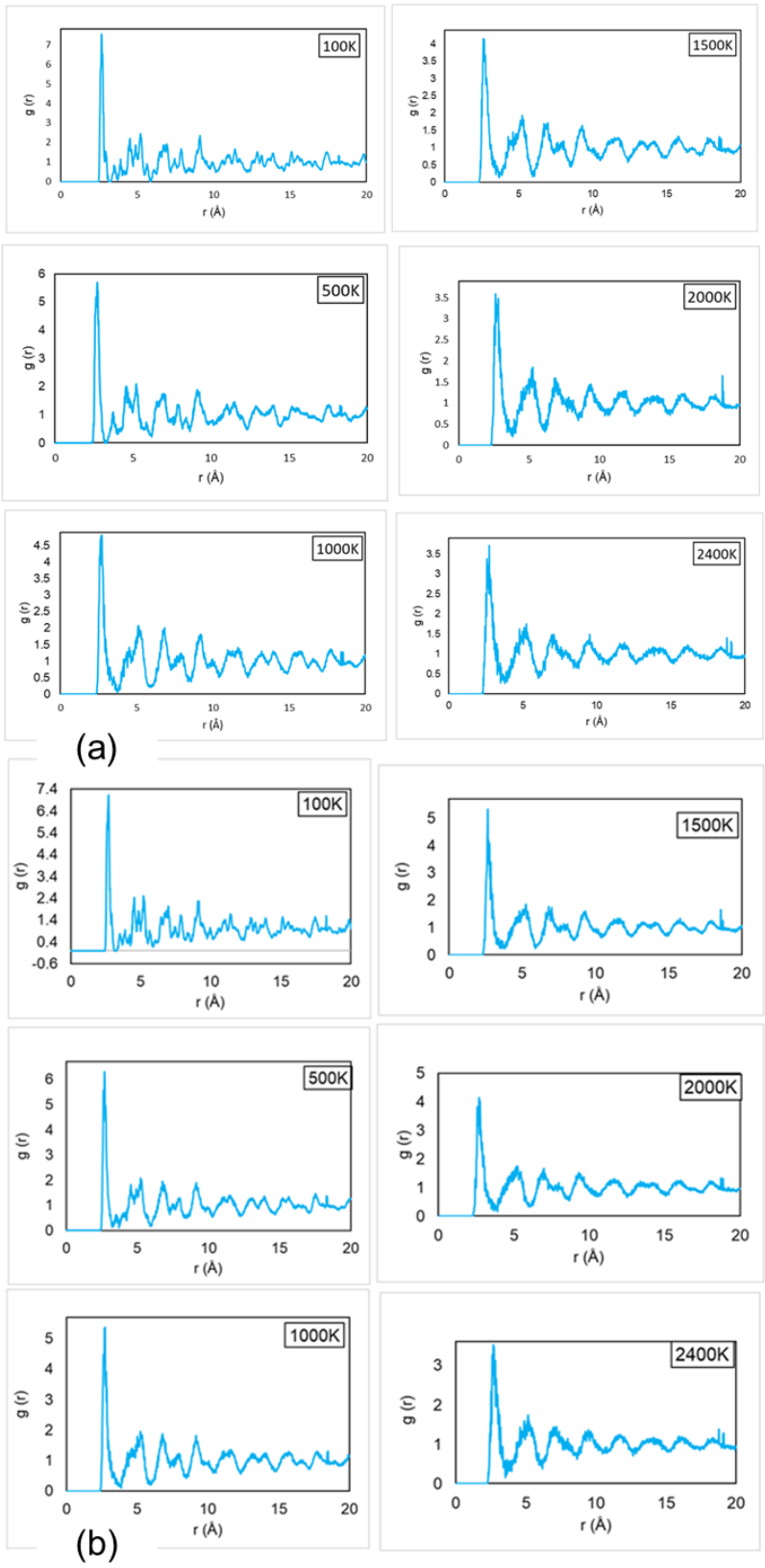

Figure 6-17: Radial distribution function of binary (a) $Fe_{50}Al_{50}$ and ternary (b) $Fe_{49.5}Ag_{0.5}Al_{50}$.

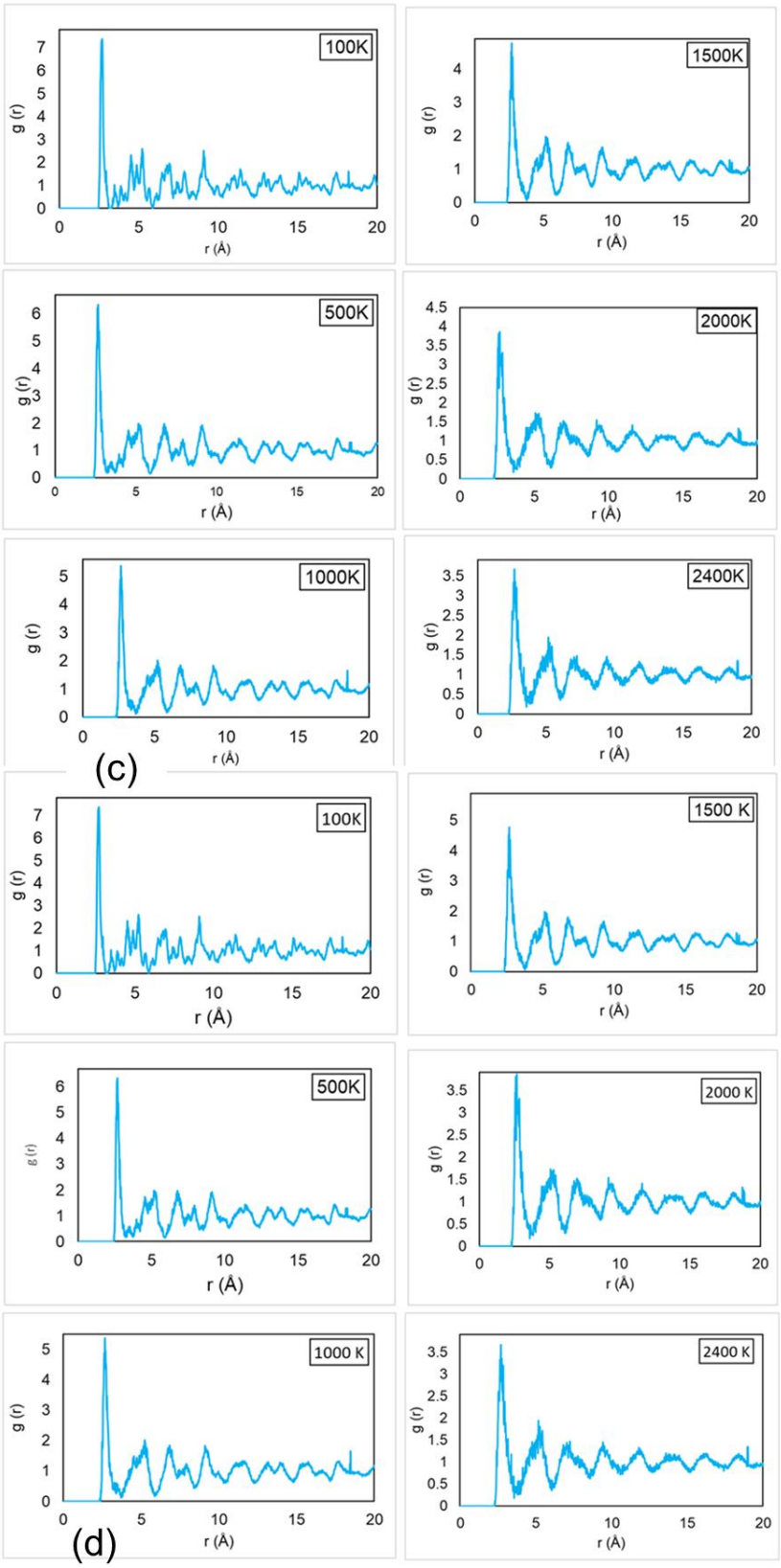

Figure 6-18: Radial distribution function of binary (c) $Fe_{49.3}Pd_{0.7}Al_{50}$ and (d) $Fe_{49.5}Pt_{0.5}Al_{50}$.

6.3.5 **X-ray diffraction pattern of $Fe_{50-x}X_xAl_x$ alloys.**

The X-ray diffraction patterns for the binary and ternary $Fe_{50}Al_{50}$, $Fe_{49.5}Ag_{0.5}Al_{50}$, $Fe_{49.3}Ag_{0.7}Al_{50}$, $Fe_{49.5}Pd_{0.5}Al_{50}$, $Fe_{49.3}Pd_{0.7}Al_{50}$, $Fe_{49.8}Pt_{0.5}Al_{50}$ and $Fe_{49.3}Pt_{0.7}Al_{50}$ compounds, are shown in Figure 6-17, 6-18, 6-19 and 6-20. This XRD is primarily used for phase identification and possible transformation occurring at increasing temperature. The intensity peak of every system differs according to the effect of the various doping concentrations and different dopants. Thus we evaluate the effect of Ag, Pd, and Pt for 0.5 and 0.7 at. % composition and establish different trends.

Firstly, the most noticeable pattern was the high-intensity peaks at about 17 a.u and 41 a.u on the binary β2 $Fe_{50}Al_{50}$ (figure 6-17). We see that the structure is preserved up to a higher temperature of 2400 K and deformed above this temperature. The XRD pattern confirmed that the structure did not configure or change the symmetry.

Secondly, the high-intensity peaks are observed at about 17 a.u and 41 a.u for the ternary $Fe_{49.5}Ag_{0.5}Al_{50}$ and $Fe_{49.3}Ag_{0.7}Al_{50}$ compound. The XRD pattern is confirming that the structures did not change, showing a similar trend as the undoped system. The small amount of Ag concentration doped on the system is negligibly small.

Thirdly, we see that the addition of 0.5 and 0.7 at. % Pd show similar XRD pattern displaying high-intensity peaks at about 17 a.u and 41 a.u for the ternary $Fe_{49.5}Pd_{0.5}Al_{50}$ and $Fe_{49.3}Pd_{0.7}Al_{50}$. The XRD pattern also confirmed that the structures did not change the symmetry as Pd content was introduced.

Lastly, figure 6-20 shows a similar pattern with high-intensity peaks at about 17 a.u and 41 a.u on the ternary $Fe_{49.5}Pt_{0.5}Al_{50}$ and $Fe_{49.3}Pt_{0.7}Al_{50}$. The XRD pattern confirmed that addition of 0.5 and 0.7 at. % Pt did not change the symmetry, this may be attributed to the small amount of Pt concentration doped on the system.

In general, it was observed that the XRD patterns preserved the β2 $Fe_{50}Al_{50}$ structure. The dopants (0.5 and 0.7 at. %) did not influence the structure. All doped systems showed that the structure is not perturbed or changed as the temperature is increased up to 2400 K.

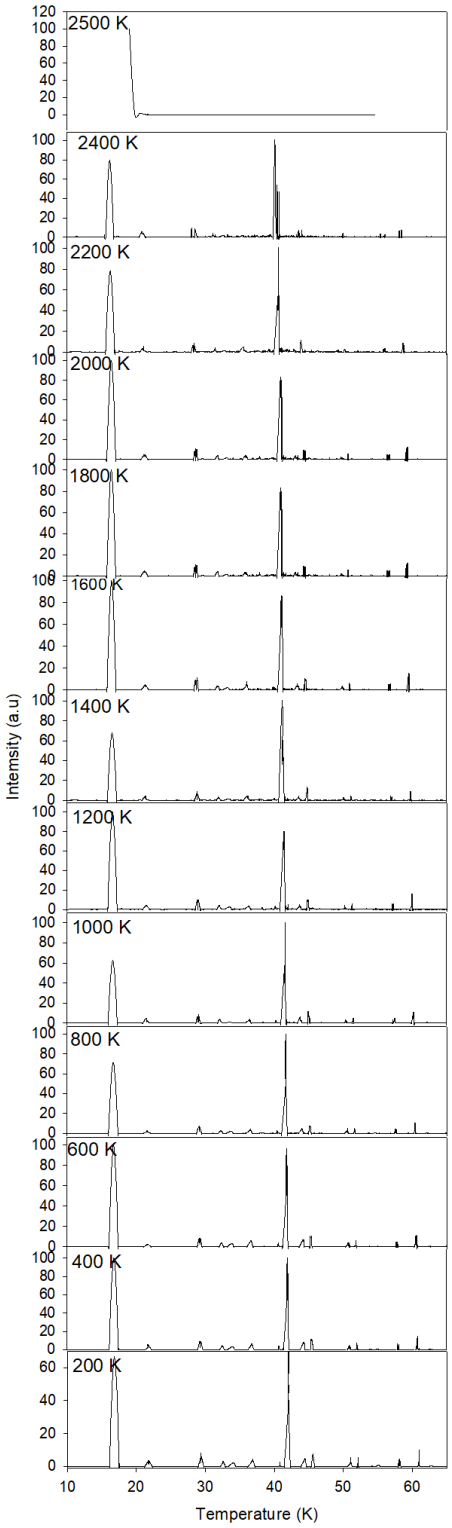

Figure 6-19: X-Ray diffraction pattern of $Fe_{50}Al_{50}$ system.

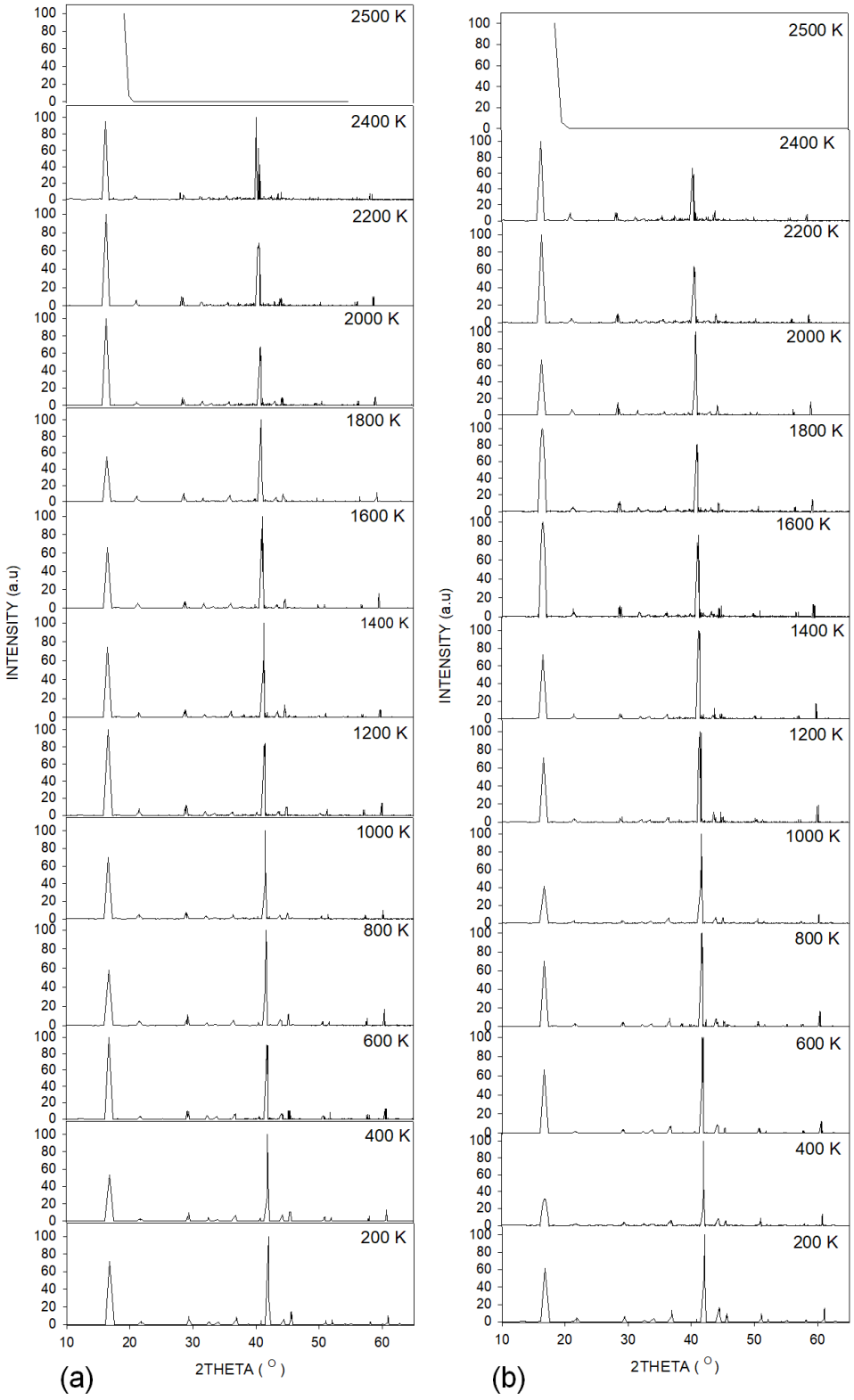

Figure 6-20: X-Ray diffraction pattern of (a) $Fe_{49.5}Ag_{0.5}Al_{50}$ and (b) $Fe_{49.3}Ag_{0.7}Al_{50}$ systems.

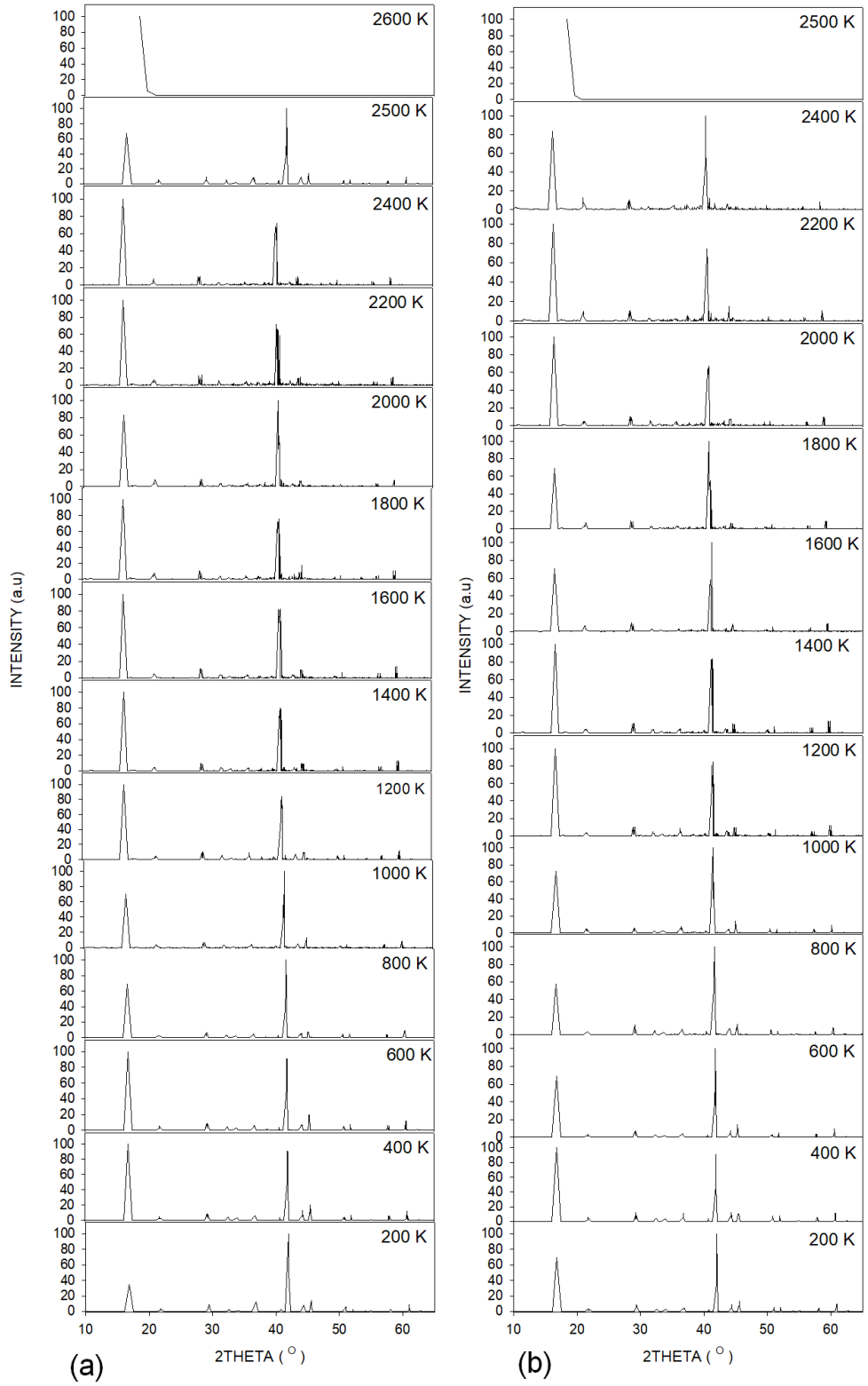

Figure 6-21: X-Ray diffraction pattern of (a) $Fe_{49.5}Pd_{0.5}Al_{50}$ and (b) $Fe_{49.3}Pd_{0.7}Al_{50}$ systems.

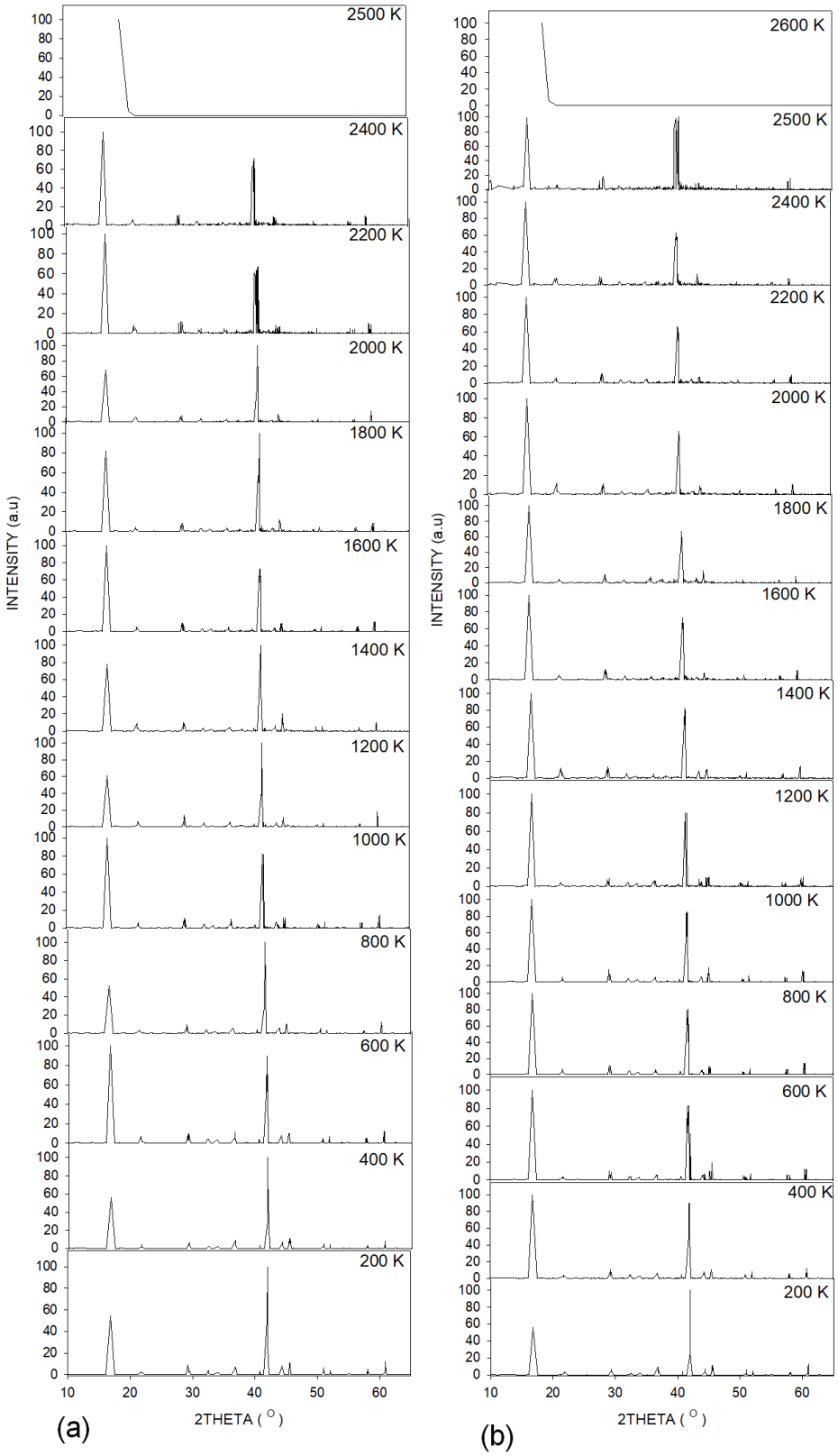

Figure 6-22: X-Ray diffraction pattern of (a) $Fe_{49.5}Pt_{0.5}Al_{50}$ and (b) $Fe_{49.3}Pt_{0.7}Al_{50}$ systems.

Chapter 7

SUMMARY AND CONCLUSION

In this chapter, we give a summary and conclusion of the important aspects for both the study of binary Fe-Al and ternary FeAl-X (X: Ag, Ru, Pd, and Pt) alloys. We employed two approaches i.e. Density functional theory was used to investigate the structural, electronic and mechanical properties of Fe-Al and FeAl-X systems; Molecular dynamics was used to study temperature dependence employing the LAMMPS code.

This chapter is sketched in order to display all achieved objectives by validating previous experimental work with the present findings. In order to ascertain that our calculations are reliable, we determined the convergence test to establish appropriate cut-off energy and k-point mesh parameters, Optimization of both binary and ternary systems by allowing all degrees of freedom to vary. Note that the ternary systems were constructed by varying the concentrations and predicting their structural stabilities. Furthermore, analysis of mechanical, thermodynamic, structural and electronic properties of each phase. For detailed clarity and providing a scientific view, the background and literature review on previous work and current work has been validated.

Calculations were performed using a very efficient computational software code CASTEP embedded within Materials studio and VASP and PHONON codes as implemented in the MedeA software. A binary Fe-Al phase diagram was considered; namely, FeAl, $FeAl_2$, Fe_3Al, Fe_4Al_{13}, Fe_5Al_8 and Fe_2Al_5. Full structure optimisation was performed to investigate the ground state energies as well as to determine the equilibrium cell parameters of these systems, elastic constants, heat of formation, DOS, phonons and XRD pattern of Fe-Al The binary Fe-Al alloys serve as a benchmark for the study of $Fe_{50-X}X_xAl_{50}$ ternaries in identifying the most stable system for alloying. Similar calculations were determined of Ag, Ru, Pd, and Pt doped on binary FeAl intermetallic. Both the binary Fe-Al and ternary $Fe_{50-X}X_xAl_{50}$ alloys calculations were performed using DFT within the GGA-PBE.

Amongst the considered phases (FeAl, Fe_4Al_{13}, Fe_5Al_8, $FeAl_2$, Fe_2Al_5 and $FeAl_3$), the most stable intermetallic phase was found to be FeAl. The heats of formation are important for determining the most stable system through the construction of the solid common-tangent line to illustrate the phase with the lowest energy. The Fe-Al phase diagram was used as a benchmark for validating the existence of these phases. For best results to be obtained, these intermetallic compounds consist of two possible sites for doping preference, the Fe-rich compounds (Fe_2Al and Fe_3Al) and Al-rich compounds ($FeAl_2$, Fe_2Al_5, Fe_5Al_8, Fe_4Al_{13} and $FeAl_3$).

Chapter 3: A systematic DFT calculation has been performed and gave consistent results on the stability of Fe-Al alloys. The FeAl phase was found to be the most stable in agreement with the binary phase diagram. Furthermore, the shear modulus (C') of the β2 FeAl phase along with Fe_4Al_{13}, Fe_2Al_5, Fe_5Al_8 were found to be positive fulfilling the condition of stability. The monoclinic structure Fe_4Al_{13} was also confirmed to be stable with a significant difference from the FeAl. This observation was confirmed from the total DOS, where the Fe_4Al_{13} showed a Fermi level falling in the pseudogap, condition of stability.

In Chapter 4: The equilibrium lattice parameter, heats of formation, elastic properties and electronic structure of the β2 FeAl phase were determined using Ab-initio calculations. Interestingly, the β2 FeAl at 50:50 was found to be energetically and mechanically stable over the other phases at different compositions. These phases exist in the range between 23 and 55 atomic percent Al of the experimental phase diagram. The DFT results were in good agreement with the experimental findings. It was found that the FeAl structure was more stable (lowest heats of formation) and VCA showed a preference of doping on Fe rather than Al-sub-lattices: $Fe_{48.8}Al_{50}Ru_{0.2}$ and $Fe_{49.5}Al_{50}Pt_{0.5}$; and finally the DOS showed that the Fermi level fell in the pseudogap which demonstrates the condition of stability.

The DFT results were in good agreement with the experimental findings. $Fe_{48.50}Al_{50}Ag_{0.5}$, $Fe_{48.80}Al_{50}Pd_{0.2}$, $Fe_{48.50}Al_{50}Pt_{0.5}$ and $Fe_{49.80}Al_{50}Ru_{0.2}$. These phases exist in the range between 50 and 100 atomic percent Al of the experimental phase diagram. The shear modulus (C') of the B2 $Fe_{50}Al_{50}$ and

$Fe_{49.80}Al_{50}Ru_{0.2}$ phases are found to be positive, satisfying the condition of stability, whereas, for $Fe_{48.50}Al_{50}Pt_{0.5}$, the C' showed condition of instability at 0.3 at. %. The fcc bulk β2 FeAl structure was found to have lattice parameters of 2.852 Å which is in good agreement with the experimental value of 2.908 Å. The Brillouin zone integrations were performed for suitable of k-points of 10 X 10 X 10 before and after doping. Minimization of forces and stress tensors was achieved by optimization of structural parameters (atomic positions and lattice parameters).

Chapter 5: To correlate the thermodynamic stability of the Fe-Al system, we compared their total density of states (tDOS) plots and literature stated that the DOS of structures of the same composition can be used to mimic the stability trend with respect to their behaviour at the E_f (Fermi level), whereby the structure with the highest and lowest density of states at E_f is considered the least and most stable, respectively. Furthermore, it was established that additions of 0.2 at. % Ru/Pd to a Fe-50 at. % Al and 0.5 at % Pt/Ag to a Fe-50 at. % alloy improved the corrosion and oxidation resistance of the Fe-Al alloys. Clearly that Ru/Pd and Pt/Ag are the most preferred alloying elements since their B/G ratio is greater (B/G > 1.75) at composition 6.25 – 43.75 at. % Pt and 6.25 – 25.00 at. % Ru.

Chapter 6: The change in Gibbs free energy, lattice parameters, elastic properties, and X-ray diffraction pattern of the $Fe_{50}Al_{50}$ and ternary $Fe_{50-X}M_XAl_{50}$ phase were determined using LAMMPS code. We found that the transformation temperature entirely depends on the concentrations and alloying elements. This was evident for Pd doping where a transformation at 0.5 and 0.7 at. % was about 2400 K and 2500 K, respectively. A similar observation for Ag and Pt dopant was seen. It was also deduced that the Pt (0.5 %) and Pd (0.7 %) dopant influence the elastic instability above 1200 K while elastic stability is attained for all the other systems. The XRD confirmed that the doped systems preserved the structural symmetry as expected since only a small amount of alloying elements was used. At higher temperatures above 2400 K, the cubic structure is lost (the structural change was observed), this observation is in line with the lattice expansion analysis.

The $Fe_{49.5}Ag_{0.5}Al_{50}$, $Fe_{49.3}Ag_{0.7}Al_{50}$, $Fe_{49.5}Pd_{0.5}Al_{50}$, $Fe_{49.3}Pd_{0.7}Al_{50}$, $Fe_{49.5}Pt_{0.5}Al_{50,}$ and $Fe_{49.3}Pt_{0.7}Al_{50}$ systems were found to be in good agreement and satisfy the stability criterion.

The $Fe_{50}Al_{50}$ structure was found to be the most stable with the lowest change in Gibbs free energy. Interestingly, the $Fe_{49.3}Pt_{0.7}Al_{500}$ was found to be energetically and mechanically stable over the other phases at different compositions. The shear modulus (C') of the β2 $Fe_{50}Al_{50}$ and $Fe_{49.5}Ag_{0.5}Al_{50}$, $Fe_{49.3}Ag_{0.7}Al_{50}$, $Fe_{49.5}Pd_{0.5}Al_{50}$, $Fe_{49.3}Pd_{0.7}Al_{50}$, $Fe_{49.5}Pt_{0.5}Al_{50,}$ and $Fe_{49.3}Pt_{0.7}Al_{50}$ phases are found to be positive, satisfying the condition of stability.

The binary systems showed that the FeAl, Fe_4Al_{13}, Fe_2Al_5, Fe_5Al_8 were found to be mechanically stable fulfilling the condition of stability and ductile systems. Whereas ternary alloying using VCA model showed that $Fe_{49.50}Al_{50}Pt_{0.5}$ () as most ductile structure. Furthermore, ternary alloying (supercell approach) on the Fe sub-lattice, prefers Fe6.25Al50Pt43.75 (3.504) and $Fe_{25}Al_{50}Ru_{25}$ (3.504), while on the Al sub-lattice $Fe_{50}Al_{12.5}Pt_{37.5}$ (3.092), $Fe_{25}Al_{50}Ru_{25}$ (3.399) are most ductile systems. Lastly temperature dependence revealed $Fe_{49.3}Al_{50}Pd_{0.7}$ (figure 6-15 (b)), $Fe_{49.5}Al_{50}Pt_{0.5}$ (figure 6-16 (a)) as ductile systems. it can be concluded that doping with Pt, Pd, Ru and Ag has a significant potential to enhance the ductility at 0 K. and high temperature 873 K.

Recommendations and future work

The study of ternary alloying remains relevant in the improvement of high-temperature applications.

In this study (chapter 5), we have demonstrated the significance of partial substitution of the $Fe_{50-X}X_xAl_{50}$ ($0 \leq x \leq 50$) compound. In particular, the β2 phase has been investigated. Various phase systems have been suggested, studied and validated with previous work. The findings have shown similar trends in the growth and stability criteria. However, the intensity of the doped Ru system was very similar to the binary FeAl phase.

To conclude chapter 4: To accurately mimic the transition/melting temperature, we analyse the of XRD patterns and mechanical properties at temperature range 200 K – 3000 K. Firstly, various $Fe_{50-X}X_xAl_{50}$ structures were generated using VCA approach. Thus, other compositions with small X_x were explored. The XRD pattern confirmed the structure and the fact that it did not change which was attributed to the small amount of Pt, Pd, Ru, Ag concentrations which dissolved into the structure. Most notable cases were the high-intensity peak at about 32 a.u and 70 a.u.

Chapter 6 concludes that the LAMMPS code was used to perform the temperature dependence while the XRD patterns were determined using the reflex tool in the Material studio to evaluate the phase constituency. The temperature variation against lattice parameters, elastic constants and X-ray diffraction patterns of the β2 and FeAl-X was studied at different temperature ranges.

Further recommendations: For future purposes this work will be expanded to study surface interaction with water and oxygen, intently on the stable systems. The surface energy and adsorption energy will be deduced to understand the interaction behavior.

APPENDIX A

Transformation of $Fe_{50-X}M_XAl_{50}$ systems observed using LAMMPS code

1. **$Fe_{50}Al_{50}$**

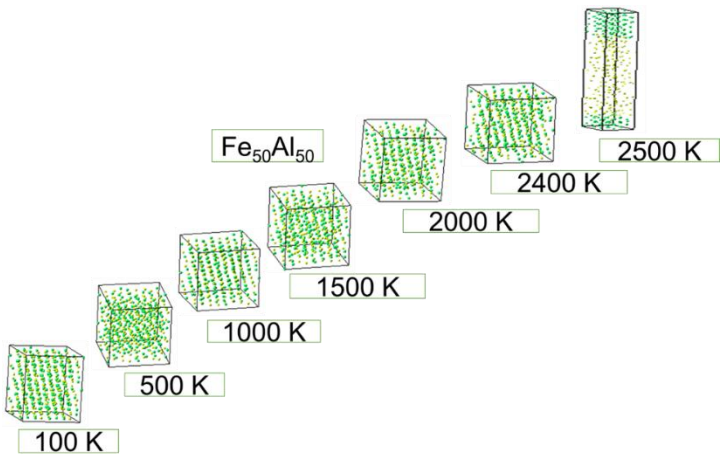

2. **$Fe_{49.5}Ag_{0.5}Al_{50}$**

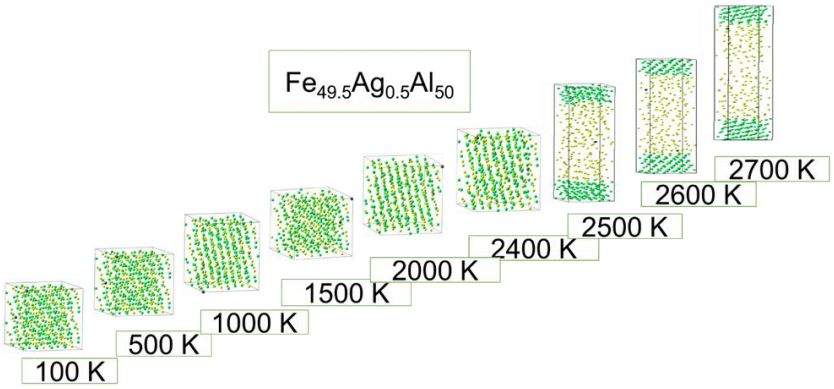

3. $Fe_{49.3}Pd_{0.7}Al_{50}$

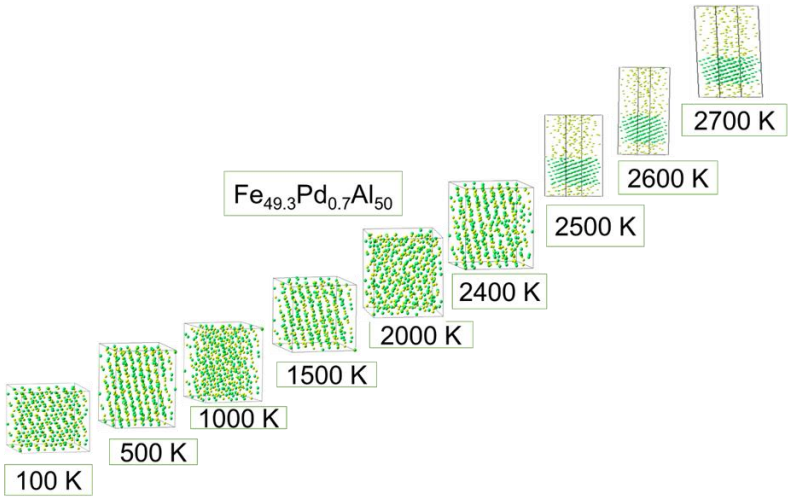

4. $Fe_{49.5}Pt_{0.5}Al_{50}$

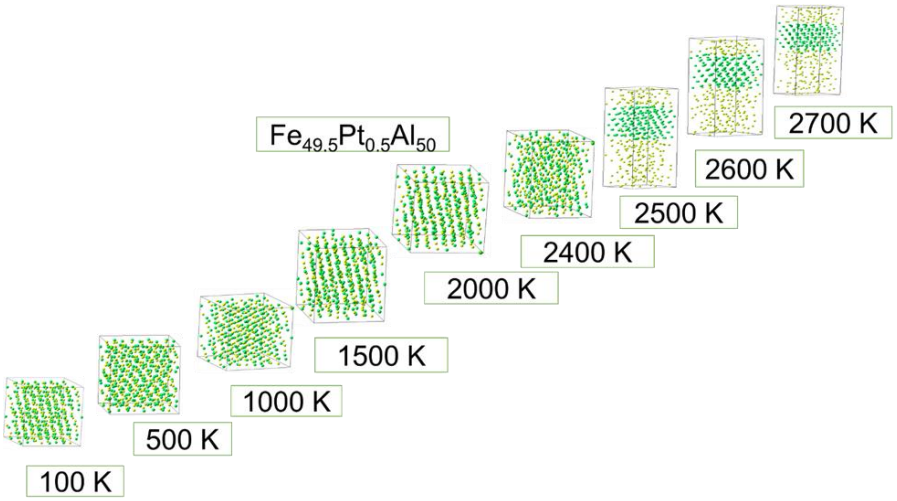

APPENDIX B

Publications

1. C.S. Mkhonto, H.R. Chauke and P.E. Ngoepe “First-principles studies of Fe-Al-X (X=Pt, Ru) alloys”, *The Journal of the Southern African Institute of Mining and Metallurgy* Vol. 117, 2017, P 1-6.
2. C.S. Mkhonto, H.R. Chauke and P.E. Ngoepe “Thermodynamic stability of doped FeAl-X (X = Pd, Ag, Pt, and Ru) systems”, *Materials Science and Engineering*, 2018, vol. 430, P 1-7.
3. C.S. Mkhonto, H.R. Chauke and P.E. Ngoepe “A molecular dynamic study of $Fe_{50-X}M_XAl_{50}$ ternary alloy (M= Ag, Pt, Pd)”, MRS Advances, 2020, vol. 177, P 1-9.

Awards

1. 2016 obtained 2nd prize for Masters oral presentation at the Faculty of Science and Agriculture conference.

2. In 2018 obtained an award for Runner up in Master's oral presentation at the CoSAami conference.

3. Obtained 2nd prize for Masters Poster presentation at SAIP conference 2019.

4. Obtained 1st prize for Masters oral presentation at Faculty of Science and Agriculture conference in 2019.

5. Obtained 1st prize for Masters Poster presentation at CoSAami conference 2019.

APPENDIX C

Papers Presented at Conferences

1. C.S. Mkhonto, H.R. Chauke and P.E. Ngoepe “High Temperature and Phase Transformation Studies of Pt_3Al Compounds” 4-8 July 2016, South African Institute of Physics Conference, University of Cape Town, Cape Town, South Africa.

2. C.S. Mkhonto, H.R. Chauke and P.E. Ngoepe “Computational Modelling Studies of Fe-Al alloys” Post Graduate Research day, 29-30 September 2016, Bolivia Lodge, Polokwane, South Africa.

3. C.S. Mkhonto, H.R. Chauke and P.E. Ngoepe “Computational studies of Fe-Al Alloys”, South African Institute of Physics Conference, 3-7 July 2017, University of Stellenbosch, Cape Town, South Africa.

4. C.S. Mkhonto, H.R. Chauke and P.E. Ngoepe “Computational Simulation of FeAl-X (X=Pt, Ru)”, Post Graduate Research day, 20-21 October 2017, Bolivia Lodge, Polokwane, South Africa.

5. C.S. Mkhonto, H.R. Chauke and P.E. Ngoepe “Principles of Simulation on FeAl-X (X=Pt, Ru)”, Centre for High-Performance Computing National Meeting, 3-7 December 2017, Velmoré Hotel Estate, Pretoria, South Africa.

6. C.S. Mkhonto, H.R. Chauke and P.E. Ngoepe “Computational Principles on FeAl-X (X=Pt, Ru)”, African Materials Research Society, 11-14 December 2017, Gaborone Botswana ICC, Africa.

7. C.S. Mkhonto, H.R. Chauke and P.E. Ngoepe “The effect of (M= Ag/Pd/Pt) on $Fe_{50-x}M_xAl_{50}$ doping at high temperature: A supercell approach”, Advanced Metal Initiative, 22-25 October 2019, Riverside sun, Vanderbijlpark, South Africa.

REFERENCES

[1] G. Inden and W. Pepperhoff, “Experimental study of the order: disorder transition in bcc Fe-Al alloys,” *Z. Metallkd,* vol. 81, pp. 770-773, 1990.

[2] E. Huape-Padilla, M. Sánchez-Carrillo, J.P. Flores-de los Rios, M.A. Espinosa-Medina, R.G. Bautista-Margulis, M. I. Ferrer-Sánchez, G. Carbajal-de la Torre, L. Bejar-Gómez, J. G. Chacón-Nava1 and A. Martínez-Villafañe, “Corrosion study of Fe-Al Intermetallic Alloys in Simulated Acid,” *Int. J. Electrochem. Sci.,* vol. 10, pp. 2141- 2154, 2015.

[3] S. Frangini, “Corrosion Behaviour of AISI 316L Stainless Steel and ODS FeAl Aluminide in Eutectic Li2CO3–K2CO3 Molten Carbonates under Flowing CO2–O2 Gas Mixture,” *Oxid. Met.,* vol. 53, pp. 139-156, 2000.

[4] X. Li, A. Scherf and M. Heilmaier, “The Al-rich part of the Fe-Al phase diagram,” *J. Phase Equilib. Diff.,* vol. 37, pp. 162-173, 2016.

[5] R. A. Rodríguez-Diaz, J. Uruchurtu-chavarín, A. Molina-Ocampo, J. Porcayo-Calderon, M. E. Mendoza, S. Valdez, J.Juárez-Islas, “Hot corrosion behavior of FeAl intermetallic compound modified with silver in molten salt mixture,” *Int. J. Electrochem. Sci.,* vol. 8, pp. 11877-11895, 2016.

[6] R.A. Couperthwaite, L.A. Cornish, I.A. Mwamba and M.J. Papo, “Effect of processing route on the microstructure and properties of an Fe-Al Alloy with additions of precious metal,” *Mater. Tod.,* vol. 2, pp. 3932-3942, 2015.

[7] R. Kant, U. Prakash, V, Agarwala and V. V. Satya Prasad, “Effect of carbon and titanium additions on mechanical properties of B2 FeAl,” *Trans. Indian Inst. Met.,* vol. 69, pp. 845-850, 2016.

[8] W. Kohn and L. J. Sham, “Self-consistent equations including exchange and correlation effects,” *Phys. Rev.,* vol. 140, pp. 1133 -1138, 1965.

[9] J.P. Perdew, K. Burke and M. Ernzerhof, “Generalized gradient approximation made simple,” *Phys. Rev. Lett.,* vol. 77, pp. 3865 -3868, 1996.

[10] K. Parlinski, Z. Q. Li and Y. Kawazoe, *Phys. Rev. Lett.,* vol. 81, pp. 3298-, 1998.

[11] A. Togo and I. Tanaka, “First principles phonon calculations in materials science,” *Scripta Materialia,* vol. 108 , p. 1–5, 2015.

[12] N.J. Ramer and A.M. Rappe, “Application of a new virtual crystal approach for the study of disordered perovskites,” *J. Phys. and Chem. of Solids,* vol. 61, pp. 315-320, 2000.

[13] D.J. Schaeffler, “An overview of austenitic and ferritic stainless steels,” *Eng. Qual. Solutions Inc.,* vol. 1, pp. 1-10, 2017.

[14] M.C.J. Marker, L.I. Duarte, C. Leinenbach and K.W. Richter, “Characterization of the Fe-rich corner of Al-Fe-Si-Ti,” *Intermetallics,* vol. 39, pp. 38-49, 2013.

[15] F. Stein, S.C. Vogel, M. Eumann and M. Palm, “Determination of the crystal structure of the e phase in the Fe-Al system by high-temperature neutron diffraction,” *Mater. Sci. Phys. Mech.,* vol. 18, pp. 10-16, 2010.

[16] I. Bednarczyk, D. Kuc and G. Niewielskid, “Influence of cumulative plastic deformation on microstructure of the Fe-Al intermetallic base alloy, Archives of metallurgy and Materials,” *Arch. Metall. Mater.,* vol. 59, pp. 988-991, 2014.

[17] M. Zamanzade, A. Barnoush and C. Motz, “A review on the properties of Iron Aluminide intermetallics,” *Crystals,* vol. 6, pp. 1-29, 2016.

[18] K. Tobita, N. Sato, K. Kitahara, Y. Takagiwa and K. Kimura, “Effect of anomalous crystal structure of Iron Aluminides Fe2Al5 and Fe4Al13: low lattice thermal conductivity and potentiality as thermoelectric materials.,” *Mater. Trans.,* vol. 57, pp. 1045-1049, 2016.

[19] P.A. Ferreiros, P.R. Alonso, P.H. Gargano and P.B. Bozzano, “Characterization of microstructures and age hardening of Fe1−2xAlxVx alloys,” *Intermetallics,* vol. 50, pp. 65-78, 2014.

[20] H.R. Chauke, “PhD thesis,” University of Limpopo, Polokwane, 2005.

[21] S.C. Vogel, F. Stein, and M. Palm, “Investigation of the ϵ phase in the Fe-Al system by high-temperature neutron diffraction,” *Int. J. Mater. Res.,* vol. 98, pp. 580-588, 2007.

[22] C. Colinet, “Ab-initio calculation of enthalpies of formation of intermetallic,” *Intermetallics,* vol. 11, pp. 1095-1102, 2003.

[23] F. Stein and M. Palm, “Re-determination of transition temperatures in the Fe–Al system by differential thermal analysis,” *Int. J. Mater. Res.,* vol. 98, pp. 580-588, 2007.

[24] M.M. Atabaki, M. Nikodinovski, P. Chenier, J. Ma, M. Harooni and R. Kovacevic, “Welding of Aluminium to steels: an overview,” *J. Manuf. Sci. Prod.,* vol. 14, pp. 2191-4184., 2014.

[25] L. Bellaiche and D. Vanderbilt, “Ab-initio calculation of complex processes in materials,” *Phys. Rev.,* vol. 58, pp. 7877-7882, 2000.

[26] P. Matysik, S. Jóźwiak and T. Czujko, “Characterization of Low-Symmetry Structures from Phase Equilibrium of Fe-Al System—Microstructures and Mechanical Properties,” *Mater.,* vol. 8, pp. 914- 931, 2015.

[27] S. Slawik, C. Pauly and F. Mücklich, “Experimental investigation of phase equilibria in the Ru–Fe–Al system at 1473 K,” *Intermetallics,* vol. 64, pp. 96-101, 2015.

[28] I. Shishkovsky, F. Missemer, N. Kakovkina and I. Smurov, “Intermetallics synthesis in the Fe–Al system via layer by layer 3D laser cladding,” *Crystals,* vol. 3, pp. 517-529, 2013.

[29] R. Nakamura, K. Takasawa, Y. Yamazaki and Y. Lijima, “Single-phase interdiffusion in the B2 type intermetallic compounds NiAl, CoAl and FeAl.,” *Intermetallics,* vol. 10, pp. 195-204, 2002.

[30] B.I. Min, T. Oguchi, H.J.F. Jansen and A.J. Freeman, “Structural, electronic and magnetic properts of NiAl and FeAl alloys,” *J. Magn. Magn. Mater,* Vols. 54-57, pp. 1091-1092, 1986.

[31] H. I. Sozen, T. Hickel and J. Neugebauer, “Ab-initio investigations of point and complex defect structures in B2 FeAl,” *Max-Planck-institut fur eisenforchung GmbH, Mx-Planck-Str. 1, 40237 Dusseldorf, Germany.,* pp. 1-11, 2021.

[32] M. Grujicic, J. S. Snipes, S. Ramaswami, R. Galgalikar, C. F. Yen and B. A. Cheeseman, “Computational analysis of the intermetallic formation during the dissimilar metal aluminium-to-steel friction stir welding process.,” *J. Mater. Desin and application,* vol. 233, pp. 1080-1100, 2016.

[33] R.A. Couperthwaite, L.A. Cornish and I.A. Mwamba, “Cold-spray coating of Fe-40 at. % Al alloy with additions of ruthenium,” *J. S. Afr. Inst. Min. Metall.,* vol. 116, pp. 2411-9717, 2016.

[34] X. Zhu, Z. Yao, X. Gu, W. Cong and P. Zhang, “Microstructure and corrosion resistance of Fe-Al intermetallic coating on 45 steel synthesized

by double glow plasma surface alloying technology," *Trans. Nonferrous Met. Soc. China.,* vol. 19, pp. 143-148, 2009.

[35] C. S. Mkhonto, H. R. Chauke and P. E. Ngoepe, "First-principles studies of Fe-Al-X (X=Pt, Ru) alloys," *J. S Afr. Inst. Min. Metall.,* vol. 117, pp. 1-6, 2017.

[36] C. S. Mkhonto, H. R. Chauke and P. E. Ngoepe, "Thermodynamic Stability of doped FeAl-X (X = Pd, Ag, Pt and Ru) systems," *Mater. Sci. Eng.,* vol. 430, pp. 1-7, 2018.

[37] C. Blaas, J. Redinger, S. Manninen, V. Honkimaki, K. Hamalainen and P. Suortti, "High resolution compton scattering in Fermi surface studies: application to FeA1," *Phys. Rev. ,* vol. 75, pp. 184-187, 1995.

[38] T. Cheng, X. Lang, G. Han, R. Yao, Z. Wen and Q. Jiang, "Nanoporous (Pt1-xFex)3Al intermetallic compounds for greatly enhanced oxygen electroreductioncatalysis," *J. Mater. Chem.,* vol. 48, pp. 18878-18884, 2016.

[39] G. Salinas, J. G. Gonzalez-Rodriguez, J. Porcayo-Calderon, V. M. Salinas-Bravo and G. Lara-Rodriguez, "Effect of Pt, Pd, Au and Ag on oxidation behaviour of Fe3Al intermetallic," *Corrosion Eng. Sci. and Technol.,* vol. 51, pp. 179-186, 2016.

[40] Y. Liu, H. Huang, y. pan, G. Zhao and Z. Liang, "Study corrosion in biocompitible metals for implants: a review," *J. Alloys and Compd.,* vol. 597, pp. 200-204, 2014.

[41] S.J.L. Kang, Sintering metallurgy, Oxford: Butterworth-Heinemann, Elsevier, 2018.

[42] I. Shon, K. Na, J. Doh, H. Park and J. Yoon, "Simultaneous synthesis and consolidation of nanocrystalline Fe2Al5 and Fe2Al5-Al2O3 by pulsed current activated sintering and their mechanical properties," *Met. Mater. Int.,* vol. 19, pp. 99-103, 2013.

[43] H.R Chauke, B. Minisini, R. Drautz, D.N. Manh, P.E Ngoepe and D.G. Petifor, "Theoretical investigation of the Pt3Al ground state," *intermetallics,* vol. 28, pp. 417-421, 2010.

[44] L. Shao, Y. Shi , J. Huang and S. Wu, "Effect of joining parametres on microstructures of dissimilar metal joints between aluminum and galvanized steel," *Mater. des.,* vol. 66, pp. 453-458, 2015.

[45] M.W. Chase, "NIST - JANAF thermochemical tables," *J. Phys. Chem. Ref. Data.,* vol. 4, pp. 1-100, 1998.

[46] S. Chou, J. Huang, D. Lii and H. Lu, “The mechanical properties of Al2O3/Aluminum alloy A356 composite manufactured by squeeze casting,” *J. Alloy Compd.,* vol. 419, pp. 98-102, 2006.

[47] P.J. Maziasz, G.M. Goodwin, C.T. Liu and S.A. David, “Effects of minor alloying elements on the welding behaviour of feA1 alloys for structural and weld-overlay cladding applications,” *Metall. et Mater.,* vol. 27, pp. 1835-1840, 1992.

[48] N.S. Stoloff, C.T. Liu and S.C. Deevi, “Emerging applications of intermetallics,” *Intermetallics,* vol. 8, pp. 1313-1320, 2000.

[49] U. Prakash and G. Sautho, “Structure and properties of Fe-Al-Ti intermetallic alloys,” *Intermetallics,* vol. 9, pp. 107-112, 2001.

[50] V.N. Antonov, O.V. Krasovska, E.E. Krasovskii, Y.V. Kudryavtsev, V.V. Nemoshkalenko, B.Y. Yavorsky, Y.P. Lee and K.W. Kim, “Experimental and theoretical study of the optical properties of FeAl alloy,” *J. Phys. Condens. Mat.,* vol. 9, pp. 11227-11238, 1997.

[51] X. W. Zhou, R.A. Johnson and H.N.G. Wadley, “Modified charge transfer embedded atom method potential for metal alloys,” *Phys. Rev. B,* vol. 69, pp. 035402(1) - 035402(20), 2004.

[52] G. Kresse and J. Furthmüller, “Efficient iterative schemes for ab initio total-energy calculations using a plane-wave basis set,” *Phys. Rev. B,* vol. 54, pp. 11169-11186, 1996.

[53] A.E. Mattson, P.A. Schultz, M.P. Desjarlais, T.R. Mattsson and K. Leung, “Designing meaningful density functional theory calculations in materials science,” *Mod. and Simul. Mater. Sci. and Eng.,* vol. 13, pp. 1-32, 2005.

[54] S. J. Clark, M. D. Segall, C. J. Pickard, P. J. Hasnip, M. J. Probert, K. Refson and M. C. Payne, “First principles methods using CASTEP,” *Zeitschrift fuer Kristallographie,* vol. 220, pp. 567-570, 2005.

[55] G. Kresse, M. Marsman, and J. Furthmulle, “VASP the guide,” *Comp. Mater. Phys., Faculty of Physics, Universit ̈at Wien,* pp. 1-234, 2018.

[56] R. Shan, A. Thompson, S. Plimpton, “Large-scale Molecular Dynamics Simulations with LAMMPS,” *Comput. Mater. Sci. Initi. Int. Symposium ,* pp. 1-48, 2013 .

[57] B. Delley, “From molecules to solids with the DMol3 approach,” *J. chem. phys.,* vol. 113, pp. 7756-7764, 2000.

[58] P.C.H. Sahu and N.V.C. Shekar, “High pressure research on materials,” *Mater. Sci.,* vol. 12, pp. 10-23, 2007.

[59] P. Hohenberg and W. Kohn, “Introduction to density functional theory,” *Phys. Rev.,* vol. 137, pp. 864-871, 1964.

[60] J.C Slater, “Quantum theory of molecules and solids: the self-consistent field for molecules and solids,” *Phys. Tod.,* vol. 4, pp. 49-64, 1974.

[61] G. Jeanmairet, N. Levy, M. Levesque and D. Borgis, “Introduction to clasical density functional theory by a computational experiment,” *Phys. Chem.,* vol. 3, pp. 1-4, 1998.

[62] R. Bader, R. Thom, W. Khon and J. Lejeune-Dirichlet, “Electronic motion: Denxity functional theory (DFT),” *Elsevier,* vol. 11, pp. 568-614, 1994.

[63] J. Harris and R.O. Jones, “The surface energy of a bounded electron gas,” *J. Phys. F: Met. Phys. F,* vol. 4, pp. 1170-1186, 1974.

[64] L. Hedin and B. I. Lundqvist, “Explicit local exchange-correlation potentials,” *J. Phys. C: Solid State Phys.,* vol. 4, pp. 2064-2082, 1971.

[65] E. Wimmer, A. Neckel and K. Schwarz, “The influence of different exchange-correlation potentials on the energy band structure of ScP,” *J. Phys. C: Solid State Phys.,* vol. 12, pp. 5441-5451, 1979.

[66] J.H. Westbrook and R.L. Fleischer and J.W. Chichester, “Intermetallic compounds, principles and practice,” *Intermetallic Compd.,* vol. 3, pp. 471-978, 1995.

[67] E. Matthias and J.P. Perdew, “Generalized gradient approximation to the angle- and system-averaged exchange hole,” *J. Chem. Phys.,* vol. 109, pp. 3313-3334, 1998.

[68] D. Vanderbilt, “Soft self-consistent pseudopotentials in a generalized eigenvalu eFormalism,” *Phys. Rev. B,* vol. 41, pp. 7892-7895, 1990.

[69] A. H. Romero, and M. J. Verstraete, “From one to three, exploring the rungs of Jacob’s ladder inmagnetic alloys?,” *Eur. Phys. J. B,* vol. 91, pp. 1-10, 2018.

[70] J. Tao, J. P. Perdew, V. N. Staroverov, and G. E. Scuseria , “TPSS: Climbing the Density Functional Ladder: Nonempirical Meta-Generalized Gradient Approximation Designed for Molecules and Solids,” *Phys. Rev. Lett.,* vol. 91, pp. 146401(1)-146401(4), 2003.

[71] J. P. Perdew, A. Ruzsinszky, J. Tao, V. N. Staroverov, G. E. Scuseria and G. I. Csonka, “Prescription for the design and selection of density

functionalapproximations: More constraint satisfaction with fewer fits," *J. Chem. Phys.,* vol. 123, pp. 1-10, 2005.

[72] Z. Xiao-lin, Y. Zheng-Jun, G. Xue-dong, C. Wei and Z. Ping-ze, "Microstructure and corrosion resistance of Fe-Al intermetallic coating on 45 steel synthesized by double glow plasma surface alloying technology," *Trans. Nonferrous Met. Soc. China.,* vol. 19, pp. 143 -148, 2009.

[73] C.J. Wu, L.H. Yang, J.E. Klepsis and C. Mailhiot, "Ab-initio pseudopotential calculations of the atomic and electronic structure of the Ta (100) and (110) surfaces.," *Phys. Rev. B,* vol. 52, pp. 11784-11790, 1995.

[74] M. Jiang, G.G. Batrouni and R.T. Scalettar, "Density of states and magnetic correlations at a metal-mott insulator interface," *Cond-Mat.str-el,* vol. 86, pp. 1-7, 2012.

[75] K.F. Garrity, J.W. Bennett, K.M. Rabe and D. Vanderbilt, "Pseudopotentials for high-throughput DFT calculations Rutgers university," *Comput. Mater. Sci.,* vol. 81, pp. 1-9, 2013.

[76] O.K. Andersen, "The Linearized Augmented Planewave (LAPW) Method," *Phys. Rev. B 12,* pp. 3060(1)-3060(21), 1975.

[77] P.E. Blöchl, "Projector augmented-wave," *Phys. Rev. B,* vol. 50, pp. 17953-17979, 1994.

[78] J.J. Mortensen, L.B. Hansen and K.W. Jacobsen, "Real-space grid implementation of the projector augmented wave method," *Phys. Rev. B,* vol. 71, pp. 1-11, 2005.

[79] M.C. Payne, M.P. Teter, D.C. Allan, T.A. Ariar and J.D. Joannopoulos., "Iterative minimizations techniques for ab initio total-energy calculations: molecular dynamics and conjugate gradients," *Rev. Mod. Phys.,* vol. 64, pp. 1045-1097, 1992.

[80] X.W. Zhou, R.A. Johnson and H.N.G. Wadley, "Interatomic potentials repository," *Phys. Rev. B,* vol. 69, pp. 144113(1)-144113(10), 2004.

[81] M. Karplus and J. A. McCammon, "Molecular dynamics simulations of biomolecules," *Nature Struct. Biol.,* vol. 9, pp. 646-652, 2002.

[82] S. Plimpton, "Fast parallel algorithms for short-range molecular dynamic," *J. Comp. Phys.,* vol. 117, pp. 1-19, 1995.

[83] M. P. Allen and D. J. Tildesley, "Molecular dynamic simulation," Oxford University Press, New York Toronto, 2002.

[84] S. Nose, “A molecular dynamics method for simulation in the canonical ensemble,” *Molec. phys.,* vol. 52, pp. 255-268, 1984.

[85] L. Onsage, “Crystal statistics, A two dimensional model with an order-disorder transition,” *Phys. Rev.,* vol. 65, pp. 3-4, 1994.

[86] M.S. Daw and M. Baskes, “Embedded-atom method: derivation and application to impurities, surfaces and other defects in metals,” *Phys. Rev. B,* vol. 29, pp. 6443-6453, 1984.

[87] V. Milman, B. Winkler, J.A. White, C.J. Pickard, M.C. Payne, E.V. Akhmatskaya and R.H. Nobes, “Electronic structure of materials,” *Int. J. Quantum Chem.,* vol. 77, pp. 799-926, 2000.

[88] M.D. Segall, P.L.D. Lindan, M.J. Probert, C.J. Pickard, P.J. Hasnip, S.J. Clark and M.C. Payne, “First-principles simulation:ideas, illustrations and the CASTEP code,” *J. Phys. Cond. Matt.,* vol. 14, pp. 2717-2744, 2002.

[89] P. Blöchl, “ Projector augmented-wave method,” *Phys. Rev. B,* vol. 50, p. 17953–17979, 1996.

[90] P. Dianat, “Unconventional photo capacitorwith giant light inducedcapacitance enhancement,” *Elsevier,* pp. 472-510, 2016.

[91] J. S. Gómez-Jeria, “A New Set of Local Reactivity Indices within the Hartree-Fock-Roothaanand Density Functional Theory Frameworks,” *Borderless Sci. Pub.,* vol. 1, pp. 25-55, 2013.

[92] M. Karplus and J. A. McCammon, “Molecular dynamics simulations of biomolecules,” *Nature Struct. Biol.,* vol. 9, pp. 646-652, 2002.

[93] E. Ippoliti, Parrallel algorithms for short-range molecular dynamics, Biophysics application project, 2001.

[94] B. Delley, “An all-electron numerical method for solving the local density functional for polyatomic molecules,” *J. chem. phys.,* vol. 92, pp. 508-517, 1009.

[95] X. W. Zhou, H. N. G. Wadley, J.-S. Filhol and M. N. Neurock, “Modified charge transfer–embedded atom method potential for metal Õ metal oxide systems,” *Phys. Rev. B,* vol. 69, pp. 035402(1)- 035402(20), 2004.

[96] X. Cai, Y. Liu, P. Feng, X. Jiao, L. Zhang, J. Wang , “Fe-Al intermetallic foam with porosity above 60 % prepared by thermal explosion,” *J. Alloys and Compd.,* vol. 732, pp. 443-447, 2018.

[97] R.G. Hennig, A.E. Carlsson, K.F. Kelton and C.L. Henley, “Ab-initio Ti-Zr-Ni phase diagram predicts stability of icosahedral TiZrNi quasicrystals,” *Phys. Rev. B,* vol. 71, pp. 144103 (1)-144103 (10), 2005.

[98] J. Breur, A. Gru, F. Sommer and E.J. Mittmeijer, “Enthalpy of formation of B2-Fe1-xAlx and B2-(Ni,Fe)1-xAlx,” *Metall. Mater. Trans. B,* vol. 32, pp. 913-918, 2001.

[99] F.S. Pierce, D.N. Basov, P. Volkov, S.J. Poon and T. Timusk, “F.S. Pierce, D.N. Basov, POptical Conductivity of Insulating Al-Based Alloys: Comparison of Quasiperiodic and Periodic Systems,” *Phys. Rev.,* vol. 73, pp. 1865-1887, 1994.

[100] A. Matsuda, S. Sugita, T. Fujii and T. Watanabe, “Study of Pseudogap Phenomena by STM and Other Probes,” *J.Phys. Chem. Solids,* vol. 62, pp. 65-87, 2001.

[101] G.J. Ackland, “High-pressure semiconductor semimental transition in TiS2,” in *Phys. Rev.* , Durham, 1998.

[102] M.J. Phasha, “MSc dissertation,” University of Limpopo, Polokwane, 2005.

[103] S. Kamran, K. Chen and L. Chen, A matter of density: exploring the electron density concept in the chemicaL, biological and materials sciences, Shiv Nadar University, India.: N. Sukumar, 2009.

[104] L.Q. Zhang, Y. Cheng and Z.W. Niu, “Elastic properties and phonon dispersion of bcc anadium under pressure from first priciples,” *J. At. Mol. Sci,* vol. 5, pp. 81-93, 2014.

[105] M.J. Mehl, B.M. Klein and D.A. Papaconstantopoulos, Structural properties of ordered high-melting-temperature intermetallic alloys from first-principles total-energy calculations, In: J.H. Westbrook and R.L. Fleischer: John Wiley & Sons Ltd, 1994.

[106] R.R. Mahlangu, “MSc dissertation,” university of Limpopo, Polokwane, 2000.

[107] I. Tamm, “From the history of Physics,” *Phys. Usp.,* vol. 38, pp. 773-790, 1995 .

[108] R. Eiblert and A. Neckelt, “The density-of-states functions of the ordered alloys FeAl and their relation to experimental data; calculations of the imaginary part of the complex dielectric function,” *J. Phys. F: Met. Phys.,* vol. 10, pp. 2179-2195, 1980.

[109] M.S. Lucas, O. Delaire, M.L. Winterrose, T. Swan-Wood, M. Kresch, I. Halevy, B. Fultz, Jingzhu, M. Lerche, M. Y. Hu and M. Somayazulu,

"Effects of vacancies on phonon entropy of B2 FeAl," *Phys. Rev. B, Cond. Mat. and Mater. Phys.,* vol. 80, pp. 214-303, 2009.

[110] J.W. Gibbs, "A method of geometrical representation of the thermodynamic properties of substances by means of surfaces," *Trans. Conn. Acad. Arts Sci.,* vol. 2, pp. 382-404, 1873.

[111] Y. Lwin, "Chemical Equilibrium by Gibbs Energy Minimization on Spreadsheets," *Int. J. Eng. Ed.,* vol. 16, pp. 335-339, 2000.

[112] T.S. Seletskaia, "Calculation of thermal expansion of iron-aluminides with transition metal," California State University, East Bay, 2002.

[113] N. Cinca, C. R. C. Lima and J. M. Guilemany , "An overview of intermetallics research and application stataus of thermal spray coatings," *J. Mater. Res. Technol.,* vol. 2, pp. 75-86, 2013.

[114] R. Mahlangu, M.J. Phasha, H.R. Chauke and P.E. Ngoepe, "Structural, elastic and electronic properties of equiatomic PtTi as potential high-temperature shape memory alloy," *Intermetallics,* vol. 33, pp. 27-32, 2013.

[115] M.J. Phasha, P.E. Ngoepe, H.R. Chauke, D.G. Pettifor and D. Nguyen-Mann, "Link between structural and mechanical stability of FCC- and BCC-based ordered Mg-Li alloys," *Intermetallics,* vol. 18, pp. 2083-2089, 2010.

[116] Y. N. Gornostyrev, O. Y. Kontsevoi, A. F. Maksyutov, A. J. Freeman, M. I. Katsnelson, A. V. Trefilov and A. I. Lichtenshtein, "Negative yield stress temperature anomaly and structural instability of Pt3Al," *Phys. Rev. B,* vol. 70, pp. 1-5, 2004.

[117] D. A. Pankhurst, D. Nguyen-Manh and D. G. Pettifor, "Electronic origin of structural trends across early transition-metal disilicides: anomalous behavior of CrSi2," *Phys. Rev. B,* vol. 69, pp. 1-9, 2004.

[118] S.F. Pugh, "XCII. relations between the elastic moduli and the plastic properties of polycrystalline pure metals," *The London, Edinburgh, Dublin Philos. Mag. and J. Sci.,* vol. 45, pp. 823-843, 1954.

[119] X. Li, "Al-rich Fe-Al base alloys: phase equilibria, microstructures, coarsening kinetics and mechanical behaviour," Aus Hohhot, Volksrepublik, China, 2016.

[120] M. Palm, G. Inden and N. Thomas, "The Fe-A1-Ti system," *J. Phase Equilib.,* vol. 16, pp. 209-222, 1995.

[121] M. Palm and J. Lacaze., "Assessment of the Al-Fe-Ti system," *Intermetallics,* vol. 16, pp. 1291-1303, 2006.